Reference-free combined analysis GIXRF-XRR for the characterization of thin film materials and uncertainties calculation

Stephanie Melhem

THESE DE DOCTORAT

NNT : 2023UPASP112

Reference-free combined analysis GIXRF-XRR for the characterization of thin film materials and uncertainties calculation

Analyse combinée GIXRF-XRR sans référence pour la caractérisation des matériaux en couches minces et calcul des incertitudes

Thèse de doctorat de l'université Paris-Saclay

École doctorale n◦576 Particules, hadrons, énergie et noyau : instrumentation, imagerie, cosmos et simulation (PHENIICS)
Spécialité de doctorat : Physique des particules
Graduate School : Physique. Référent : Faculté des sciences d'Orsay

Thèse préparée dans l'unité de recherche **Institut LIST** (Université Paris-Saclay, CEA), sous la direction de **Marie-Christine LÉPY**, directrice de recherche et le co-encadrement de **Yves MÉNESGUEN**, ingénieur de recherche.

Thèse soutenue à Paris-Saclay, le 25 septembre 2023, par

Stephanie Melhem

Composition du Jury

Membres du jury avec voix délibérative

Anne LAFOSSE Professeur, Université Paris-Saclay/ Institut des sciences moléculaires d'Orsay CNRS	Présidente
Daniel CHATEIGNER Professeur, Université de Caen Normandie (IUT Caen)	Rapporteur & Examinateur
Philippe JONNARD Directeur de recherche CNRS, Sorbonne Université/ Laboratoire de Chimie Physique Matière et Rayonnement (LCPMR)	Rapporteur & Examinateur
Burkhard BECKHOFF Directeur de recherche, Physikalisch-Technische Bundesanstalt (PTB)	Examinateur
Emmanuelle BRACKX Ingénieure de recherche, Université de Montpellier/ CEA Marcoule (DES/ISEC/DMRC/SASP/LMAT)	Examinatrice
Frank DELMOTTE Professeur, Université Paris-Saclay/ Institut d'Optique Graduate School	Examinateur

Acknowledgements

First, I wish to express my gratitude to the Laboratoire National Henri Becquerel of CEA LIST for granting me the privilege to work in such a pioneering environment, where collaboration, innovative spirit, and groundbreaking scientific pursuits thrive.
I would like to express my deepest appreciation and gratitude to my supervisor, Yves Ménesguen, and my thesis directress, Marie-Christine for their patience, kindness, constant guidance, clear expertise, and steady support that have been foundational to my research. This thesis would not have come to fruition without the distinct roles both of you played throughout these three years. I am profoundly thankful for having both of you as my bosses, not only for your professional guidance but also for the personal connections we created. From the shared laughter, the invaluable moments in the lab, to the memories created during conferences, I'll forever be indebted for your support, especially during the most challenging phases of my thesis.
Deep appreciation is extended to Philippe Jonnard and Daniel Chateigner for their role as reporters. Their feedback and evaluation have been instrumental in refining this work. I'm also grateful to Emmanuelle Brackx, Anne Lafosse, Burkhard Beckhoff, and Franck Delmotte to be part of the jury and dedicating their time to examine my work.
A special acknowledgment goes out to Emmanuel Nolot from CEA LETI for providing samples for the experimental measurements. This thesis would indeed be incomplete without the critical facilities and expertise from the SOLEIL Synchrotron. In this regard, I would like to thank Pascal Mercere and Paulo Da Silva from the Metrology beamline of SOLEIL synchrotron for their support.
Immense gratitude to the head of the LNHB Mark Kellett for his invaluable support and his help in revising and fine-tuning my manuscript.
My colleague and friend, Victor Hernandez, deserves a special mention for his active contribution and assistance in my experimental work. Also a big thank is extended to my colleague Benoit Sabot for for his invaluable assistance in the 3D drawing and his expertise in the use of SolidWorks software which was invaluable and significantly enhanced my work.
I extend my heartfelt thanks to all my friends and colleagues in the lab, with whom I've shared countless moments of friendship. From shared laughter to coffee breaks and lunch discussions, those seemingly small interactions often offered the most cherished breaks in my days. The moments we spent together during those crucial times were refreshing, and they kept me grounded and energized throughout my thesis.
Lastly, it is of utmost significance to express the deepest gratitude towards my family, who were sources of support and resilience. The unconditional love, limitless support, and unwavering belief in my abilities have served as a consistent source of strength and encouragement in my PhD studies.

Résumé étendu

1. Introduction

Avec le progrès technologique croissant, il est impératif de développer de nouveaux matériaux qui non seulement répondent aux exigences technologiques, mais sont également respectueux de l'environnement. L'amélioration des cellules photovoltaïques, des batteries, et la capacité des mémoires sont des priorités clés. Ces dispositifs s'appuient en grande partie sur des matériaux nanostructurés et sur des films minces. Pour assurer la qualité de ces films minces, une technique de caractérisation précise et non destructive, comme la fluorescence et la réflectivité des rayons X sous incidence rasante, est indispensable.

2. Objectif

Le but principal de cette recherche est de développer et d'optimiser une méthode d'analyse combinant les techniques GIXRF (Fluorescence X sous Incidence Rasante) et XRR (Réflectométrie de Rayons X) pour une caractérisation plus complète et précise des couches minces, et calculer les incertitudes sur leur structure. L'analyse combinée nécessite en plus la connaissance des paramètres fondamentaux atomique, d'où l'objectif de les mesurer et de calculer leurs incertitudes. En plus des paramètres fondamentaux atomiques, l'angle solide de détection est un autre paramètre important à calculer pour cette analyse. L'objectif est d'explorer et d'affiner l'analyse combinée GIXRF-XRR pour les films minces et d'évaluer l'efficacité de cette combinaison en caractérisant des échantillons de GeSbTe (GST) et de tantale (Ta). De plus, cette technique a été appliquée pour analyser les effets d'un recuit sur la structure des échantillons GST.

3. Techniques Analytiques

Dans cette thèse, on a utilisé la combinaison de la GIXRF et de la XRR pour la caractérisation des couches minces. La GIXRF est sensible à la densité élémentaire et renseigne sur la distribution en profondeur des éléments et la XRR est sensible à la densité électronique, elle permet d'obtenir des informations sur la densité, l'épaisseur et la rugosité des films.

4. Instruments et Méthodes

4.1. Ligne de MÉTROLOGIE

Les expériences ont été réalisées à SOLEIL, source de rayonnement X par effet synchrotron. Parmi ses 29 lignes de lumière, la ligne de Métrologie, située à la sortie d'un aimant de courbure, a été utilisée pour les expériences de cette thèse. Cette ligne fournit un faisceau de photons avec une divergence horizontale totale de 8 mrad pour alimenter 2 branches distinctes et s'étend sur une gamme énergétique de 45 eV à 40 keV. Les mesures de fluorescence ont été effectuées sur la branche de rayons X durs de la ligne. Cette branche est caractérisée par une acceptance de 1,7 mrad horizontalement et 0,153 mrad verticalement. Elle est équipée de fentes de collimation, d'un monochromateur à double cristal Si (111) pour fournir des photons monochromatiques de haute énergie (entre 3 keV et 30 keV) et d'une série de fentes de sortie pour ajuster la taille du faisceau.

4.2. Le Goniomètre CASTOR

L'instrument CASTOR (Chambre d'Analyse Spectrométrique en Transition ou/et en Réflexion) est un goniomètre dédié, utilisé pour faire les mesures combinées de GIXRF-XRR (Figure 1). Ce goniomètre comporte plusieurs moteurs de translation et de rotation permettant de changer la position des échantillons, l'angle d'incidence, la position du détecteur et l'angle de détection. Sa précision est primordiale pour garantir la fiabilité des données. Un étalonnage des détecteurs et un alignement précis des moteurs sont essentiels pour assurer la qualité des mesures.

4.3. Alignement

La moindre erreur d'alignement peut entraîner des imprécisions significatives. Il est donc crucial d'assurer une parfaite orientation des échantillons. L'importance des moteurs rotationnels et du positionnement ne peut être sous-estimée et toute mesure commence par l'alignement précis des échantillons par rapport au faisceau incident, en suivant une procédure stricte.

5. Paramètres fondamentaux et calcul des incertitudes

Ces paramètres, tels que le rendement de fluorescence, le coefficient d'atténuation massique et le coefficient d'absorption photoélectrique, sont très importants pour l'analyse GIXRF-XRR. Des éléments clés comme Fe et Y ont été étudiés pour mesurer leurs rendements de fluorescence, leurs coefficients d'atténuation massiques, et leurs coefficients d'absorption photoélectrique. Le coefficient d'atténuation massique a été obtenu en mesurant l'atténuation subie par le rayonnement traversant un échantillon de référence grâce à la loi de Beer-Lambert. Cette mesure a été effectuée à l'aide d'une photodiode positionnée derrière l'échantillon. Le coefficient d'absorption photoélectrique, a été calculé à partir du coefficient d'atténuation massique, en faisant des extrapolations linéaires pour des énergies inférieures aux seuils d'absorption : le coefficient d'absorption photoélectrique est égal à la différence entre le coefficient d'atténuation massique et la courbe extrapolée. Finalement le rendement de fluorescence est calculé grâce à l'équation de Sherman en mesurant l'intensité de la fluorescence à 45° avec un détecteur à

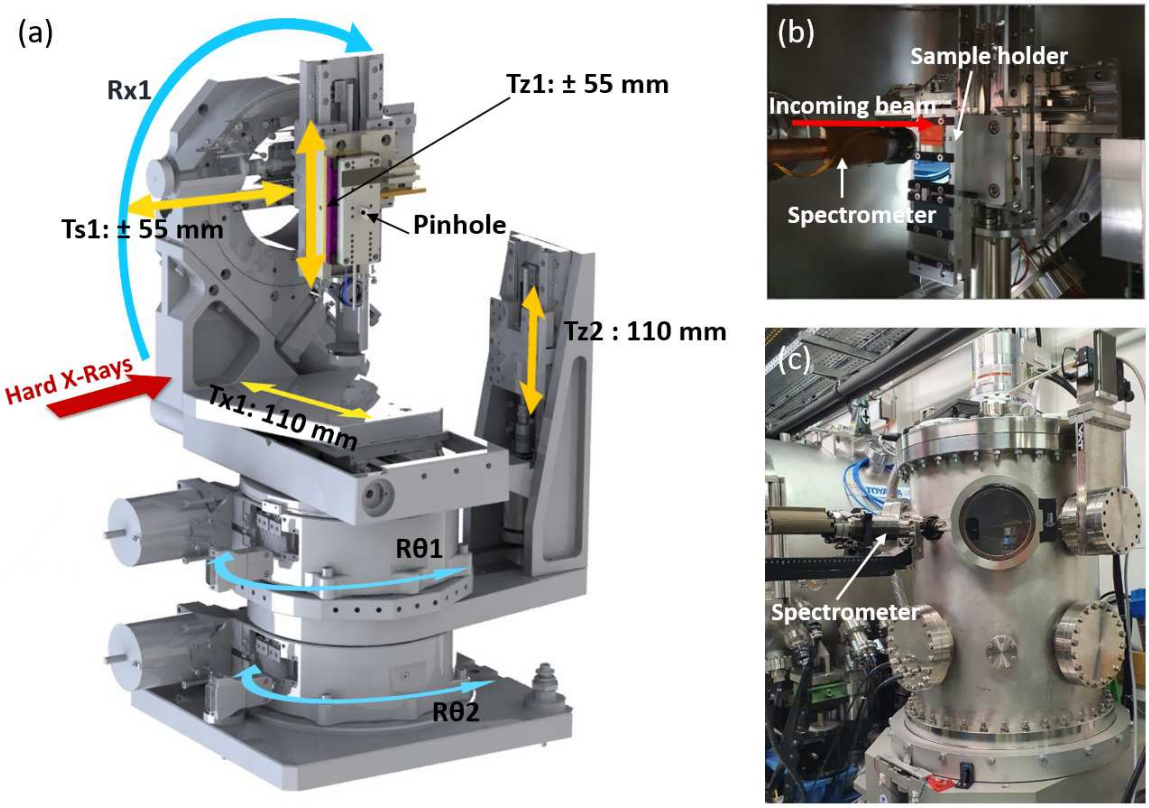

Figure 1: Goniomètre CASTOR à 7 axes. (a) Croquis 3D de l'intérieur, (b) vue intérieure avec le SDD et le porte-échantillons et (c) photo de l'extérieur de CASTOR.

dispersion d'énergie (silicon drift detector, SDD). Les incertitudes sur les paramètres fondamentaux ont été calculées, en faisant des répétitions de mesure à différentes énergies d'incidence, et en utilisant l'équation de propagation des incertitudes pour prendre en compte toutes les contributions.

6. Optimisation

L'objectif est de déterminer la structure du film mince qui correspond le mieux aux données expérimentales, à la fois en XRR et GIXRF. Dans la GIXRF, l'optimisation est basée sur l'ajustement d'un modèle théorique aux intensités de fluorescence expérimentales en fonction de la profondeur. Les paramètres de ce modèle (épaisseur, densité, composition, rugosité) sont ensuite ajustés pour correspondre aux données expérimentales. L'analyse XRR suit une approche similaire, mais se focalise sur la courbe de réflectivité. L'association de ces deux méthodes permet une caractérisation précise des couches nanométriques, en éliminant les résultats ambigus dus à la présence potentielle de minima locaux lors de l'optimisation par recherche globale. Toutefois, pour réussir cette procédure d'optimisation, une connaissance préalable de la structure de l'échantillon est essentielle. Sans cela, les résultats peuvent être non réalistes ou incorrects. Le logiciel COLEGRAM est utilisé pour l'analyse des spectres de fluorescence X (XRF). Il propose plusieurs formes de pics pour traiter les spectres complexes. Dans cette étude, l'ajustement des données de XRF est réalisé en minimisant les moindres carrés. Par

ailleurs, le logiciel IMD (Interactive Multi-layer Design) est utilisé pour analyser initialement les données de réflectivité. Il aide à modéliser et analyser les structures de films minces à l'aide de données de réflectivité de rayons X. Pour ce faire, un algorithme génétique est utilisé. L'analyse combinée du GIXRF et du XRR est ensuite effectuée par le logiciel ELIXIR, développé au LNHB. Ce logiciel de pointe comprend tous les outils nécessaires pour le calcul de la XRR et de la GIXRF ainsi qu'une procédure d'optimisation, en utilisant les paramètres de la configuration expérimentale, la structure multicouche de l'échantillon et les mesures expérimentales. Initialement, nous nous concentrons sur les paramètres clés qui influencent le plus la mesure, ainsi que sur les considérations spécifiques nécessaires pour ajuster les données générées par chaque technique. Nous prenons en compte les facteurs géométriques tels que l'empreinte du faisceau incident sur l'échantillon et l'angle solide de détection. Par la suite, l'analyse complète et la méthode d'optimisation utilisée dans le logiciel ELIXIR s'appuie sur les données expérimentales de la XRR et de la GIXRF, ainsi que sur la première estimation de la structure réalisée grâce à IMD basée uniquement sur la XRR. En comprenant et en connaissant ces éléments, la combinaison de la XRR et de la GIXRF est capable de trouver un modèle précis et exact des paramètres de structure de l'échantillon.

7. Calcul des incertitudes

L'angle solide entre l'échantillon et le détecteur SDD est une mesure essentielle en GIXRF qui influence la qualité des résultats. Son calcul exact dépend de plusieurs paramètres, dont l'alignement précis de l'échantillon, la position de l'empreinte et les facteurs géométriques du spectromètre SDD. L'alignement en XRR ou GIXRF nécessite des étapes itératives pour s'assurer que l'axe de rotation coïncide avec l'axe du faisceau et que l'échantillon est bien aligné avec le faisceau. L'incertitude associée à l'angle solide est tout aussi cruciale. Elle est influencée par divers paramètres, tels que les dimensions de la fente de collimation du faisceau, l'angle d'incidence, la distance entre le collimateur du SDD et les échantillons, et la précision des composants du détecteur. Pour estimer cette incertitude, une méthode basée sur les simulations de Monte Carlo est employée. Les résultats montrent que l'incertitude sur les angles solides est relativement faible (entre 0,4 % et 0,8 %), principalement en raison de faibles incertitudes sur les dimensions des composants du détecteur mesurées par radiographie.
La combinaison des analyses XRR-GIXRF présente une complexité qui rend difficile le calcul d'incertitude avec des méthodes analytiques conventionnelles. Cette complexité découle du grand nombre de paramètres d'ajustement et de la procédure de double optimisation. Une méthode alternative a été explorée en utilisant le « Bootstrap » à poids aléatoire. Ce procédé statistique ne nécessite pas de connaissance préalable des distributions de probabilité pour extraire des données statistiques telles que les écarts-types ou les intervalles de confiance. Sa base repose sur les simulations de Monte Carlo pour recréer plusieurs ensembles de données simulés à partir d'un jeu unique initial par re-échantillonnage. Cette approche modifiée a été adoptée, en considérant chaque valeur d'intensité de XRR et GIXRF pour chaque angle d'incidence comme un échantillon individuel. Dans ce contexte, des fonctions de coût normalisées pour la XRR et la GIXRF ont été formulées en utilisant des poids appliqués à chaque angle de mesure. Après la mise en œuvre répétée de cette méthode « Bootstrap », il est possible de générer de nouvelles structures d'échantillons possibles avec des variations dans les paramètres. Cela permet ensuite de faire une étude statistique pour chaque paramètre ajusté. En résumé, cette application innovante de la méthode « Bootstrap » au contexte GIXRF-XRR montre qu'il est

possible d'évaluer efficacement les incertitudes pour les paramètres des échantillons sans répéter les mesures, ce qui offre un avantage en terme d'efficacité.

8. Échantillons mesurés

Au cours de nos recherches, nous avons mesuré des couches minces de deux catégories différentes. La première catégorie comprend des couches minces de GST : certaines riches en Ge, d'autres en Te, et enfin celles qui sont riches en Sb. Pour chaque structure, deux échantillons ont été élaborés. Le premier est conservé dans son état d'origine, tandis que le second a été soumis à un processus de recuit. Le but de mesurer ces échantillons et de voir si la GIXRF-XRR est capable de détecter le changement de la structure des échantillons après le recuit. La seconde catégorie est une série de couches minces à base de tantale Ta_2O_5. Ces couches ont été spécifiquement dopées avec différents éléments, tels que l'oxyde de fer Fe_2O_3 et l'oxyde d'yttrium Y_2O_3. Le but est de comparer la concentration des dopants calculée par GIXRF-XRR, avec les valeurs estimées par le fabricant, afin de valider la précision et la fiabilité des processus de fabrication utilisés. Il est à noter que l'ensemble de ces échantillons a été élaboré en utilisant la méthode de pulvérisation cathodique. Le but ultime de l'analyse de tous ces échantillons est d'approfondir notre compréhension des propriétés et comportements variés de ces films minces et de calculer les incertitudes sur les paramètres structurels.

9. Résultats

9.1. GST riche en Te

La comparaison entre les données expérimentales et simulées, que ce soit pour les résultats XRR ou GIXRF, montre une excellente cohérence (Figure 2). Cette concordance valide la fiabilité de l'analyse structurale des échantillons à l'aide de la méthode combinée GIXRF-XRR. En comparant les résultats de l'analyse GIXRF-XRR avec les données du fabricant, de légères différences ont été observées. Par exemple, l'épaisseur et la densité mesurées étaient légèrement différentes des valeurs nominales, suggérant quelques imprécisions possibles lors du dépôt des échantillons. L'analyse d'incertitude est également cruciale. Deux approches ont été envisagées : la technique « Bootstrap » seule et une combinaison de « Bootstrap » avec les incertitudes des paramètres fondamentaux et d'angle solide. Si l'inclusion des incertitudes des paramètres fondamentaux a augmenté les intervalles de confiance, ces derniers sont restés dans des limites acceptables. Toutefois, l'étude n'a pas encore pris en compte certaines incertitudes, telles que celles liées aux coefficients d'atténuation massique ou à la configuration expérimentale. Ces éléments pourraient influencer de manière significative les résultats et méritent donc d'être explorés dans des travaux futurs. En conclusion, l'étude a montré la pertinence et la précision des techniques GIXRF-XRR pour l'analyse structurale des échantillons GST riches en Te. Il est essentiel d'inclure toutes les sources potentielles d'incertitude pour garantir la fiabilité des résultats.

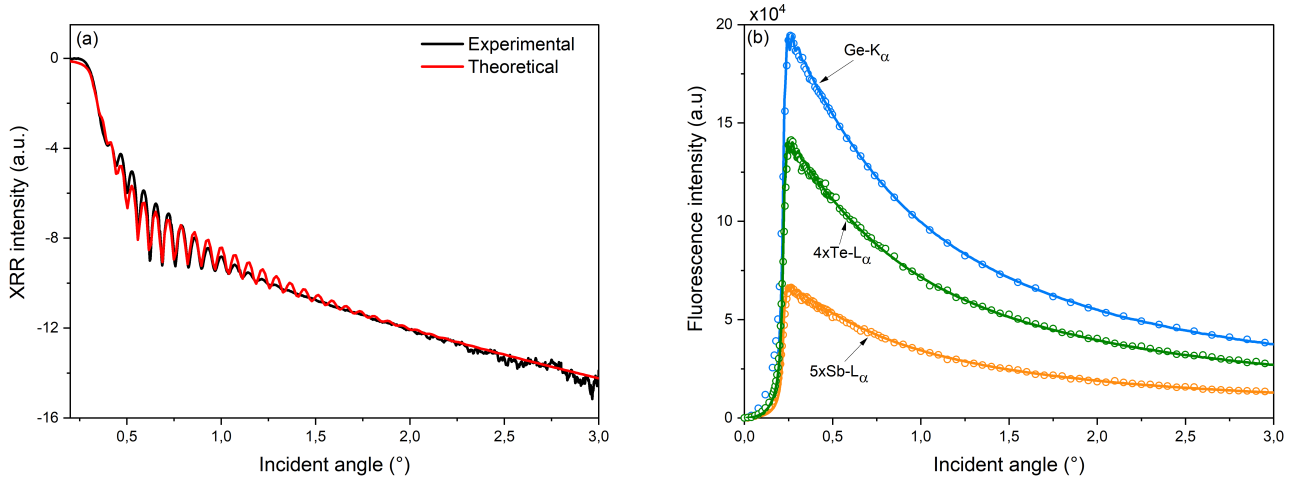

Figure 2: Intensité XRR mesurée à 8 keV en échelle logarithmique (gauche). Les courbes noires et rouges représentent respectivement la réflectivité mesurée et ajustée (a) et la GIXRF de Ge-K_α (bleu), Sb- L_α (orange) et Te- L_α (vert) mesurée à 11,5 keV (droite).

9.2. GST riche en Sb

Les échantillons de GST riches en Sb se présentent sous deux formes : tel que déposé et après recuit. Le processus de recuit, qui consiste à chauffer l'échantillon à 300°C, provoque une transition de l'état amorphe à l'état cristallin, entraînant des modifications structurales. Les mesures par XRR et GIXRF ont été utilisées pour analyser ces échantillons. Les résultats montrent que le modèle ajusté pour l'échantillon tel que déposé s'accorde bien avec les données expérimentales (Figure 3 (a)). Cependant, pour l'échantillon recuit, malgré un accord en termes d'intensité réfléchie et de position des franges de Kiessig, des différences significatives sont observées (Figure 3 (b)). Ces divergences pourraient être dues à des changements dans les densités des couches après recuit ou à des complexités dans les effets de diffusion et les erreurs de mesure.

En outre, les mesures GIXRF montrent une augmentation de l'intensité des lignes d'émission des trois éléments après recuit, indiquant des changements dans la densité ou l'épaisseur de la couche de GST (Figure 4). L'analyse structurale révèle que l'échantillon tel que déposé est proche des données du fabricant. Toutefois, après recuit, des modifications notables sont observées. La couche de recouvrement en Si se divise en deux, indiquant une possible oxydation pendant le processus de recuit. De plus, la couche GST se divise également en deux, montrant une transition partielle de l'état amorphe à l'état cristallin. Les incertitudes associées à l'épaisseur, la densité et la rugosité sont faibles pour les deux échantillons, démontrant la précision de l'analyse combinée GIXRF-XRR pour la caractérisation des films minces.

Pour l'échantillon tel que déposé, on obtient des incertitudes relatives d'environ 4,3% pour l'épaisseur, 5,3% pour la densité et 5% pour la rugosité de la première couche; et 4,3% pour l'épaisseur, 3,7% pour la densité et 5,7% pour la rugosité de la seconde couche. Pour l'échantillon recuit les incertitudes relatives sont d'environ 5,7% pour l'épaisseur, 5,6% pour la densité et 5% pour la rugosité de la première couche. Pour les couches suivantes, ces valeurs varient légèrement mais restent proches, indiquant une précision similaire pour les deux échan-

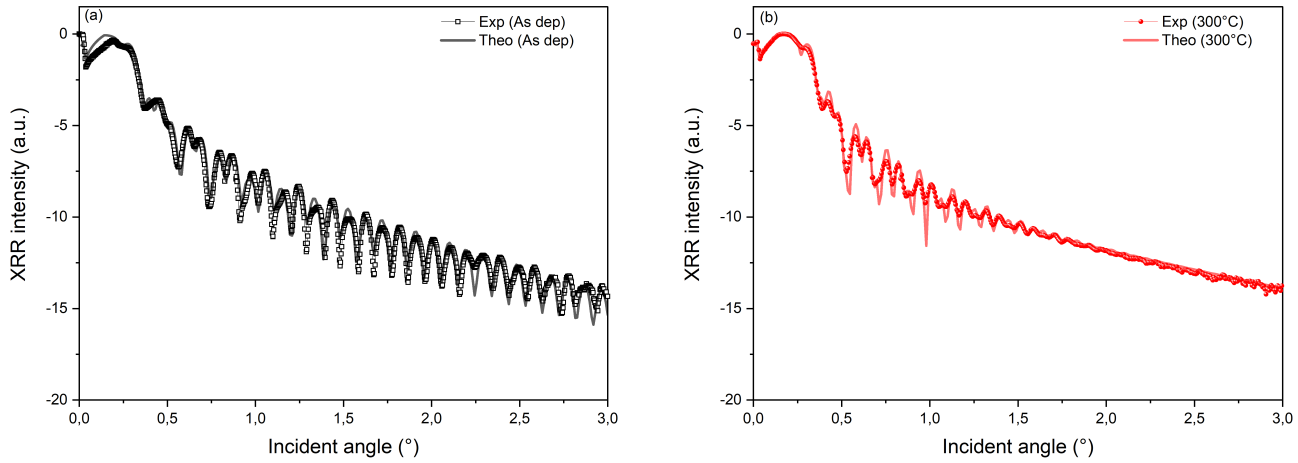

Figure 3: Analyse XRR du GST riche en Sb : (a) et (b) balayages et ajustements pour les échantillons tels que déposés et recuits respectivement. Les courbes avec des symboles pleins représentent les données expérimentales, tandis que les courbes de couleur légèrement transparente représentent les ajustements correspondants.

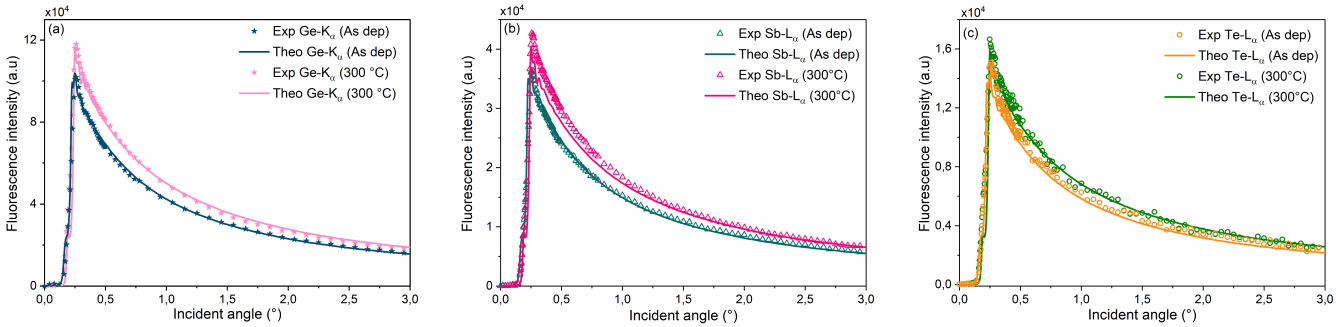

Figure 4: (a), (b) et (c) Balayages GIXRF et ajustement de Ge- K_α, Sb- L_α et Te- L_α respectivement des échantillons tels que déposés et recuits.

tillons, bien que légèrement plus élevée pour l'échantillon recuit.

9.3. Échantillons Ta_2O_5 dopés avec Fe_2O_3 ou Y_2O_3

Pour l'échantillon dopé au fer, bien que l'épaisseur et la densité mesurées correspondent étroitement aux données du fabricant, la concentration de dopage a montré une différence significative. Une couche additionnelle d'oxyde de silicium a également été identifiée, indiquant une possible oxydation du substrat ou un résultat du processus de fabrication. L'échantillon dopé avec Fe_2O_3 a montré une épaisseur de 32,1(17) nm, une densité de 7,98(42) g/cm3 et une concentration de dopage de 0,32 %, alors que la spécification du fabricant pour la concentration était de 0,1 %. L'incertitude relative associée à ces mesures était respectivement de 5 %, 5,3 % et 5,3 %. En ce qui concerne l'échantillon dopé à l'oxyde d'yttrium, malgré une équivalence en épaisseur, il a été observé un écart important dans la concentration de dopage par rapport à la spécification du fabricant. Cet échantillon présentait également une fine couche d'oxyde de silicium. Les incertitudes sur les résultats ont été calculées grâce à la méthode « Bootstrap »

présentée précédemment. L'échantillon dopé avec Y_2O_3 a révélé une épaisseur de 27,6(21) nm, une densité de 7,30(49) g/cm3 et une concentration de dopage de 0,95 %, en contraste avec la cible du fabricant de 6,0 %. Les incertitudes pour les paramètres de cet échantillon étaient de 7,6 %, 6,7 % et 7,2 % respectivement.

Table 1: Comparaison entre les résultats GIXRF-XRR et les données du fabricant des paramètres de structure de l'échantillon de la coucheTa_2O_5 dopée avec Fe_2O_3 avec les incertitudes associées.

	Composition	Epaisseur (nm)	Densité (g/cm^3)	Concentration de dopant (%)	Rugosité (nm)
Données fabricant	Ta_2O_5/Fe_2O_3	32	8.18	0.1	-
GIXRF-XRR	$Ta_2O_{5.03}Fe_{0.018}$	32.1(17)	7.98(42)	0.32	1.14(6)

Table 2: Comparaison entre les résultats GIXRF-XRR et les données du fabricant des paramètres de structure de l'échantillon de la couche Ta_2O_5 dopée avec Y_2O_3 avec les incertitudes associées.

	Composition	Epaisseur (nm)	Densité (g/cm^3)	Concentration de dopant (%)	Rugosité (nm)
Données fabricant	Ta_2O_5/Y_2O_3	28	8.18	6	-
GIXRF-XRR	$Ta_2O_{5.09}Y_{0.06}$	27.6(21)	7.30(49)	0.95	0.69(5)

En résumé, les techniques GIXRF-XRR ont prouvé leur valeur en fournissant une caractérisation détaillée de ces échantillons, mettant en évidence des écarts par rapport aux données du fabricant. Ces résultats soulignent l'importance d'une méthode de caractérisation approfondie pour les films minces.

10. Développement d'un spectromètre à dispersion de longueur d'onde (WDS)

Dans le cadre de l'amélioration de la résolution énergétique des spectres de fluorescence (XRF) nous avons entrepris le développement d'un nouveau spectromètre à dispersion de longueur d'onde (WDS) avec une géométrie von Hamos simplifiée. L'objectif dans cette thèse était de réaliser un prototype de détecteur de haute résolution nouvellement conçu pour mesurer la fluorescence (Figure 5), en vue de son intégration dans le goniomètre CASTOR. Le prototype du WDS a été spécifiquement développé pour être pleinement opérationnel à l'air libre sur la ligne de faisceau MÉTROLOGIE du synchrotron SOLEIL. Il est composé de trois éléments principaux : la source de rayons X, un cristal dispersif et un détecteur sensible en position. Contrairement à la géométrie von Hamos classique, ce prototype utilise un cristal plat. Plusieurs cristaux peuvent être utilisés pour varier la gamme d'énergies détectées pour

une gamme d'angles de Bragg donnés. Le prototype a été testé sur des éléments métalliques purs. Comparé au spectromètre à dispersion d'énergie, le WDS offre une résolution énergétique nettement supérieure. Par exemple, avec ce WDS, il a été possible de séparer et d'identifier clairement les lignes Kα1 et Kα2 du cuivre, ce qui n'était pas possible avec un EDS (Energy Dispersive Spectrometer). Cependant, certaines difficultés ont été rencontrées, telles que de faibles intensités du signal et une collecte inefficace des rayons X diffractés. Pour y remédier, l'utilisation d'une optique polycapillaire est prévue, permettant d'augmenter l'efficacité de la collecte des rayons X au point source. En conclusion, ce travail met en évidence le potentiel du WDS pour l'analyse élémentaire à haute résolution. Tout en démontrant une résolution supérieure par rapport à d'autres techniques comme l'EDS, le prototype a néanmoins révélé certaines limites qui doivent être prises en compte pour des applications futures. Le futur ajout d'une optique polycapillaire pourrait pallier certaines de ces lacunes, ouvrant la voie à des mesures encore plus précises.

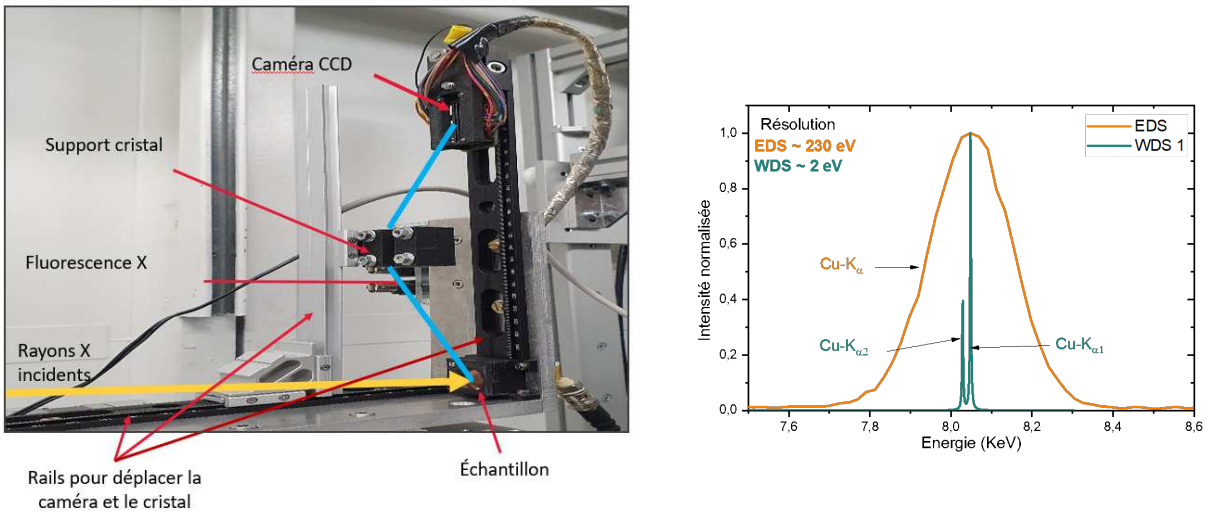

Figure 5: Image de l'instrument prototype WDS sur la MÉTROLOGIE au synchrotron SOLEIL (gauche). Comparaison des spectres WDS normalisés avec les spectres EDS d'un film mince de Cu métallique pur (droite). La résolution énergétique des deux spectres est indiquée.

11. Conclusion

Cette thèse explore les potentialités de la combinaison de l'analyse GIXRF et XRR pour la caractérisation précise des films minces utilisés dans les matériaux innovants. Les tests sur des échantillons GST et Ta ont mis en évidence des différences structurales significatives par rapport aux données du fabricant. Il a été montré que le recuit sur les échantillons GST entraîne des modifications structurelles, détectées par plusieurs indicateurs. Des méthodes basées sur les techniques de Monte Carlo ont été utilisées pour calculer les incertitudes associées à l'angle solide de détection et aux paramètres fondamentaux. De plus, la méthode « Bootstrap » a été utilisée pour calculer les incertitudes liées à l'optimisation. Les résultats de l'analyse combinée GIXRF-XRR sont prometteurs, avec des valeurs d'incertitude faibles, reflétant la précision des mesures. Cependant, des améliorations peuvent encore être apportées à la méthode d'estimation de l'incertitude. Un spectromètre dispersif en longueur d'onde (WDS) de haute résolution a

également été développé pour améliorer la résolution énergétique des spectres de fluorescence. Bien que performant, le prototype WDS présente des performances limitées et des améliorations futures sont envisagées pour renforcer sa sensibilité et sa résolution.

Contents

List of Figures

List of Tables

Introduction

To meet both technological and environmental requirements, there is considerable ongoing development of new materials, with the aim of improving computing power and energy production and storage capacities. For example, photovoltaics cells and battery materials have to be improved in terms of their performance, lifetime and safety. In another field, new memories capacity is becoming a priority because data production is growing exponentially (connected objects, artificial intelligence, data centers); it is thus essential to improve memory performance and density, while limiting energy consumption. Part of these devices are based on nano-structured materials and on the arrangement of thin film layers in the nanometer range. The metrology involved in the development of these thin films requires highly accurate and ideally, non-destructive techniques that can be integrated into the manufacturing process. X-ray fluorescence (XRF)-based techniques maintain significant advantage in this regard, as they are non-destructive and offer high precision characterizations. However, these techniques require specialized expertise to operate and control thin film production process to ensure the reliability and accuracy of the obtained data. Thus, implementing them in the fabrication process such as cleanroom environments can be a challenging process. As the demand for novel materials with specific properties continues to grow, it becomes increasingly important to use a precise characterization technique that can efficiently characterize thin film structures without causing any damages.
In France, the National Henri Becquerel Laboratory (LNHB) is the designated institute for the metrology of ionizing radiations. As a part of the European network EURAMET, LNHB ensures that radioactivity measurements are both consistent and traceable to international standards. The Laboratory for Activity Metrology (LMA), is in charge of primary metrology for activity measurement (unit = becquerel, Bq) and transfers these references to secondary calibration laboratories and users across various sectors, such as nuclear medicine, nuclear industry, and environmental monitoring. In this context, the accuracy and reliability of measurements are important for ensuring the quality of data. In this context, LNHB works on the metrological calibration of radiation detectors and possesses absolutely calibrated detectors that can be used in different measurement techniques. These include the goniometer CASTOR (Chambre d'Analyse Spectrométrique en Transmission ou en Réflexion) instrument, which is implemented at the *MÉTROLOGIE* beamline at SOLEIL synchrotron. This goniometer is designed for the measurement of grazing incidence X-ray fluorescence (GIXRF) and X-ray reflectivity (XRR), two techniques that can be used to probe the profiles of multilayers and determine their chemical compositions and structures for non-destructive characterization of thin film materials.
X-ray reflectivity (XRR) is a technique used to analyze single and multi-layered thin films with nanometer-scale thickness by measuring the intensity of the X-ray beam reflected at different incident angles. The resulting graph reflects variations in the electron density of the sample,

and in the case of layers, specific oscillations called Kiessig fringes can be observed. Grazing incidence X-ray fluorescence (GIXRF) is a technique used to analyze the angle-dependent X-ray fluorescence signal in grazing incidence. GIXRF scans angles from 0° to several times the critical angle (i.e. the angle corresponding to total reflection of the incident radiation) to study variations in the X-ray standing wave-field. This gives element-specific information about composition, concentration profiles, thickness and density of near-surface layers. Combining GIXRF and XRR enhances the quality of information obtained, reducing uncertainties and ambiguities.
To maintain the metrological standards, in this thesis we introduce a method to calculate uncertainties in the sample structure parameters using the combined GIXRF-XRR technique. Evaluating uncertainties is essential for establishing confidence in the measurement of GIXRF-XRR, as well as the result obtained using the combination of these two techniques.
Chapter I presents the bases by introducing the fundamentals of atoms and X-rays. This chapter discusses the electronic structure of atoms and the characteristics of X-rays. In addition, the Auger effect and other atomic relaxation processes are explained. The interaction processes of X-rays with matter, which includes photoelectric effect, scattering, reflection and refraction are also discussed. Finally, this chapter presents different sources of X-rays, with a focus on their applications.
Chapter II presents various types of X-ray detectors including the gas-based detectors, such as gas proportional counters and ionization chambers and the solid-state detectors such as photodiodes, scintillation counters, semiconductor detectors (i.e., silicon drift detectors and charge-coupled devices). The chapter also provides detailed information on X-ray spectrometry, including different types of X-ray spectrometers, their instrumentation, energy resolution, detection efficiency, and other characteristics. At the end of this chapter, we present a prototype of a high resolution spectrometer that was developed in the frame of this thesis.
Chapter III gives a detailed description of the experimental environment, i.e. the *MÉTROLOGIE* beamline of the SOLEIL synchrotron facility, focusing on the quality of the hard X-ray beam and techniques employed for precision energy selection and optimal beam purity. In addition a description of the instrument CASTOR with the proper alignment procedure for an accurate measurement are made. The final section of the chapter describes the process of calibrating the instruments for the X-ray detection.
Chapter IV introduces the concept of reference-free combined GIXRF-XRR, detailing the measurement procedures and calculations involved in the combination. Moreover, this chapter presents the methodologies for measuring and calculating the atomic fundamental parameters, which are crucial factors in the application of reference-free combined GIXRF-XRR, and their application to some elements.
Chapter V describes the evaluation method of GIXRF-XRR. In this chapter we discuss the optimization procedures, which includes fitting the GIXRF and XRR curves with the experimental data, optimizing the model structure using different software and the uncertainty calculation of the sample structure parameters.
Chapter VI is divided into two sections: application and results and discussion. The application section presents the samples studied, including chalcogenide materials and tantalum-based thin films with their fabrication and synthesis methods. In the last part, the results of the reference-free combined analysis, with a focus on uncertainty calculations are presented and discussed.
Finally in Chapter VII, the results presented in this thesis are summarized and potential future research related to this work is proposed.

Chapter 1

Fundamentals

1.1 The atom

1.1.1 Brief history of atom and X-rays

The development of atomic theory in the early 20th century was marked by the model of the atom as a positively charged structure, filled with negatively charged electrons [1]. A major breakthrough came afterwards with the proposition of a nucleus-centric atomic structure with electrons in orbit. Subsequently, this model was refined to include distinct electron shells characterized by unique energy levels [2], where the transition between them occurs by absorbing or emitting energy. The model later evolved to consider that electrons exhibit wave-like behavior with their positions being unpredictable and their existence probability in an orbit depends on its energy level [3].
X-rays, another significant scientific achievement, were discovered by Wilhelm Conrad Röntgen in 1895, while studying cathode rays in high-voltage using an air filled Hittorf-Crookes tube (Figure 1.1) shaded with black paper [4]. The discovery of this newly observed radiation was the result of interaction of electron beams with the tube's wall [5].

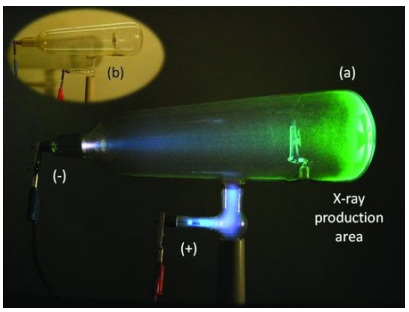

Figure 1.1: Crookes tube with shadow cross in use. X-rays emerge upon impact of electrons (cathode rays) on the glass wall at the right. Sub-picture: the uncharged tube [6].

In 1908, Barkla and Sadler discovered that X-rays include components that are characteristics of the target material, named K and L radiations. These components exhibit distinct wavelengths, represented by the diffraction experiment of William Henry Bragg [7]. A year later, Walter Friedrich, Paul Knipping and Max von Laue defined the essential wave nature of X-rays by

demonstrating their diffraction by a crystal which operates as a grating diffractor [8]. According to their theory, interference patterns occur as a result of the space lattice constant being 10 times greater than the wavelength of X-rays. This discovery was confirmed later by William Henry Bragg and William Lawrence Bragg, father and son. In 1913, Henry Moseley developed a basic relationship between the wavelength of characteristic X-ray photons and atomic number of the excited element, which led to the use of X-rays for element characterization [9]. With the introduction of the first commercial X-ray spectrometer in 1948, the technique of X-ray-sample interaction had become practical [10]. The first spectrometer was a wavelength-dispersive spectrometer, which measures the wavelength of a single element at a time. Multi-element research was later made possible by the invention of energy-dispersive spectrometers (EDS).

1.1.2 Electronic structure

Atoms are defined as tiny particles composed of a central nucleus including protons and neutrons, surrounded by a cloud of electrons. The nuclear model of the atom is a theoretical representation of the distribution of the electrons around the nucleus. It depends on the atomic number (number of protons in the nucleus) that defines the chemical property of each element. In the electronic structure of the atom, electrons occupy energy levels defined by the principal quantum number n. Each shell has a maximum capacity of $2n^2$. Consequently, the outer shells which have a higher n value can hold a larger number of electrons. The energy levels corresponding to $n = 1$, $n = 2$, $n = 3\ldots$ are also denoted as K, L, $M\ldots$ as illustrated in Figure 1.2 (a).
Due to the orbital motion of the electrons around the nucleus, each principal quantum number n has an angular momentum quantum number l between 0 and $n-1$, corresponding to subshells s, p, d, f. The order of subshells filling is defined by Klechkowski's rule (Figure 1.2 (b)). In addition, within each subshell, electrons are grouped into orbitals, where each orbital can hold a maximum of two electrons with opposite spins $s = \pm 1/2$ [11]. As a result of spin-orbit coupling, the electron has a total angular momentum quantum number of $j = l + s$. In the presence of a magnetic field, the electron has $2j + 1$ magnetic sub-states (m_j) that range from $-j$ to $+j$.

To summarize, the state of an electron in an atom may be defined using the following quantum numbers and their respective values;

- Principal quantum number, n ; $n = 1, 2, 3, 4\ldots$
- Orbital angular momentum quantum number or the azimuthal quantum number $l = 0$ to $n - 1$,
- Spin angular momentum quantum number, s; $s = \pm 1/2$,
- Total angular momentum quantum number, j; $j = l + s$,
- Total magnetic quantum number m_j; $m_j = -j$ to$+j$.

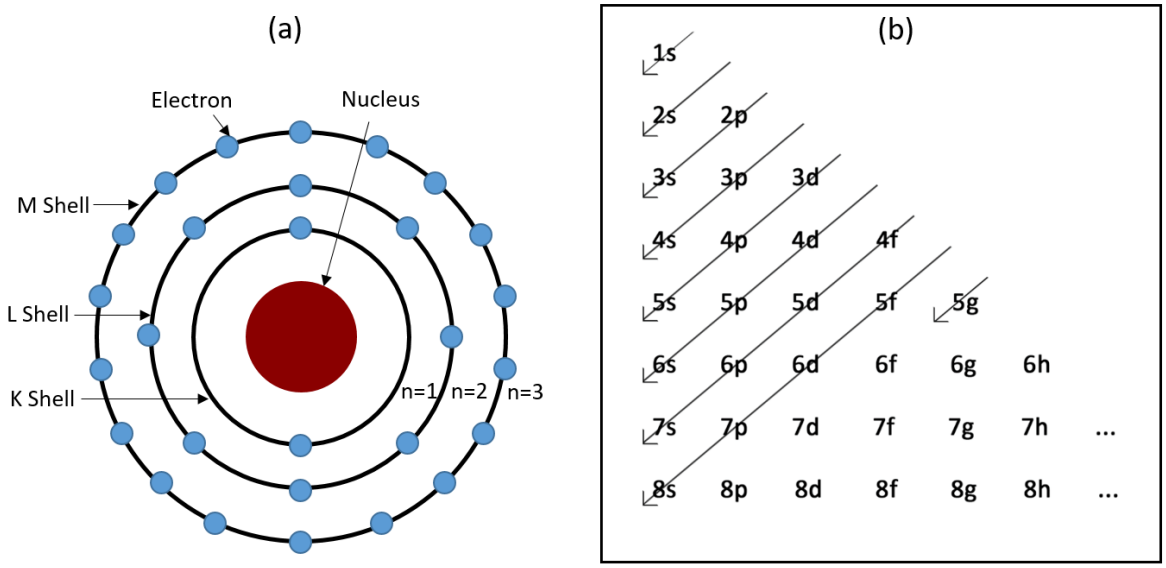

Figure 1.2: (a) The atomic structure with arrangement of electrons on each energy level or shell and (b) Klechkowski's rule.

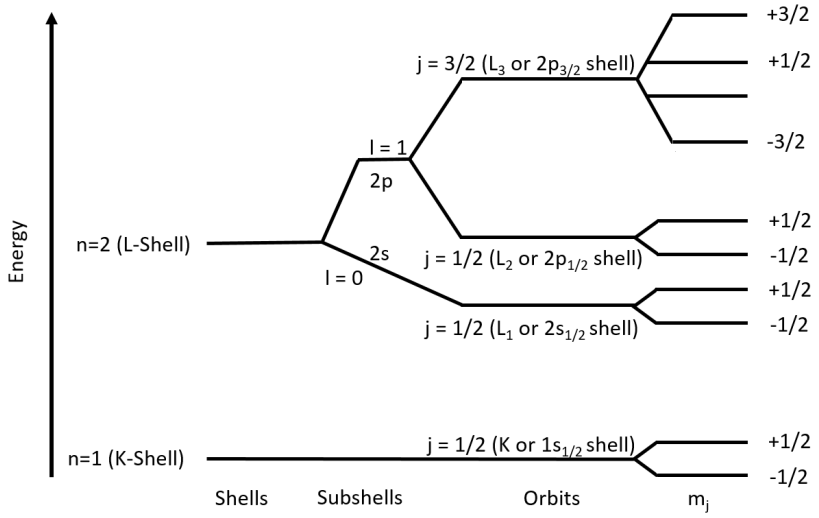

Figure 1.3: Level diagram of different quantum states for K- and L-shells

The energy levels of different subshells are quoted by $1s_{1/2}$, $2s_{1/2}$, $2p_{1/2}$ and $2p_{3/2}$... equivalent to K, L_1, L_2 and L_3 respectively. For example, the state $1s_{1/2}$ means $n = 1$, $l = 0$, $j = \frac{1}{2}$. Figure 1.3 represents the energy levels with the splitting of the K, L_1, L_2 and L_3 states. While the energy levels provide insight into the electron configuration of an atom, it is also important to consider the binding energies of electrons in different shells. Binding energies allow a better understanding of the stability of an electron in a specific shell and the energy required to remove it from this shell. A semi-empirical equation for K binding energy can be expressed as [12]:

$$E_B = 13.6 \cdot Z_{eff}^2 \,, \tag{1.1}$$

where Z_{eff} =Z - 2.5 for Z = 10 - 18, $Z_{eff} = Z - 3$ for $19 \leqslant Z \leqslant 70$ and $Z_{eff} = Z - 1.5$ for

$71 \leqslant Z \leqslant 95$.
The approximation for the K shell binding energy for all elements having an atomic number between 1 and 60 is expressed as [12]:

$$E_{K_{ab}}\,(eV) = 6.852 \cdot Z^{2.1324} \cdot e^{-1.168 \cdot 10^{-7} Z^3}\,. \tag{1.2}$$

These two equations reveal that the binding energy of the electron shells increases with increasing the atomic number. Comparing these empirical formulas with references data, enables the assessment of the equation's validity and accuracy, and identify whether the models are strong or require refinement. Furthermore, this comparison contributes to a better understanding of atoms physical properties as well the nature of their electron binding energies. A comparison between the binding energy calculations for the K-shell derived from Equations 1.1 and 1.2 and the references values from Fuggle *et al.* $(Z = 1 - 9)$ [13], Deslattes $(Z = 10 - 95)$ [14] and Larkins $(Z = 96 - 104)$ [15] is shown in Figure 1.4.

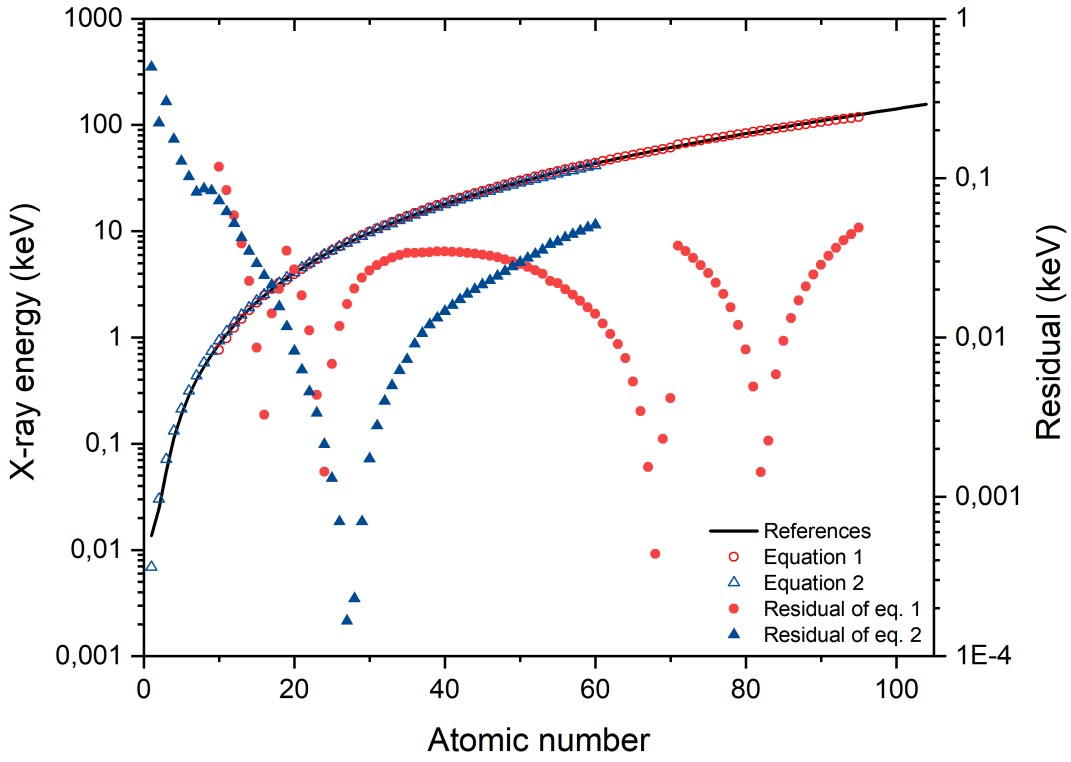

Figure 1.4: X-ray binding energy data as a function of atomic number, with the relative residuals of Equations 1.1 and 1.2 with respect to the reference data.

The relative residuals are calculated to evaluate the accuracy and reliability of the respective equations in determining binding energies compared to the data from Deslattes. For Equation 1.1, the residuals exhibit fluctuations across different atomic numbers, with a minimum residual of 0.04 % (at $Z = 68$) and a maximum of 11.75 % (at $Z = 10$). This indicates that the equation's accuracy in calculating binding energy varies significantly among atomic numbers. Similarly, for Equation 1.2, the residuals also vary across the atomic numbers with a minimum of 0.02 %

(at $Z = 27$) and a maximum of 49.62 % (at $Z = 1$). The highest residuals for both equations are obtained at the lowest atomic numbers, demonstrating that the equations have difficulty to accurately calculate binding energies for elements with low atomic numbers. In addition, several atomic numbers exhibit residuals exceeding 1 %, which highlights some limitations in the performance of these equations for certain atomic numbers.

1.1.3 Characteristics of X-rays

X-rays are classified as electromagnetic waves with energies ranging from about 100 eV to 100 keV [16] as shown in Figure 1.5. Their energy is inversely proportional to the wavelength and can be obtained according to this equation:

$$E = \frac{hc}{\lambda} \tag{1.3}$$

where h is Planck's constant and c is the speed of light. X-rays with wavelengths near the ultraviolet range are called soft X-rays or X-UV rays, while shorter wavelength rays close to or even extending beyond the gamma ray range are called hard X-rays. The high energy of X-rays provides them with some characteristics, such as high penetration depth, which depends on the density of the target material, as well as on the energy of the photon. X-rays are characterized by an ionizing power [17], which enables high-energy X-rays to eject electrons by energy transfer. They have the property of diffraction due to their short wavelength, similar to the crystal's lattice spacing as well as being refracted and reflected by the material.

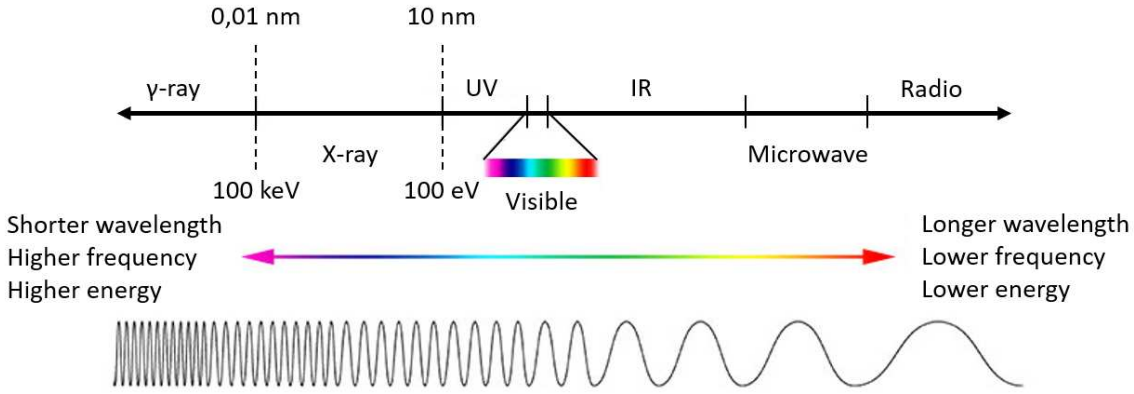

Figure 1.5: Comparison of wavelength, frequency and energy for the electromagnetic spectrum.

1.1.4 Atomic relaxation

Atomic relaxation is a process that occurs when the energy of an atom is changed, for example when an inner shell electron is removed or displaced. This can happen not only through excitation, but also via processes like ionization or chemical reactions. As the atom seeks to regain stability, an electron from a higher energy level falls into the created vacancy, releasing excess energy through two main rearrangement processes, either X-ray fluorescence (characteristic or diagram lines) or Auger electron emission both illustrated in Figure 1.6. This section provides a detailed explanation of the atomic relaxation phenomenon, focusing on the X-ray diagram

lines that represent the characteristic X-ray emissions resulting from electron transitions and their associated probabilities.

1.1.4.1 X-ray fluorescence

The X-ray fluorescence (XRF) presented in Figure 1.6 (a), results in the emission of a photon during the electronic rearrangement characterized by the transition of an electron from a higher to a lower orbital. The energy of this photon is thus given by the difference between the electron binding energies as:

$$E_{photon} = E_{in} - E_{fin} \tag{1.4}$$

where E_{in} and E_{fin} represent the binding energies of the initial and final levels respectively. Furthermore, based on the atomic structure described in section 1.1.2, selective transitions are allowed to fill the vacancy in the atomic shell illustrated in Figure 1.7. A notation for identifying transitions is introduced by Siegbahn, based on the relative intensity of lines from various series [18]. This historical notation includes the letter of the initial vacancy (K, L, M...), followed by a Greek letter (α, β ...) representing the electron shell of the final vacancy, and a subscript number for its sub-shell identification. The notation α is used for the emission from the first upper shell, β is for the second and third next shells and so on in alphabetical order. For example, $K_{\alpha 1}$ and $K_{\alpha 2}$ represent the transitions from L_3 and L_2 sub-shells towards the K shell respectively, whereas, $K_{\beta 1}$ and $K_{\beta 3}$ lines indicate the transitions from M_3 and M_2 subshells [19]. As the X-ray lines were progressively named after their discoveries, some problems appears when some lines could not be distinguished between the origin shell of the electron. For example, $K_{\beta 2}$ stands for transitions between N_2 or N_3 to K. This is why the Siegbahn notation is not perfect, although its widespread use, and the International Union of Pure and Applied Chemistry (IUPAC) recommended to use the notations presented in Table 1.1.

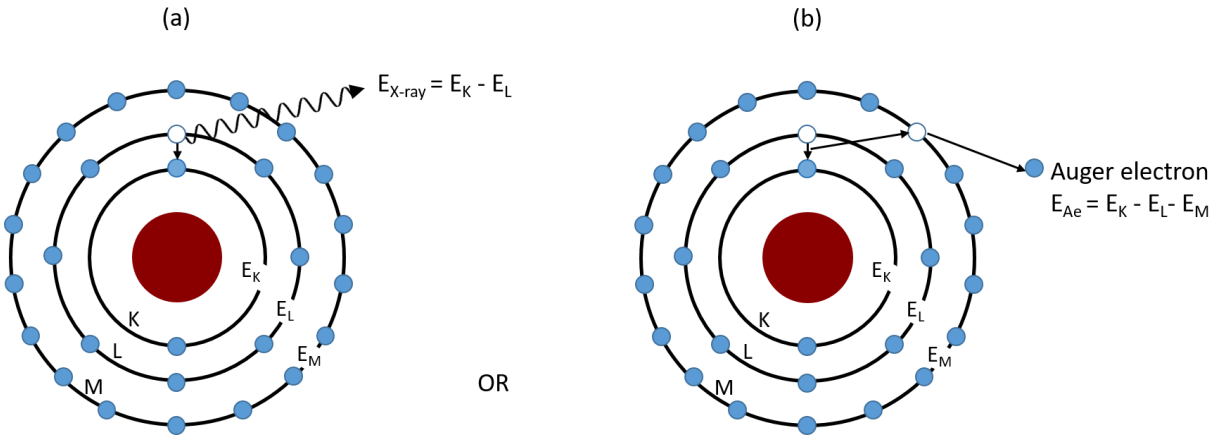

Figure 1.6: (a) Emission of fluorescence photon and (b) emission of Auger electron.

Table 1.1: Correspondence between Siegbahn and IUPAC notation diagram lines [20].

Siegbahn	IUPAC	Siegbahn	IUPAC	Siegbahn	IUPAC	Siegbahn	IUPAC
$K_{\alpha 1}$	$K - L_3$	$L_{\alpha 1}$	$L_3 - M_5$	$L_{\gamma 1}$	$L_2 - N_4$	$M_{\alpha 1}$	$M_5 - N_7$
$K_{\alpha 2}$	$K - L_2$	$L_{\alpha 2}$	$L_3 - M_4$	$L_{\gamma 2}$	$L_1 - N_2$	$M_{\alpha 2}$	$M_5 - N_6$
$K\beta_1$	$K - M_3$	$L_{\beta 1}$	$L_2 - M_4$	$L_{\gamma 3}$	$L_1 - N_3$	M_{β}	$M_4 - N_6$
$K\beta_2^{\mathrm{I}}$	$K - N_3$	$L_{\beta 2}$	$L_3 - N_5$	$L_{\gamma 4}$	$L_1 - O_3$	M_{γ}	$M_3 - N_5$
$K\beta_2^{\mathrm{II}}$	$K - N_2$	$L_{\beta 3}$	$L_1 - M_3$	$L_{\gamma 4}$	$L_1 - O_2$	M_{γ}	$M_{4,5} - N_{2,3}$

The production of the diagram lines is governed by the quantum-mechanical rules known as selection rules that depend on the quantum numbers (n, l, j) of the initial and final electron shells:

$$\Delta n \geq 1, \Delta l = \pm 1, \Delta j = 0, \pm 1 \tag{1.5}$$

in which the j transition $0 \rightarrow 0$ is forbidden.
These selection rules determine whether a transition is allowed or not. In addition, K_{α_1} is the most probable electron transition, K_{α_2} and $K_{\beta 1}$ also occur but with lower probability, and thus lower relative intensity. In the case of the K series, the transition probability PK_{α} is defined by K_{α} fraction intensity of the total K spectrum given by [21]:

$$PK_{\alpha} = \frac{I\left(K_{\alpha 1} + K_{\alpha 2}\right)}{I_{K,Total}} \tag{1.6}$$

where $I_{K,Total}$ represents the intensity of all K lines. Certain lines with a weak probability do not follow the basic selection rules and arise from outer orbital levels may also occur in X-ray spectra known as forbidden lines. In addition, after ejection of the initial electron, atom can remain in the excited state for so long that there is a significant probability that another electron will be ejected before the vacancy is filled. The loss of one electron changes the energy of the electrons around it, resulting in the emission of X-rays with different energies. These low intensity lines, known as satellite lines, are not analytically significant, but may generate uncertainty in spectral interpretation [7]. These satellite lines are particularly significant when produced through ionization by charged particles or radioactive decay through electron capture [22, 23].

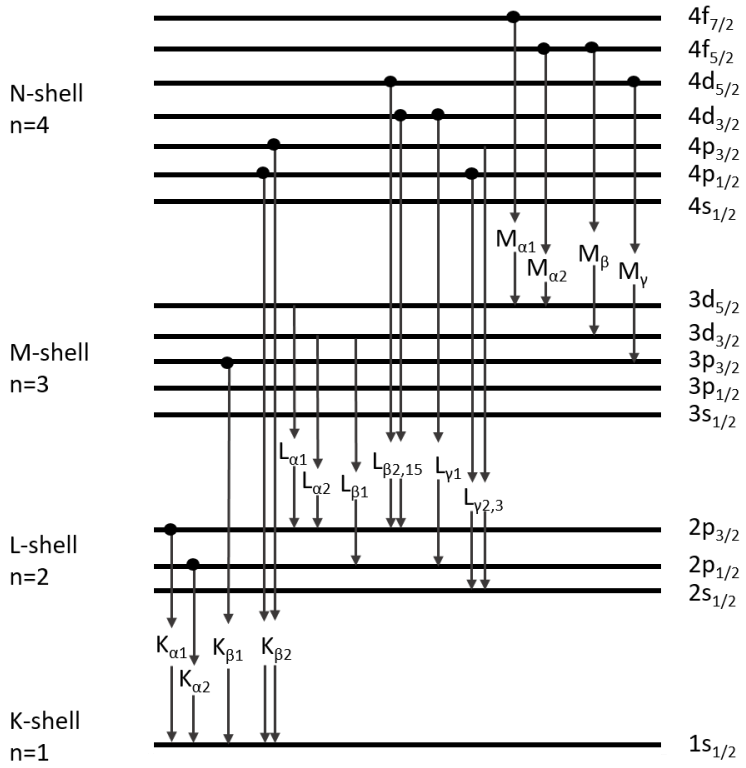

Figure 1.7: X-ray transitions diagram for different shells and nomenclature of major X-ray lines.

1.1.4.2 Auger effect and Coster-Kronig transitions

The Auger effect is the other process that can occur when a vacancy is created in the inner electron shell. When an outer-shell electron fills this vacancy, instead of emitting a photon, the released energy is transferred to another electron, causing it to be ejected from the atom as shown in Figure 1.6(b). This secondary electron emission is known as the Auger effect, and the ejected electron is called an Auger electron with a kinetic energy expressed as:

$$E_{Ae} = E_{in} - E_1 - E_2 \tag{1.7}$$

where E_{in} is the binding energy of the electron in the inner-shell, E_1 is the binding energy of the electron filling the vacancy and E_2 is the binding energy of the electron ejected during the Auger process.
In addition, a special case of Auger emission is a Coster-Kronig transitions where one of the final vacancies is in the same shell as the initial vacancy. If both are in the same subshell, these are called "super Coster-Kronig". These transitions release less energy than those involving an electron from a higher shell filling the vacancy. Consequently, the emitted electron in a Coster-Kronig transition possesses less kinetic energy than in a standard Auger transition. A diagram of these two effects is shown in Figure 1.8.

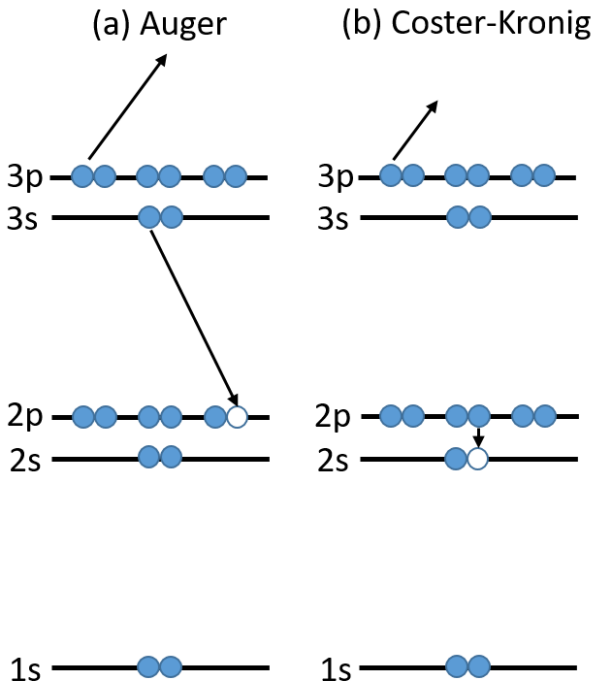

Figure 1.8: (a) Auger and (b) Coster-Kronig electron emission schematic diagrams.

1.1.4.3 Fluorescence yield and Auger yield

The fluorescence yield is the major parameter that determines the intensities of X-ray spectra. It is a fundamental property of an element, determined by its electron shell structure, and it is specific to each X-ray emission line of that element. As mentioned earlier (subsection 1.1.4.1), X-ray fluorescence emission occurs with a certain probability, competing with the non-radiative transition known as Auger emission. The fluorescence yield ω_f is defined as the probability of filling the vacancy through radiative transition, resulting in the emission of an X-ray photon. The fluorescence yield of the K shell is given by [24]:

$$\omega_K = \frac{I_K}{n_k} \tag{1.8}$$

where I_K is the total number of characteristic K X-ray photons emitted from a sample and n_K is the number of primary vacancies in the K shell. Similarly, the Auger yield a_f is defined as the probability of filling the vacancy with an electron of an outer shell, the energy being transferred to a secondary electron that is ejected (Auger electron). Since higher atomic shells include more than one subshell, they are affected by Coster–Kronig transitions between subshells of an atomic shell with the same principal quantum number. As a result, the definition of the fluorescence yield for L and upper shells becomes more complicated.

- In the case of the absence of the Coster-Kroning factor, the fluorescence yield of higher order shells becomes:

$$\omega_i^X = \frac{I_i^X}{n_i^X} \tag{1.9}$$

with X refers to the quantum number indicated by L, M, $N\ldots$ and i refers to the subshell. For the X shell, an average fluorescence yield ω_X is calculated as:

$$\bar{\omega}_X = \sum_{i=1}^{k} N_i^X \cdot \omega_i^X \tag{1.10}$$

where N_i^X is the relative number of primary vacancies in the subshell i of shell X expressed as:

$$N_i^X = \frac{n_i^X}{\sum_{i=1}^{k} n_i^X} \text{ and } \sum_{i=1}^{k} N_i^X = 1. \tag{1.11}$$

In order to eliminate Coster-Kronig transitions from the definition of the average fluorescence yield, the primary vacancy distribution must be fixed. Generally, $\bar{\omega}_X$ is not a fundamental property of the atom, instead, it depends on both atomic subshell fluorescence yields ω_i^X and on the relative number of primary vacancies N_i^Xcharacteristic of the method used to ionize the atoms.

- In the presence of Coster–Kronig transitions, two approaches are used to compute the average fluorescence yields. In the first one, we consider the average fluorescence yield $\bar{\omega}_X$ as the linear combination of the subshell fluorescence yields ω_i^X with the vacancies distribution modified by Coster–Kronig transitions as:

$$\bar{\omega}_X = \sum_{i=1}^{k} V_i^X \cdot \omega_i^X \text{ and } \sum_{i=1}^{k} V_i^X > 1 \tag{1.12}$$

whereV_i^X is the relative number of vacancies in the sub-shell i of shell X, including vacancies affected by Coster–Kronig transitions.
In the second approach, the mean fluorescence yield $\bar{\omega}_k$ is defined as the linear combination of the relative numbers of primary vacancies N_i^X as:

$$\bar{\omega}_k = \sum_{i=1}^{k} N_i^X \cdot v_i^X \tag{1.13}$$

where v_i^X denotes the total number of distinctive X-rays produced per primary vacancy in the X_i sub-shell.The Auger and the fluorescence yields are related by:

$$\omega_i^X + a_i^X + \sum_{i=1}^{k} f_{ij}^X = 1 \tag{1.14}$$

in which f_{ij}^X accounts for the Coster–Kronig transition probabilities.
The fluorescence yield increases with the atomic number and it changes from one electron shell to another in which ω_K is much larger than ω_L and ω_L is much larger than ω_M and so on. The probabilities become approximately equal at $Z \approx 30$ for K shell ionization. More information on the dependence of the fluorescence and Auger yields on the atomic number is illustrated in Figure 1.9. For atoms with low atomic numbers, e.g. $Z < 25$, ω_L and ω_M yields are close to 0 because of the lack of electrons in the outer shells.

In heavier atoms, there are more electrons in the outer shells, increasing the probability of an electron transitioning to the K shell and emitting an X-ray in the rearrangement process. On the other hand, the probability of Auger electron emission decreases with increasing atomic number (Z) as a result at the increase of the fluorescence yield.

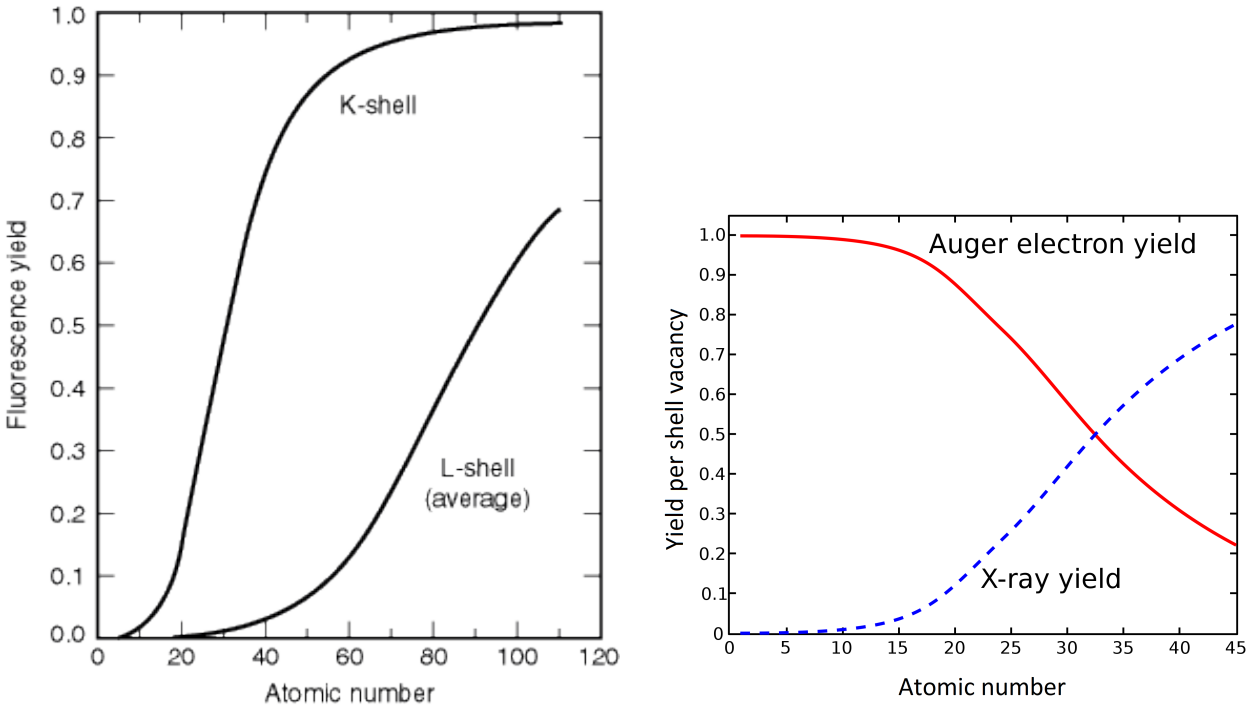

Figure 1.9: X-ray (fluorescence) yield ω as a function of atomic number for electron ionization within the K and L electron shells (left). Fluorescence and Auger electron yields per K vacancy as a function of atomic number (right) [25].

1.2 X-ray matter interaction

Understanding the interaction between X-ray radiation and matter plays a crucial role in a wide range of applications. As illustrated in Figure 1.10, this complex phenomenon involves various processes that occur when X-ray photons interact with the atoms of a target material, leading to different outcomes based on their energy levels. The resulting interactions can provide valuable insights into the structural and composition properties of materials at the atomic level. As mentioned before, X-rays can produce secondary radiation emission after interaction with the atoms of a target material. When X-rays pass through an absorbing medium, they become attenuated, resulting in a decrease of the intensity of the incident beam [16]. This decrease depends on the thickness, density and on the attenuation cross section of the material as well as on the photon energy.
In this section, the concept of attenuation will be explained in detail, accompanied by a discussion on various types of X-ray interactions with matter, including photoelectric absorption, X-ray scattering, reflection and refraction.

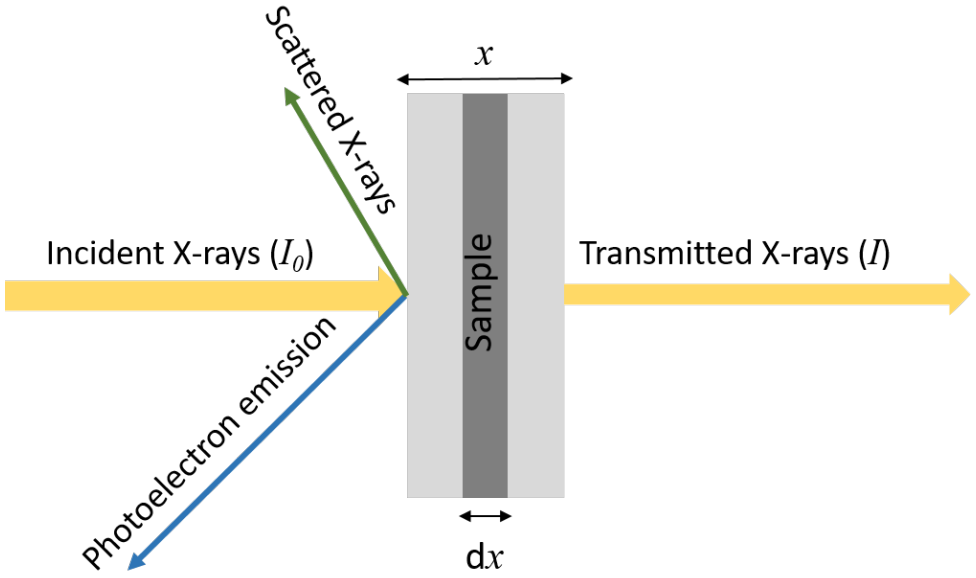

Figure 1.10: Schematic of interactions of an X-ray beam with matter.

1.2.1 Attenuation process

The attenuation of a collimated X-ray beam under normal incidence with respect to the surface of a material layer with density ρ and thickness $\mathrm{d}x$ is characterized according to Beer-Lambert law as:

$$\frac{dI}{I} = -\left(\frac{\mu}{\rho}\right) \cdot \rho \cdot \mathrm{d}x \tag{1.15}$$

or as:

$$I = I_0 \exp\left(-\left(\frac{\mu}{\rho}\right) \cdot \rho \cdot x\right) \tag{1.16}$$

where I_0 and I represent the incident and the transmitted intensity respectively, $\mu(\mathrm{cm}^{-1})$ is the linear attenuation coefficient, $\frac{\mu}{\rho}(\mathrm{cm}^2 \cdot \mathrm{g}^{-1})$ is the mass attenuation coefficient which depends on the element composition and the X-rays energy [16] and $\rho(\mathrm{g} \cdot \mathrm{cm}^3)$ is the density of the material. In the case of a mixture of elements, the mass attenuation coefficient follows an additive law and can be calculated from the sum of the mass attenuation coefficient of each element as:

$$\frac{\mu}{\rho} = \sum c_i \left(\frac{\mu}{\rho}\right)_i \tag{1.17}$$

where the values of c_i denote the mass fractions of each element in the mixture. X-rays interact with the inner or outer-electrons shell, according to different elemental processes, namely photoabsorption, elastic and inelastic scattering and pair creation where the total attenuation coefficient is the sum of the partial interaction coefficients as:

$$\mu = \tau_{ph} + \sigma_{elastic} + \sigma_{inelastic} + \kappa_{pairs} \tag{1.18}$$

where τ_{ph} is the photoabsorption coefficient, $\sigma_{elastic}$ and $\sigma_{inelastic}$ are respectively the elastic and inelastic scattering coefficients and κ_{pairs} is the pair production coefficient. The X-ray attenuation allows investigation of the local electronic structure of the target material using

particular energy. Indeed, these elemental effects provide spectroscopic signatures as a function of photon energy, mainly via inter-atomic multiple scattering and photoelectric process [16]. Figure 1.11 represents the dominant effects with energy transfer for different atomic numbers at different excitation energies. The photoelectric effect is dominant for energy less than 100 keV, while pair production occurs at high X-ray energies (greater than 0.511 MeV) and becomes dominant for energies more than several MeV. In the X-ray range, only photoabsorption and Compton will be considered.

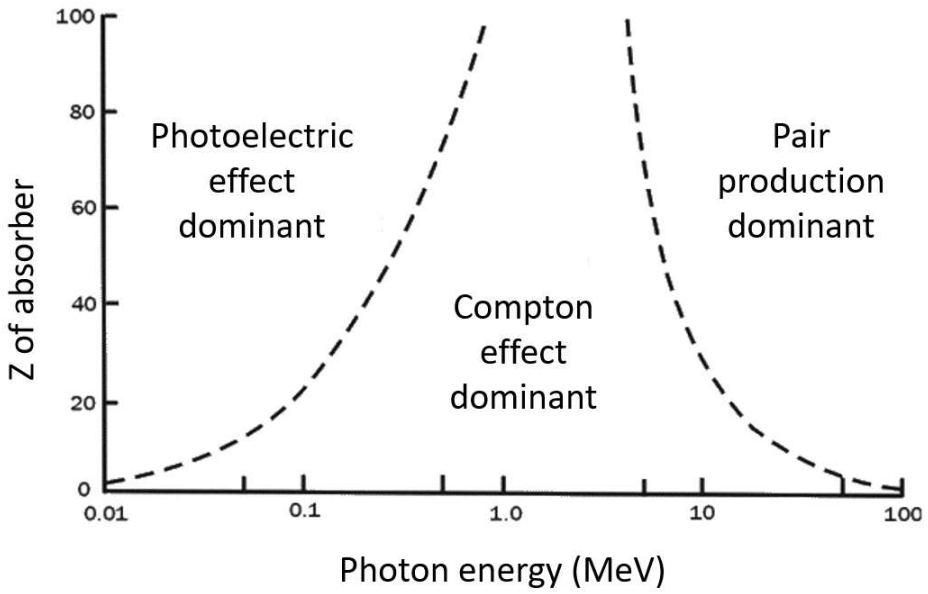

Figure 1.11: Predominant processes of the interaction between X-rays and matter as a function of atomic number and X-ray energy [26].

1.2.2 Photoelectric absorption

X-ray photoelectric absorption occurs when an X-ray photon interacts with an inner-shell electron. This interaction can happen when the energy of the incoming X-ray photon is greater than or equal to the binding energy of the electron in the atom. In this case, the electron is ejected creating a vacancy in the electron shells, leaving the atom in an excited state. Therefore, the primary photon is completely absorbed and the ejected electron is called a photoelectron. Figure 1.12 represents (a) the photoelectric interaction with an atom and (b) the photoelectron ejection after photoabsorption. The energy of the photoelectron is equal to the difference between the incident photon energy and the binding energy of the electron in its shell as:

$$E_{pe} = E_i - E_b \tag{1.19}$$

where E_{pe} is the kinetic energy of the photoelectron, E_i is the energy of the incident photon and E_b is the required energy to remove the electron, equivalent to its binding energy in the atom presented in Equations 1.1 and 1.2.

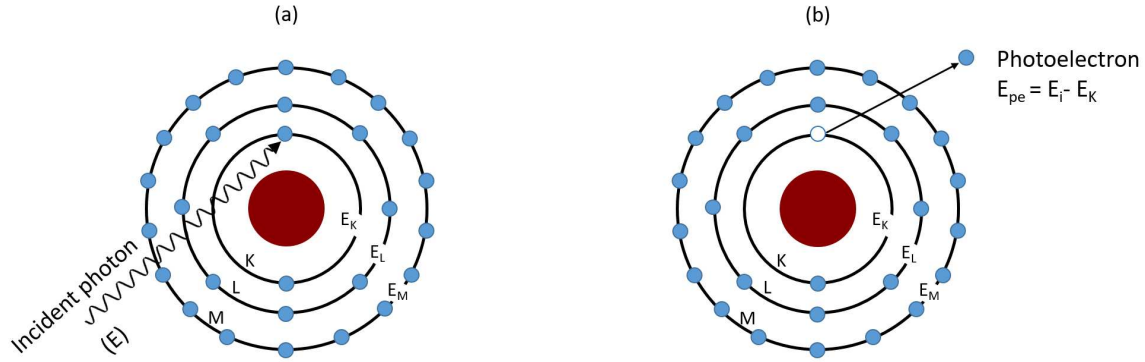

Figure 1.12: (a) Photoelectric interaction and (b) photoelectron ejection. An incident photon is shown interacting with an atom, leading to the ejection of an inner-shell electron, known as a photoelectron.

As a consequence, the vacancy can be filled by an electron from an outer shell and the energy difference is either carried away as X-ray fluorescence or it can also be transferred to an electron of an external shell that is ejected known as Auger electron as explained in section 1.1.4.2. The total photoelectric absorption can be calculated as the sum of the partial photoelectric mass-absorption coefficient of the individual shells as:

$$\frac{\tau_{abs}}{\rho} = \left(\frac{\tau_{abs}}{\rho}\right)_K + \left(\frac{\tau_{abs}}{\rho}\right)_L + \left(\frac{\tau_{abs}}{\rho}\right)_M + \ldots \tag{1.20}$$

A plot of the photoelectric-mass absorption coefficient versus energy for tungsten ($Z = 74$) is presented in Figure 1.13.

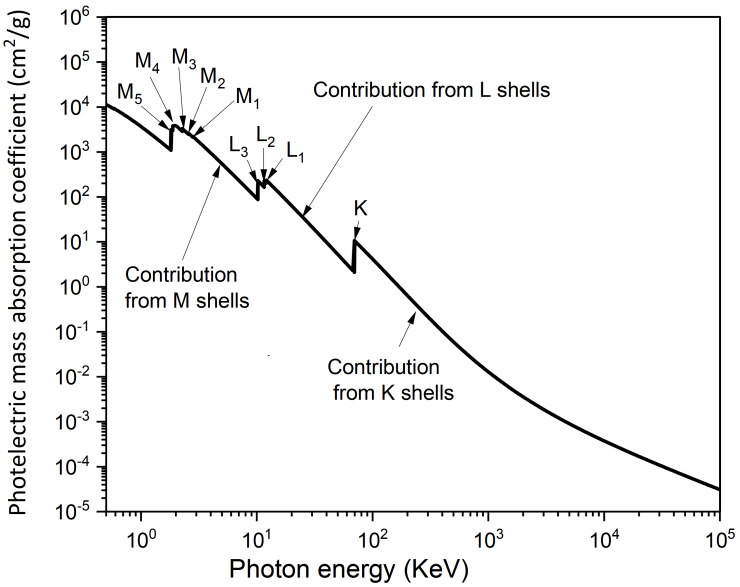

Figure 1.13: Photoelectric mass absorption coefficient vs. photon energy for tungsten.

The photoabsorption coefficients decreases with the energy, and the abrupt jumps on the absorption edges are caused by the fact that some outer shell electrons can be ejected if the incident photon energy exceeds their binding energy.

1.2.3 X-ray scattering

The interaction between X-rays and matter can also lead to a change in the incident photon direction, known as X-ray scattering. The manner in which X-rays are scattered depends on the properties of the electrons and the atomic structure of the material. X-ray scattering can be defined according to two processes as illustrated in Figure 1.14: elastic (Rayleigh) scattering and inelastic (Compton) scattering. X-ray scattering based techniques are used to investigate the structure and properties of materials on the microscopic scale, providing information about the arrangement and orientation of atoms and molecules within a material.

1.2.3.1 Rayleigh scattering or elastic scattering

Rayleigh scattering is a type of scattering of X-ray photons that occurs when X-rays interact with the electrons of atoms in a medium, causing the X-rays to scatter in any directions without any change in energy. The probability of Rayleigh scattering depends on the atomic number of the atoms in the medium, and the resulting signal can contribute to the overall background in X-ray fluorescence experiments.

1.2.3.2 Compton scattering or inelastic scattering

Compton scattering is defined as a two-particle interaction where an incoming high-energy photon interacts with a loosely bound electron. Upon interaction, part of the photon energy is transferred to the electron, resulting in a change in the direction and the energy of the photon.

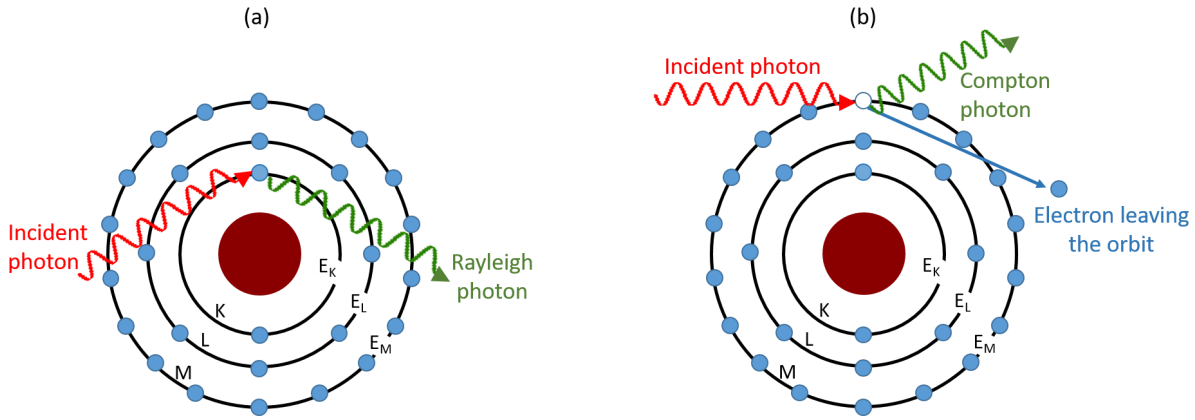

Figure 1.14: Comparison between (a) Rayleigh and (b) Compton scattering.

The energy of the Compton-scattered photon depends on the scattering angle, θ (Figure 1.15) as:

$$E_{Compton} = \frac{E_i}{1 + \alpha\,(1 - \cos\theta)} \tag{1.21}$$

where $\alpha = \frac{E_i}{m_e \cdot c^2}$ and $m_e \cdot c^2 = 511$ keV.

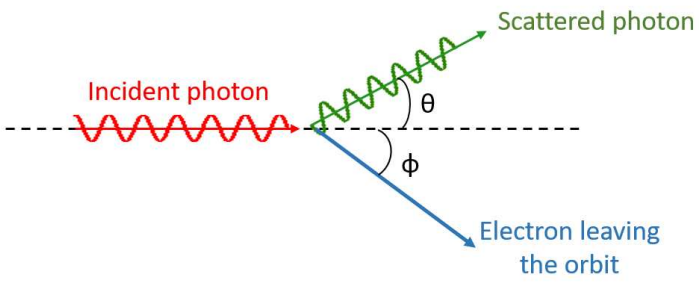

Figure 1.15: Compton scattering; Collision of a photon with an electron at rest and scattering angles.

1.2.4 Reflection and refraction

Reflection and refraction occur when photons interact at the interface between two media. As shown in Figure 1.16, when X-rays encounter the boundary between two different materials, the incident wave is split into two parts: one part is reflected back into the first medium, while the other part is transmitted through the second medium at a different angle, undergoing refraction.

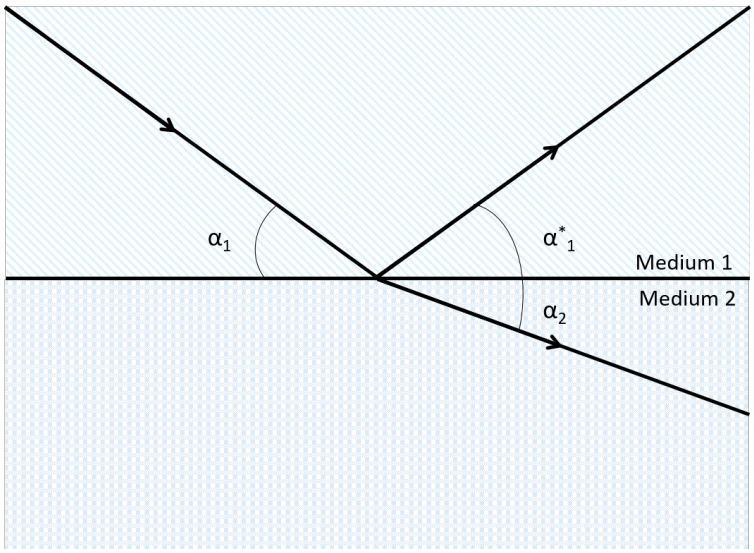

Figure 1.16: Incident, reflected, and refracted beams at the interface of media 1 and 2.

When X-rays enter a surface of a flat sample under grazing incidence, they are reflected with the same angle as the incident beam. In this case:

$$\alpha_1 = \alpha_1^* \tag{1.22}$$

where α_1 is the glancing angle and α_1^* is the angle of the reflected beam.
According to Snell's law, the refraction of X-rays occurs when they passes from one medium to another of different refractive index:

$$v_2 \cos \alpha_1 = v_1 \cos \alpha_2 \tag{1.23}$$

where α_2 is the refraction angle and $v1$ and $v2$ are the phase velocities of the beam in medium 1 and 2 respectively, which depend on the refractive index of the medium n, expressed as:

$$v = \frac{c}{n}. \tag{1.24}$$

Therefore, Equation 1.23 can be written as:

$$n_1 \cos \alpha_1 = n_2 \cos \alpha_2 \tag{1.25}$$

where n_1 and n_2 are the refractive indices of medium 1 and 2 respectively. Equation 1.25 shows that X-rays are deflected off the boundary if medium 2 is denser than medium 1 (i.e $n_2 > n_1$) and vice versa. After irradiating an atom with an X-ray, the quasi-elastically bound electrons are forced to oscillate; these forced oscillations are created with a phase difference and thus, a modification of the phase velocity of the propagating wave. As a result, the refractive index deviates from the vacuum value ($n_{vac} = 1$) by a small amount δ (10^{-6} – 10^{-7}). The refractive index in the X-ray energy range is expressed as [27]:

$$n = 1 - \delta + i\beta \tag{1.26}$$

with β, the imaginary part of the refractive index is related to the absorption and it is proportional to the mass attenuation coefficient of the medium. This component characterizes the absorption or attenuation of X-rays as they pass through the medium.

1.2.5 Diffraction of X-rays - Bragg's law

Diffraction of X-rays on crystals is a fundamental phenomenon that was extensively studied in the field of physics and crystallography. This phenomenon occurs after interaction of X-rays parallel wave with crystalline materials characterized by the arrangement of their components (atoms, ions or molecules) in three-dimensional lattice structure. In fact, crystals are made up of regular three-dimensional groupings of atoms by the repetition of a motif known as the unit cell [28]. The unit cells are classified into six crystal families based on angles and lengths of the axis sides: cubic, tetragonal, hexagonal, orthorhombic, monoclinic and triclinic, in which the hexagonal family can be divided into two systems, which are trigonal lattice and hexagonal lattice. In addition, the lattices are divided into primitive and non-primitive depending on the position of the atoms. A primitive lattice, has the smallest possible atomic coordination number in which atoms lie on the eight corners of the cube. Based on the position of the atoms in the unit cell, the non-primitive lattices are divided into three types: face centered (F), base centered (B) and body centered (I) displayed in Figure 1.17.

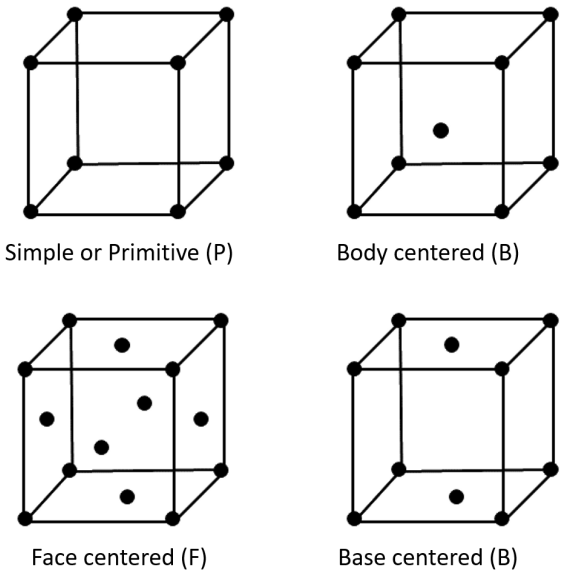

Figure 1.17: Four different crystal lattice structures exhibited by the cubic lattice systems.

The geometry of lattice planes in a crystal is described by their orientation and the d-spacing, known as the lattice or interplanar distance. This distance indicates the separation between parallel planes of atoms and is expressed using the Miller indices (h, k, l). To describe the geometry of lattice plane in X-ray diffraction, the Miller indices and reciprocal lattice are used. The reciprocal space is used to describe the arrangements of atoms in a crystal structure and it is identified by the reciprocal lattice vector $\overrightarrow{d^*}$, perpendicular to the atomic planes and has a length proportional to the inverse of the interplanar distance d ($d^* \simeq 1/d$). Additionally, the Miller indices h, k and l play a role in determining the family of lattice planes. These indices represent the family of planes that are perpendicular to the vector $ha^* + kb^* + lc^*$, where a^*, b^*, and c^* are the reciprocal lattice vectors of the direct unit cell vectors a, b and c [29].
Thus, the reciprocal lattice vector d^* can be calculated as:

$$\overrightarrow{d}^*_{hkl} = h\overrightarrow{a}^* + k\overrightarrow{b}^* + l\overrightarrow{c}^*. \tag{1.27}$$

By using Miller indices and the lattice parameter a, b, c, the interplanar distance d is generally defined as:

$$\frac{1}{d^2_{hkl}} = \frac{h^2}{a^2} + \frac{k^2}{b^2} + \frac{l^2}{c^2}\,. \tag{1.28}$$

In the particular case of a cubic lattice, the interplanar spacing is given by the following formula:

$$d_{hkl} = \frac{a}{\sqrt{h^2 + k^2 + l^2}}\,. \tag{1.29}$$

The diffraction of X-rays can only arise if they are scattered by a periodic array of particles with long-range order. As shown in Figure 1.18, the phenomenon is produced after the scattering of coherent X-ray radiations from the atoms of a crystal, by virtue of their uniform spacing, causing the interference of the waves present in the incident beam of X rays. The interference pattern of the waves depends on the relations between two or more waves, such as differences in phase being produced from the differences in path length and a change in amplitude related to the phase difference [30].

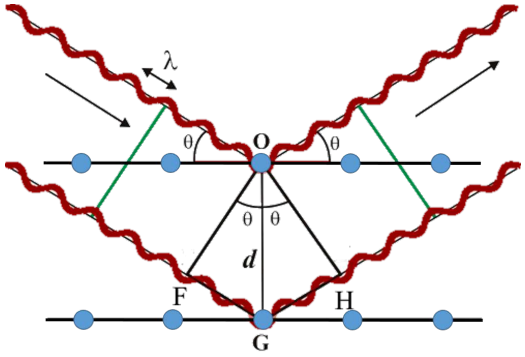

Figure 1.18: Bragg's law: X-ray diffraction by two atomic planes.

For constructive interference and high intensity of reflected wave, two or more waves should be in phase with each other [31]. The condition for maintaining phase coherence after reflection, is that the path length FGH should be an integer multiple of the wavelength, so that the overlapping waves produces high reflection intensity at the scattered angle θ. This is equivalent to saying that the sum of the FG and GH segments is equal to an integer (n) times the wavelength λ [32]:

$$FG + GH = n.\lambda \tag{1.30}$$

with $FG = GH$ and $\sin(\theta) = \frac{FG}{d}$. Finally, the condition of constructive interference is given by Bragg's law as [33]:

$$n.\lambda = 2d.\sin(\theta) \tag{1.31}$$

where λ is the wavelength of the scattered radiation, d is the lattice distance, θ is the Bragg's angle and n is the integer that defines the Bragg's order.
Considering the refraction effect discussed earlier (section 1.2.4), Bragg's law becomes:

$$n.\lambda = 2d.(1 - T).\sin(\theta) \tag{1.32}$$

with T being a correction factor that takes into account the refraction effect. At low energies, using a Johann geometry (described later in section 2.3.2.2), this factor is calculated as:

$$T = \frac{4d^2}{n^2}\frac{\delta}{\lambda^2} \tag{1.33}$$

where δ is the decrement of the real part of the optical index

1.3 Sources of X-rays

X-rays can be produced in various contexts and the emitting sources exhibit a broad range of properties. These sources include natural phenomena such as black holes, neutron stars, plasma, radionuclides, etc., as well as human-made sources like X-ray tubes, synchrotrons, X-ray free-electron lasers, laser plasma or inverse Compton sources. For the practical application of X-rays in material analysis, it is convenient to have sources with well-known emission characteristics that are capable of ejecting an electron from a specific atomic level of a target element. In the following discussion, we will provide an overview of X-ray tubes and synchrotron radiation that are the most commonly used X-ray sources for such analytical studies.

1.3.1 X-ray tube

X-ray tubes are used in a wide range of applications in numerous fields, including the medical sector, security inspections, as well as scientific research and industrial applications. A conventional X-ray tube (Figure 1.19) is a vacuum tube that includes a metal resistive filament serving as the cathode, which emits electrons via thermionic emission when heated to over 1000°C [34]. The metal enclosure around the filament is generally shaped to focus the electron onto a small portion of the target, in order to decrease the focal source point to achieve a larger brilliance of the source. These electrons are then accelerated with a high bias voltage to bombard the metal target known as the anode, resulting in the emission of X-rays of two different natures [35].

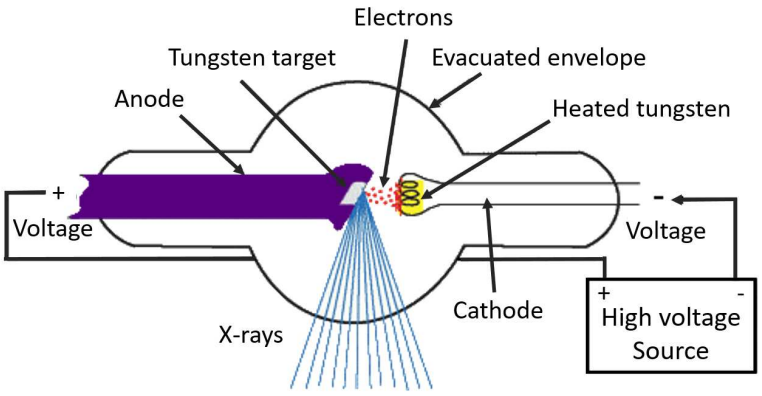

Figure 1.19: Simple X-ray tube. The anode is the positive end of the tube; the target is part of the anode. The cathode is the negative end of the tube; the filament is part of the cathode.

X-rays are produced through two types of interactions between electrons and the atoms in the target, as depicted in Figure 1.20. In the first interaction, electrons lose their energy due to electrostatic interactions while passing through the Coulomb field of a nucleus, resulting in the production of X-rays. This process is known as Bremsstrahlung, a German term meaning "braking radiation". This type of interaction generates a continuous spectrum characterized by a maximum energy limit corresponding to the applied high voltage (kV) [7] as well as an intensity that is proportional to the electron current and the square of the accelerating voltage. The second type of interaction produces a discrete spectrum which occurs when electrons interact with the atoms of the target material and leads to the ejection of electrons from the inner shells of the atom followed by atomic rearrangement (discussed earlier in section 1.1.4.1). In X-ray tubes, various types of anodes are used to enable the production of X-rays, such as fixed, rotating, and liquid anodes. Fixed anodes, typically made of tungsten, are fixed in position and have a limited capacity to dissipate heat. Rotating anodes, on the other hand, are designed to spin at high speeds, allowing for a larger target area and better heat dissipation. This enhanced capability enables rotating anodes to generate higher-intensity X-rays [36]. More recently developed, liquid metal anode X-ray tubes employ a high-speed jet of liquid metal as the target anode material, facilitating the generation of high-intensity X-rays while efficiently dissipating heat [37].

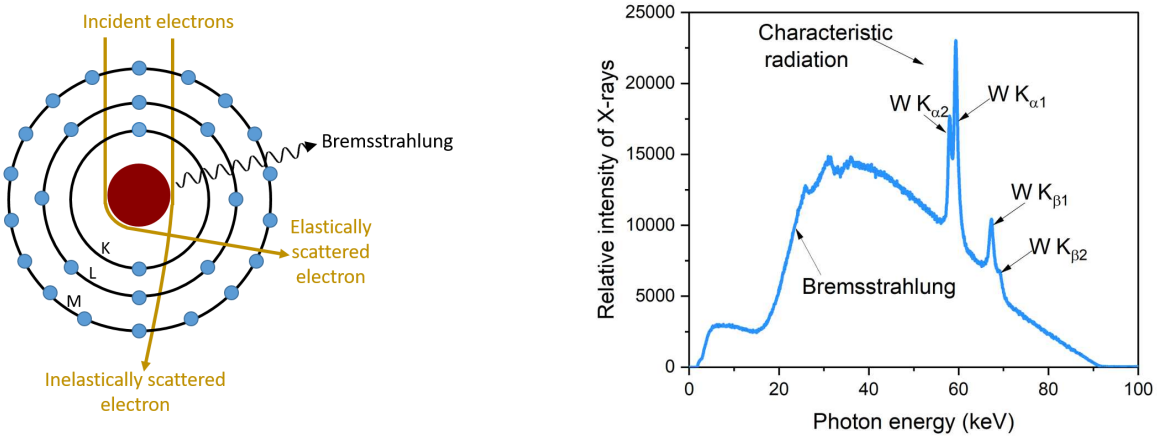

Figure 1.20: X-ray generation: (Left) Scheme of X radiation or Bremsstrahlung radiation. Electrons are scattered both elastically and inelastically by the positive nucleus. In the inelastic scattering, the electron loses energy, leading to the production of Bremsstrahlung. On the other hand, elastically scattered electrons are generally scattered through large deviation angles which do not contribute to the Bremsstrahlung. (Right) Spectrum of emission from a tungsten target.

1.3.2 Synchrotron radiation

The synchrotron radiation corresponds to the electromagnetic radiation emitted when charged particles are accelerated radially [38]. The interest of synchrotron radiation is its coverage of a wide range of the electromagnetic spectrum: X-rays, UV light, visible and infra-red light. The generation of synchrotron radiation begins in the linear accelerator (LINAC), where electrons are extracted from a source and linearly accelerated up to several millions of electron volts (MeV). Then, the booster increases the energy of these electrons to reach the nominal energy required for injection in the synchrotron storage ring (GeV). The electrons in the storage ring are guided through a strong magnetic field into a quasi-circular high vacuum tube of few hundreds of meters circumference, as illustrated in Figure 1.21.
This ring is an alternation of straight and curved sections, where in each curved section, the trajectory of the electrons is then controlled with magnetic devices (dipoles [bending magnets] and undulators). As the electrons change direction, they emit synchrotron radiation and lose some of their energy. To compensate for this energy loss, electrons are re-accelerated using radio-frequency (RF) cavities placed throughout the circular path. In the end, the light beams tangent to the storage ring are transported into the beamlines that surround the storage ring where the experiments are performed. Each beamline is designed for a specific technique and energy range, with monochromatic systems in place to select the desired energy.
At the SOLEIL synchrotron, the linear accelerator (LINAC) measures 16 meters in length and is capable of accelerating electrons up to 100 MeV. The storage ring has a circumference of 354 m with a nominal energy of 2.75 GeV. To compensate for electron loss, a bunch of 6 GeV electrons is injected from the booster every 50 milliseconds.
Synchrotron radiation is not only produced artificially; it can also be found in space around black holes when matter is accelerated before being absorbed, and also in the nebulae of pulsars and quasars that can create such phenomena [16].

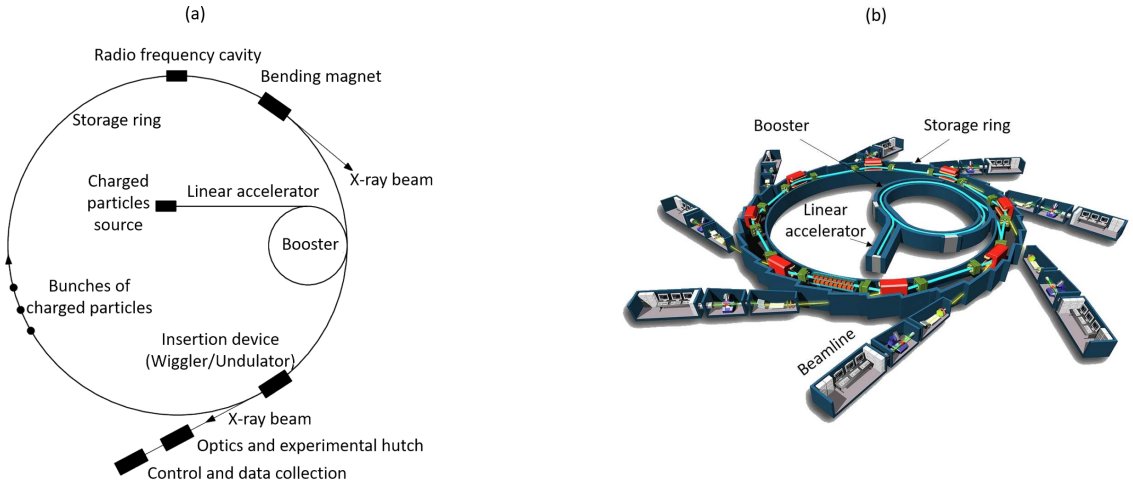

Figure 1.21: (a) Schematic synchrotron source with storage ring and magnets and (b) SOLEIL synchrotron.

1.3.3 SOLEX

SOLEX (Source Of Low-Energy X-rays), is a tunable monochromatic X source in the 600 eV – 28 keV energy range developed at LNHB [39, 40]. The SOLEX system includes an X-ray tube as a photon source and a monochromator crystal, both motorized and arranged in a pantograph configuration to ensure that the tube, crystal and exit slit maintain equidistant positioning on the focusing circle (Rowland circle) and that the output direction remains unchanged during a Bragg angle shift. Energy selection is accomplished by adjusting the incidence angle on the crystal for a given crystal and fulfilling Bragg's law. Two output directions can be selected to direct the monochromatic X-ray beam towards two detectors for comparative purposes. Dedicated signal processing, amplification systems, and multichannel analyzers are employed to record spectra. The second position is permanently equipped with the REFLEX gas proportional counter, which serves as a reference for flux measurement.

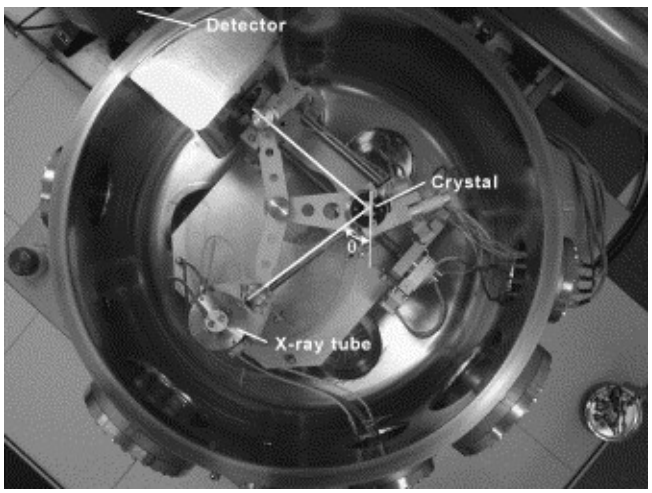

Figure 1.22: Tunable X-ray source SOLEX.

1.4 Application to X-ray fluorescence

X-ray fluorescence (XRF) is defined as the emission of secondary X-rays with the characteristic energies of an the element after X-ray photon excitation, enabling the chemical composition of a sample to be identified. It can be used as an analytical method for elementary quantification (stoichiometric or compounds) as well as for the determination of layered structures (thickness and density) [41]. The beginning of the XRF as a spectrometric technique began in the twentieth century. After the first use of XRF as an analytical technique, it was improved after finding the relation between the frequency of characteristic X-ray emission lines and the atomic number of the elements by Moseley.
However, XRF has limitations, particularly when it comes to detecting light elements (those with low atomic numbers), making it an insufficient method for their identification, specially when using poor spectral resolution detector such as silicon drift detectors. This problem for light elements is further accentuated by different factors. Firstly, the fluorescence of these elements occurs at low energy levels, where lines are most numerous, making it difficult to distinguish them among the large number of other lines (other atoms of the measured target, components of the apparatus, atmospheric gases...). Secondly, the low energy fluorescence of light atoms is also difficult to measure due to absorption by materials in the path of the fluorescence photons. In such cases, other X-ray scattering techniques can be employed, including grazing-incidence small-angle scattering GISAXS, wide-angle X-ray scattering WAXS or small-angle X-ray scattering SAXS...
In this study, we concentrate on XRF for detection and quantification of heavier elements $Z > 13$. One practical challenge with these elements, which have well-spaced XRF lines at high energies, is having a sufficiently energetic excitation source (described in Section 1.3). Another challenge lies in the detection capability of measuring the high energy of their X-ray fluorescence photons with adequate precision discussed later in Chapter 2.

Chapter 2

X-ray detection

X-ray detectors are based on the principle of converting X-ray photon energy into easily measurable and quantifiable information. Photon detectors, which are commonly used, operate based on the ionization process that occurs following the photoelectric effect in the detecting material: an ejected electron interacts with the material through successive inelastic collisions, leading to the creation of pairs of charges (e^-, e^+). These travel in opposite directions upon the effect of an applied voltage to produce a signal. This fundamental principle is the basis for gas and semi-conductor detectors. Another type of detector is based on scintillation, which involves light emission following photon interaction. This principle underlies a wide variety of detectors. In addition to ionization-scintillation based detectors, bolometers are another type of X-ray detector. They operate based on the principle of a temperature increase resulting from photon interactions. However, their implementation can be challenging due to the need for operation at extremely low temperatures [42].
Historically, early X-ray detection relied on photographic plates followed few years later by gas-filled counter [43]. Gas detectors offer high spatial and energy resolution and are not affected by the electronic interference. However, these detectors suffer from low efficiency for X-ray detection due to their low density. Later on, scintillation detectors consisting of scintillating material coupled to a photomultiplier were used due to their high efficiency for hard X-rays despite their low energy resolution [5]. Subsequently, scintillator detectors were replaced for example by solid state detectors Si(Li) and HPGe, then silicon drift detectors (SDD) which contributed to the development of modern energy-dispersive X-ray analyzing techniques with higher resolution.
In this chapter, we will introduce various types of X-ray detectors, focusing on their main functions and respective applications in the field of X-ray analysis.

2.1 Gas detectors

2.1.1 Gas proportional counter

As shown in Figure 2.1, a gas proportional counter consists of a chamber filled with a noble gas with a thin wire along its radial axis, held under high positive voltage. When photons enter the detector, they ionize the gas atoms in the chamber, producing a number of ion pairs (n) that travel in opposite directions, with the cations moving towards the cathode and the electrons towards the wire (anode). As the electrons approach the high field region, they are accelerated

enough to cause additional ionizations by colliding with gas atoms. This multiplication effect results in a current pulse proportional to the energy of the incoming photons [44]. Gas counters can be used either in this pulse mode (proportional counter) or in avalanche mode where there is no more linearity between the energy of incident photons and the output pulse amplitude (application e.g., to Geiger-Muller detectors). The most frequently used gases are argon, xenon, neon and krypton. Argon flow proportional counters are used to detect fluorescence X-rays in the range up to ∼6 keV while krypton or xenon are used for the higher-energy range. When compared to other detectors, the low density of the gas and the relatively small thickness of these detectors result in a very low efficiency for medium and hard X-rays. Finally, these detectors produce a signal for each X-ray photon and the time-accumulation result is a histogram where all events are sorted by energy. This histogram (or spectrum) presents peaks with an energy resolution of 12 % at 5.9 keV, which is halfway between the high resolution of semiconductor detectors and the low resolution of scintillation detectors [5].

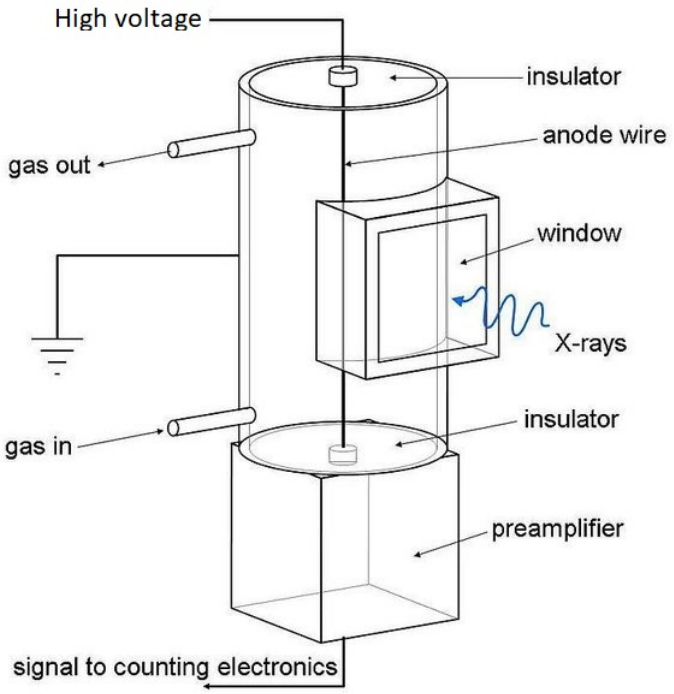

Figure 2.1: Arrangement of a gas flow proportional counter [45].

2.1.2 Ionization chamber

An ionization chamber is a type of gas detector consisting of a cylindrical chamber filled with gas at a specific pressure, along with two opposing electrodes (anode-cathode) to collect electrical charges using an external circuit. The principal function is based on ionizing the gas atoms inside the cylinder with an X-ray or γ-ray source. A high voltage is then applied between the electrodes; in this case, the negative charges migrate towards the anode and the positive charges towards the cathode resulting in an electric current in the circuit allowing for radiation detection. The applied voltage should be sufficient enough to prevent recombination, allowing a complete collection of the positive and negative charges. The rate at which ionizing radiation

enters the ionization chamber is measured as a current with an electrometer and it is directly proportional to the radiation's entrance rate [46]. Figure 2.2 represents an ionization chamber used to monitor photon fluxes at synchrotron facilities.

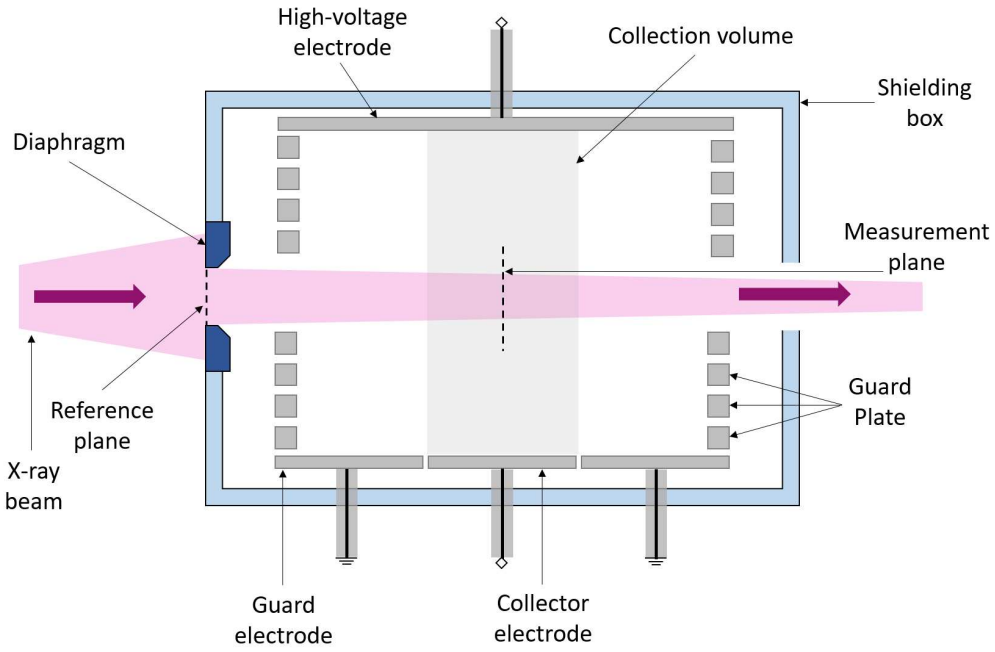

Figure 2.2: Schematic of a parallel-plate free-air ionization chamber.

2.2 Solid-state detectors

2.2.1 Photodiode

The working principle of photodiodes relies on the photoelectric effect, where the interaction of a photon with the photodiode active material leads to the creation of an electron-hole pair. All photodiodes function using either a P-N junction [47, 48] or a P-I-N junction [49] work in photovoltaic mode or under reverse bias, with the P-side connected to the anode and the N-side connected to the cathode. A P-N junction includes a P-type semiconductor (where holes are the majority charge carriers) joined to an N-type semiconductor (where free electrons are the majority), while P-I-N junction includes an intrinsic semiconductor separating the P and N-doped semiconductors. Electron transfer is slowed down by a depletion region at the P-N junction interface [50]. If photoabsorption of the photon occurs within the diffusion length or inside the depletion region, the carriers are separated by the built-in field of the depletion region. As a result, electrons move towards the cathode and holes move towards the anode, generating a photocurrent. The working principles of a P-N junction photodiode is presented in Figure 2.3. As for the ionization chambers, the photodiodes are frequently used as beam intensity monitors as they produce a current proportional to the incoming flux. Their great stability and linearity are a significant advantage for accurate flux measurement.

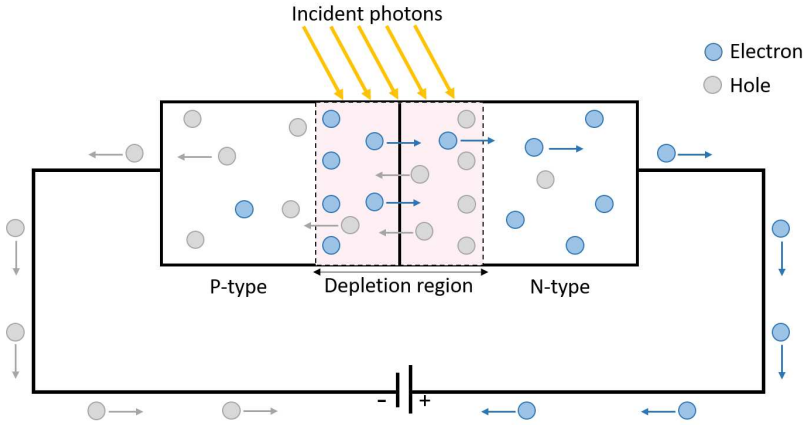

Figure 2.3: Working principle of a P-N junction photodiode.

2.2.2 Scintillation counter

The scintillation counter (SC) consists of a scintillating material linked to a photomultiplier tube (PMT) composed of a photocathode followed by a series of dynodes (Figure 2.4). Different types of scintillators can be used, such as organic, inorganic, or liquid scintillators depending on the specific application. The working principles of these counters relies on the interaction of a photon with the scintillator material, resulting in the emission of near visible or visible light [45]. Afterwards, the light photon strikes the photocathode, producing photoelectron emission. The photoelectrons are then focused onto the first dynode, generating further electrons that are amplified at the subsequent dynodes all the way down the chain. The signal is amplified and collected at the anode before being sent to the measuring circuit.

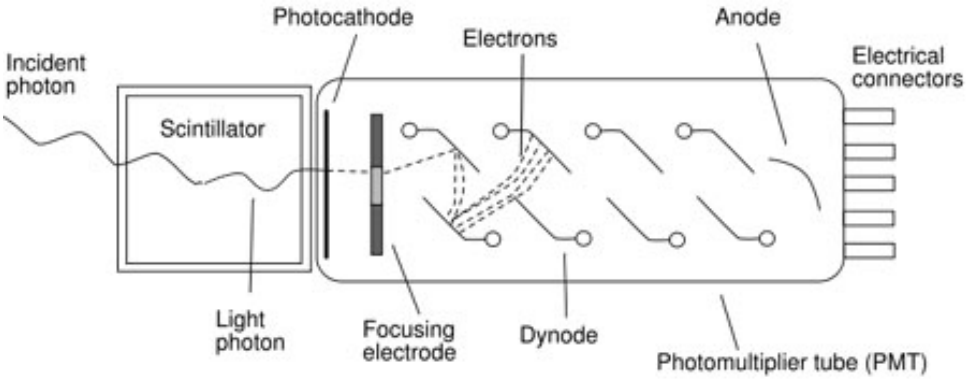

Figure 2.4: Schematic diagram of a scintillation detector comprising a scintillation material coupled to a photomultiplier tube.

2.2.3 Semi-conductor detector

Semiconductor detectors work similarly to gas proportional counters, except that the gas is replaced by a semiconductor material [51]. Silicon (Si) and germanium (Ge) are the most widely used semiconductor detector materials. In the semiconductor material, atomic electron states are expanded into energy levels where the outer electrons are located in the valence band

while the next higher states are in the conduction band, separated from the valence band by a bandgap energy E_g (Figure 2.5(a)). When the semi-conductor material is excited by a photon with energy exceeding the bandgap energy, an electron from the valence band absorbs the energy and moves to the conduction band, leading to an electron-hole pair generation by photoelectric effect (Figure 2.5(b)). The output signal is created by collecting the charges without any multiplication procedure. Due to the applied high voltage, the electrons in the conduction band drift towards the anode and the holes in the valence bands move in the opposite direction towards the cathode (Figure 2.5(c)). The voltage signal in relation to the photon energy is then produced after amplification of collected charges. However, the semiconductor detectors must be cooled down to reduce the thermal charge carrier generation (noise) [52]. High-purity germnaium (HPGe) detectors must be cooled down to liquid nitrogen temperatures (-196°C) whereas new silicon detectors only needs -20°C.

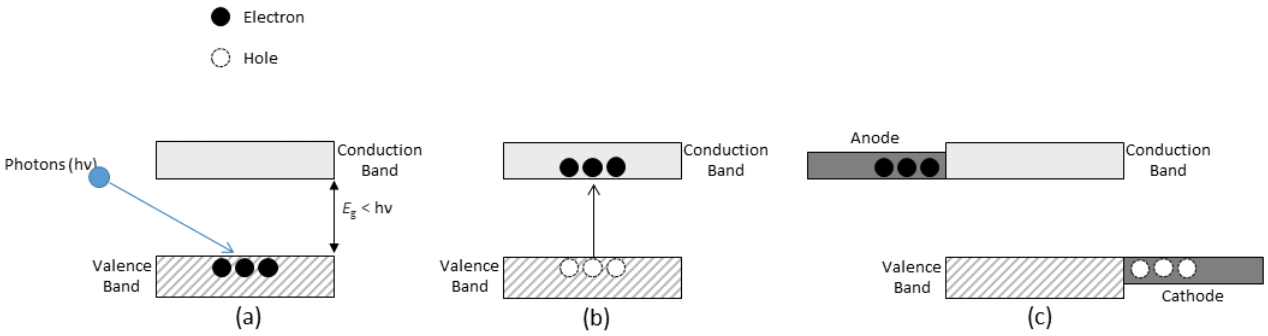

Figure 2.5: (a) Photoelectric effect after excitation of the material with an energy higher than its bandgap, (b) electron-hole pair creation after absorption of the incident photon and (c) charge separation and collection.

Germanium and silicon are the main elements used as detecting material for energy-dispersive spectrometers. HPGe detectors are most often used in γ-ray measurements [53] while some small-sized HPGe detectors can be dedicated to low-energy X-ray measurements. In the X-ray energy range (below 100 keV), two primary types of silicon detectors are used: the classical geometry (large anode) such as the silicon lithium detectors Si(Li) or the Si-PIN, the new geometry with a reduced anode size for better signal/noise ratio with the silicon drift detectors (SDD). Overall, the choice of detecting material depends on the specific energy range and type of radiation being measured, as well as the desired sensitivity and energy resolution of the detector.

2.2.4 Silicon drift detector

The silicon drift detector (SDD) (Figure 2.6) is semiconductor detector. The SDD consists of fully depleted high-resistivity silicon, in which after photoelectric effect, the generated electrons are driven through concentric rings towards a small collecting anode [54, 55]. The N-type Si wafer is used to create a pattern on the silicon chip. The P+ concentric rings implanted on the front side of the device are biased with a decreasing voltage to provide a field gradient to drift the generated electrons towards the anode. In addition, the continuous and homogeneous P+ junction implanted on the back of the detector acts as a radiation entrance window. After

collection of the electrons at the anode, they are transferred to the field-effect transistor (FET) or any equivalent circuit to amplify the signal.

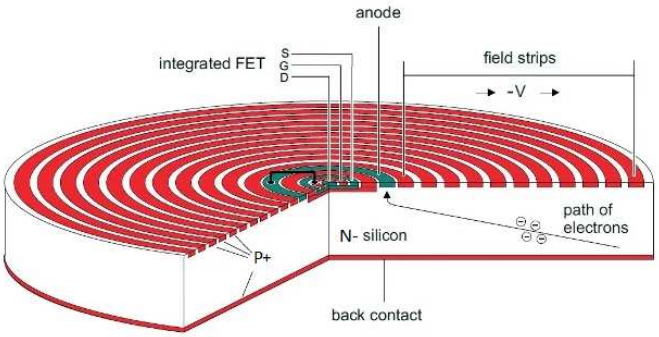

Figure 2.6: Schematic of a cylindrical SDD with an integrated amplifier. Electrons are guided by an electric field towards the collecting anode in the center of the device [55].

SDDs feature an anode with a ring structure and a larger bandgap energy than other semiconductors, such as germanium detectors [56]. The larger bandgap of silicon implies that more energy is necessary for electron transition, limiting the spectral resolution of the detector. To achieve proper functioning of SDDs in the X-ray energy range, they need to be cooled down to temperatures around -20°C, which can be done easily by a Peltier cooling module. This is necessary to reduce noise resulting from thermal agitation [57].

2.2.5 Charge-coupled device

The charge-coupled device (CCD) is a photodetector relying on a metal-oxide-semiconductor structure unlike P-N junction-based photodiodes. It consists of a P-type semiconductor body, a thin insulating layer such as silicon oxide (SiO_2), aluminum oxide (Al_2O_3), gallium arsenide (GaAs)..., and an array of gating electrodes. Figure 2.7 is a representative example of a SiO_2 CCD structure.

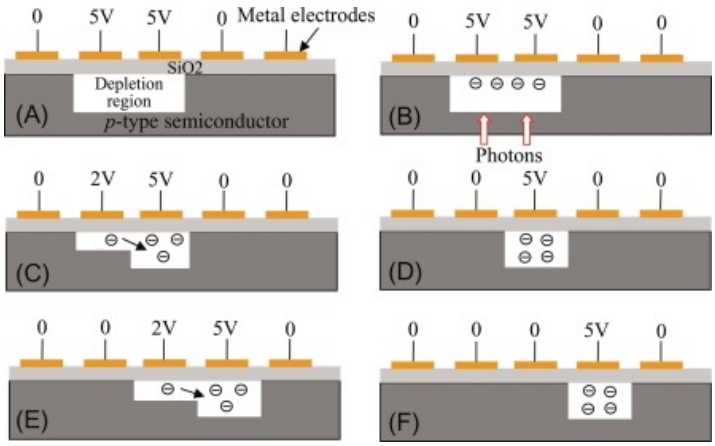

Figure 2.7: (A) Cross-sectional structure of CCD and (B)-(F) illustration of programmable charge shift in the readout process [58].

By applying a positive bias voltage to a gate electrode, holes are repelled, creating a depletion region where incoming photons generate photoelectrons (Figure 2.7.B). These charges are programmably shifted horizontally to be electrically amplified and collected, as illustrated in Figure 2.7 C-F. A schematic representation of the CCD scanning procedure can be seen in Figure 2.8. As depicted in Figure 2.8, the gating electrodes of imaging CCDs are typically arrayed in a two-dimensional (2D) array. The CCD, as the imaging sensor, is typically situated on the camera's focal plane. Upon exposure, the charges from the initial row are relocated to an area on the sensor known as the read-out register. Subsequently, these signals are channeled to an amplifier before being directed to an analog-to-digital converter. Once the row is read, its charges on the read-out register are deleted, allowing the subsequent row to enter while the rows above it shift down by one row. The charges within each row exhibit a coupling relationship with the row above, enabling the rows to move down in a coordinated manner as the first row progresses. This mechanism allows for the sequential reading of each row [59]. The structure of the CCD allows them to be used as position-sensitive detectors.

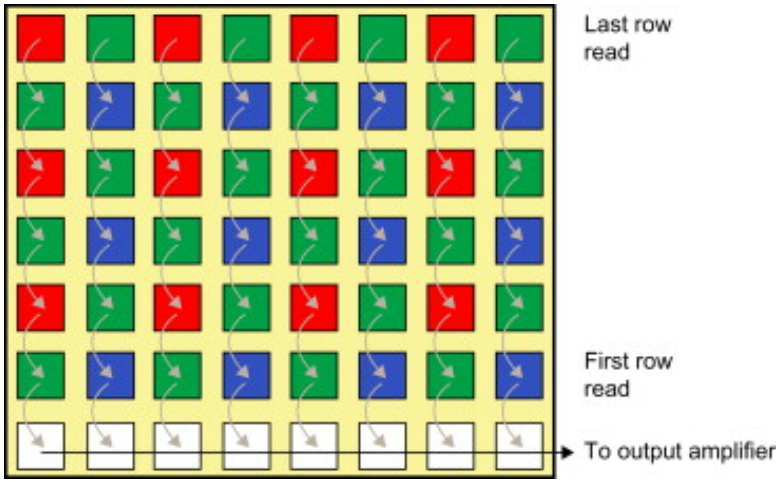

Figure 2.8: Interline-transfer CCD. The CCD image sensor transfers an entire row of pixel data to the readout register. Subsequently, the readout register conveys individual pixel values to the output amplifier in a systematic manner [59].

A summary of some of X-ray detectors characteristics is presented in Table 2.1.

2.3 X-ray spectrometry

The analysis of a sample by means of an X-ray spectrum, emitted under X-ray excitation, allows the characteristic components of the chemical elements to be identified. Therefore, X-ray spectrometry is one of the most used techniques, due to its coverage of a large range of densities and a great variety of materials. Modern X-ray spectrometers can either use an energy-selective detector to extract narrow energy bands (energy-dispersive XRF (EDXRF)) from the polychromatic radiation emitted by the sample or a single crystal's diffracting power to select a narrow wavelength band (wavelength-dispersive XRF (WDXRF)). In both techniques, the information is extracted from X-ray detectors by absorbing X-ray radiations and converting it into an electric signal, which can be then processed by digital electronics. This section provides

Table 2.1: Overview of common radiation detectors: composition, measurement technique, and energy resolution.

Detector type	Detector composition	Measurement technique	$\Delta E/E$ at 5.9 keV (%)
Gas proportional counter	Gas-filled	Counting and spectrometry	12
Ionization chamber	Gas-filled	Counting	n/a
Photodiode	Solid-state	Counting	n/a
Scintillation counter detector	Solid-state	Counting	40
Silicon drift detector (SDD)	Solid-state	Spectrometry	~2.1
High-purity germanium (HPGe)	Solid-state	Spectrometry	~1.9
Charge-coupled device (CCD)	Solid-state	Counting, spectrometry and position	n/a

a short description of the general features of the main X-ray spectrometers, to understand their different performances and operating features.

2.3.1 Energy-dispersive spectrometers

Energy-dispersive spectrometry is a powerful characterization method used in the physical and biological sciences, engineering and manufacturing. Energy-dispersive spectrometers (EDS) were initially developed for X-ray measurements made with semiconductor detectors [60], which involves physical calculations and/or empirical measurements for corrections of matrix effects [61]. The EDS has been shown to produce accurate analytical results for elements with atomic numbers $Z \geq 11$ with at least 95 % of measurements falling within $\pm$ 5 % relative of the correct value for major constituents [61, 62]. The use of a semiconductor detector in the EDS, enables the measurement of a wide photon energy range [63] which revolutionized X-ray microanalysis by providing continuous measurement of the majority of the periodic table. However, quantifying low atomic number elements ($Z \leq 10$) that must be measured with characteristic X-ray peaks below 1 keV has always been a challenge to X-ray microanalysis. These low-energy peaks are traditionally measured with another type of spectrometer such as the wavelength dispersive spectrometer (WDS).

2.3.1.1 Instrumentation

As illustrated in Figure 2.9, the geometric arrangement of EDXRF is rather simple, as the EDS directly records the X-ray fluorescence emitted by the sample irradiated by an X-ray

source. After excitation, the sample's fluorescence radiation is simultaneously collected by the detector, combined with a multi-channel analyzer, which separates the different energies of the characteristic lines corresponding to each element in the sample. A collimator is used to avoid any parasitic radiation that might come directly from the X-ray source, ensuring that only X-rays emitted by the sample are collected. In addition, filters, collimators, monochromators, and focusing optics may be used to modify the shape or intensity of the source spectrum or the X-ray beam shape. Nowadays, EDSs are quite exclusively SDDs due to their practicability and low cost. The EDS being cooled down to a negative temperature, it must be protected from the air in a high vacuum and the window must be as thin as possible to minimize the absorption of low-energy photons.

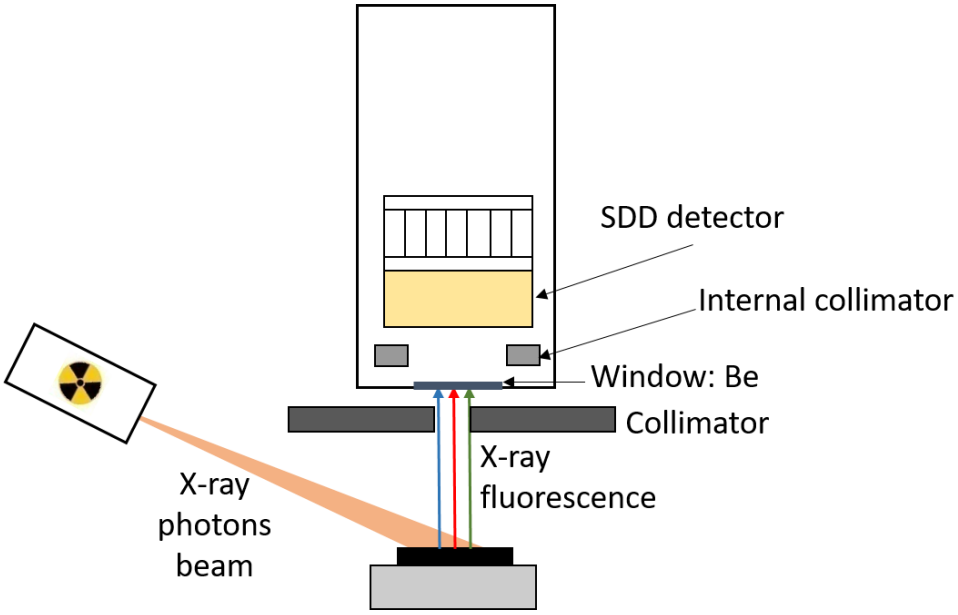

Figure 2.9: Schematic of an energy dispersive X-ray fluorescence (EDXRF) setup.

The energy dispersive spectrometer uses both analog and digital components for processing spectral data. As shown in Figure 2.10, the initial steps of the process use an analog circuit, which includes a preamplifier, amplifier, and an analog-to-digital converter (ADC). First, the preamplifier receives the small electrical signals from the SDD and converts them into a voltage signal with minimal noise and high gain. Two integral mechanisms within the preamplifier, the resistive feedback and the reset mechanism, can be used to return the SDD signal back to its background level. The resistive feedback mechanism helps maintain signal stability by feeding part of the output back into the input, preventing signal saturation and preserving signal integrity. The reset mechanism clears accumulated charge in the feedback capacitor after several events, preparing the preamplifier for the next incoming signal from the SDD. Following the preamplifier, the signals then proceed to the amplifier, which further increases the power level of the signals and shapes them for subsequent processing stages, such as analog-to-digital conversion, while minimizing any increase in noise level to maintain the accuracy of the data. The amplified signal then enters the ADC, which is responsible for transforming the analog signal into a digital format, making it readable and processable by digital systems. The digitized signal is sent to the multi-channel analyzer (MCA), a digital device that processes the

digital signals, sorting them by energy into a histogram which represents the energy spectrum of the detected radiation. The spectrum obtained contains the energy of X-rays on the horizontal axis and the number of recorded events on the vertical one.

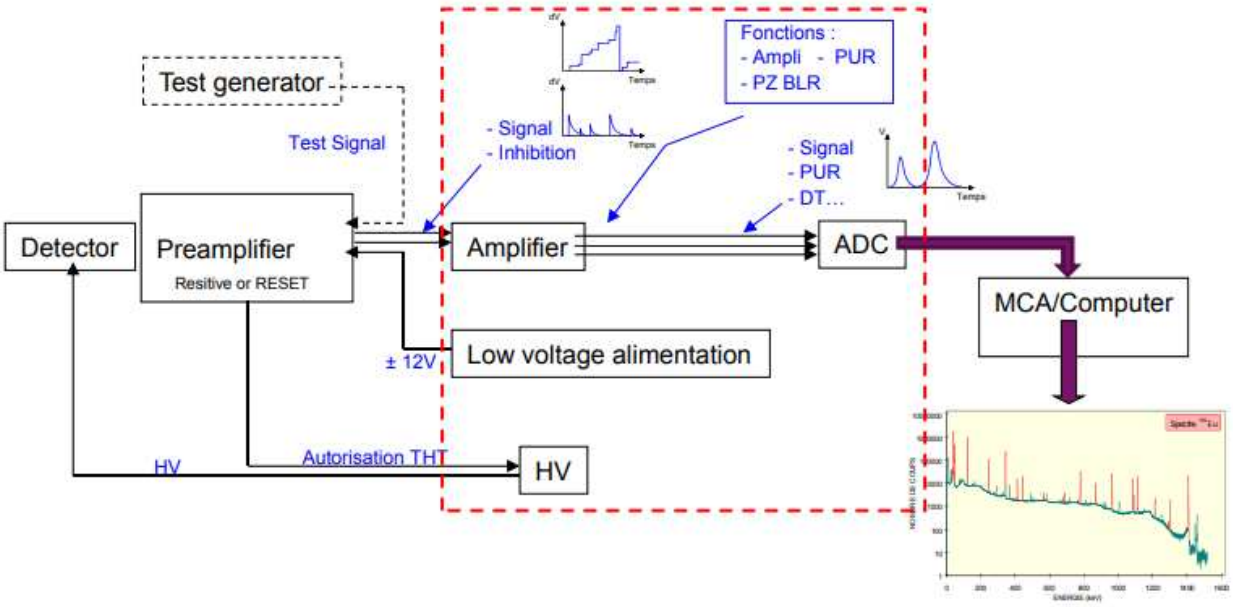

Figure 2.10: Digital signal processing of an EDS.

The SDD positioning system used for energy-dispersive spectrometry in this study is shown in Figure 2.11. The Amptek X-123 Fast SDD installed on a translation stage, equipped with a vacuum extender was used, feed-through coupling and a beryllium window. To minimize the electronic noise, the detector is cooled to -20°C using a Peltier module. The active area of the detector is 18.2 mm^2 (Figure 2.12 on the right), defined by the aperture of the internal collimator ∼4.41(6) mm (Figure 2.9). This detector is capable of analyzing a wide range of elements with high sensitivity and precision, with an energy range spanning from 650 eV to 50 keV.

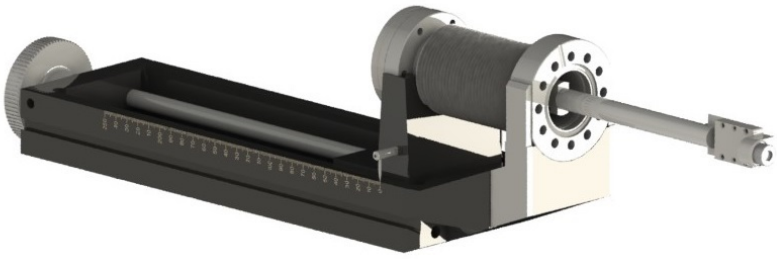

Figure 2.11: A 3D schematic drawing of the EDS using an X-123 Fast SDD. The spectrometer is placed on a translation stage to change its position relative to the sample.

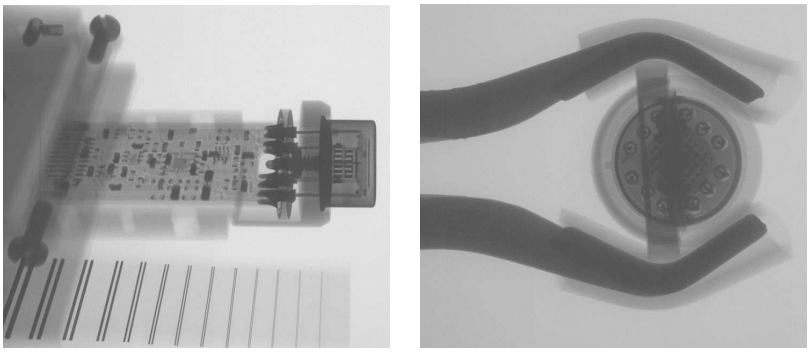

Figure 2.12: Radiography images for the SDD (left) and the SDD active area (right).

2.3.1.2 Energy resolution

In X-ray spectrometry, the energy resolution represents the capability of distinguishing photons closely separated in energy. The energy resolution of an EDS is substantially poorer than other X-ray detectors such as the WDS, causing the fluorescence lines to overlap. The recorded voltage pulses are affected by numerous causes of fluctuations influencing the measurements. Due to these fluctuations, the pulse height distribution of photons of energy E_0 is broadened in comparison to an ideal Dirac-δ-like distribution and the energy resolution is expressed as the full width at half-maximum (FWHM) of the resulting peak (Figure 2.13). The lower the FWHM, the better the resolution and the better it will be at resolving peaks of closely spaced X-ray lines [5]. As shown in Figure 2.13, the EDS of the LNHB presents a resolution of ∼125 eV at 5.41 keV for the K_α lines of chromium.

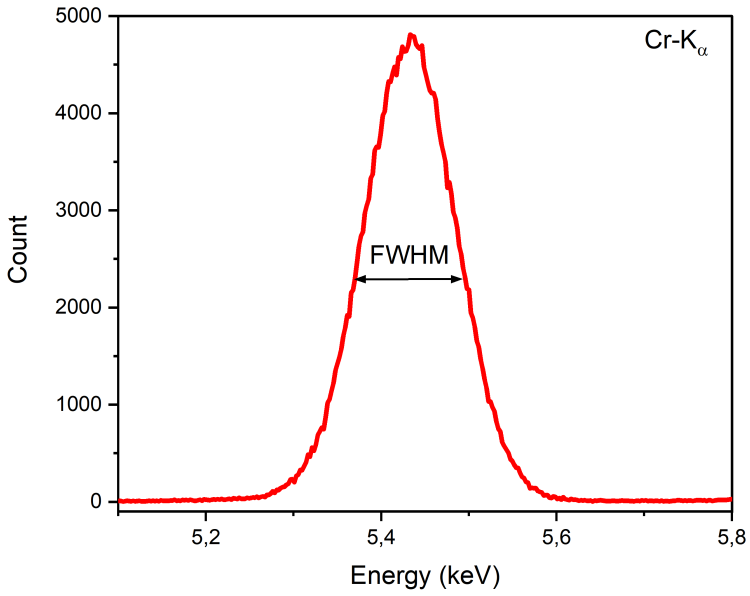

Figure 2.13: Peak of Cr- K_α, centered at 5.41 keV, measured with an energy-dispersive spectrometer. The FWHM of the peak (∼125 eV) is commonly used as an indicator of the energy resolution of the system.

The energy resolution ($\Delta E = \text{FWHM}$) of an EDS system can be calculated taking into account all fluctuation sources as:

$$\Delta E^2_{\text{meas}} = \Delta E^2_{\text{collection}} + \Delta E^2_{\text{multiplication}} + \Delta E^2_{\text{statistical}} + \Delta E^2_{\text{el.noise}} \,. \tag{2.1}$$

- $\Delta E_{\text{collection}}$ represents the fluctuations of the collection charges,
- $\Delta E_{\text{multiplication}}$ represents the energy resolution contribution due to the noise in the charge multiplication process which occurs in the detector when incoming X-rays create a charge (electron-hole pairs), which is then amplified to produce a measurable signal. The variation in this amplification process contributes to the overall uncertainty in the energy measurement.
- $\Delta E_{\text{statistical}}$ represents the intrinsic detector resolution that depends on the statistical fluctuations (Poisson statistics) related to the conversion mechanism.
- $\Delta E^2_{\text{el.noise}}$ represents the contribution to the energy resolution of the electronics noise of the detector amplifying and shaping system.

The statistical contribution $\Delta E_{\text{statistical}}$ is characterized by a variance proportional to the number of generated charge carriers σ^2_E and the measured distribution can be then described by means of a Gaussian function, with standard deviation, σ_E , then:

$$\Delta E_{\text{statistical}} = 2.35\sigma_E = 2.35\varepsilon\sigma_n \,, \tag{2.2}$$

where σ_n stands for the standard deviation in the number of generated carriers equal to the average number of these carriers $\widetilde{n}$ and ε represents the conversion factor from energy to number of carriers (mean pair creation energy). For an SSD detector, the variance is deviated from Poisson statistics due to the correlation in the processes of generation of the individual carriers and becomes as follows:

$$\sigma^2_n = F\widetilde{n} \,, \tag{2.3}$$

in which F is the Fano factor [64]. In this case, the intrinsic detector resolution becomes:

$$\Delta E_{\text{statistical}} = 2.35\sqrt{FE\epsilon} \,. \tag{2.4}$$

The last term, $\Delta E^2_{\text{el.noise}}$ is related to the equivalent noise charge (ENC) as:

$$\Delta E_{\text{el.noise}} = 2.35\epsilon\frac{ENC}{q} \tag{2.5}$$

with q is the electric charge. The electric noise of the spectrometer depends on the three main sources:

- ENC_s: the white series noise or the voltage noise affected by the FET gain and the sum of the components capacitance in the sensor/FET circuit.
- $ENC_{/\!/}$: the parallel noise due to the leakage current, which results from the bias voltage applied to the sensor.
- $ENC_{1/f}$: the $1/f$ series noise related to the properties of the detector.

Therefore, the squared value of the ENC can be written as:

$$ENC^2 = ENC_s^2 + ENC_{/\!/}^2 + ENC_{1/f}^2 \,. \tag{2.6}$$

These three contributions are given by [65]:

$$\begin{aligned} ENC_s^2 &= A \cdot Ct^2/\tau \\ ENC_{/\!/}{}^2 &= B \cdot i_n^2 \cdot \tau \\ ENC_{1/f}^2 &= C \cdot Ct^2 \end{aligned} \tag{2.7}$$

where Ct denotes for the value of the detector and amplifier capacitance and τ is the shaping time used for signal processing. The coefficients A, B and C are constants that depend on the "shape factors". The ENC is affected by the shaping time, hence this parameter has an optimal value (τ_{opt}) that minimizes the ENC. In addition, the detector capacitance should be as low as possible to minimize both the ENC_s and the $ENC_{/\!/}$ contributions, and hence the ENC value. In this case, both the τ_{opt} and the $ENC(\tau_{opt})$ are reduced. The detector capacitance depends on the physical structure of the detector. It is proportional to the detector sensitive area for standard diodes. However, in SDD detectors, the capacitance is independent of the active area. It depends mainly on the anode area, which needs to be small in order to reduce the white serial and the $1/f$ noises. Furthermore, reducing the values of the capacitance, and therefore the shaping time, improves also the maximum counting rate of the system. In addition to the effect of white series and the $1/f$ series on the resolution, there is the effect of the leakage current, which depends on the temperature. As shown in Figure 2.14, the resolution tends to be constant below some temperature, in this case the resolution depends only on the white series and the $1/f$ series noises, and starts to decrease once this value is exceeded.

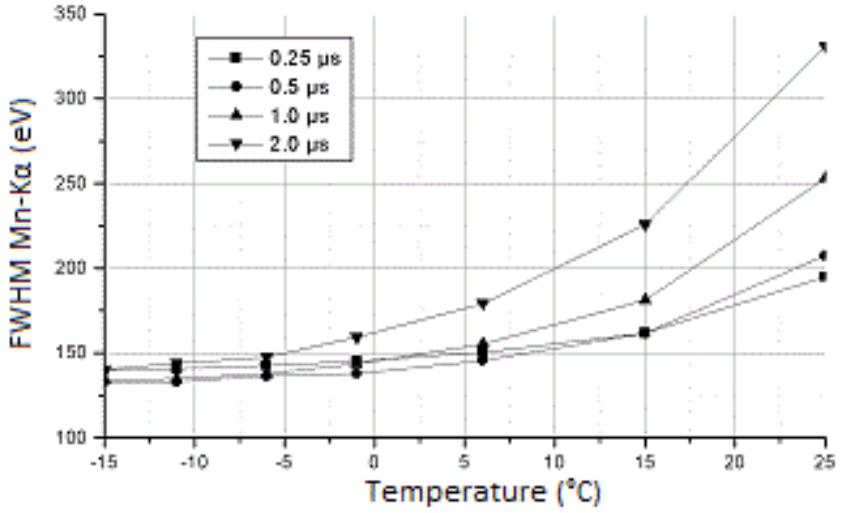

Figure 2.14: Energy resolution of a SDD as a function of the temperature and of the shaping time (from https://www.pnsensor.de/Welcome/Detectors/SDD/).

Since the leakage current depends mainly on the active area, there is a need to reduce the temperature when a large active area is required.

2.3.1.3 Detection efficiency

The experimental setup efficiency is defined as the fraction of the total number of photons emitted by the sample that interacts within the detector volume and are completely absorbed. The primary limiting factor of the detection efficiency is the solid angle which affect the geometrical efficiency. The solid angle depends mainly on the detector active area, the distance with respect to the source and the sample dimensions.
The second limitation of the detection efficiency is the intrinsic efficiency, or quantum efficiency, defined as the fraction of the number of photons entering the detector which interact in the detector material. The intrinsic efficiency depends on the transmission and absorption of both the detector material and the absorbing layers placed in the path of the beam (window, dead zone, ...), expressed as:

$$\eta_i = \left[\prod \exp\left(-\mu_s \cdot x_s\right)\right] \cdot \left[1 - \exp\left(-\mu_d \cdot x_d\right)\right] \tag{2.8}$$

where μ_s and μ_d represent the linear attenuation coefficient (in cm^{-1}) of the screen and the active detector material at the given photon energy respectively and x_s and x_d represent the thickness (in cm) of the active detector material and the screen respectively.
The third limitation of the detector efficiency arises from events that affect the full-energy peak (photopeak) efficiency by transferring only a part of the energy to the detector. The full-energy peak efficiency (FEP) is described as the fraction of the photons interacting in the detector, that deposit their full energy in the material: The first event affecting the FEP is represented by the re-absorption of Compton scattered photons in the detector itself for energies up to 100 keV. The second event corresponds to the escape process. This process results from the fact that there is a probability that the fluorescence photons emitted by the detector material may escape from the detector without being absorbed [66]. As a result, the spectrum contains an escape peak with an energy equal to the difference between the photon excitation energy on the detector and the energy of the escaping photon. The energy of the K escape peak can be calculated as:

$$E_{escape} = E_{incident} - E_{ki} \tag{2.9}$$

where $E_{incident}$ is the energy of the incident X-ray photon on the detector and E_{ki} is the energy of the K_i X-ray emission lines for the detector material (1.74 keV for Si-K_α and 9.89 keV for Ge-K_α). Figure 2.15 shows the X-ray spectrum of chromium, including K silicon escape peaks from both Cr-K_α and Cr-K_β.

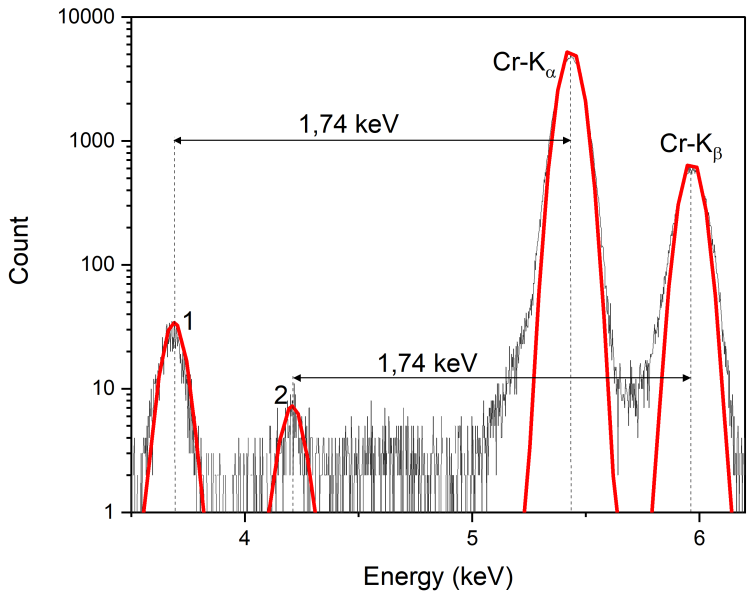

Figure 2.15: X-ray spectrum illustrating Si escape peaks 1 and 2 for Cr-K_α and K_β respectively.

2.3.1.4 Dead time and count rate performance

Every radiation detection system is inherently limited by the dead time, specially for high count-rate applications. Indeed, the processing of an output pulse through the shaping and coding electronics circuit requires a certain time (typically a few microseconds) and the dead time (DT) corresponds to this time after each event during which the system is not able to record another event. As a result, events that occur during the dead time are lost. DT is expressed as a percentage that reflects the number of unprocessed events and can be calculated using the observed output count rate (OCR) and the input count rate (ICR) as:

$$DT = \left(1 - \frac{OCR}{ICR}\right) \cdot 100\,.$$

This is dependent of the shaping time constant, t, which is characteristic of the shaping parameters, following this equation:

$$OCR = ICR \exp\left(-ICR \cdot t\right) \tag{2.10}$$

The relation between the output and the input count rate and the resolution as a function of several shaping times is shown in Figure 2.16.

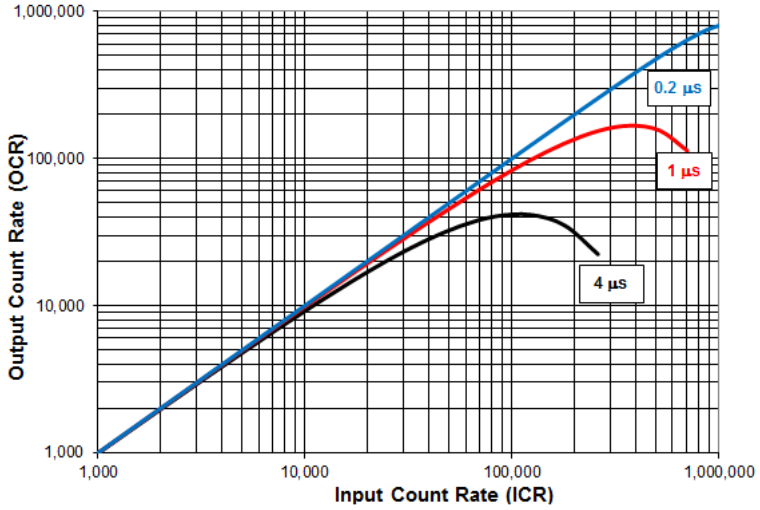

Figure 2.16: Experimental data showing the output count rate (OCR) as a function of the input count rate (ICR) with several shaping times (product information supplied by Amptek Inc., www.amptek.com).

2.3.1.5 Pulse pile-up

Pulse pile-up occurs when multiple radiation events arrive simultaneously at the detector in such a way that the voltage signals are not discriminated by the pulse processor as separate signals. Consequently, the multiple X-rays are measured as if they were one and a count is added to the spectrum in the channel which is the sum of the energy of the multiple X-rays. In addition, pulse pile-up coincidences can have an impact on the spectrum. Pulse pile-up changes with count rate and is particularly noticeable at high-count rates and for soft X-rays, such as those emitted by light elements [65].

2.3.2 Wavelength-dispersive spectrometer

2.3.2.1 Instrumentation

A major difference between energy-dispersive spectrometer and wavelength-dispersive spectrometer instrumentation is the requirement of a dispersive element in the latter case, which selects a specific wavelength (energy) towards the direction of the detector.
The operational principle of a wavelength-dispersive spectrometer relies essentially on the grating law (using grating diffractor that determines the diffraction condition.) or on Bragg's diffraction from a crystalline material (as described in Chapter 1, Subsection 1.2.5), which depends on the reflective properties of these materials for specific wavelengths and X-ray incidence angles. This phenomenon occurs due to the constructive interference of the scattered X-rays at particular angles. Consequently, crystals are used to disperse the fluorescence spectrum into individual wavelengths. Different configurations using different crystal geometries can be used in a WDS system.
The first geometry uses a curved crystal, either operating in the Johann/Johansson geometry (discussed in section 2.3.2.2). In this configuration, the sample, the analyzing crystal and the X-ray detector are positioned along the circumference of a circle called the Rowland circle

(Figure 2.17). While the sample position remains fixed, both the crystal and the detector can move around the Rowland circle, ensuring that the distance between the X-ray source and the analyzing crystal is always equal to the distance between the analyzing crystal and the X-ray detector [62]. Changing both the position of the crystal and the position of the detector, leads to change the angle of incidence θ, enabling particular X-ray wavelengths from the sample to be reflected into the detector, while other wavelengths are absorbed by the crystal.

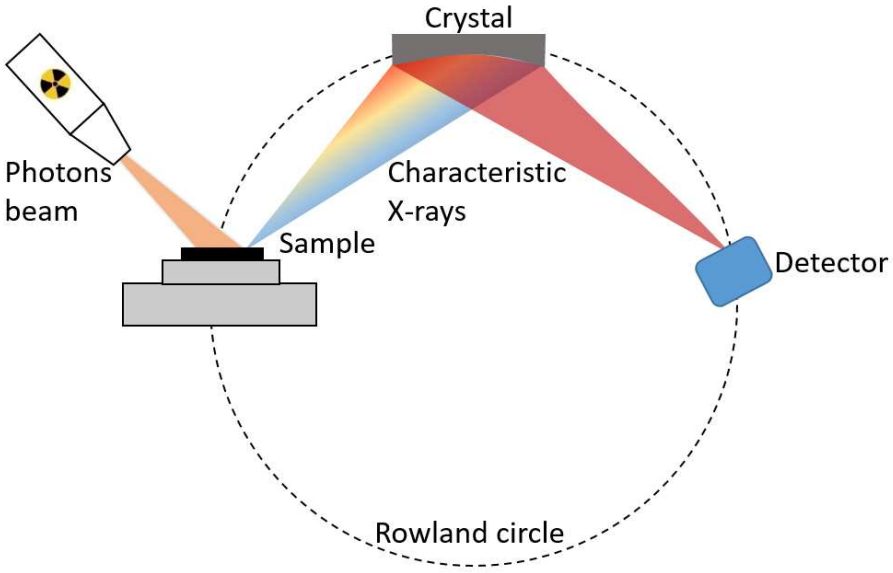

Figure 2.17: Schematic illustration of a wavelength-dispersive X-ray spectrometer set-up on Rowland circle using Johansson geometry.

The second geometry is the von Hamos geometry [67]. It consists of a cylindrical crystal to disperse the polychromatic light and a solid-state device, such as a one-dimensional CCD, which is mounted on the axis of a cylindrical spectrometer (Figure 2.18). To reduce aberrations, the spectrometer's axis corresponds to the location of the source.

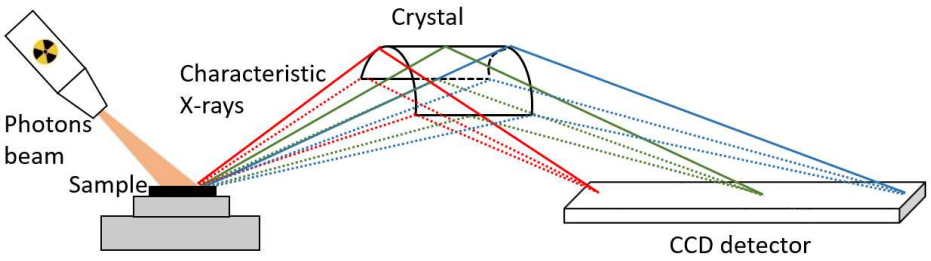

Figure 2.18: Schematic representation of von Hamos spectrometer geometry WDS. Photons of different energies (colors) are diffracted with different Bragg angles to different positions on the CCD detector.

2.3.2.2 Diffracting crystal

To cover a wide range of characteristic X-rays with high resolution, different diffracting crystals with appropriate $2d$ spacings for particular element ranges are required. Some common crystals used in WDS are lithium fluoride (LiF), pentaerythritol (PET), thallium acid phthalate (TAP), silicon (Si) and cesium biphthalate (CsAP). Table 2.2 details the different crystals employed in the WDS with their characteristics. Since Bragg's angle has a limited range in the WDS [68], crystals with a large spacing distance allow low energy lines to be diffracted (e.g K lines for light element). In addition, for heavy elements, crystals with a small lattice distance must be used. For some heavy elements, high-energy lines may not be accessible and less energetic lines (e.g L and M) can be used instead. Besides the crystals, synthetic multilayers diffractors with larger d spacing have been utilized for soft X-rays [69]. These synthetic layers are often formed as a multiple periodic stack of refraction layers made up of a heavy element, and transmission layers, which consist of a light element. The properties of these multilayers depend mainly on the layer refraction coefficients, the thickness ratio of the refraction and transmission layers, total layer number, sharpness of the layer boundaries, etc. Moreover, as mentioned before, different crystal geometries can be used in the WDS setup. Crystals that can be used in the Johansson and Johann geometries are represented in Figure 2.19. In the Johansson geometry, crystals are bent to twice the radius of the Rowland circle and further machined to the radius in order to have their surface ideally following the curvature of the circle, while in a Johann geometry the crystal is bent to twice the radius and so is tangent to the circle in the center only, this geometry is sometimes called semi-focusing [70]. The Von Hamos geometry uses cylindrically bent crystals to disperse the X-ray fluorescence, in which the energy range covered is limited by the length of the crystal and detector along the dispersion axis. Another type of X-ray dispersive spectrometer like single or double crystal spectrometer uses a flat crystal [71], which is easy for construction but suffers from low efficiency [72].

Table 2.2: Common crystals for WDXRF [5].

Crystal	Miller indices	$2d$ (nm)	Lightest measurable element	Typical energy resolution	Remarks
LiF	(220)	0.281	Cr	14 eV, Mn-K_α	High resolution
LiF	(200)	0.403	K	25 eV, Mn-K_α	General use
NaCl	(200)	0.564	S	5.5 eV, S-K_α	For sulfur high resolution deliquescent
Ge	(111)	0.653	P	5 eV, P-K_α	Eliminate second order reflection
InSb	(111)	0.748	Si	4.5 eV, Si-K_α	For silicon
PET	(002)	0.876	Al	4 eV, Al-K_α	Higher reflectivity
ADP	(101)	1.065	Mg	4 eV, Mg-K_α	For magnesium deliquescent
Beryl	(10-10)	1.595	Mg	N/A	N/A
TlAP	(001)	2.576	O	15 eV, Na-K_α	Deliquescent

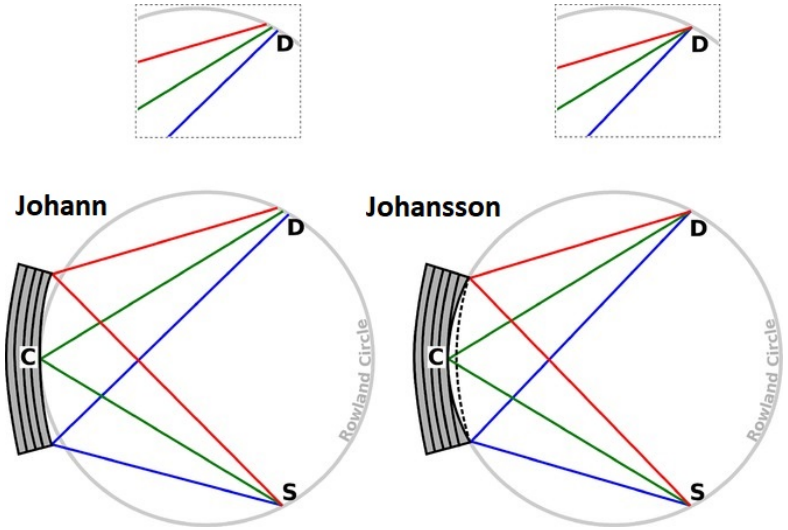

Figure 2.19: Representation of the Johann and Johansson geometries. The focus in Johann geometry is not exactly on the detector (D), which results in an extra geometrical contribution to the overall energy resolution. This contribution can be reduced via the Johansson geometry, in which the curvature of the crystal is ground to the radius of the Rowland circle after it has been bent, resulting in no geometrical aberration [73].

2.3.2.3 Efficiency

It is crucial to understand the factors that impact the efficiency of the WDSs for its effective use. The absolute efficiency of a spectrometer is described as the ratio of the X-ray intensity registered by the detector to the X-ray intensity emitted by the source [74]. For a WDS, the efficiency depends, on crystal reflectivity, solid angle subtended by the crystal and efficiency of the detector [68]. An increase in the solid angle results in the collection of a greater number of photons and consequently, a higher overall efficiency of the WDS system. The solid angle of detection of a WDS depends on the distance between the sample and the crystal and can be calculated as:

$$\Omega = \frac{A}{4r^2} \sin(\theta_B) \tag{2.11}$$

where A is the area of the crystal, r is the radius of the "Rowland circle" and θ_B is the Bragg's angle.

The main factor affecting the WDS efficiency is the characteristics of the crystal which affect the amount of reflected X-rays. The primary characteristics of the crystal are reflectivity, spectral resolving power (the capacity to separate two close lines) and signal/noise ratio. The first three characteristics can be measured for a particular line by measuring the diffracted intensity around the Bragg location for a parallel incident beam; known as "Rocking Curve" (Figure 2.20). These characteristics depend on the thickness of the crystal, on its structure (e.g. multilayered crystals) and on its refraction coefficient, which in turn depends on the energy of the X-rays [75]. Thus, for a given incident photon, the count rate of the detector varies greatly over the wavelength range of each crystal.

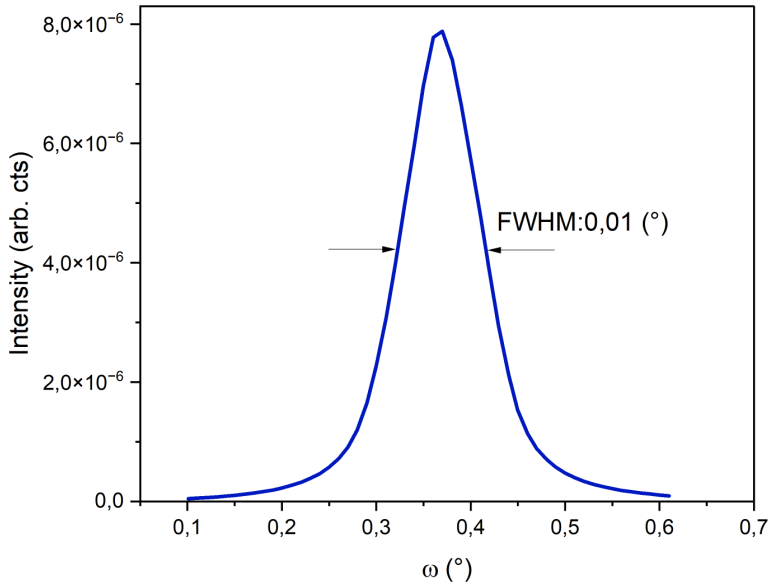

Figure 2.20: X-ray rocking curve of Si crystal measured at 8 keV.

2.3.2.4 Energy resolution

Practically, the majority of WDS have a range of rotational movement from 0° to 150° [5]. Since the WDXRF spectrometer uses Bragg diffraction with crystals to disperse X-rays, its angular dispersion is calculated by differentiating the Bragg equation as:

$$\frac{\mathrm{d}\lambda}{\mathrm{d}\theta} = \frac{2d\cos(\theta)}{n} \tag{2.12}$$

which indicates that a larger reflection angle and/or a higher diffraction order n provides better angular dispersion. This is because dispersion is proportional to the wavelength and the geometrical broadening effect is reduced at high Bragg angles. Hence, the combination of Equation 1.31 and 2.12 gives the relation between angular resolution and relative wavelength resolution as:

$$\frac{\mathrm{d}\lambda}{\lambda} = \frac{\mathrm{d}\theta}{\tan(\theta)} \tag{2.13}$$

Wavelength dispersive spectrometers generally offer a higher resolution compared to energy dispersive spectrometers [76, 77], due to their inherent physical properties which allow for better spectral resolution and elemental separation. Developing a WDS can be intriguing to validate this aspect and to highlight the ability of WDS in providing more precise measurements, particularly when dealing with elements with close atomic numbers or complex samples, thereby proving its superior resolution.

2.3.3 WDS LNHB prototype

As part of improving the energy resolution, we have initiated the development of a new Wavelength Dispersive Spectrometer (WDS), in an adapted von-Hamos geometry. A key objective

of this thesis was to evaluate a newly designed, high-resolution detector for measuring fluorescence, with the intention of integrating it into the goniometer CASTOR. Detailed discussions about the experimental approach and results will follow.
Figure 2.21 (a) presents a picture of the WDS prototype, developed to be installed fully in-air at the *MÉTROLOGIE* beamline at the SOLEIL synchrotron facility. This spectrometer consists of three main components: the X-ray source, a crystal and the position-sensitive detector. Unlike other von-Hamos geometries, this prototype uses a flat crystal instead of a curved or cylindrical one. A variety of crystals can be used to change the range of energy detected for a particular Bragg angle which corresponds different interplanar distances "d". These crystals include: Si ($2d = 0.627$ nm), Beryl ($Be_3Al_2Si_6O_{18}$, $2d = 1.595$ nm), lithium fluoride crystal (LiF, $2d = 0.281$ nm) and cesium hydrophthalate (CsAP, $2d = 2.565$ nm). The peak reflectivity of these crystals is a critical parameter that characterizes their ability to reflect X-rays at specific energies and angles of incidence. The detector employed is a HAMAMATSU S11156-2048-02 back-thinned CCD (coupled-charged detector) image sensor (2056 pixels of 14×200 μm). The pixel size of the detector provides an advantage in achieving high energy resolution.
Figure 2.22 displays the peak reflectivity of various crystals within the energy range of 2 keV - 20 keV as a function of X-ray energies (Bragg angle) calculated using XRVision [78] (a software program that is no longer available online). The low reflectivity of crystals at low energies can be attributed to the insufficient energy of X-rays to penetrate the crystal lattice, causing either absorption or scattering by the crystal surface. An increase in X-ray energy enables deeper penetration into the crystal lattice and interaction with the atoms, resulting in enhanced reflectivity. However, a trend is observed for CsAP in the energy range of 5 keV - 5.9 keV, where the peak reflectivity decreases. This behavior can be explained by the absorption properties of Cs: L_3 at 5.012 keV, L_2 at 5.359 keV and L_1 at 5.714 keV.
Furthermore, the crystal is mounted on a vertical and horizontal translation rails, whereas the detector is placed on a vertical translation rail to enable position changes, maintaining the crystal at an equidistant distance from the sample and the detector. Thus, changing the vertical position of the crystal i.e changing the Bragg angle, requires changing the vertical position of the detector. Alternatively, the Bragg angle can be changed by fixing the vertical position of the crystal and the detector and changing only the crystal's horizontal position. Figure 2.21 (b) represents a schematic of the WDS showing the crystal and camera movement positions (X and Y), as well as the minimum and maximum angles (θ_{min} and θ_{max}) according to these positions. The center of the detector can be placed at a maximum distance (Y_{max}) of 240 mm from the sample and the crystal can be placed at a maximum position X_{max} of 200 mm . The crystal and the detector positions are selected according to the desired energy range detected by the CCD. The energy range depends also on the crystal and CCD dimensions, which limit the minimum and maximum angles (θ_{min} and θ_{max}). Additionally, to avoid overlapping between the CCD and the point source, Y should be larger than $\frac{L_{CCD}}{2}$.
The whole setup is placed on a fully in-air goniometer to adjust its position in front of the beam exit for the alignment. The monochromatic photons emitted from the synchrotron source irradiate a large area of the sample at 90°.

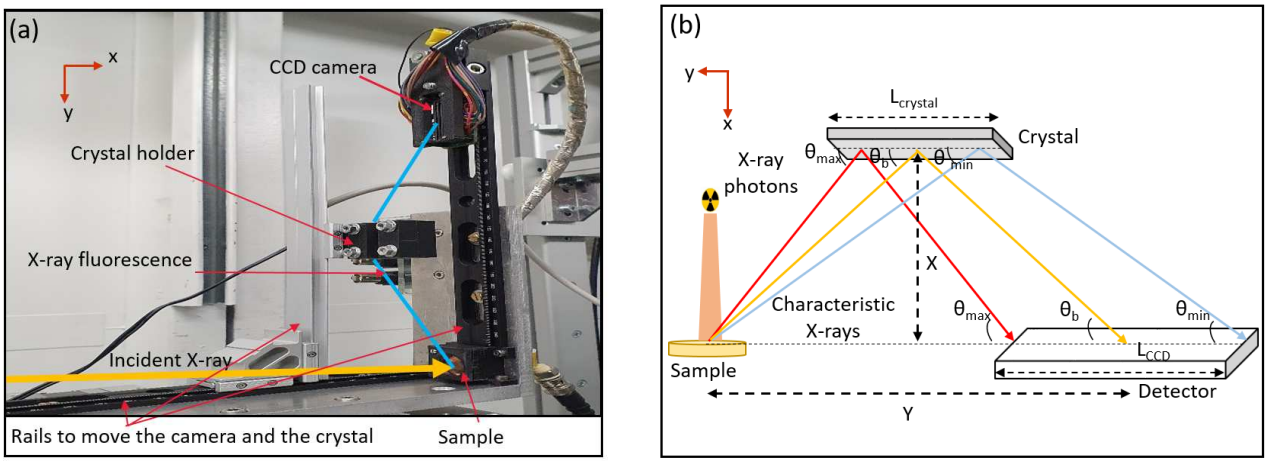

Figure 2.21: (a) Picture of the WDS prototype instrument on the *MÉTROLOGIE* at the SOLEIL synchrotron. (b) Schematic of the WDS showing the maximum and the minimum angles on the crystal so that all the reflected X-rays by the crystal reach the detector. These angles depends on the values of X and Y chosen according to the energy range.

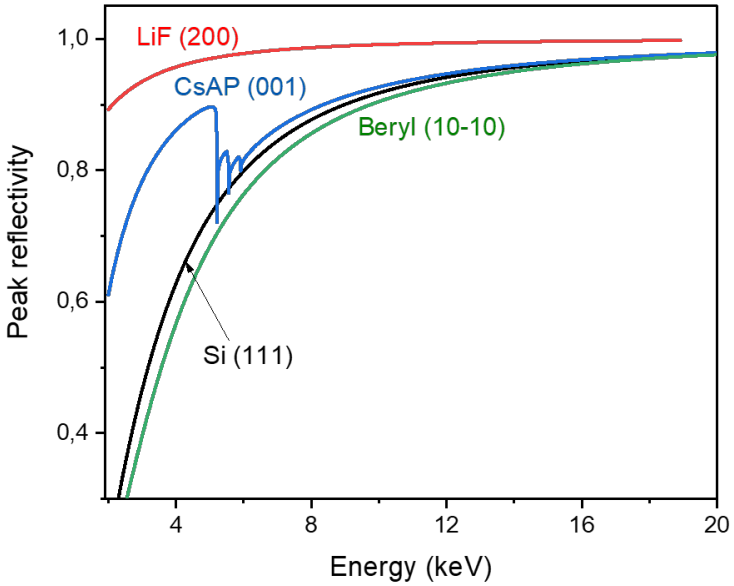

Figure 2.22: Peak reflectivity of Si, Beryl, LiF and CsAP crystals as a function of X-ray energy (Bragg angle) using the XRVision software.

The minimum and maximum angles are calculated using Bragg's law as:

$$\begin{aligned} \theta_{min} &= \arcsin\left(\frac{h \cdot c}{2d \cdot E_{max}}\right) \\ \theta_{max} &= \arcsin\left(\frac{h \cdot c}{2d \cdot E_{min}}\right) \end{aligned} \tag{2.14}$$

where E_{min} and E_{max} are the minimum and the maximum energies on the CCD.
In this case the distance Y is calculated as:

$$Y = \frac{L_{CCD}}{2} \cdot \frac{\tan(\theta_{max}) + \tan(\theta_{min})}{\tan(\theta_{max}) - \tan(\theta_{min})}, \tag{2.15}$$

and the distance X is expressed as:

$$X = \frac{2Y - L_{CCD}}{4} \cdot \tan(\theta_{max}) . \tag{2.16}$$

The energy resolution of the WDS is influenced by the energy range affected by the position of the detector and the interplanar distance of the crystal, and by the number of pixels of the detector and can be expressed as:

$$R = \frac{2\Delta E}{Nb\,of\,Pixels} . \tag{2.17}$$

The count rate of the signal depends on the sample position relative to the crystal and the detector, as well as the crystal reflectivity.
The WDS was tested on pure metallic elements using a Si (111) crystal measuring 26 mm in length. The normalized measurement result of a thin film copper (Cu) sample is shown in Figure 2.23. To achieve high resolution, a relatively narrow working energy range of 7.4 keV to 8.3 keV was selected for measuring the copper spectrum.

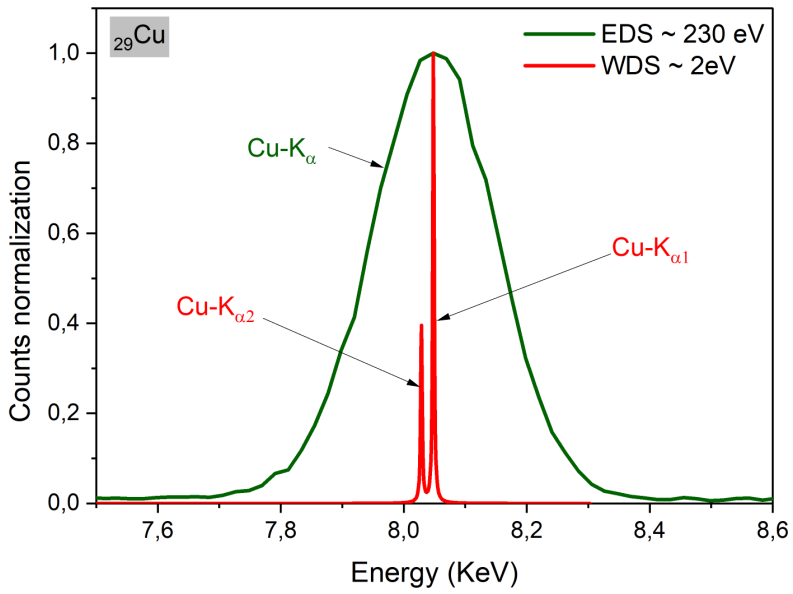

Figure 2.23: Comparison of normalized WDS with an EDS spectra of pure metallic Cu thin film. The energy resolution for the two are shown.

Compared to the energy dispersive spectrometer, the WDS presents much higher energy resolution and peak-to-background ratios that are unmatched with the EDS measurement. The results of this study demonstrate the superiority of the WDS over EDS in terms of spectral

resolution. The WDS provided a resolution of 2 eV allowing for the clear separation and identification of $K_{\alpha 1}$ and $K_{\alpha 2}$ lines of Cu. In contrast, the EDS presented a resolution of 230 eV resulting in an overlap of these Cu-K_α lines, making their separation impossible. This highlights the limitations of EDS in resolving closely spaced spectral lines, and further emphasizes the potential of WDS for high-resolution elemental analysis. The high resolution obtained in this study can be attributed to the use of a flat crystal in the WDS, which allows for precise measurement of the energies of the diffracted X-rays. Additionally, the narrow detected energy range further improved the resolution, by reducing the spectral overlap of different energy lines. Despite the features of this WDS configuration, the system encountered some challenges related to low signal intensities and inefficient collection of diffracted X-rays due to insufficient focusing, which can impact the sensitivity and limit the analytical capabilities. Thus, to solve these difficulties, it is planned to employ a polycapillary optics before the sample. This should allow for an increased collection efficiency of diffracted X-rays, resulting in a higher signal-to-noise ratio and better sensitivity.

Chapter 3

Experimental equipment at the MÉTROLOGIE beamline

3.1 Description of the beamline

The SOLEIL (an acronym for "Optimized Source of LURE Intermediary Energy Light") synchrotron in France, is a research facility located near Paris, which emits synchrotron radiation from 2.75 GeV electrons that travel in a 354 m circumference storage ring. There are currently twenty-nine operating beamlines, which are located on dipoles or insertion devices, such as undulators or wigglers. The top-up mode, which consists of regularly re-injecting bursts of electron to compensate for losses, is the most commonly used mode, which delivers a constant current of 450 or 500 mA with a stability better than 0.4 %. The experiments in this thesis were carried out at the *MÉTROLOGIE* beamline [79], which is positioned at the exit of a bending magnet and has a photon source divergence of 8 mrad. A first cooled diaphragm with motorized apertures shapes the incident white beam, providing photons to both the hard X-ray and X-UV branches of the beamline, covering an energy range from 45 eV to 40 keV. Fluorescence measurements were carried out at the hard X-ray branch of the beamline.

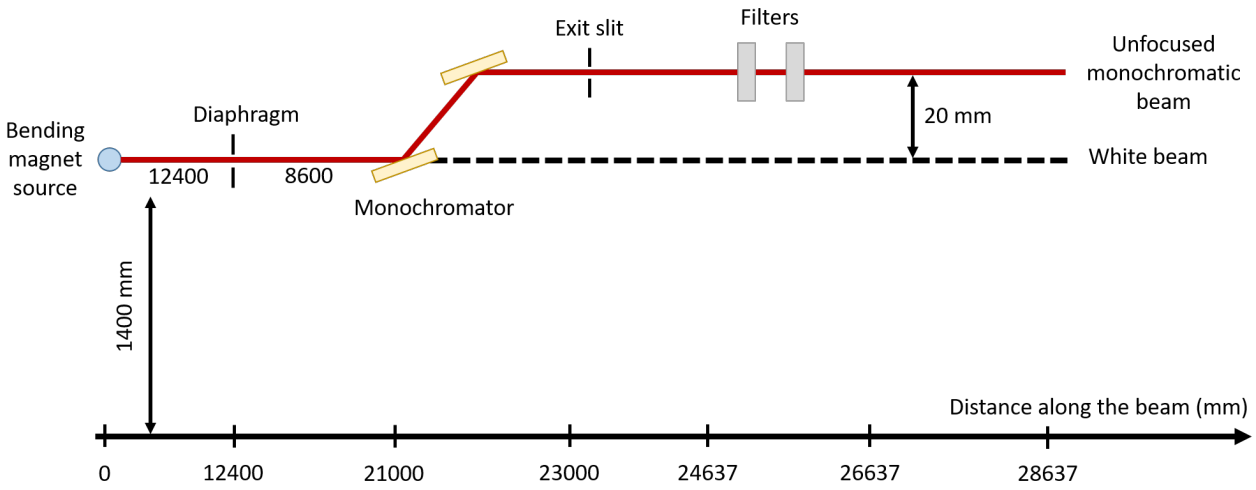

Figure 3.1: The hard X-ray branch of the *MÉTROLOGIE* beamline at SOLEIL.

The acceptance for this branch is 1.7 mrad horizontally and 0.153 mrad vertically. The composition of the hard X-ray beamline is illustrated in Figure 3.1. This branch is equipped first of a collimating slit situated at 12.4 m from the source to reduce the vertical beam divergence, thus improving the spectral resolution if necessary. Then a Si (111) double-crystal monochromator situated at 21 m from the source can provide monochromatic photons in the high energy range from 3 keV to 40 keV. The Bragg's angle of the crystal monochromator is equipped with a rotary position encoder that requires a calibration to link it to the selected energy. Exit slits with four independent lips (2 for the vertical collimation and 2 for the horizontal one) are placed afterwards to change the photon beam size with a maximum dimension of 48(horizontal) × 40(vertical) mm^2. The typical flux is around 10^{10} photons/s for a photon energy of 10 keV in a 22 mm^2 area. The monochromatic beam is then delivered to the measurement position in an unfocused mode. In addition, two sets of filters can be placed in order to reduce the photon flux. These filters can also be used as reference binding energies to calibrate the monochromator's energy by scanning the energy around their absorption edges.

3.1.1 Hard X-ray beam quality

In order to ensure the quality of the beam, it is necessary to take into account various sources of variations related to the beamline equipment. These sources include flux stability, monochromaticity, and the contribution of harmonics and stray light. First, the synchrotron top-up mode (Figure 3.2) induces a relative fluctuation of the flux intensity better than 0.4 %. However, an injection of new electrons into the storage ring during measurement causes a maximum variation of the flux intensity and can lead to incorrect or unreliable results, making it difficult to draw valid conclusions from the data. Second, the energy calibration of the monochromator is achieved by scanning energy levels around the absorption edges of selected filters, and analyzing the first derivative of the transmission measurements. The measured absorption edge energies are then compared with data in the Deslattes table [14], and Bragg's law is applied to derive the corresponding angles. The differences between encoder position and tabulated absorption edges are corrected, with the residual difference kept under 0.04 %.

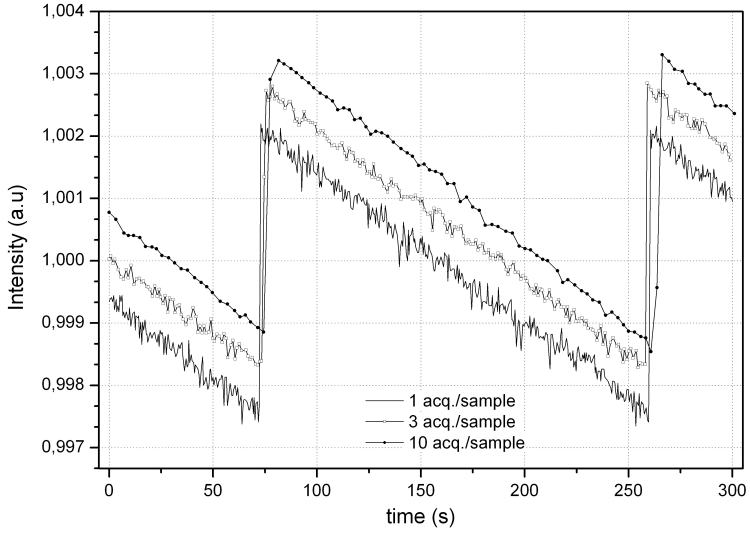

Figure 3.2: Flux fluctuations at 9 keV for 1, 3 and 10 acquisition/ sample.

Finally, the method of minimizing harmonics and stray light is managed similarly to the method described in [80]. Harmonics are significant below 7 keV, and a small adjustment of the second monochromator crystal is required to reduce their contribution to 0.1 %. The stray light was monitored using copper filters with varying thicknesses, and no indication of a deviation in their normalized transmittance was observed within the detector's sensitivity limit, which would indicate the presence of stray light, as outlined in reference [80].

3.1.2 Double-Crystal technique for precision energy selection

In this study, energy selection is performed using the two parallel crystals monochromator capable of independent movement. This double-crystal approach not only refines energy selection but also ensures the beam's exit direction aligns with the incident (horizontal) direction. The precision placement of the crystals, in relation to each other, plays a vital role in obtaining maximum photon intensity. To achieve this, the first crystal is strategically positioned at the desired energy, using a pre-established angle-energy calibration. Subsequently, the second crystal's position is optimized via an angular scan (pitch) around its axis. During this process, the intensity of the emergent photon beam is continuously monitored using an AXUV photodiode. The measurements are used to plot the rocking curve (RC) corresponding to the selected energy. Figure 3.3 presents a series of RCs spanning the energy range of interest (3 keV - 30 keV).

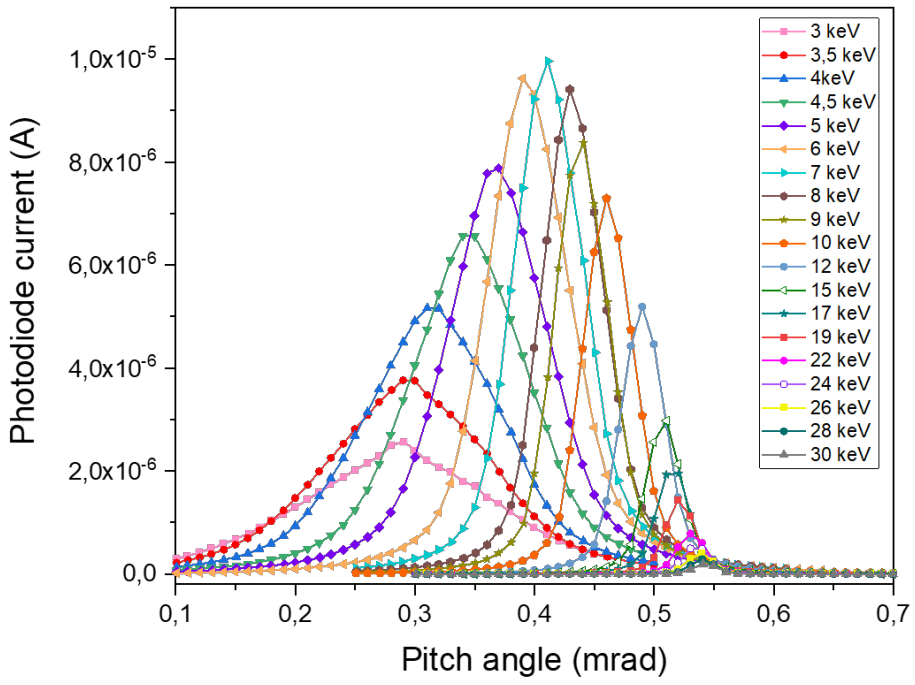

Figure 3.3: Set of rocking curves for the energy range between 3 keV to 30 keV.

These curves collectively represent the evolution of the current delivered by the photodiode as a function of the second crystal's angular rotation (between 0.3 mrad and 0.85 mrad). Finally, each of these curves identifies the position of the second crystal corresponding to a maximum

current for a particular energy. This analysis highlights the effective energy selection through the double-crystal approach.

3.1.3 Optimal beam purity technique

Based on the principle of Bragg diffraction, the double-crystal monochromator allows for the selection of a specific energy from the broad spectrum of synchrotron radiation. Intrinsically, the Bragg's diffraction phenomenon enables not only the desired energy to satisfy the Bragg's condition but also its multiples, known as harmonics. The harmonics are considered undesirable due to their potential interference with experimental measurements. A series of tests was therefore carried out to determine the contribution of the harmonics to the total power of the beam according to this monochromator setting, in order to be able to select the one that minimizes the contribution of higher order harmonics while ensuring sufficient power of the main harmonic. And, potentially, this information allows for the calculation of the required correction if the contribution of the higher order harmonics is not negligible. Afterwards, for each value of the energy, the pitch was tuned in order to minimize high-order harmonics.
In order to accomplish this objective, the high purity germanium energy-dispersive detector (HPGe) was positioned at the exit point of the goniometer, facing the monochromatic beam directly. This detector records the energy data of individual photons, enabling the distinction of the energy components within the incident beam. Spectra were therefore successively recorded by varying the pitch for different values of the beam energy (3, 4, 5, 6, 7, 8, 10, 12, 15, 20, 25, and 30 keV. The direct beam was not measured; instead, filters were introduced to ensure a moderate counting rate, enabling the detector to record spectra with an acceptable dead time and minimal pile-up events. In this aspect, the Si (111) crystal helped as it does not produce second harmonics due to crystallographic laws of diffusion.

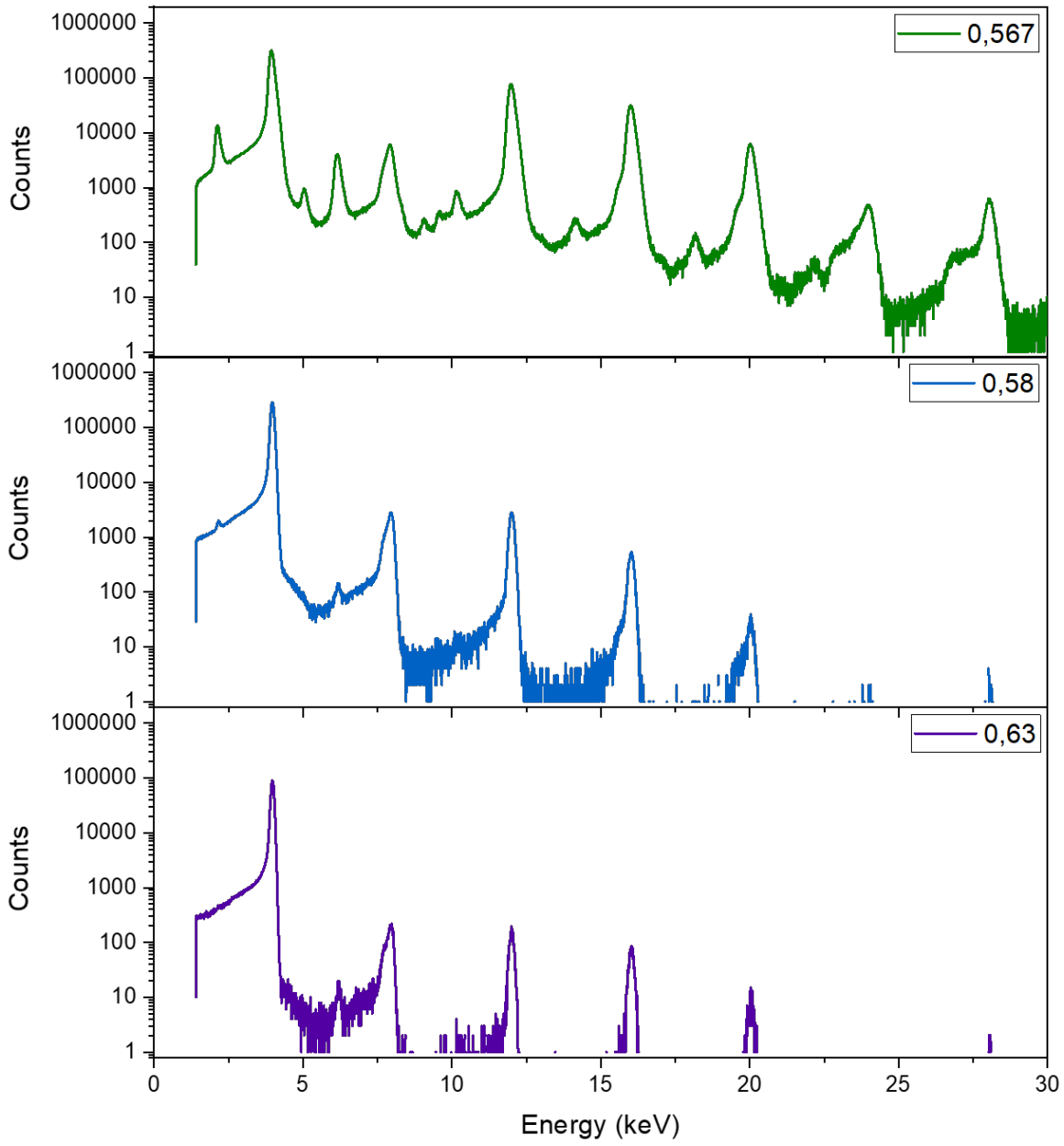

Figure 3.4: Spectra measured at 4 keV incident photons for different values of the pitch angle to reduce harmonic contribution.

Figure 3.4 presents a measurement of a spectrum obtained with incident photons set at 4 keV. In each spectrum, the main peak and those corresponding to harmonics $n = 3$, $n = 4$ and $n = 5$ were adjusted by a Gaussian function to calculate their area and deduce their count rate. Indeed, the obtained areas must be corrected for the detector yield and the attenuation by the inserted filters. The count rates were corrected by an estimate of the detector's intrinsic efficiency. Similarly, they were corrected for radiation attenuation in the filters. Therefore, the contribution of each harmonic to the total power of the beam was estimated.
The first spectrum at the top is obtained for a value of pitch angle (0.567 mrad) that provides maximum photon flux, but, as expected, includes a strong contribution from harmonics. The middle spectrum, obtained with a pitch angle of 0.58 mrad, reduces this contribution. The

contribution of harmonics decreases further for a pitch of 0.63 mrad in the bottom spectrum. As shown for the three spectra, the peaks appearing at $2 * E$, are not attributable to second-order harmonic ($n = 2$) as the crystal in use doesn't permit this. Instead, these peaks are the result of the pile-up phenomenon due to a high counting rate. In addition to the reduction of the count rate and pile-up by increasing the pitch, a drop in the relative proportions of the third ($n = 3$) and fourth order ($n = 4$) harmonics (at 12 keV and 16 keV respectively) is noted. With the monochromator pitch set to 0.567 mrad, these harmonics represented 24 % and 10 % of the total, respectively. Upon adjustment of the monochromator pitch to 0.63 mrad, these contributions are significantly reduced to 0.22 % and 0.1 % respectively.

3.2 CASTOR setup

GIXRF-XRR measurements were performed using the goniometer CASTOR [81] installed on the *MÉTROLOGIE* beamline at SOLEIL synchrotron. Figure 3.6 shows the geometry setup for reference-free XRR-GIXRF measurements. The irradiation chamber was designed by the Physikalisch-Technische Bundesanstalt (PTB, Germany) and Technical University of Berlin [82, 83], the instruments and sample holder were designed by the Laboratoire National Henri Becquerel. The goniometer CASTOR is shown in Figure 3.5 from the inside and outside. The irradiation chamber encloses a seven-axis manipulator, of which four axes are for translation and three for rotation.

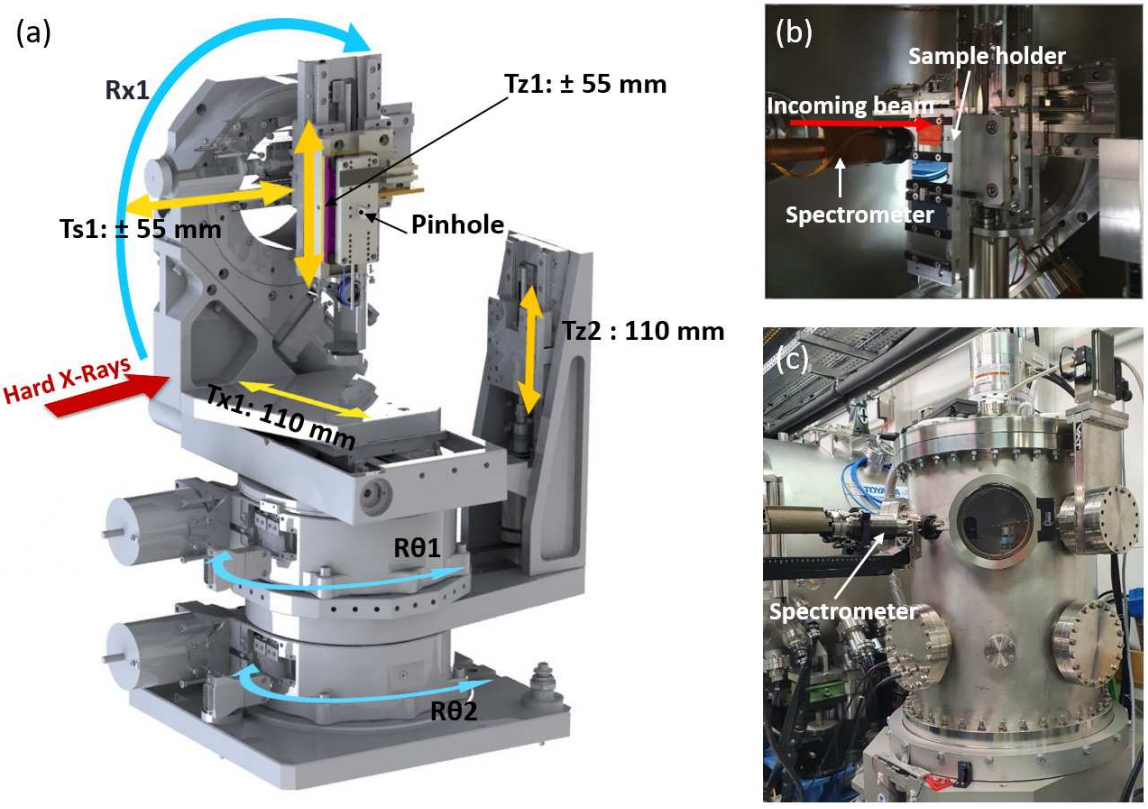

Figure 3.5: Schematic view of the 7-axis CASTOR goniometer. (a) 3D sketch from inside, (b) image of the SDD and the sample from the inside and (c) photo of CASTOR from the outside.

Among these axes, five are used to control the sample position (Tz, Ts1, Tx1, Rx1 and Rθ1) and two for the position of the detection arm which accommodates several photodiodes (Tz2 and Rθ2) as shown in Figure 3.5 (a). The rotation axes (Rθ1 and Rθ2) are the critical ones, since they can move freely to adjust the incident angle on the sample, as well as the detection angle. The sample holder installed in the goniometer setup includes a pinhole, which is used during the alignment procedure for GIXRF-XRR measurements. The XRR measurements were taken in the $\theta/2\theta$ configuration using an AXUV photodiode (IRD Optodiode) placed on the Rθ2 arm. The XRF signals were acquired with an energy-dispersive spectrometer (Silicon Drift Detector (SDD) from Amptek) placed at 90° from the incident photon beam and at a distance between 13-15 mm from the sample surface. Finally, the goniometer CASTOR is placed on a lateral translation stage to adjust the vertical and horizontal position of the whole to ensure accurate and precise chamber alignment with respect to the incident X-ray beam in all measurements. Figure 3.6 shows the geometry setup for reference-free XRR-GIXRF measurements.

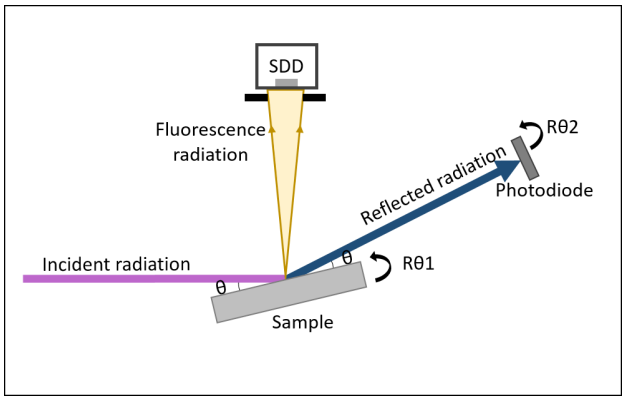

Figure 3.6: Geometry setup for reference free XRR-GIXRF measurements, composed of an energy dispersive spectrometer to record the fluorescence and a photodiode to measure the reflectivity while varying the incident angle.

3.2.1 Alignment procedure

A proper beam alignment in GIXRF-XRR is crucial to ensure the quality and the reproducibility of the GIXRF-XRR measurements. It maximizes the signal-to-noise ratio and ensure that accurate and reliable results are obtained. Therefore, the alignment of CASTOR is an essential step that consists of first aligning the rotating axis with the beam axis and then aligning the sample with respect to the beam. The rotation axes in the goniometer are encoded with Renishaw optical encoders with an accuracy of 0.0003° and a minimum pitch of 0.002° resulting in a combined uncertainty on the position of the rotation axis of 0.0005°. Meanwhile, the minimum increment size for the translation axis is 0.02 mm, leading to a positional uncertainty of 0.004 mm.

3.2.1.1 Chamber alignment

At the beginning, the beam path is localized with the help of the photodiode equipped with a 100 μm wide vertical slit using the Tz2 and Rθ2 motors (Figure 3.7). The process begins by fixing Tz2 at an approximate position, followed by searching the maximum intensity on the photodiode with Rθ2 (Figure 3.8 on the left). Upon finding the maximum, the position of Rθ2

is fixed, and the search for the optimal height is done by a scan on Tz2 (Figure 3.8 on the right). Subsequently, the positioning of the photodiode center can be improved by iteratively realigning the two axes.

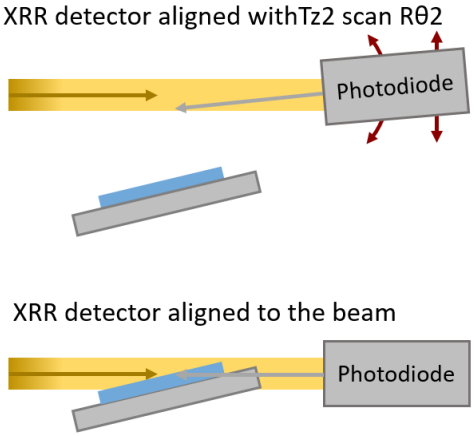

Figure 3.7: Alignment of the photodiode. Sketch showing the alignment of the photodiode by rotating Rθ2 and translating Tz2.

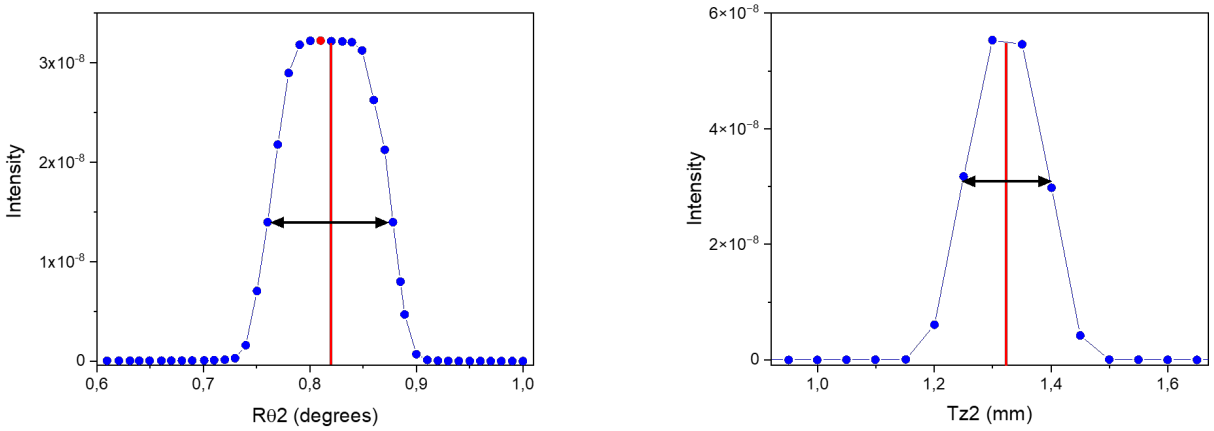

Figure 3.8: Alignment of the photodiode. Intensity scan by rotating Rθ2 (left) and translating Tz2 (right) where the red lines represent the center position and the red point is the maximum.

For GIXRF-XRR measurements, the photodiode serves as a consistent reference point for measuring the intensity of the incident X-ray beam during the alignment procedure. This ensures accurate and precise alignment of the sample with respect to the incident X-ray beam in all measurements. Subsequently, the pinhole of the sample holder (Figure 3.5 (a)) is aligned on the beam path by adjusting the two translation stages, Tx1 and Tz1, so that the maximum beam intensity is found and serves as reference position (Figure 3.9).

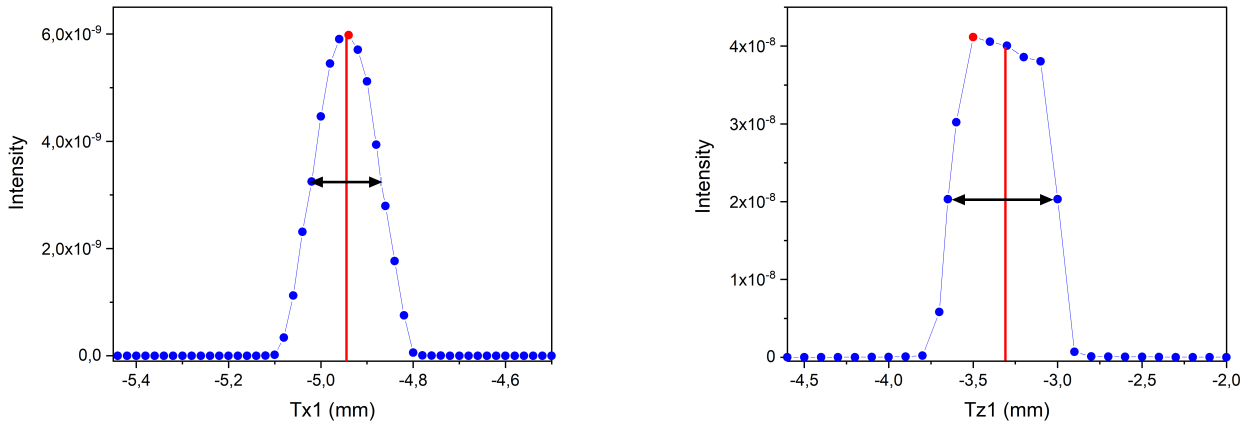

Figure 3.9: Alignment of the sample holder pinhole. Intensity scan on Tx1(left) and intensity scan on Tz1(right). In each graph, the red line represents the center position, and the red point indicates the position of maximum intensity.

The resulting curves exhibit a Gaussian shape. The horizontal scan Tx1 shows a clear maximum (Figure 3.9 on the right), while the vertical scan Tz1 curve also shows a Gaussian shape but with a tilted, cutoff head. The observed tilted cut-off on the Tz1 intensity scan is a result of the beam's shape along the vertical axis. Afterwards, the alignment of the rotation axes, Rθ1 and Rθ2, with the beam is established through the following steps: setting Rθ2 to the opposite position of 180° and repeating the pinhole alignment procedure. Finally, half of the ΔTx1 offset derived form these two measurements is applied to the lateral translation stage of the CASTOR chamber.

3.2.1.2 Sample alignment

The first step in the sample alignment is determining the location of each sample using Tz1. The axis of translation Tx1 must be adjusted so that the beam intersects the sample ties, as illustrated on the left side of Figure 3.10. Afterwards, a scan is performed in Tz1 to determine the position of each sample as shown on the right side of Figure 3.10. Once the vertical positions are localized, the beam is directed to the center of each sample to align them individually with respect to the incident beam. Subsequently, the samples are aligned in Tx1 (Figure 3.11 on the left) such that the beam strikes the sample at the mid-height position of the intensity as illustrated on the right side of Figure 3.11.

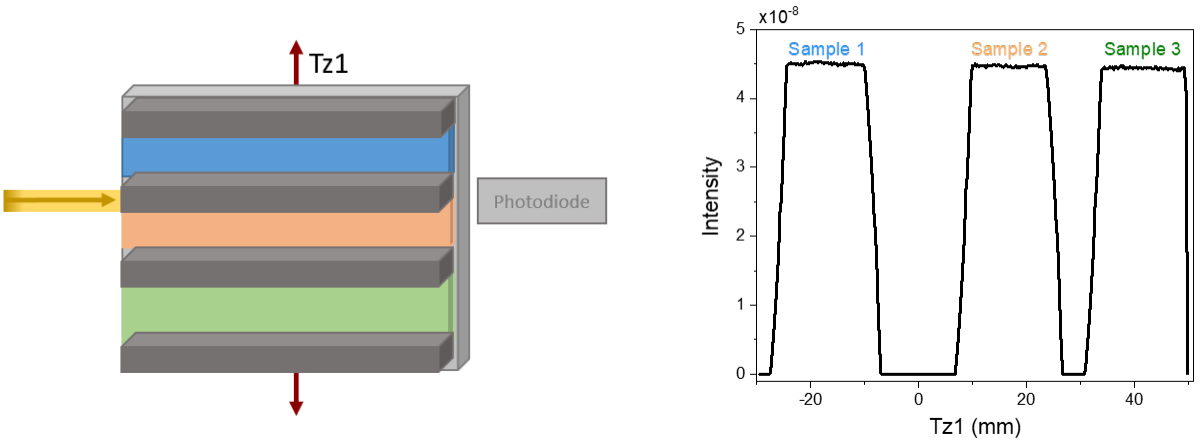

Figure 3.10: Alignment of the samples with the beam (Tz1 scan). Sketch showing the movement of Tz1 to find the vertical position of each sample (left) and the intensity scan on Tz1 showing the position of each sample (right).

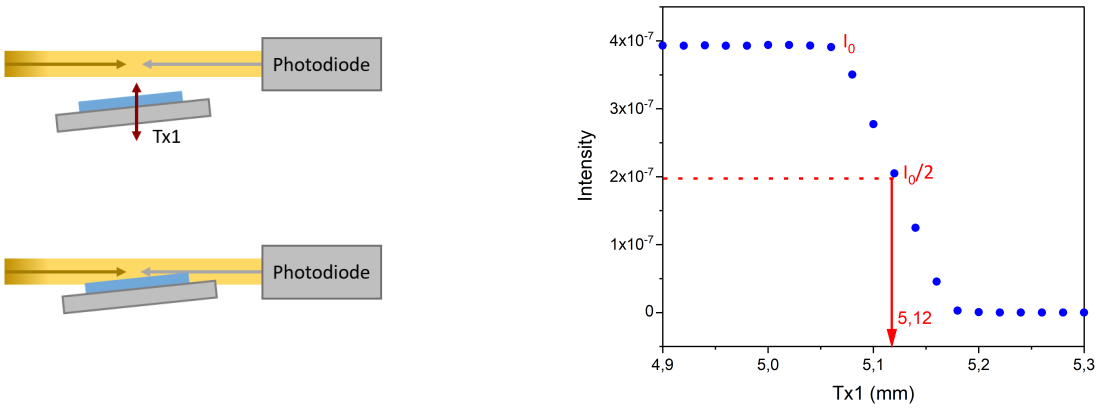

Figure 3.11: Translation alignment of the sample with respect to the beam. Sketch showing the horizontal alignment of the sample by translating Tx1 (left) and intensity scan on Tx1 where the red lines represent the mid-height position (right).

The alignment process is completed by aligning the sample surface with the beam, by scanning on Rθ1 and adjusting its zero position to the maximum (Figure 3.12).

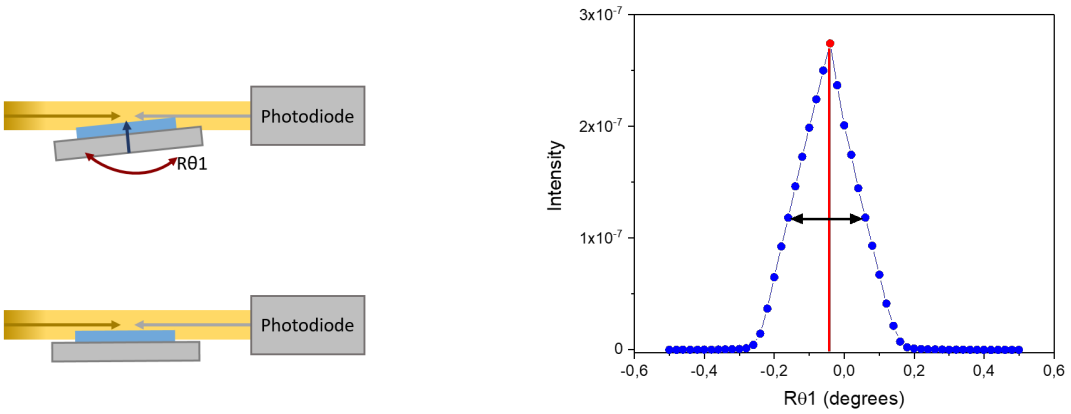

Figure 3.12: Alignment of the normal to the sample surface position with the beam using Rθ1. Sketch showing the alignment Rθ1 (left) and intensity scan where the red line and the red point represent the center and the maximum position respectively (right).

To refine the sample alignment and minimize ambiguity, iterative alignments are carried out in Tx1 (Figure 3.13) and Rθ1.

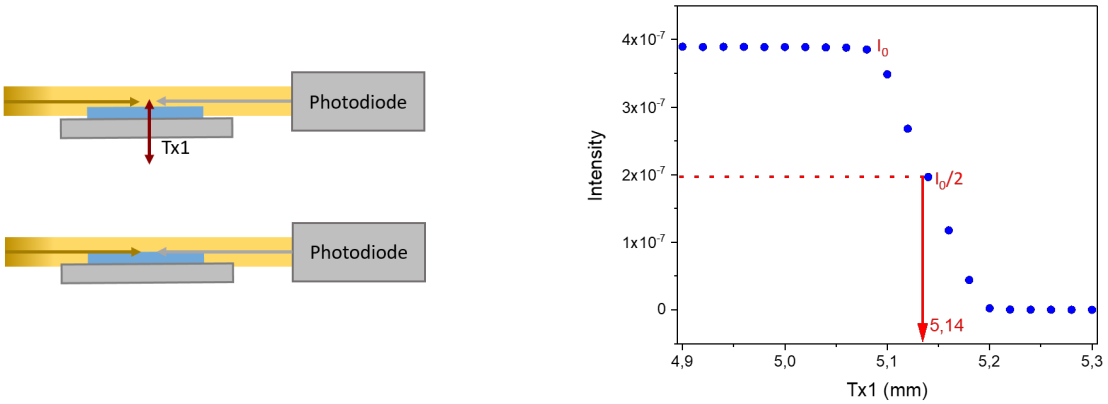

Figure 3.13: Fine alignment of the sample Tx1 position to the beam. Sketch showing the movement of Tx1 (left) and intensity scan on Tx1 (right).

Finally, the sample is aligned for reflection conditions by adjusting the incident angle θ1 to a value near the critical angle (i.e., 0.4°), and performing a scan on Rθ2 around the reflection angle ($2\mathrm{R}\theta 1 - \varepsilon \leq \mathrm{R}\theta 2 \leq 2\mathrm{R}\theta 1 + \varepsilon$). Typically, the maximum of the peak intensity is expected at an angle of $\mathrm{R}\theta 2 = 2\mathrm{R}\theta 1$, however, this is not observed in this instance (Figure 3.14 on the right). To refine the alignment, we thus apply half of the offset to $R\theta 1$.

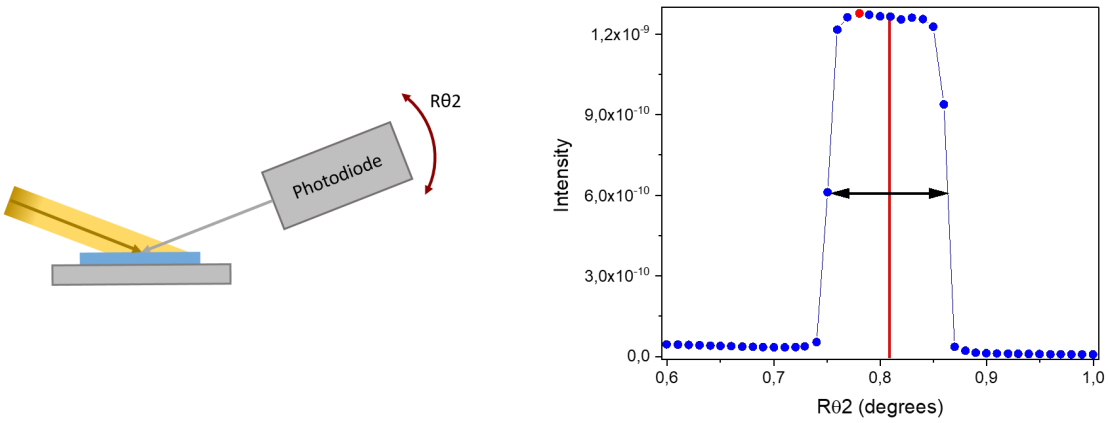

Figure 3.14: Sample alignment of the reflection condition. Sketch showing the alignment Rθ2 (left) and intensity scan on Rθ2 (right) where the red line and the red point represent the center and the maximum position respectively.

This alignment procedure follows a rigorous and systematic method that enhances the precision and reliability of GIXRF-XRR measurements.

3.2.1.3 Positioning precision

The shapes of the translation and rotation curves depend on the specific measurement setup and the sample being used. These curves are not always predictable or easily characterized. Therefore, it is necessary to adjust the alignment several times and make other modifications to the setup in order to obtain accurate and reliable results. For the photodiode and the pinhole alignment, the peak intensities of when scanning along Tx1, Tz1 or Rθ2 are supposed to be located at the centers of the curves. However, as depicted in Figure 3.8 (left) and Figure 3.9, there is a deviation from this expectation. For Rθ2, the middle point is at the 0.82° while the maximum position is at 0.81° resulting in a difference of 0.01°. For Tx1, a slight difference between the maximum and the center is shown, which is attributed to the minimum pitch that can be selected on this stage. For Tz1, a difference of 0.2 mm between the maximum position (-3.5 mm) and the center (-3.3 mm) with a tilted head cutoff was observed. This deviation can be due to the non-uniformity in size or shape of the beam in the vertical axis. For the sample alignment, the center of Rθ1 is at -0.05° which is a discrepancy of 0.01° from the maximum at -0.04°. For the sample alignment in the reflectivity conditions, the maximum for Rθ2 is found at 0.78° and a center at 0.8°, which make a difference of 0.02°. These differences between the center and the maximum positions are related to the mechanical inaccuracies that affect the accuracy of the positions, as the axes may not move precisely as intended. They can also be linked to data acquisition errors as the data acquisition process may introduce errors, such as noise or fluctuations in the signal [80].

3.3 Calibration of instruments

The precise measurement and characterization of X-ray emission intensities necessitates the use of well-calibrated spectrometers, with a key parameter being their efficiency calibration.

Traditional calibration methods, relying on known photon emission intensities, have an inherent circular dependency, limiting their effectiveness. An approach to overcome this issue is use of well-known photon fluxes for calibration, independent of any prior knowledge of photon emission intensities. Measurement of photon fluxes were carried out using the radiometer BOLUX (BOLometer for Use in the range of X-rays) [84] as shown in Figure 3.15 at the *MÉTROLOGIE* beamline of the SOLEIL synchrotron.

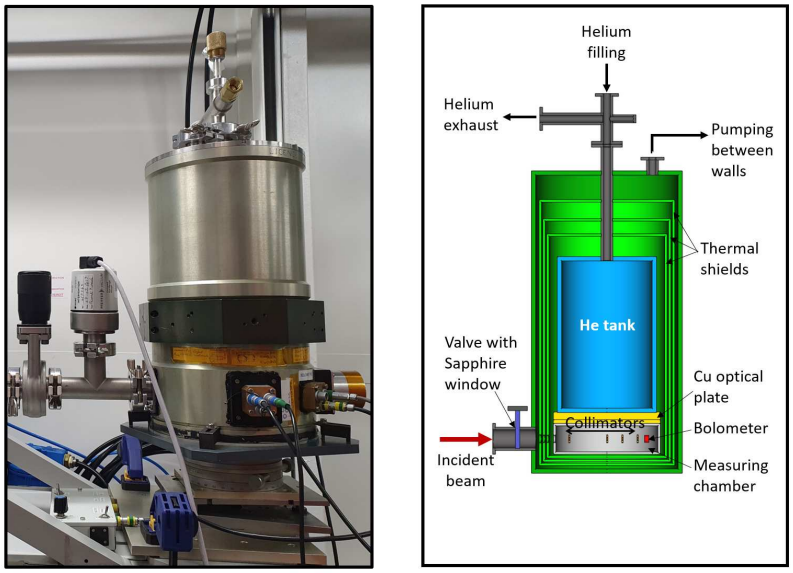

Figure 3.15: Photograph (left) and diagram (right) of the radiometer BOLUX used for the calibration [85].

3.3.1 Primary calibration of the photon flux

The first step involves measuring the flux power of the photon beam using a cryogenic radiometer by means of the electrical substitution, as described in [85]. The measurement principle is based on the change in temperature experienced by an absorber when struck by photon radiation. The temperature increase is proportional to the total beam power and inversely proportional to the heat transfer coefficient between the absorber and the medium. The principle of electrical substitution is to determine the electrical power that must be dissipated in the absorber so that the temperature rise is the same as that induced by the radiant power (Figure 3.16). The temperature changes are monitored with a thermistor, made from a suitable semiconductor material, that is attached to the absorber. To ensure optimal sensitivity, these operations are performed at extremely low temperatures. In the radiometer BOLUX, the absorber is a germanium disc and the thermistor employed to monitor the temperature is also made of germanium. Measurements are performed at liquid helium temperature (4 K), in order to steepen the dependence of the resistance with temperature. The change in voltage in the thermistor is measured when the absorber is exposed to radiation. Subsequently, an electrical current is introduced until the same voltage change is observed. As a result, by knowing the radiant power and the energy of the incident monochromatic beam, the intensity of the photon flux (photons/s) can be derived.

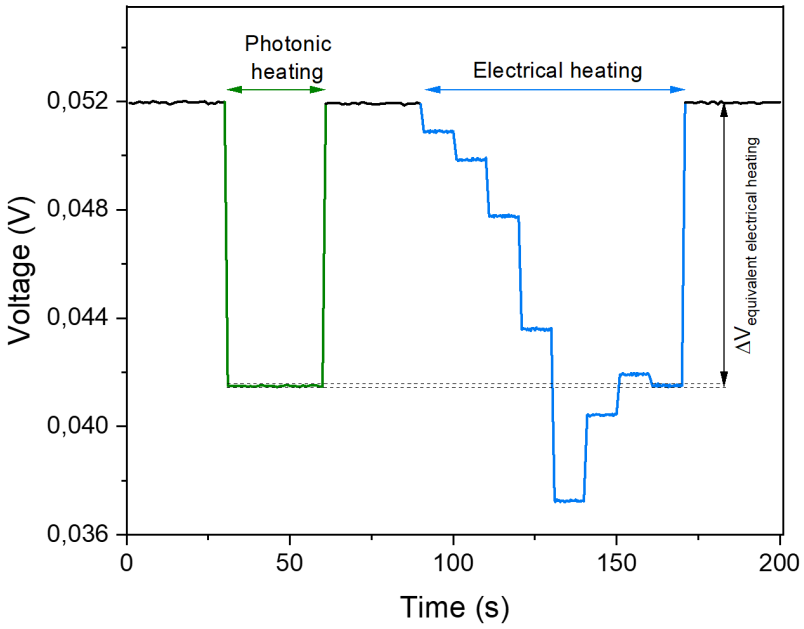

Figure 3.16: Electrical equivalence.

3.3.1.1 Photodiode calibration

The procedure for primary calibration of photodiodes is carried out at the *MÉTROLOGIE* beamline at the SOLEIL synchrotron within the energy range of 3.5 keV to 30 keV. For each energy level, the pitch was adjusted to minimize high-order harmonics, and the beamline power was measured with BOLUX, taking into account a correction factor for the selected energy (absorbed energy $<$ incidence energy). The radiometer was used to calibrate two classic commercial silicon-based photodiodes, OptoDiode AXUV100 [86] and Hamamatsu S8193 [87] in terms of efficiency. The calibration of these photodiodes is performed by measuring their efficiency at different energies of the monochromatic photon beam [85]. The first step involves measuring the flux power of the photon beam using BOLUX where the thermistor's voltage change is measured when the absorber is exposed to the radiation, and afterwards an electrical current is introduced until the same voltage change is reached. In the second step, the photodiode is exposed to the same photon beam, and the current induced by the radiation (after subtracting the background current) is measured. The photodiode's sensitivity is then calculated as:

$$\eta_{Ph} = \frac{I\,(A)}{P\,(W)} \tag{3.1}$$

where I is t the current induced by the radiation and P is the power of the beam. The procedure is repeated for different energies between 3.5 keV and 30 keV to determine the photodiode's efficiency at each energy. The detailed procedure for this experimental calibration is illustrated in Figure 3.17.

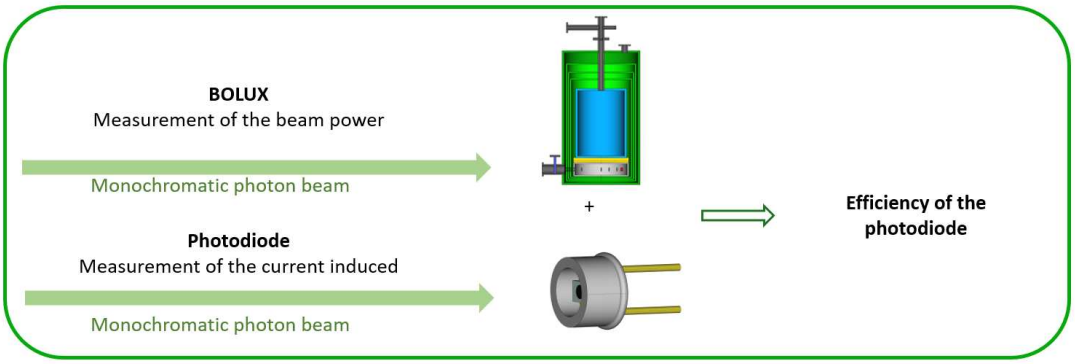

Figure 3.17: Photodiode calibration procedure

In this study, the uncertainties play a critical role and originate from several distinct sources. In the case of beam power measurement, the uncertainty primarily emerges from the determination of the equivalent current, derived from the voltage change, ΔV. This uncertainty propagates approximately linearly, as the electrical power is proportional to the current squared, considering the heating element's resistance remains essentially constant. Here, the relative uncertainty in power measurement can be approximated by the relative uncertainty of ΔV, ranging from a few tenths of a percent for higher beam power measurements to around 1.5 % for the weakest beam.
The uncertainty in the correction factor for the absorbed energy calculation arises from the statistical variations from the simulations (around 0.3 % below the germanium K-edge and approximately 0.5 % above), the uncertainties in the interaction cross-sections used by the code (assumed to be 5 % across the interval), and the thickness of the absorber. For the absorber's thickness, a conservative estimation of 10 % uncertainty was taken into account. The contribution to the total uncertainty from the absorber's thickness is less than 1 % below 25 keV, increasing significantly above that point.
Additionally, the photodiode's current uncertainty is obtained from the standard deviation of a sequence of twenty measurements per energy, influenced by the photodiode's noise and minor oscillations in the beam power due to fluctuations in the synchrotron current. This is particularly notable in certain high energy range measurements with photodiode AXUV and at 10 keV and 11 keV with S8193, leading to higher uncertainties in the photodiode's efficiency. These various factors underscore the importance of accurate uncertainty accounting to maintain the validity and reliability of our experimental results.

3.3.2 Efficiency calibration of a SDD

The silicon drift detector (SDD) was calibrated for its efficiency by referencing to an AXUV photodiode, which had been calibrated with BOLUX. Considering the high photon flux requirements of a radiometer like BOLUX, energy-dispersive spectrometers, such as the one calibrated in this study, cannot measure these directly. Instead, a "transfer device" or reference standard, like a photodiode, is used due to its linear response to a wide range of beam powers.
The process involved measuring the beam-induced current in the reference photodiode for each energy value. Knowing the photodiode's efficiency allowed us to determine the beam power. This power, divided by the energy of each photon, gives the number of photons emitted per unit time. This same photon beam was then measured by the SDD, with the ratio of the

detector's count rate to the total emitted photon count giving the SDD's intrinsic efficiency (Figure 3.18). The derived efficiency curve was compared with Monte Carlo simulations using the PENELOPE code as presented in Figure 3.19. This procedure also compares with the measurements performed with the laboratory tunable monochromatic source based on an X-ray tube and a proportional counter as a reference detector [88]. Figure 3.19 shows a strong agreement between the simulation and the experimental results, presenting an opportunity for the calibration of energy-dispersive spectrometers using a monochromatic photon beam.

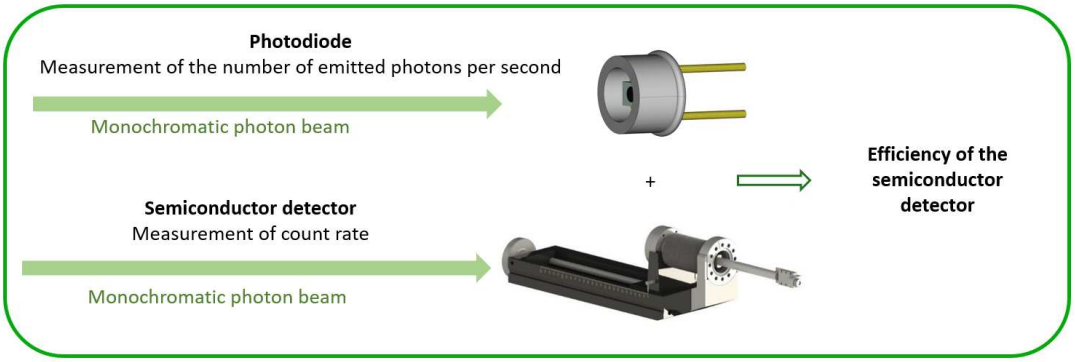

Figure 3.18: Calibration of the SDD with respect to the photodiode

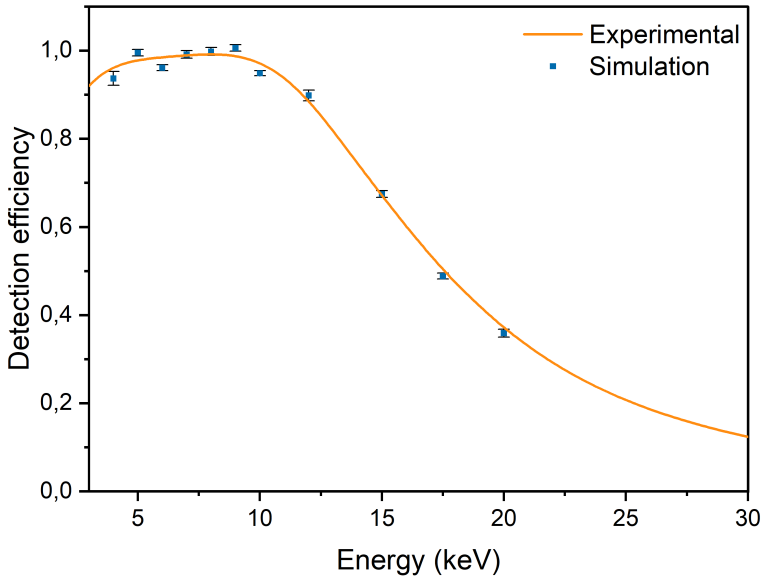

Figure 3.19: Efficiency curve of an SDD spectrometer calibrated with the photodiode AXUV, calibrated with the bolometer BOLUX and the efficiency calculated by Monte Carlo simulations with PENELOPE code [85].

In this context, uncertainty arises from two main sources: the determination of the photon flux and the determination of the count rate by the SDD. The photon flux uncertainty comes from the photodiode's efficiency uncertainty, which is usually close to or below 1 % in this energy

range, except at 20 keV where it may be higher, and from the uncertainty in the current induced in the photodiode. This induced current has a relative uncertainty ranging from a few tenths of a percent to 1.5 % due to a lower signal-to-noise ratio with weaker photon fluxes.
On the other hand, uncertainty in the SDD count rate comes from the stochastic nature of radiation emission, though it's usually below 0.1 % due to high count numbers in measured spectra. The other contribution may happen with the difficulty in fitting the full-energy peaks, if for example a deviation from the ideal Gaussian shape occurs, especially at high count rates. The combined uncertainty of the detection efficiency is around 1 %, occasionally higher at 4 keV, due to high relative standard deviation in the photodiode's current, and at 20 keV due to the uncertainty of the photodiode efficiency. These occasional increases in uncertainty are attributed to instabilities in the beam, leading us to conclude that the relative uncertainty using this calibration techniques typically close to 1 % [85].

Chapter 4

Reference-free combined GIXRF-XRR

In many technical applications, the use of layered materials is becoming increasingly important. Contamination in the production of thin film layered materials such as semi-conductors, photovoltaic cells, thin film batteries and integrated circuits, as well as design error and manufacturing defects, can result in quantifiable yield losses. Thus, defect detection and process cleanliness monitoring are necessary, but not sufficient preconditions for profitable operation [89]. As a result, the fabrication of these materials requires precise control of the film thickness and elemental composition, as well as accurate information on implantation depth and implant distribution [90].
For this purpose, analysis of these materials is essential in order to control their production and to carry out investigations for new developments and research. Generally, X-ray techniques, such as X-ray fluorescence (XRF) spectrometry, proton-induced X-ray emission (PIXE) spectroscopy, and X-ray diffraction (XRD) can be employed to analyze layered materials. These techniques provide extensive information on elemental composition and concentration, as well as material morphology, making them extremely useful in layered material analysis. X-ray fluorescence (XRF) based techniques, such as total reflection X-ray fluorescence (TXRF), grazing incidence/exit X-Ray fluorescence (GIXRF/GEXRF), are particularly valuable for thin films characterization. These nondestructive techniques offer accurate elemental composition and concentration analyses, ideal for layered material examination. The capabilities of TXRF are enhanced by its superior surface sensitivity and ability to detect trace elements, which is achieved by directing the incident beam towards the sample at small grazing angles.
This chapter, focuses on the X-ray analysis techniques used to study and determine the composition and physical properties of layered materials, such as the combination between grazing incident X-ray fluorescence (GIXRF) and X-ray reflectivity (XRR). Additionally, it provides a theoretical description of the calculation of the reflectivity that occurs at the interface and the X-ray induced fluorescence intensities in the total reflection and near total reflection regime using the propagation equations of electromagnetic waves.
It must be mentioned that these techniques were applied using monochromatic photon beams from synchrotron radiation (SR) which represents an attractive excitation source for X-ray qualitative and quantitative trace element analysis: it presents notable qualities such as the tunability of the energy spectrum, high brightness, natural collimation, and polarization.

4.1 X-ray standing waves

At grazing incidence, the reflected part of the incident X-ray beam interferes with the incoming beam at their intersection point. This interaction forms, within the limits of coherence, X-ray standing waves (XSW) above the surface [91, 92] (Figure 4.1) and within the first few tenths of a nanometer inside the material. XSW are produced when constructive and destructive interference occurs within a multilayer stack which can have either periodic or non-periodic structures in the nanometer range. The intensity distribution (i.e the positions of minima and maxima) within the X-ray standing wave field depends on the energy of the X-rays and the angle of incidence [91]. Consequently, atoms located at the maxima positions emit X-ray fluorescence radiations that can be detected, allowing the determination of the depth positions of the atoms by varying the angle of incidence in XSW.

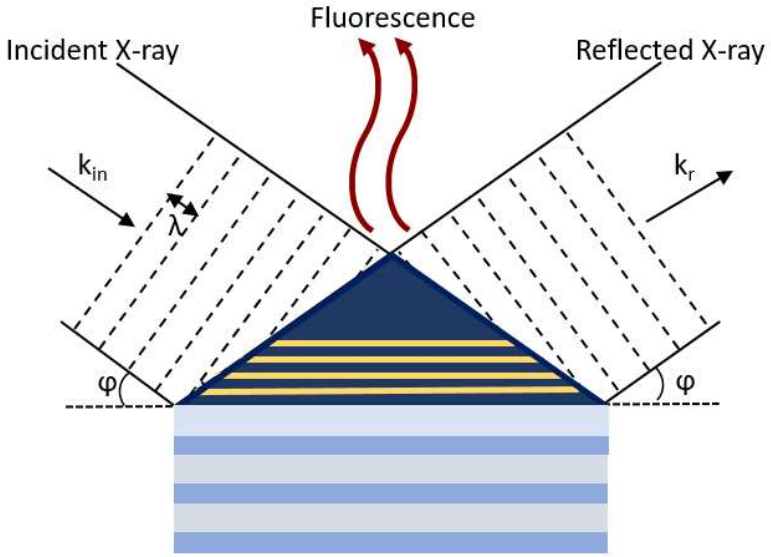

Figure 4.1: A schematic illustration describing formation of an X-ray standing wave (XSW) field under total external reflection of X-rays on a multilayer stack.

The generation of X-ray standing waves by periodic multilayers have been demonstrated to be a highly sensitive probe for determining depth profiles of impurity element and interfacial roughness [93]. To determine the XSW field in a multilayered system, reflection and transmission coefficients for each layer are calculated as functions of the angle of incidence, wavelength and refractive index of the materials in the layer, taking into account absorption inside the layer. The interference between the electrical fields of reflected and incoming beams in each layer is calculated, considering the path length and phase for each beam. Additionally, the interaction of the incident X-rays with multilayers is characterized by specific polarization dependence which affect the phenomenon of interference. In fact, the synchrotron beam is linearly polarized in the plane of the ring, either being S or P polarized depending on the position of the sample [94]. As illustrated in Figure 4.2, the P polarization is characterized by a magnetic field perpendicular to the plane of incidence, while the S polarization exhibits a magnetic field parallel to the plane of incidence.

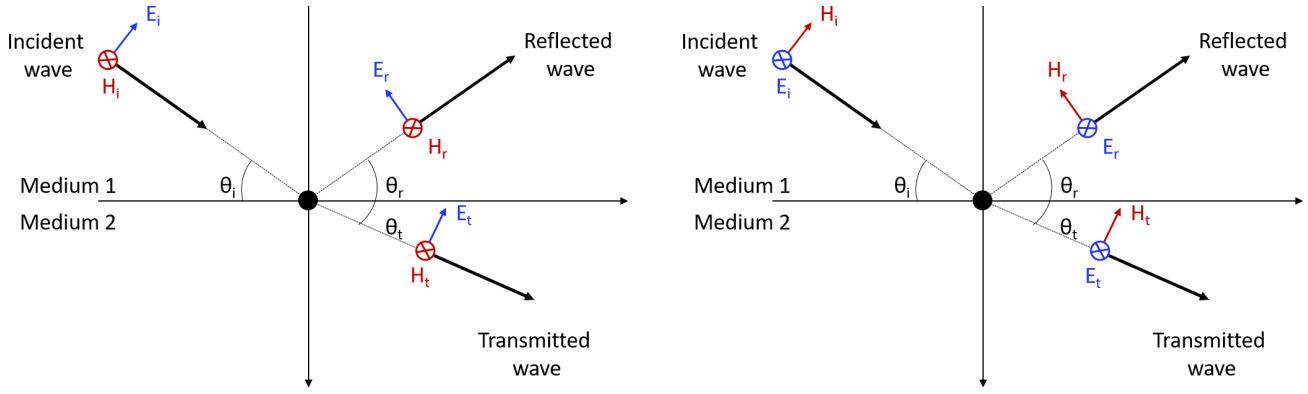

Figure 4.2: Parallel P (left) and perpendicular S (right) polarization of incident X-rays.

4.2 X-ray reflectivity

The birth of X-ray reflectivity (XRR) as an experimental technique can be traced back to Compton's discovery in 1923 of the total reflection of X-rays from solid samples with flat and smooth surfaces [95]. XRR is a powerful non-destructive technique used to study the near-surface structure of materials. It probes the contrast in electron density in depth to determine roughness, density, and thickness of samples ranging from a few, to several hundred nanometers [96, 97], as well as the optical properties of the reflecting interfaces. As shown in Figure 4.3, this technique is based on varying the glancing angle in the grazing range (0°-10°) while recording the intensity of the reflected X-ray beam. The development of XRR began with the study of the effect of wavelength on reflection, including absorption in the refractive index for Fresnel's formula with the discovery of "Kiessig fringes" which marked a significant breakthrough in grazing incidence X-ray reflectivity [98]. In fact, at grazing incidences, below the critical angle, X-rays are specularly reflected with high efficiency due to the phenomenon of total external reflection. The critical angle θ_c is proportional to the square root of the sample's surface density ρ, and linearly proportional to the wavelength of the X-rays λ [99] as:

$$\theta_c = C \cdot \lambda \cdot \sqrt{\rho} \tag{4.1}$$

where C is a material constant.
By increasing the incidence angle above the critical angle, refraction on the sample surface occurs, leading to a decrease in the reflected intensity. Moreover, the reflected intensity is related to the sample roughness, in which it decreases more significantly at higher roughness levels [100]. For angles ranging from the critical angle to several times the critical angle, both reflection and refraction can take place, leading to the formation of interference fringes (Kiessig fringes) in a thin-film sample. This is due to the constructive interference of X-rays that are reflected from the top surface of the sample and from interfaces within the sample, such as the thin-film/substrate interface, that exhibit a contrast in density. In addition, the thickness and density of the thin film can be determined by the position of the maxima of the fringes [101], without reference to the fringe amplitude. However, the roughnesses of the sample's surface and interfaces have an impact on the fringe amplitudes. These roughnesses can be quantified through a recursive solution of the Fresnel equations, which describe the behavior of electromagnetic radiation at boundaries within a sample.

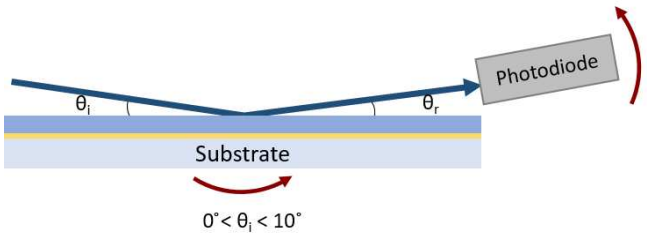

Figure 4.3: Sketch for experimental X-ray reflectivity (XRR) measurement with a photodiode. In the XRR technique, we operate in the $\theta - 2\theta$ mode, where the detector angle is twice the glancing angle, with $\theta_i = \theta_r$.

X-ray reflectivity based on total reflection has become a valuable tool for analyzing surfaces and thin film interfaces. This is attributed to the significant advancements in experimental techniques and instrumentation, especially the widespread use of synchrotron radiation and improvements in detector technology. The development of theoretical modeling and data analysis techniques, along with the fast pace of computer evolution, has also played a key role in this growth. Additionally, the mutually reinforcing relationship between theoretical modeling and experimentation continues to drive further advancements in this field [102]. Figure 4.4 illustrates an example of an XRR curve of Al (7 nm)/ ZrC (5 nm)/ Al (15 nm)/ W (50 nm)/Si measured at 6.25 keV.

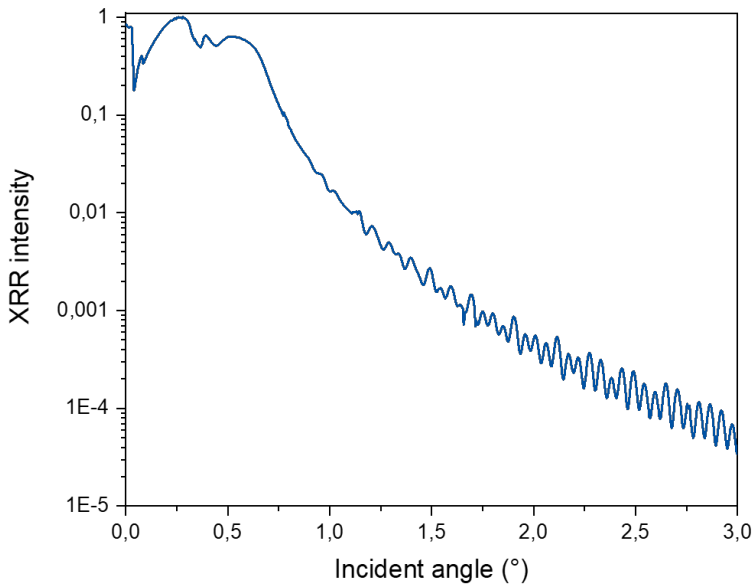

Figure 4.4: X-ray reflectivity (XRR) of Al (7 nm)/ ZrC (5 nm) / Al (15 nm)/ W (50 nm) deposited on a Si substrate measured at 6.25 keV.

Each oscillation period in the reflectivity curve corresponds to a specific layer within the sample [103], with the oscillation frequency and number being indicative of the layers thicknesses, where a higher frequency implies a thicker layer, and a lower frequency indicates a thinner one.

Furthermore, the amplitude of these oscillations is related to the electron density of the respective layer, where higher amplitude oscillations represent a layer of higher electron density, while those of lower amplitude represent a less dense layer. The decay in the oscillations amplitude, relative to the scattering angle, is related to the surface and interface roughnesses [104]. A rapid decay corresponds to a rougher surface or interface, while a slower decay represents a smoother surface or interface. Lastly, the elemental composition of the material, which determines the total electron density, is related to the critical angle of the reflectivity curve.

4.3 Grazing Incidence X-ray fluorescence

Grazing Incidence X-Ray Fluorecence (GIXRF) is a powerful non-destructive characterization technique used for elemental depth profiling of thin films, ranging up to several hundred nanometers in thickness [105, 106, 107, 101, 108]. This technique is equivalent to total reflection X-ray fluorescence (TXRF) [109, 110], where the angle of incidence is well below the critical angle required for total external reflection. GIXRF is based on measuring the fluorescence intensity emitted by the elements present in the sample while varying the incidence angle in the grazing range as illustrated in Figure 4.5. GIXRF was initially used as a method to reduce background scattering effect when studying small quantities of material on a flat surface. Subsequently, it has been widely used in evaluating periodic multilayers [111], adsorbed molecules [112] and thin films deposited on substrates [113]. As mentioned earlier, in the grazing range, the incident and the reflected beam interfere with each other to generate XSWs. Increasing the incidence angle, leads to a deeper penetration into the sample, thus modifying the characteristics of the XSW field.

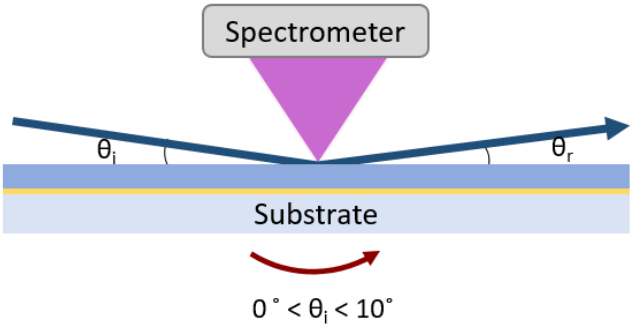

Figure 4.5: Sketch for experimental grazing incidence X-ray fluorescence (GIXRF) measurements with a spectrometer.

Thus, GIXRF relies on the angle of incidence and photon energy to determine the penetration depth and intensity distribution of the incident radiation within a sample. Consequently, the measured fluorescence radiation of the target elements varies with the angle of incidence, allowing for a depth-dependent quantification of layers or elements. To illustrate this, Figure 4.6 shows a fluorescence spectrum of a multilayered sample of Cr (2 nm)/ Mg (20 nm)/ Sc (20 nm) at 0.2°, 0.5°, 1°, 2°, and 3°: The results are plotted between 1.2 keV and 7 keV, showing fluorescence peaks corresponding to Si-K_α and K_β, Sc-K_α and K_β, and Cr-K_α and K_β. However, the Mg-K_α peak is not apparent despite the thickness of the Mg layer in the linear scale spectrum, due to its relatively low contribution and its location close to the Si-K_α peak, causing it to be

hidden by the signal of the substrate and the background noise. For clearer visualization, a zoomed-in section of the Mg and Si area is presented on using a logarithmic scale, highlighting the presence and details of the Mg-K_α peak.

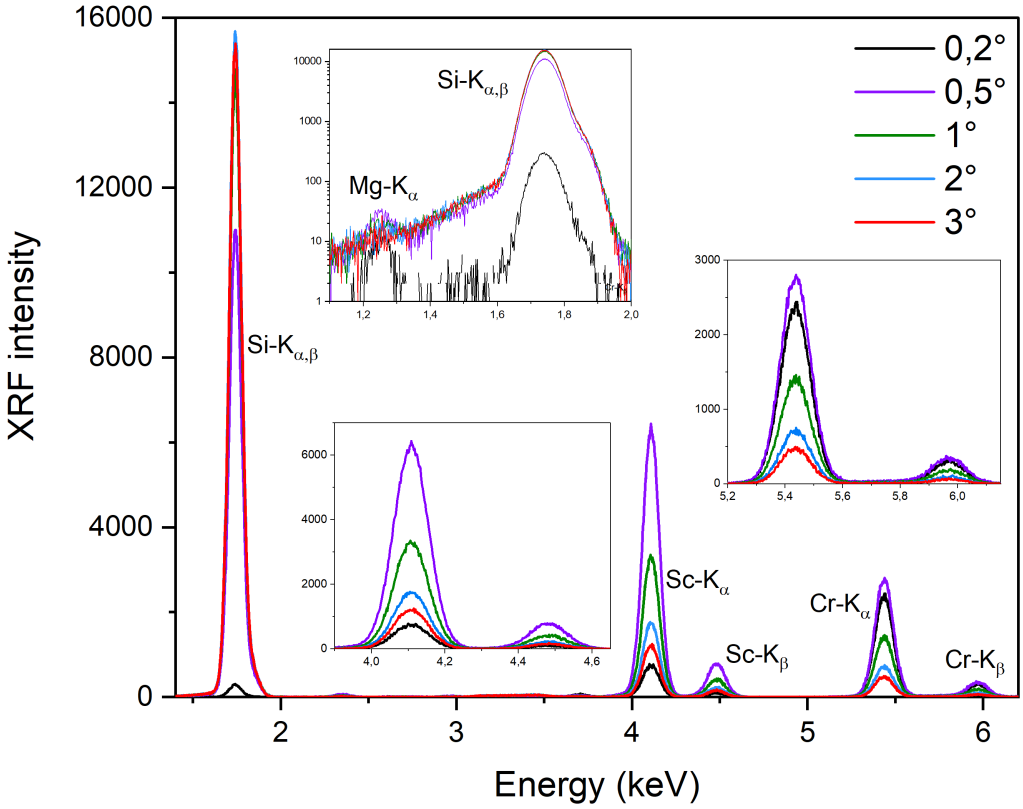

Figure 4.6: Spectrum fluorescence of a multilayered sample of Cr (2 nm)/ Mg (20 nm)/ Sc (20 nm) deposited on a Si substrate measured at different incident grazing angles.

The GIXRF curves are derived by plotting the intensity of each fluorescence peak as a function of the incident angle, as shown in Figure 4.7. The intensity of K_α fluorescence peaks varies with the incident angle, giving information about the depth distribution of each element in the layered sample. At smaller angles, the incident beam primarily interacts with the surface layers, as shown by the increase in the intensity of Cr-K_α peaks up to a maximum at 0.33°. As the incident angle increases, this intensity starts to decrease thereby penetrating deeper into the underlying layers. This deeper penetration corresponds to an increase in the intensity of Sc-K_α peaks, which reach a maximum at 0.41°. The Si-K_α GIXRF curve shows a very low intensity value at smaller incident angles as the incident beam does not reach the substrate. By increasing the incident angle, thereby enhancing the beam's penetration depth, the intensity of the Si-K_α peak begins to increase and remain relatively constant.

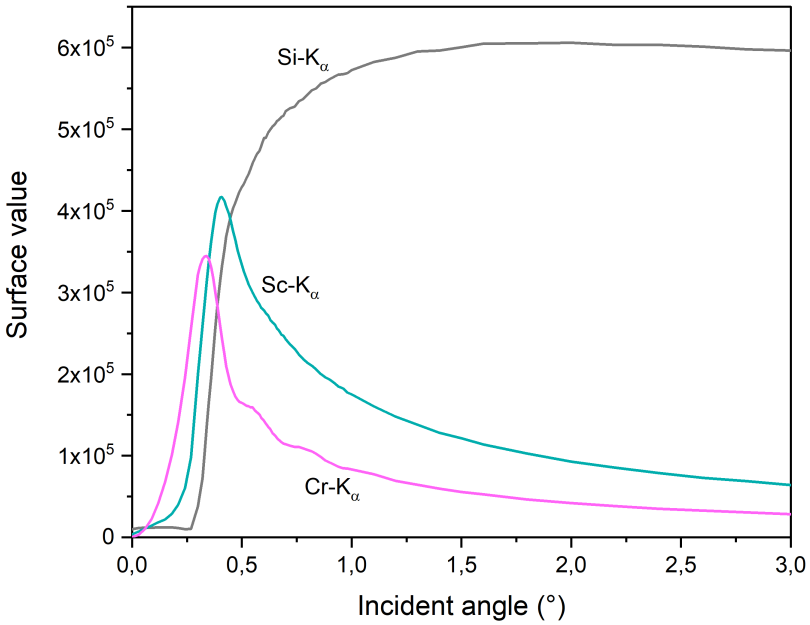

Figure 4.7: Grazing incidence X-ray fluorescence (GIXRF) of Si-K_α , Cr-K_α and Sc-K_α from a Cr (2 nm)/ Mg (20 nm)/ Sc (20 nm) sample.

4.4 Reference-Free combined GIXRF-XRR

The combination of Grazing Incidence X-ray Fluorescence (GIXRF) and X-ray Reflectivity (XRR) offers several advantages over using either technique alone, allowing for non-destructive investigations of both bulk and layered samples [114, 115, 116, 117, 118]. The combination of these two techniques yields both compositional and structural information, providing a more complete understanding of the material properties. This results in increasing the analysis accuracy, reducing the potential for errors and ambiguities [81, 101, 119, 120]. In addition, XRR measurement can be used to correct the background scattering that can affect GIXRF analysis, resulting in a more accurate determination of the elemental composition of thin films. In traditional GIXRF-XRR, a reference or calibration sample is used to calibrate the instrument and the instrumental variations. However, the number of nanoscale reference materials available is quite limited compared to the growing number of technologically and scientifically relevant material systems [121, 122]. This limitation can cause accuracy issues in traditional GIXRF-XRR measurements. Therefore, to overcome this limitation, the reference-free GIXRF-XRR method is used, which eliminates the need for a reference sample. In reference-free GIXRF-XRR, the analysis is based on a simulation model that requires: a prior knowledge of the physical parameters of the experimental setup (solid angle, detection efficiency), a knowledge of the atomic fundamental parameters (photoelectric absorption coefficients, fluorescence yields ...) and a prior approximation on the sample structure, such as thicknesses, densities, roughnesses and order of the layers, as well their composition [123]. These parameters are essential inputs for reference-free GIXRF-XRR, as they provide the expected X-ray fluorescence yield

and reflectivity for a given set of sample parameters and X-ray energy. However, this technique requires X-ray detectors that are absolutely calibrated [85] either to measure the number of incoming photons in the incident beam or to quantify the number of emitted X-rays.

4.4.1 Reflection from a layered surface

The studied structure is a multilayer thin film with parallel interfaces, which has been deposited on a thick substrate as shown in Figure 4.8. Each layer, j, has a thickness d_j and an index of refraction n_j. To calculate the reflectivity, one starts with Maxwell's equations, describing the relation between the electric and magnetic fields in medium j at position $\vec{r}$ given by:

$$\begin{aligned} E_j(r) &= E_j(0)\exp\left[i\left(\omega\cdot t-\overrightarrow{k_j}\cdot\overrightarrow{r}\right)\right] \\ H_j(r) &= H_j(0)\exp\left[i\left(\omega\cdot t-\overrightarrow{k_j}\cdot\overrightarrow{r}\right)\right] \end{aligned} \tag{4.2}$$

where$E_j(0)$ and $H_j(0)$ represent the electric and magnetic field amplitude at the top of layer j and ω is the frequency of the electromagnetic wave. The wave vector of the j layer can be expressed as [124]:

$$k_j = k'_j - ik". \tag{4.3}$$

The propagation of the electromagnetic wave within each layer is influenced by the properties of the medium, specifically the dielectric constant ϵ_j of a medium j. This latter is related to the refractive index (Chapter 1, Subsection 1.2.4) as [124, 5]:

$$\epsilon_j = n_j^2 \approx 1 - 2\delta_j - 2i\beta_j = \epsilon'_j - i\epsilon"_j. \tag{4.4}$$

In Equation 4.4, δ_j and β_j represent respectively the deviation from unity of the refractive index and the imaginary part of the refractive index related to the absorption of the X-rays of the layer j. In the X-ray range, the refractive index can be related to the atomic scattering factor of the individual atoms by [75]:

$$n = 1 - \frac{r_0}{2\pi}\lambda^2\sum_q n_q f_q. \tag{4.5}$$

where r_0 is the classical electron radius, λ is the wavelength of the primary beam, n_q is the number of atoms q per unit volume, and f_q is the complex atomic scattering factor written as:

$$f_q = f'_q + if"_q \tag{4.6}$$

wheref' is the real part of f and $f"$ its imaginary part. The deviation of the refractive index δ_j can be related directly to the density ρ and the atomic scattering factor of each element as:

$$\delta = \frac{r_0}{2\pi}\lambda^2 N_0\frac{\rho}{A}f' \tag{4.7}$$

where A is the atomic mass of the respective element and N_0 is Avogadro's number. Consequently, δ can be easily calculated for a given X-ray energy. In addition, β is related to the mass attenuation coefficient μ as [16, 125]:

$$\beta = \frac{r_0}{2\pi}\lambda^2 N_0\frac{\rho}{A}f" = \frac{\lambda}{4\pi}\left(\frac{\mu}{\rho}\right)\rho \tag{4.8}$$

The complete refractive index of a material can be calculated from measurements of only the imaginary part using the Kramers-Kronig relations [126, 127]. These relations provide a link between the real and imaginary parts of the refractive index which can be written as:

$$\delta(E) = \frac{r_0}{2\pi}\lambda^2 n_{/V} Z^* + \frac{1}{\pi r_0 hc}\int_0^\infty \frac{\mu(x)\,x^2}{x^2 - E^2}\mathrm{d}x \tag{4.9}$$

where Z^* represents the relativistic correction, $n_{/V}$ is the number of atoms per unit volume and E represents the photon energy. The integral ranges from zero to infinity which implies that, to compute δ for a specific photon energy, the complete β spectrum must be considered. Additionally, there is an undefined point at $x = E$ within the integral, and therefore, it must be approached using the Cauchy principal value method.
In addition, for layers including a mixture of elements, δ and β have to be calculated following the additive law written as:

$$\delta_{Total} = \sum c_i \delta_i \tag{4.10}$$

and

$$\beta_{Total} = \sum c_i \beta_i \tag{4.11}$$

with c_i represents the mass fraction of element i and δ_i and β_i denote respectively the deviation and the imaginary component of the refractive index for the respective element.
The theoretical calculation of the reflectivity is often presented in S-polarization and rarely in P-polarization [128]. However, in the hard X-ray region i.e. in small δ_j and β_j approximations, the calculation of the electric field is similar for S and P polarizations [129, 130]. Here we present the method of calculating the electric field perpendicular to the propagation surface (P polarization). In this case, the electric and magnetic fields, as well as the flow relationships at interfaces, become:

$$\overrightarrow{E_j} = \overrightarrow{E_0}\exp\left(i\left(\omega\cdot t - k_{j,x}x \pm k_{j,z}z\right)\right) \tag{4.12}$$

and:

$$\overrightarrow{H_j} = \overrightarrow{H_0}\exp\left(i\left(\omega\cdot t - k_{j,x}x \pm k_{j,z}z\right)\right) \tag{4.13}$$

where $k_{j,x}$ and $k_{j,z}$ represent the components of the wave vector in the plane of incidence $\widehat{xOz}$ along x and z axes respectively in the j. The $\pm$ symbol indicates whether the wave is being reflected $(+)$ or transmitted $(-)$. The transition to an interface involves the equality of the components along the x-axis as:

$$k^i_{j,x} = k^r_{j,x} = k^t_{j+1,x}, \tag{4.14}$$

where $k^i_{j,x}$ and $k^r_{j,x}$represent the incident and the reflected wave vector respectively in the j^{th} layer and and $k^t_{j,x}$ represents the wave vector transmitted from the j^{th} layer in the $j+1^{\text{th}}$ layer. The dispersion relation in layer j is calculated as:

$$k_j^2 = \epsilon_j \mu_j \omega^2 \tag{4.15}$$

with the dielectric constant expressed as:

$$\epsilon_j = \epsilon_0 \epsilon_{j,relative} \tag{4.16}$$

and the magnetic permeability expressed as:

$$\mu_j = \mu_0 \mu_{j,relative}\,, \tag{4.17}$$

where ϵ_0 and μ_0 are the vacuum electric and magnetic permeability, respectively. The component of the transmitted wave vector along z is then calculated using the optical index defined as the ratio of the speed of light to the propagation speed:

$$n_j = \frac{c}{v_j} = \frac{\sqrt{\epsilon_j \mu_j}}{\sqrt{\epsilon_0 \mu_0}} \tag{4.18}$$

and then Equation 4.15 becomes:

$$\begin{aligned} k^t_{j+1,z} = \sqrt{\left(k^t_{j+1}\right)^2 - \left(k^t_{j+1,x}\right)^2} = \sqrt{\left(k^t_{j+1}\right)^2 - \left(k^t_{j,x}\right)^2} = \sqrt{\left(n^t_{j+1}k_0\right)^2 - \left(n^i_j k_0 \cos\left(\theta_j\right)\right)^2} \\ = \\ k_0\sqrt{\left(n^t_{j+1}\right)^2 - \left(n^i_j \cos\left(\theta_j\right)\right)^2} = k_0\sqrt{\left(n^t_{j+1}\right)^2 - \left(n^i_0 \cos\cos\left(\theta_j\right)\right)^2} \end{aligned} , \tag{4.19}$$

with $k_0 = \frac{2\pi}{\lambda_0}$, n^t_{j+1} and n^i_j are the optical indexes in the transmitted ($j+1^{\text{th}}$ layer) and incident (j^{th} layer) medium respectively. The x-components of the wave vector are equal at each interface, either vacuum or air ($n_0 = 1$) leading to $k_x = k_0 cos(\theta_0)$ for all layers.
Maxwell's equations for the electric $\overrightarrow{E}$ and magnetic fields $\overrightarrow{H}$ are expressed as:

$$\begin{aligned} \overrightarrow{\text{rot}}\overrightarrow{E} &= -\mu_0 \frac{\partial \overrightarrow{H}}{\partial t} \text{ Maxwell} - \text{Faraday law} \\ \overrightarrow{\text{rot}}\overrightarrow{H} &= \epsilon \frac{\partial \overrightarrow{E}}{\partial t} \text{ Maxwell} - \text{Ampere law} \end{aligned} . \tag{4.20}$$

In the case of transverse magnetic (TM) polarization, only the x and z components of the electric field E and the y components of the magnetic field H are non-zero. The Maxwell-Ampere law can then be used to relate these non-zero components as follows:

$$\begin{aligned} -\frac{\partial \overrightarrow{H_{j,y}}}{\partial z} &= i\omega\epsilon_j E_{j,x} \\ \frac{\partial \overrightarrow{H_{j,y}}}{\partial x} &= i\omega\epsilon_j E_{j,z} \end{aligned} . \tag{4.21}$$

By applying the derivative of Equation 4.13, Equation 4.21 becomes:

$$\begin{aligned} ik^{i,t}_{j,z} \times H^{i,t}_{j,y} &= i\omega\epsilon E^{i,t}_{j,x} \\ -ik^{i,t}_{j,x} \times H^{i,t}_{j,y} &= i\omega\epsilon E^{i,t}_{j,z} \end{aligned} \tag{4.22}$$

for the propagating (incident or transmitted) waves, while for the counter-propagating (reflected) waves it becomes:

$$\begin{aligned} -ik^{r}_{j,z} \times H^{r}_{j,y} &= i\omega\epsilon E^{r}_{j,x} \\ -ik^{r}_{x} \times H^{r}_{j,y} &= i\omega\epsilon E^{r}_{j,z} \end{aligned} . \tag{4.23}$$

Moreover, in the case of TM-polarization, the electric-field relations at an interface can be expressed as:

$$\begin{aligned} E^i_{j,x} + E^r_{j,x} &= E^t_{j+1,x} + E^r_{j+1,x} \\ H^i_{j,y} + H^r_{j,y} &= H^t_{j+1,y} + H^r_{j+1,y} \end{aligned} . \tag{4.24}$$

Equation 4.25 can then be expressed in terms of the y-component of the magnetic field using the equalities of Equations 4.22 and 4.23 as:

$$\begin{aligned} -\frac{k^t_{j+1,z}}{\epsilon_{j+1}} \times H^i_{j,y} + \frac{k^r_{j,z}}{\epsilon_j} \times H^r_{j,y} &= -\frac{k^t_{j+1,z}}{\epsilon_{j+1}} \times H^t_{j+1,y} \\ H^i_{j,y} + H^r_{j,y} &= H^t_{j+1,y} \end{aligned} . \tag{4.25}$$

The complex coefficients of reflection r_j and transmission t_j at the j and $j+1$ interfaces are calculated using Fresnel's formulae [102]:

$$r_j = \frac{k_{j,z} - k_{j+1,z}}{k_{j,z} + k_{j+1,z}} \tag{4.26}$$

and

$$t_j = \frac{2k_{j,z}}{k_{j,z} + k_{j+1,z}}. \tag{4.27}$$

For rough surfaces, these formulae are no longer correct and have to be modified. Therefore, to include the effect of roughness r_j is multiplied by the Debye–Waller factor as [102]:

$$S_j = \exp\left[-2\sigma_j^2 k_{j,z} k_{j+1,z}\right] \tag{4.28}$$

where σ_j represents the root mean square deviation of the interface atoms from perfectly smooth conditions. The Debye–Waller factor approximation is only applicable to small roughnesses ($\sigma_j |k_{j,z}| < 1$) [128]. Another approach to include the roughness effect is by using the Nevot-Croce model [27]. In this model, the roughness effect is calculated using the distorted-wave Born approximation where the roughness is considered as a small perturbation of an electromagnetic potential with a Gaussian random distribution along the interface. In this case, r_j is multiplied by S_j and t_j is multiplied by T_j, where:

$$T_j = \frac{\exp\left[\sigma_j^2 \left(k_{j,z} - k_{j+1,z}\right)^2\right]}{2} \tag{4.29}$$

This method is applicable in case of a single layer. In a multilayer thin-film sample, the electric field at the interfaces is calculated using the Parratt recursive formalism [129].

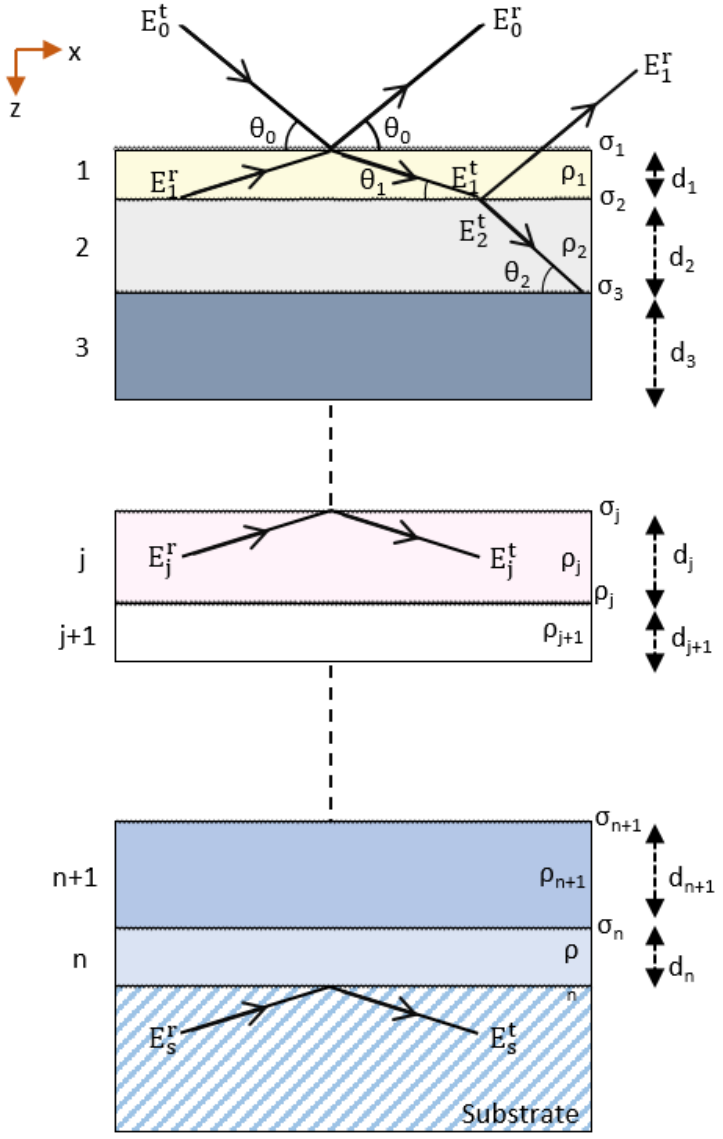

Figure 4.8: Reflection and refraction of X-rays in a multilayer thin film structure deposited on a thick substrate.

4.4.2 Parratt recursive formalism

By applying the Parratt recursive formalism [129] through all the layers, the transmitted and reflected components of the electric and magnetic fields at the top of the layers can be calculated. In the case of XSW, the Parrat formalism is modified to allow for the determination of the electric and magnetic fields intensities at any point within the multilayer. To calculate the reflectivity of a multilayer for P-polarization, the recursive formalism is based on the continuity of the tangential components of the H-field vectors at the j-$j+1$, taking the middle of each layer as the origin for the field. In this case, Equation 4.25 is then written as [131]:

$$\begin{aligned} \left[a_j H_j^t(z_j) + a_j^{-1} H_j^r(z_j)\right] \frac{k_{j,z}^r}{n_j^2} &= \left[a_{j+1}^{-1} H_{j+1}^t(z_{j+1}) + a_{j+1} H_{j+1}^r(z_{j+1})\right] \frac{k_{j+1,z}^t}{n_{j+1}^2} \\ a_j H_j^t(z_j) + a_j^{-1} H_j^r(z_j) &= a_{j+1}^{-1} H_{j+1}^t(z_{j+1}) + a_{j+1} H_{j+1}^r(z_{j+1}) \ . \end{aligned} \tag{4.30}$$

The amplitude factor a_j in Equation 4.30 represents the phase retardation effects incurred by the waves traveling within the respective layers and it is given by:

$$a_j = \exp\left(-ik_0 N_j \frac{d_j}{2}\right) \tag{4.31}$$

where d_j represents the thickness of the j^{th} layer and $N_j = \sqrt{n_j^2 - \cos^2(\theta_0)}$. By developing the whole calculation, the reflection coefficient at the interface between the j^{th} layer and the $j+1^{\text{th}}$ layer can be written as:

$$R_{j,j+1} = a_j^2 \frac{H_j^r}{H_j} = a_j^4 \frac{R_{j+1,j+2} + F_{j,j+1}}{R_{j+1,j+2} F_{j,j+1} + 1} \tag{4.32}$$

in which $F_{j,j+1}$ is the Fresnel coefficient for the reflectivity given by:

$$F_{j,j+1} = \frac{\frac{N_j}{n_j^2} - \frac{N_{j+1}}{n_{j+1}^2}}{\frac{N_j}{n_j^2} + \frac{N_{j+1}}{n_{j+1}^2}}. \tag{4.33}$$

Furthermore, since there is no reflection for the substrate, $H_s^r = 0$. The recursive formulation (Equation 4.32) is then solved in reverse order, by calculating the magnetic field amplitude in the j^{th} layer and then progressively the magnetic amplitudes for the first layers are obtained. Finally, the reflectivity in P polarization is obtained from the ratio of the magnetic fields at $j = 0$ (i.e. at the surface of the sample) as:

$$R(\theta) = \left\| \frac{H_0^r}{H_0^i} \right\|^2 \tag{4.34}$$

4.4.3 XRF calculation

The X-ray fluorescence intensity I_{aj} is defined as the number of photons emitted per unit of time by an atom of a particular element a in the j^{th} layer of a multi-structure. This fluorescence intensity [132] can be calculated as:

$$\begin{aligned} I_{aj} = \frac{\lambda}{hc} C_{aj} \frac{\tau_{a\lambda}}{\mu_{j\lambda}/\rho_j} J_{a\lambda} \omega_a g_a \exp\left[-\sum_{n=1}^{j-1} \frac{\mu_{na} d_n}{\sin\theta_d}\right] S_1 \times \\ \int_0^{dj} \mathrm{d}z \left[-\frac{\partial P_{j,z}}{\partial z}\right] \exp\left[\frac{\mu_{ja} z}{\sin\theta_d}\right] \ . \end{aligned} \tag{4.35}$$

- C_{aj} is the mass fraction of element a in layer j,
- $\tau_{a\lambda}$ is the photoelectric part of the mass attenuation coefficient for element a at wavelength λ,
- $\mu_{j\lambda}$ is the linear attenuation coefficient of the incident radiation in layer j,
- ρ_j is the atomic density of layer j,

- $J_{a\lambda}$ is the absorption jump factor at wavelength λ for the considered shell of element a,
- ω_a is the fluorescence yield,
- g_a is the relative emission rate,
- μ_{na} is the linear attenuation coefficient of the considered fluorescence of element a in layer n,
- d_n is the thickness of layer n,
- S_1 is the irradiated detected sample area,
- θ_d is the detector angle,
- P_{jz} is the z component of the Poynting vector
- and μ_{ja} the linear attenuation coefficient of the fluorescence of element a in layer j.

First we calculate the time-averaged, energy flux density given by the Poynting vector as [133]:

$$P_j = \frac{1}{2}\mathrm{Re}\left(E_j \times H_j^*\right) = \frac{1}{2}\mathrm{Re}\left(E_j^* \times H_j\right). \tag{4.36}$$

In the case of transverse magnetic polarization, only the x and z components of the electric field and y of the magnetic field are non-zero, which gives:

$$\overrightarrow{P} = \frac{1}{2}\mathrm{Re}\left(\begin{pmatrix} E_x \\ 0 \\ E_z \end{pmatrix} \wedge \begin{pmatrix} 0 \\ H_y^* \\ 0 \end{pmatrix}\right) = \frac{1}{2}Re\begin{pmatrix} -E_z H_y^* \\ 0 \\ E_x H_y^* \end{pmatrix} \tag{4.37}$$

Using relations 4.22 and 4.23, the z-component of the Poynting vector in the layer j can be written as:

$$\begin{aligned} P_j &= \tfrac{1}{2}\mathrm{Re}\left(E_x \times H_y^*\right) = \tfrac{1}{2}\mathrm{Re}\left(\tfrac{k_{j,z}}{\omega\epsilon_j} H_y H_y^*\right) = \\ &\tfrac{1}{2}\mathrm{Re}\left(\tfrac{k_0 N_j}{\omega\epsilon_j}\|H_y\|^2\right) = \tfrac{1}{2}Z_0\|H_y\|^2\mathrm{Re}\left(\tfrac{N_j}{n_j^2}\right) \end{aligned} \tag{4.38}$$

where $Z_0 = \sqrt{\frac{\mu_0}{\epsilon_0}}$ is the impedance of a vacuum. In Equation 4.38, H_y represents the y-component of the magnetic field resulting from the recursive calculation of the field in the structure. Furthermore, in the reference-free approach, the incident power on the first interface needs to be measured with a calibrated photodiode. This is defined as the number of incident photons per unit time as:

'where Nb_{ph} is the number of photons and S_0 is the total area over which the incident photon flux is spread. This area may be larger than the spectrometer area or even the sample length, especially at incident angles close to 0°. The number of photons per second at a particular depth z for a given incidence energy is calculated as:

$$I_z = I_0\frac{S}{S_0} \times \frac{\|H_y\|^2}{\|H_{0,y}\|^2} \times \frac{\mathrm{Re}\left(\frac{N_j}{n_j^2}\right)}{\sin\left(\theta_0\right)} \tag{4.39}$$

where S represents the effective area of the sample excited by the incident beam. The number of emitted photons detected in a characteristic emission line of an element present in the multilayer

can be calculated as the sum of the fluorescence emitted by each layer of thickness dz by using the Sherman equation as [134]:

$$\begin{aligned} XRF\left(i,\theta\right) \;=\; & I_0 \times \tfrac{S}{S_0} \times \tfrac{\Omega(\theta)}{4\pi} \times T \times \eta_i \times \omega_i \times \tau_i \times \\ & \int W_i\left(z\right) \rho\left(z\right) \tfrac{\|H_y(z,\theta)\|^2}{\|H_{0,y}(z,\theta)\|^2} \times \tfrac{\mathrm{Re}\left(\frac{N_j}{n_j^2}\right)}{\sin(\theta_0)} \times \exp\left(-\mu_i \cdot \rho\left(z\right) \cdot z\right) \mathrm{d}z \end{aligned} \quad . \tag{4.40}$$

- T is the acquisition time of the spectrum,
- η_i is the detection efficiency of the spectrometer for emission line i,
- ω_i is the partial fluorescence yield of emission line i,
- τ_i is the photoelectric absorption coefficient for the excited element at the incident photon energy,
- $W_i(z)$ is the mass fraction of element i as a function of depth corresponds to C_{aj} in equation 4.35,
- $\rho(z)$ is the density of the layers as a function of depth,
- and μ_i is the mass attenuation coefficient of the crossed layers for emission at the energy of emission line i.

Note that $\Omega(\theta)$ represents the solid angle of detection taking into account the limitation of the sample surface accessible to the spectrometer's field of view. Finally, a quick calculation is done in an approximate way by dividing the thickness of the sample into slices as:

$$\begin{aligned} XRF(i,\theta) \quad = & I_0 \times \tfrac{S}{S_0} \times \tfrac{\Omega(\theta)}{4\pi} \times T \times \eta_i \times \omega_i \times \tau_i \times \\ & \textstyle\sum_j W_i\left(z_j\right) \rho_j(z_j) \times (z_j - z_{j-1}) \tfrac{\|H_y(z_j,\theta)\|^2}{\|H_{0,y}(z_j,\theta)\|^2} \times \tfrac{\mathrm{Re}\left(\frac{\mathrm{N_j}}{\mathrm{n_j^2}}\right)}{\sin(\theta_0)} \\ & \times \textstyle\sum_{h=1}^{j-1} \exp\left(-\mu_i\left(z_h\right) \rho\left(z_h\right) \left(z_h - z_{h-1}\right)\right) \end{aligned} \quad . \tag{4.41}$$

In summary, this comprehensive procedure provides a robust method for computing the number of photons emitted per unit time by atoms of a specific element from different layers of a stacked structure. By accounting for several parameters such as attenuation coefficients, atomic density, fluorescence yield, emission rate, and detector angle, we are able to accurately measure the incident power on the interface, calculate the number of emitted photons detected in a particular emission line, and estimate the fluorescence emitted by each layer. This advanced model ensures a precise and thorough understanding of X-ray fluorescence intensity, which is crucial in a wide range of applications in materials science and analytical chemistry.

4.5 Fundamental parameters

For accurate quantification of X-ray fluorescence (XRF), it is important to understand the physics of photon-matter interactions that includes the ionization and the absorption processes. This involves knowledge of the atomic Fundamental Parameters (FPs) [135, 136, 137, 80, 138], which has been a necessary requirement since the 1980s for all XRF-based methods and other techniques such as electron-probe micro-analysis (EPMA) and particle-induced X-ray emission (PIXE) [139]. The quantification method, relies on the correlation between the measured X-ray intensities and the concentrations of the sample's elements, taking into account interactions among the incident and emitted X-ray photons as well as the interactions with the atoms in the sample along the depth [134]. The FP method takes into consideration various parameters, such as the thicknesses of the layers and the sample's elemental composition. The main fundamental parameters used in reference-free GIXRF-XRR are the diagram line energies, the mass attenuation coefficients, the photoelectric absorption coefficients and the fluorescence yields. X-ray fluorescence quantification techniques that rely on fundamental parameters, are thus heavily dependent on the quality of the available data to produce a comprehensive and useful set of parameters. Multiple databases related to XRF contain important atomic parameters such as transition and Coster-Kronig probabilities, fluorescence yields, photo-ionization, and scattering absorption coefficients [24, 140, 75, 141, 25]. These datasets are based on either theoretical calculations or old measurements generally performed in the 1950s period. However, the methods used are now considered outdated and the uncertainties poorly documented [138] especially for low-Z elements and L- and M- lines of heavier elements [136]. Additionally, there have been limited experiments in the past few decades focused on determining atomic data with improved relative uncertainties [115, 142, 143].
To remedy this situation the Laboratoire National Henri Becquerel is performing systematic experiments, making use of modern instrumentation, to provide new atomic fundamental parameters values, measured at the *MÉTROLOGIE* beamline of the SOLEIL synchrotron facility. The accurate measurement of the fundamental parameters with low uncertainties relies on very well-known experimental and instrumental parameters. In this part, we present the measurement procedures and techniques used to calculate these parameters, with their application to the cases of iron and yttrium.

4.5.1 Samples characterization

Before measuring the fundamental parameters, it is imperative to thoroughly characterize the samples under investigation. A first step is to ascertain the purity of these samples, as any impurities could substantially alter the interactions between the material and the incident photon beam, leading to potentially incorrect results. Similarly, the physical state of the samples, including their crystalline structure, can influence radiation interaction parameters and must, therefore, be accurately known. The density of the samples, a property with a direct influence on the mass attenuation coefficient, should also be precisely determined. Another important consideration is the sample thickness, which affects the depth of penetration of the radiation, thereby influencing the observed attenuation and fluorescence. By means of precise characterization of these parameters, it is possible to guarantee the accuracy and reliability of the resulting measurements. To achieve greater precision and ensure independence from X-ray analysis methods, the mass and the area of the samples are measured instead of relying on

tabulated densities. They can be determined irrespective of their material or compositional properties, which makes these measurements applicable to different samples and helps mitigate the influence of specific material properties such as density and crystalline structure, which can introduce additional complexities into the measurements. The samples (some tenths of a mg) were weighed using a calibrated microbalance with an uncertainty of 8.5 μg, in a room with controlled hygrometry, temperature and atmospheric pressure. The measurement of the area was conducted using a vision machine, including a microscope equipped with two calibrated stages and a picture analyzer. This setup offered multiple magnifications that facilitated appropriate enlargement, essential for the accurate characterization of a complex shape. For this study, the samples were supplied from Goodfellow, a supplier recognized for providing high-purity materials. The two samples chosen for this investigation are pure iron (Fe) and pure yttrium (Y), both elemental metals with unique properties that make them ideal for this study.

4.5.1.1 Iron (Fe)

The experimental measurements were conducted on a high purity iron foil (product number FE00-FL-000107) due to its desirable characteristics for the investigations. This iron foil sample has a thickness of 10 μm with a purity level of 99.99 %, providing maximum accuracy in the experiments by limiting the possibility of undesired interactions caused by impurities. Iron is also characterized by its high density (7.874 g/cm^3) at 20°C, a vital factor affecting the mass attenuation coefficient. As one of the most commonly used metals, iron is known for its magnetic properties and abundant availability, making it an ideal choice for probing fundamental interactions between electromagnetic radiation and matter. For improved accuracy, multiple measurements of the mass were conducted, yielding an average mass value of 20.21 mg. Additionally, the surface area was determined to 262.03 mm^2 with an uncertainty, which was calculated by taking into account the inaccuracies of the contour of the sample defined by the vision machine and its associated software.

4.5.1.2 Yttrium (Y)

Fundamental parameters measurements were also conducted on 25 μm high-purity yttrium foil (product number Y-00-FL-000100) with a purity of 99.0 %. Yttrium is a rare-earth metal and is difficult to separate from other rare-earth elements, that is why Nb and Ce may appear as noticeable impurities. Despite being a rare earth metal with more limited applications compared to iron, yttrium's unique properties make it a valuable element in various domains [144, 145], including electronics and materials science. The sample density is 4.472 g/cm^3 at 20°C, providing an interesting contrast to the iron sample. Repetitive measurements were taken on the mass leading to an average mass value of 12.88 mg while the surface area was determined to be 106.55 mm^2.

4.5.2 Mass attenuation coefficients

4.5.2.1 Measurement of mass attenuation coefficients

The mass attenuation coefficient is the probability of interaction of a photon beam with matter, which depends on both material and photon energy. The mass attenuation coefficient can be obtained from the mass per unit area $\frac{A}{M}$ of the target sample, using Beer-Lambert law introduced in Chapter 1, Section 1.2 as:

$$\frac{\mu}{\rho} = -\frac{1}{\rho \times x} \times \ln\left(\frac{I_t}{I_0}\right) = -\frac{A}{M} \times \ln\left(\frac{I_t}{I_0}\right), \tag{4.42}$$

where, I_0 and I_t represent the incident and the transmitted intensity respectively, μ is the linear attenuation coefficient and A and M are the surface area and the total mass of the sample.
To determine the absolute mass attenuation coefficients of thin films, measurements were carried out using transmission method on the X-UV and the hard X-ray branches of the SOLEIL *MÉTROLOGIE* beamline with monochromatic radiation of low divergence. In transmission mode, monochromatic X-ray beam radiation was directed through the material, under normal incidence, and the intensity of the radiation was measured both before and after passing through the sample (Figure 4.9) sequentially. The direct and transmitted photon intensities were recorded by means of an AXUV:Al photodiode whose dark noise was subtracted from all acquired current values to derive an unbiased transmittance. The ratio of the two intensities, i.e., the transmission, is then used to calculate the mass attenuation coefficient of the material as a function of the incident energy. Changing the incident energy is accomplished using a double Si(111) crystal monochromator when working on the hard X-rays branch, or using a diffraction grating when working on the X-UV branch.

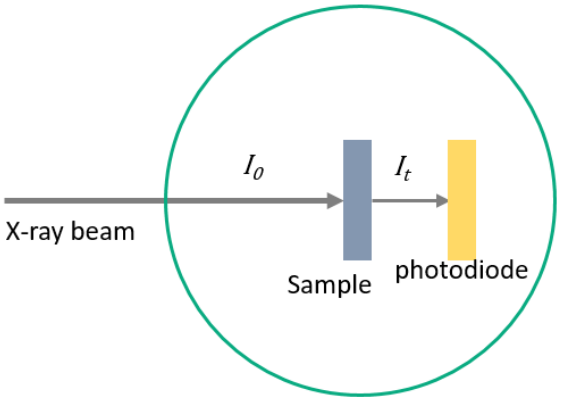

Figure 4.9: A schematic of a transmission measurement for the calculation of the mass attenuation coefficient.

4.5.2.2 Uncertainties on the mass attenuation coefficients measurements

According to the criterion of Nordfors *et al.* [146], the best possible uncertainty budget associated to the transmission measurement is achieved when the sample thickness satisfies $2 \leq \ln(\frac{I_0}{I_t}) \leq 4$. To best meet this criterion, several thicknesses are used during the experiments. In general, sample thicknesses must be within the range of several micrometers or less, particularly when working with soft X-rays. This is due to the fact that the extent of X-ray absorption is determined by the thickness of the sample. The uncertainty budget is a comprehensive analysis of the different sources of uncertainty that affect the mass attenuation coefficients measurement. It includes contributions from both statistical and systematic sources of uncertainty, such as measurement errors, sample preparation, and instrument calibration. The uncertainty contributions were estimated as in the paper of *Menesguen et al.* [80] where several experiments and simulations were conducted.

The relative uncertainty of the transmittance measurement is determined as the standard deviation arising from the measurements and a smoothed transmittance curve. Including the uncertainty due to the elemental purity, Equation 4.42 becomes:

$$\frac{\mu}{\rho} = -\frac{1}{\rho \times x} \times \ln\left(\frac{I_t}{I_0}\right) \times k_p = -\frac{A}{M} \times \ln\left(\frac{I_t}{I_0}\right) k_p \tag{4.43}$$

where k_p is the the correction factor responsible for an additional uncertainty due to the elemental purity. In order to calculate the uncertainty associated with the experimentally determined mass attenuation coefficients, a general equation must reflect the contribution of all parameters that could potentially influence the measurement, following the guidelines provided in the 'Guide to the expression of uncertainty in measurement' [147]. The uncertainty budget can be expressed as follows:

$$\left(\frac{u\left(\frac{\mu}{\rho}\right)}{\frac{\mu}{\rho}}\right)^2 = \left(\frac{u\left(M\right)}{M}\right)^2 + \left(\frac{u\left(A\right)}{A}\right)^2 + \frac{\left(\frac{u(T)}{T}\right)^2}{\ln\left(T\right)^2} + \left(\frac{u\left(k_p\right)}{k_p}\right)^2. \tag{4.44}$$

This expression implies that uncertainties intrinsically connected to transmission measurements are presenting the smallest uncertainties in relation to the mass attenuation coefficients, and these cannot be further minimized. Overall, the uncertainty budget provided a quantitative measure of the reliability of the mass attenuation coefficient measurement and helped to identify the most significant sources of uncertainty.

4.5.2.3 Iron mass attenuation coefficients

The transmission of the iron sample was measured between 0.6 keV to 27 keV with variable energy steps down to 1 eV close to the absorption edges. From this experimental measurement, the energy-dependent mass attenuation coefficients were determined, covering both the K- and L- absorption edges.

Table 4.1: Relative uncertainty contributions to the total uncertainty budget of iron.

Contribution	Iron (%)
Mass	0.05
Area	0.016
Sample purity	0.006
Transmittance	0.0014
Energy calibration	0.0004

The uncertainty on the mass attenuation coefficient measurement was calculated including all the contributions detailed in Table 4.1 using Equation 4.44. The result of the mass attenuation coefficients with the associated uncertainty is presented in Figure 4.10 (left). This result presents high precision mass attenuation coefficient measurements for Fe, with relative standard uncertainties ranging between 0.8 % and 2 %. This demonstrates the application of reliable methodologies and precision calibrations throughout the experimental procedure.
The experimental data were compared with the XCOM database values from the National Institute of Standards and Technology [148] for energy range between 1 keV and 100 keV. This

comparison aims to provide an additional perspective on the estimated uncertainties associated with instrumental and experimental contributions cited in Table 4.1. Given that the mass attenuation coefficients were not assessed at the same photon energies in the database, an interpolation method was applied to the dataset. This was aligned with the energy points of the measurement to introduce the least possible bias from the interpolation method. Figure 4.10 (right), presents the relative differences between the new measurements and the reference values from XCOM NIST between 1 keV and 27 keV, calculated as:

$$\frac{\Delta\mu}{\mu} = \frac{\mu_{Exp} - \mu_{XCOM}}{\mu_{XCOM}} \times 100\,, \tag{4.45}$$

where μ_{Exp} represents the measured mass attenuation coefficients and μ_{XCOM} represents the values from the XCOM database.

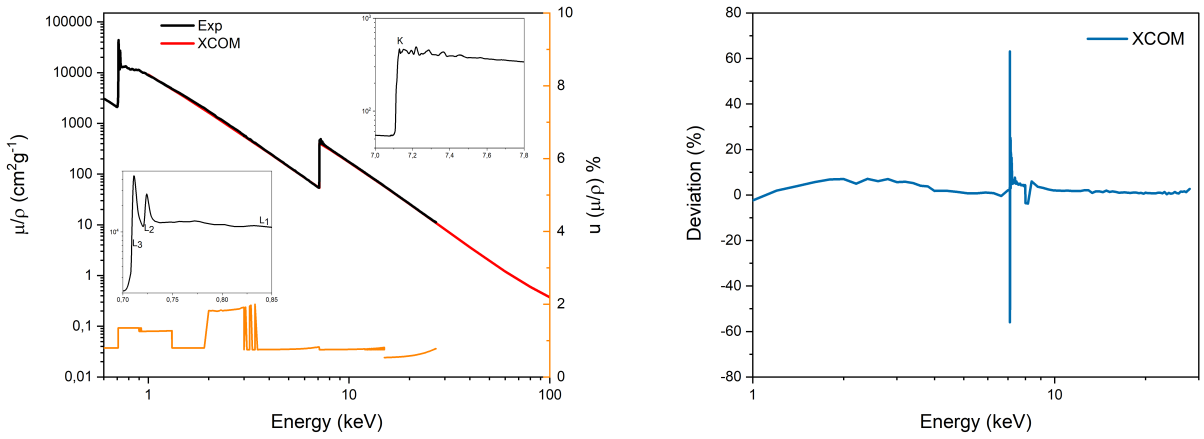

Figure 4.10: (Left) mass attenuation coefficients of iron measured around the K- and L- absorption edges (black) and XCOM reference values around K- absorption edge (red). The lower data points (orange) represent the relative standard uncertainties. The inset graphs are details of the mass attenuation coefficients of iron around the K- and L- absorption edges. (Right) comparison of the experimental values with the XCOM database.

The deviation around the K-absorption edge of Fe (6 keV-8 keV) is considerable, reaching up to 63 %. This significant relative difference observed near the K- edges is mostly due to the fine structures observed in the measurements which are not considered in the literature. At lower photon energies, no significant deviations were observed when compared with the XCOM data.

4.5.2.4 Yttrium mass attenuation coefficients

The transmission of the yttrium sample was evaluated within the energy range of 3 keV to 35 keV with energy steps of 50 eV at largest with closer values at the K- absorption edge. Based on these measurements, the energy-dependent mass attenuation coefficient was deduced, covering only the K-absorption edge. The uncertainty of the mass attenuation coefficients measurement was ascertained, incorporating all the contributions listed in Table 4.2, using Equation 4.44.

Table 4.2: Relative uncertainty contributions to the total uncertainty budget of yttrium.

Contribution	Yttrium (%)
Mass	0.05
Area	0.055
Sample purity	0.006
Transmittance	0.0014
Energy calibration	0.0004

The resulting mass attenuation coefficients, along with the associated uncertainties, illustrated in Figure 4.11 (left). The relative standard uncertainty range for these measurements is between 0.2 % and 0.7 %. The precision of the mass attenuation coefficient measurements for Y is remarkable, indicating the effective application of reliable techniques and accurate calibrations during the experimental process. As shown in Figure 4.11 (right), the measurements of the mass attenuation coefficient for yttrium, displayed a low deviation when compared with XCOM data, indicative of a largely consistent experimental setup and reliable results. As for iron, a noticeable increase in deviation for yttrium was observed around the K-absorption edge reaching a maximum of ∼18 %. This is also attributed to the fine structures observed in our measurements which are not accounted for in the literature.

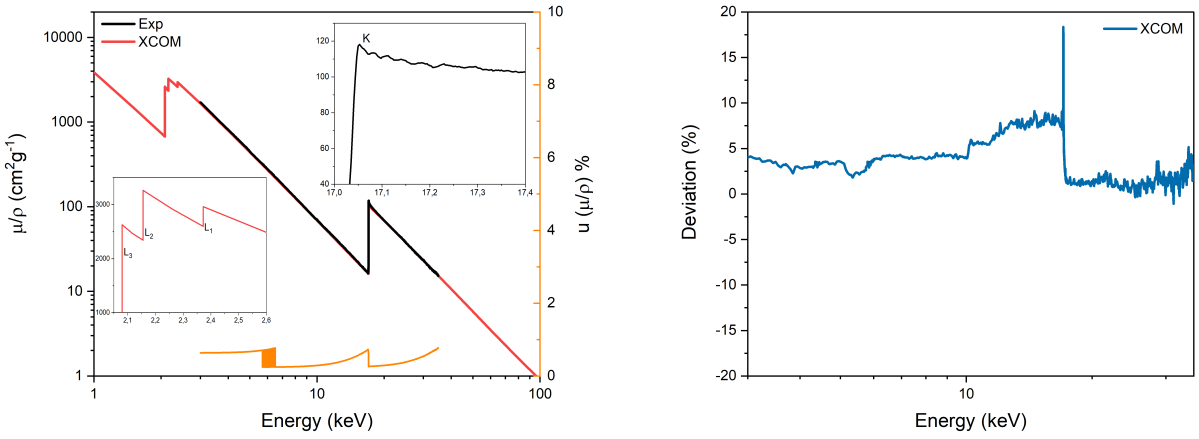

Figure 4.11: (Left) mass attenuation coefficients of yttrium measured around K- absorption edge (black) and XCOM reference values around K- and L- absorption edges (red). The lower data points (orange) represent the relative standard uncertainties. The inset graphs are details of the mass attenuation coefficients of yttrium around the K- and L- absorption edges. (Right) comparison of the experimental values with the XCOM database.

4.5.3 Photoelectric absorption coefficients

The photoelectric absorption coefficient is defined as the probability of the photoelectric effect (photoabsorption) in which an incident photon is absorbed by an electron in a specific shell of the atom causing its ejection. However, these quantities cannot be measured directly from an experiment, instead they can be deduced from the measurement of the mass attenuation coefficient, which includes contributions from the photoelectric effect, Compton and Rayleigh scattering, and pair production [149]. To calculate the photoelectric absorption coefficients for

both L- and K- lines, we used a method based on linear extrapolation of the mass attenuation coefficient for energies below their respective absorption edges. In the case of L-lines, the photoelectric absorption coefficient is computed as the difference between the overall mass attenuation coefficient (μ) and the summed contributions from incoherent scattering (μ_{Compton}), coherent scattering (μ_{Rayleigh}), and the photoelectric absorption coefficients of the M and N shells (τ_{MN}) as [137]:

$$\tau_L = \mu - \mu_{\text{Compton}} - \mu_{\text{Rayleigh}} - \tau_{MN} \,. \tag{4.46}$$

For the K lines, the photoelectric absorption coefficient is evaluated as the difference between the total mass attenuation coefficient (μ) and the summed contributions from incoherent scattering (μ_{Compton}), coherent scattering (μ_{Rayleigh}), and the photoelectric absorption coefficients of the L, M, and N shells (τ_{LMN}) as:

$$\tau_K = \mu - \mu_{\text{Compton}} - \mu_{\text{Rayleigh}} - \tau_{LMN} \,, \tag{4.47}$$

In both cases, the linear extrapolation of the mass attenuation coefficient for energies lower than the absorption edges effectively accounts for the coherent and incoherent scattering and lower shells photoelectric absorption coefficient. Consequently, the photoelectric absorption coefficient as a function of the energy can be derived from these extrapolation values by subtracting them from the mass attenuation coefficients.

4.5.3.1 Iron photoelectric absorption coefficients

The photoelectric absorption coefficient of the K-lines of iron was calculated employing the extrapolation method, for energies higher than the absorption edge, specifically between 8 keV and 27 keV. To evaluate the precision the results, a comparative analysis was conducted with data obtained from the Xraylib library [150].

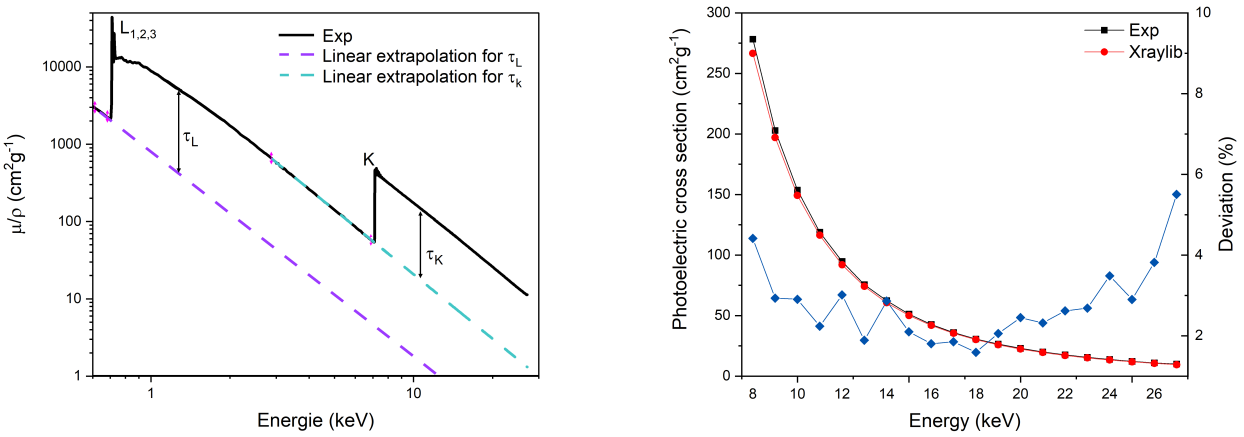

Figure 4.12: (Left) mass attenuation coefficients and linear extrapolations for L- (purple) and K- (green) lines of iron. (Right) comparative analysis of the calculated K- lines photoelectric absorption coefficient (black) with Xraylib reference data (red) and the energy-dependent deviation (blue).

Figure 4.12 (left) illustrates the mass attenuation coefficients, with the linear extrapolations for the calculation of the photoelectric absorption coefficient for both L and K-lines and on the right, a comparison between the calculated photoelectric absorption coefficient for K-lines and the Xraylib data. To provide a quantitative analysis of the accuracy between experimental values and reference data, we calculated the deviation between the two datasets (Figure 4.12 on the right).
The analysis of the data reveals that the relative deviation is relatively low, ranging between approximately 1.6 % and 5.5 %. The deviation starts at 4.4 % at 8 keV and decreases, decreases to around 1.6 % at 18 keV, and then increases to 5.5 % at 27 keV. The calculated values are generally in good agreement with the Xraylib reference data [150], particularly in the middle of the energy range, where the deviation is the smallest. However, the increase in the relative deviation at higher energies implies that there may be factors affecting the accuracy of the calculated photoabsorption coefficients, especially at energies greater than 20 keV, such as experimental conditions or limitations in the extrapolation.

4.5.3.2 Yttrium photoelectric absorption coefficients

Here we present the analysis of the photoelectric absorption coefficient for the K-lines of yttrium, over an energy range from 17.5 keV to 30 keV, and the comparison with Xraylib reference data. Figure 4.13 shows the linear extrapolation of the mass attenuation coefficient and the calculation of the photoelectric absorption coefficients compared with the Xraylib reference data.

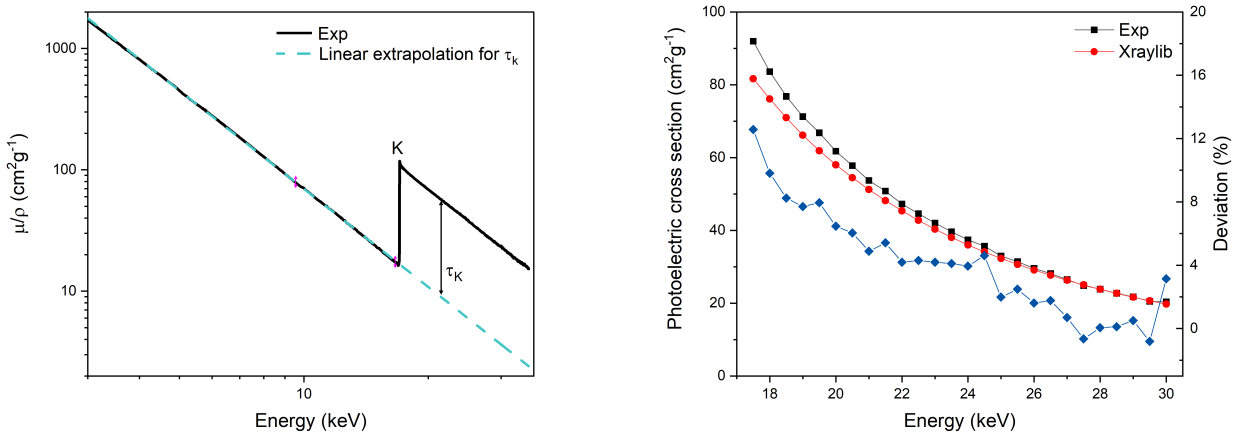

Figure 4.13: (Left) mass attenuation coefficients and linear extrapolations for K- lines (green) of Y. (Right) comparative analysis of calculated K- lines photoelectric absorption coefficient (black) with Xraylib reference data (red) and the energy-dependent deviation (blue).

The relative deviation begins at relatively high value of approximately 12.6 % at 17.5 keV, and decreases as the energy increases. Above approximately 21 keV, the deviation fluctuates with minor increases and decreases. The deviation reaches its lowest value of approximately -0.8 % at 29.5 keV, showing that at this energy point, the calculated value slightly exceeded the reference data. Towards the higher end of the energy range, at 30 keV, the deviation increases again to about 3.1 %. This variation in deviation indicates that the agreement between the calculated photoelectric absorption coefficients and Xraylib data varies across the energy range.

The fluctuation of the deviations, particularly in the higher energy range, may be indicative of complexities in the interactions of the X-rays with yttrium, potentially arising from impurities, or could be due to the experimental conditions and calculations made during the linear extrapolation process. The deviations remain within a relatively small range, demonstrating an overall agreement with the reference data.
Comparing the deviations observed for iron and yttrium, it is noticeable that iron exhibits more consistent and smaller deviations. The reasons for the increased differences observed in yttrium, may be attributed to the photon flux coming from the synchrotron, which decreases at higher energies. The reduction in photon flux can affect the signal, particularly at higher energies, which can consequently impact the precision of the measurements.

4.5.4 Fluorescence Yields

4.5.4.1 Fluorescence yield measurements

The fluorescence yields measurements were performed on the *MÉTROLOGIE* beamline at the hard X-rays branch using monochromatic X-rays in the 3 keV to 30 keV energy range. Only the fluorescence yield of K-lines was measured, as it is difficult to measure the fluorescence yield of the L- lines under the experimental conditions used. Here, the target sample is placed in the path of the monochromatic beam with energy E_0 and intensity I_0. The incident beam irradiates the sample at an angle of incidence θ, and the emitted fluorescence radiation is detected at an angle φ. The incident beam is attenuated according to the linear attenuation coefficient at the specific energy $\mu(E_0)$. It interacts with the target material at a depth x by photoelectric effect in the K-shell, with the probability τ_K, the K-photoelectric absorption coefficient. Characteristic X-rays are emitted with energy $E_{\alpha,\beta}$ in all directions according to the partial fluorescence yield. The samples were positioned in the conventional 45° - 45° geometry, oriented vertically, to make use of the linear polarization of the excitation radiation and reduce the impact of scattered photons in the spectrum. The center of the sample is aligned with respect to the incident beam using translation stages. The emitted fluorescence radiation is detected with a solid angle Ω using the SDD, while the transmitted beam is detected at the same time with a calibrated photodiode as illustrated in Figure 4.14.

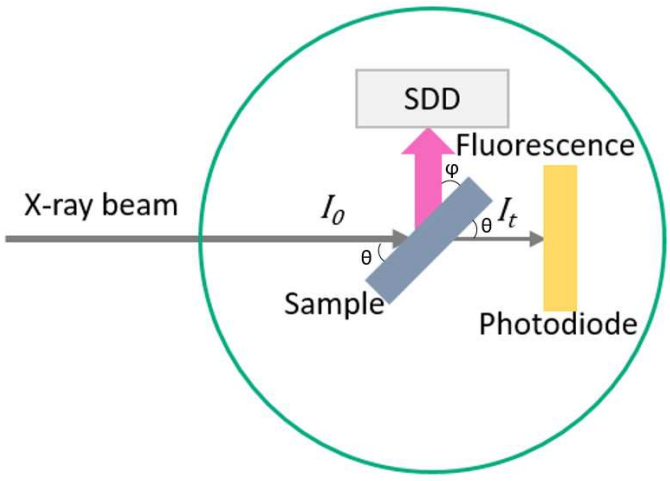

Figure 4.14: A schematic of the fluorescence yield measurement.

The fluorescence yield is related to the fluorescence and emitted intensities as:

$$\begin{aligned}\frac{I_{K_{\alpha,\beta}}}{\eta_{K_{\alpha,\beta}}} = & \int_0^1 \frac{\Omega}{4\pi} I_0 \exp\left(-\mu_0 \cdot \frac{M}{A} \cdot \frac{z}{\sin(\theta)}\right) \cdot \\ & \tau_0 \cdot \omega_{k_{\alpha,\beta}} \exp\left(-\mu_{K_{\alpha,\beta}} \cdot \frac{M}{A} \cdot \frac{z}{\sin(\varphi)}\right) \cdot \frac{M}{A} \cdot \frac{z}{\sin(\theta)} dz.\end{aligned} \tag{4.48}$$

$I_{K_{\alpha,\beta}}$ represents the fluorescence intensity of $K_{\alpha,\beta}$ calculated as the net peak area of $K_{\alpha,\beta}$ over the acquisition time, $\eta_{K_{\alpha,\beta}}$ is the SDD efficiency at K_α and K_β energies, I_0 is the intensity of the incident beam, and $\mu_0 = \mu(E_0)$ and $\tau_0 = \tau_K(E_0)$ are the attenuation and photoelectric absorption coefficients respectively at the specific incident energy, $\mu_{K_{\alpha,\beta}}$ is the attenuation coefficient at K_α and K_β energies and $\omega_{k_{\alpha,\beta}}$ is the fluorescence yield at K_α and K_β energies. The transmitted intensity is related to the incident intensity at a specific angle using the Beer-Lambert law as:

$$I_t = I_0 \exp\left(-\mu_0 \cdot \frac{M}{A} \cdot \frac{z}{\sin(\theta)}\right), \tag{4.49}$$

where the transmitted intensity can be calculated from the measured intensity on the photodiode $I_{measured}$ at a specific incident energy as:

$$I_t(E_0) = \frac{I_{measured}(E_0)}{\eta_{ph}(E_0) \cdot E_0 \cdot q}. \tag{4.50}$$

wehre $\eta_{ph}(E_0)$ is the photodiode efficiency as a function of the incident energy and q is the electron charge. Finally, after computing the integral of Equation 4.48 in the 45° - 45° configuration, the fluorescence yield as a function of the incident energy can be expressed as:

$$\omega_{k_{\alpha,\beta}}(E) = \frac{I_{K_{\alpha,\beta}}}{I_t(E_0)} \cdot \frac{4\pi}{\Omega} \cdot \frac{1}{\tau_0} \cdot \frac{1}{\eta_{K_{\alpha,\beta}}} \cdot \frac{\left(\mu_0 + \mu_{K_{\alpha,\beta}}\right) \cdot \exp\left[-\mu_0 \frac{M}{A \cdot \sin(45)}\right]}{1 - \exp\left[-\frac{M}{A \cdot \sin(45)}\left(\mu_0 + \mu_{K_{\alpha,\beta}}\right)\right]}. \tag{4.51}$$

The evaluation of the uncertainties in the measured fluorescence yields necessitates the combination of uncertainties from various parameters, including the fluorescence intensity, the SDD efficiency, the intensity of the incident beam, the attenuation and the photoelectric absorption coefficients, the mass per unit area and the detection solid angle. To quantify the uncertainty in the fluorescence yield, the propagation of uncertainties through the uncertainties propagation equations can be employed. This involves derivatives of the fluorescence yield with respect to each parameter, and summing these, considering their uncertainties as:

$$u_c = \sqrt{\sum_{i=1}^{n} \left(\frac{\partial f}{\partial x_i}\right)^2 u^2(x_i)}, \tag{4.52}$$

where f is the fluorescence yield, x_i represents each of the parameters it depends on and $u(x_i)$ represents the standard uncertainty of each of the parameters. However, performing this calculation is complicated due to the large number of parameters involved and the lack of available data on the uncertainties for certain parameters as obtaining or measuring accurate uncertainties for these parameters can be difficult.

The fluorescence yield is a constant specific for each element; however, there may still be some subtle effects that can cause slight variations in the fluorescence yield with changing the incident energy, such as uncertainties in the experimental setup and changes in the ionization state of the atom and the excitation of inner-shell electrons. To ensure the reliability of the values obtained and the associated uncertainties, measurements of the fluorescence yields were repeated over a range of incident photon energies. In fact, when varying the incident energy, several parameters including the intensity of K_α and K_β peaks, the efficiency of both the photodiode and the SDD, the mass attenuation and photoabsorption coefficients change. Thus, obtaining a constant fluorescence yield for a given energy in spite of these changes indicates well controlled, experimental conditions, validating the accuracy and reliability of the results.

4.5.4.2 Result for iron (Fe)

The acquisitions were acquired over a range of incident photon energies between 7.5 keV and 15 keV with an incident energy step of 0.5 keV, for which the mass attenuation coefficients were previously measured. The spectra obtained were processed with COLEGRAM, using Voigt functions to calculate the surface area of the fluorescence peaks, with a Lorentzian widths of 1.6 eV and 2.42 eV for K_α and K_β respectively. An example of the spectrum measured at 10 keV is shown in Figure 4.15.

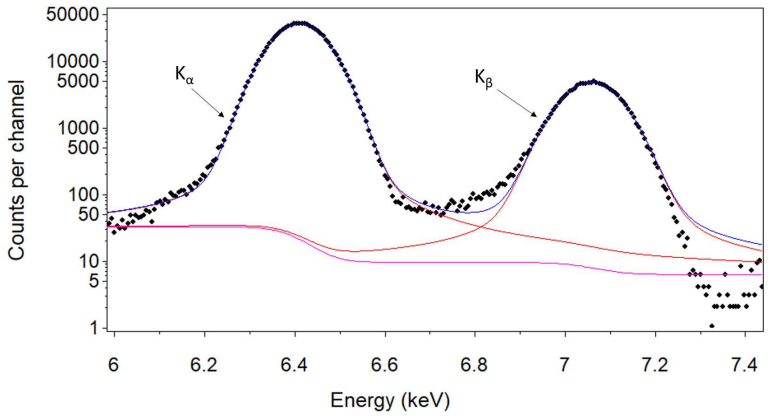

Figure 4.15: Example of an iron fluorescence spectrum measured at 10 keV and the processing with COLEGRAM using Voigt functions.

Figure 4.16 (left) shows all the results of the fluorescence yield measurements carried out, including the partial fluorescence yields ω_{K_α} and ω_{K_β} with an average value of 0.298 and 0.039 respectively. Additionally, Figure 4.16 presents the total fluorescence yield ω_K with an average value of 0.337, with an associated reproducibility uncertainty of 2.9 %. The uncertainty associated with ω_K is determined by performing a weighted averaging, employing the algorithm detailed in Browne *et al.* [151], taking into consideration the repetition of measurements at various energy levels. Figure 4.16 (right) shows the fluorescence yield measurement at the synchrotron SOLEIL obtained for iron and its comparison with other experimental and theoretical reference values extracted from the paper by Bambynek *et al.* [24]. The results present a relative difference of $\sim$ 0.6 % - 7.4 % when compared to the other values. Specifically, the difference between the fluorescence yield measured and the experimental values is between 1.5 % - 3 %,

indicating a degree of agreement with the experimental data of Bailey *et al.*[152], Rubinson *et al.* [153] and Bambynek *et al.* [154]. On the other hand, the difference between our measurements and the old theoretical values ranged from 2 % - 7.4 %, indicating some differences with the theoretical model of McGuire [155], Kostroun *et al.* (not puplished but it is mentioned in the paper) and Walters *et al.* [156]. In addition, our value closely aligns with the newest theoretical data, differing by only 0.6 % from the most recent value [157].

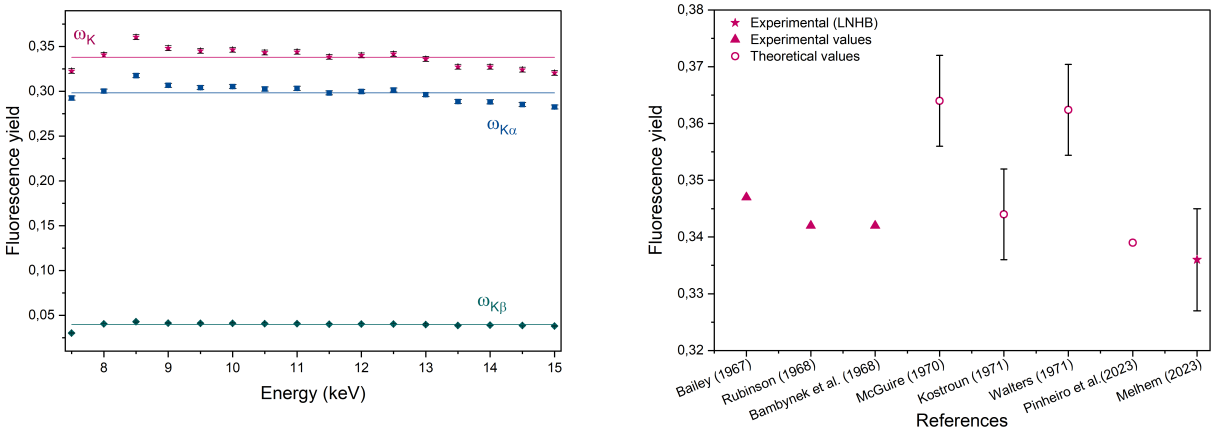

Figure 4.16: Partial and total fluorescence yields of the iron measured at different incident energies (left) and a comparison of Fe K-fluorescence yield with reference values (right).

These differences between our experimental measurements and the theoretical values could arise from various factors. The theoretical models are often based on approximations which may not take into account all the complex atomic effects. Additionally, the calibration of instruments, the quality of the samples, the measurement techniques and the fitting with COLEGRAM, could contribute to these differences. However, the closer agreement of our measurements with other experimental values strengthens the experimental measurement values and on the other hand, it emphasizes their importance for the validation of the theoretical models.

4.5.4.3 Result for yttrium (Y)

For the calculation of the fluorescence yield of yttrium, the attenuation and fluorescence intensities were measured as a function of the incident energy between 17.5 keV and 30 keV with a step size of 0.25 keV.

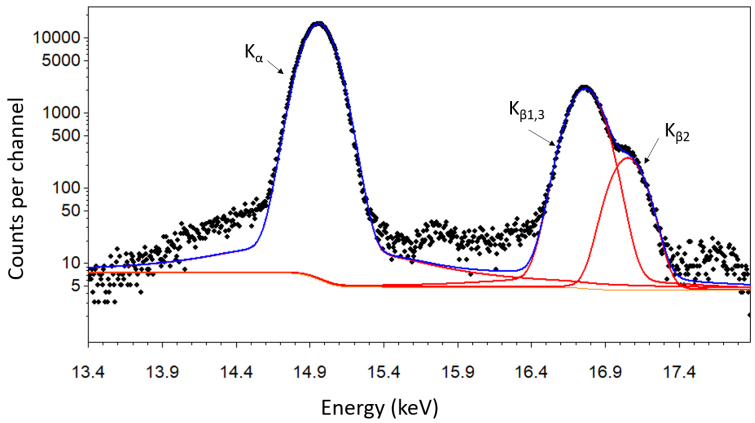

Figure 4.17: Example of Y fluorescence spectrum measured at 25 keV and the processing with COLEGRAM using Voigt functions. The peak at 15.7 represents the Fluorescence Yeild measurement K_α of zirconium Zr due to contamination.

Subsequently, the spectra were analyzed using COLEGRAM, employing Voigt functions with Lorentzian widths of 4.94 eV and 5.46 eV for K_α and K_β respectively. An example of the fluorescence spectrum of an yttrium sample measured at 25 keV is illustrated in Figure 4.17. Figure 4.18 (left) displays the partial fluorescence yields $\omega_{K\alpha}$ and $\omega_{K\beta}$ with the total fluorescence yield ω_K for the yttrium K-lines. The results obtained indicate that the fluorescence yield of yttrium exhibits fluctuations as a function of incident energy, specially at higher photon energies. This high fluctuation between 23 and 25 keV is due to the poor yield of the photodiode at these energies. The data present average values of approximately 0.577 for $\omega_{K\alpha}$, around 0.116 for $\omega_{K\beta}$, and around 0.693 for the total fluorescence yield of K-lines. The uncertainty in reproducibility associated with the total fluorescence yield calculated by performing a weighted averaging is 2.9 %.

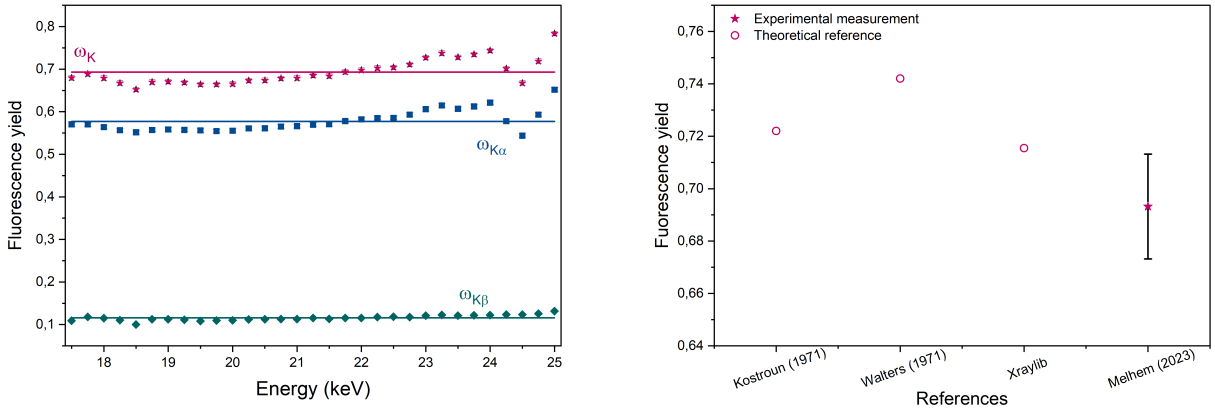

Figure 4.18: Partial and total fluorescence yields of yttrium measured at different incident energies (left) and a comparison of yttrium K- fluorescence yield with reference values (right).

The comparison of the measured fluorescence yield of yttrium with reference data is presented in Figure 4.18 (right). The values from Kostroun and Walters are higher at around 0.722 and 0.742 respectively, while the value from Xraylib is relatively close to our measurement at

approximately 0.7155. One possible explanation for the deviation in our result as compared to the reference data could be attributed to the poor yield of the photodiode, in addition to the decrease in the photon flux at high energies. This shows the importance of considering and accounting for the performance characteristics of measurement equipment, especially at higher energy ranges. Further investigation into the photodiode yield may be necessary to better understand these differences.

Chapter 5

Evaluation

5.1 Optimization procedure

For GIXRF, the optimization involves fitting a theoretical model to the experimental fluorescence intensities as a function of depth. This fitting is related to the elemental composition and density of the layers within the sample. The model parameters are then adjusted until a satisfactory match between the calculated and experimental data is obtained. Similarly, for the XRR, the optimization involves fitting a theoretical model to the experimentally obtained reflectivity curve, which includes the thickness, density and roughness of the layers within the sample. By combining these two methodologies, the characterization of nanometer layers and depth profiles becomes more precise, eliminating any uncertain results (local minima in the optimization procedure). This leads to improved accuracy in determining the thickness, roughness, density, and elemental composition of each layer in a sample.
To obtain an appropriate model, a prior knowledge about the sample structure is necessary for the optimization procedure using combined GIXRF-XRR. This prior knowledge can come from the manufacturer data or from other analytical techniques. Without a prior knowledge, the optimization procedure may not converge to a unique solution or may result in physically unrealistic values for the sample structure parameters. The quality of the data and the appropriateness of the chosen theoretical model are critical factors that affect the accuracy and precision of the final results. Therefore, having a good understanding of the sample structure before attempting to calculate it using GIXRF and XRR is essential to ensure a successful optimization procedure.
The combined optimization procedure for GIXRF and XRR can be a complex and challenging task due to the large number of fitting parameters involved. This requires a careful consideration of many factors and additional constraints or assumptions to be placed on the model parameters. Another factor that complicates the optimization procedure is the uncertainty and error associated with each measurement. GIXRF and XRR data are subject to various sources of noise and uncertainties, including instrumental noise and counting statistics. These uncertainties must be carefully considered in the optimization procedure otherwise, unrealistic values for the model parameters can be obtained. Furthermore, the optimization procedure may require the preliminary use of specialized software and algorithms to efficiently define the parameter space and find the optimal solution.
This section aims to provide a detailed explanation of the optimization procedure involved in GIXRF and XRR analysis. The procedure includes several steps, such as using software to

extract the GIXRF data from the XRF measured spectra, fitting the reflectivity alone initially, then performing the combined fitting to obtain more accurate and precise results.

5.1.1 XRF fitting with COLEGRAM

COLEGRAM [158] is a versatile and freely available software designed for the analysis of ionizing radiation spectra, including alpha, beta, gamma, and X-ray spectra. The software developed at LNHB offers twenty-eight distinct peak shapes to accurately process complex spectra using a non-linear least-squares fitting method [159]. COLEGRAM provides a range of optimization cost functions to perform mathematical adjustments. These functions can be easily accessed through an intuitive interface. Additionally, COLEGRAM supports batch processing of multiple spectra, which enables the replication of fitted peak information based on a predefined model. The typical spectra being studied have overlapping peaks on a continuous background. To determine the position and area of each peak, the software proposes three options for the cost-function (i.e. a difference between the calculated function and the actual experimental values) to minimize: the least squares, χ^2 criterion, and Poisson.
The approach for XRF fitting in this study involves a simple minimization of least squares without considering any weighting of the experimental data (standard deviation of experimental value $\sigma_i = 1$). The minimization function in the case is expressed as:

$$\Phi = \sum_{i=0}^{n} [f(x_i, \overrightarrow{a}) - y_i]^2 \tag{5.1}$$

where n is the number experimental data points, $f(x_i, \overrightarrow{a})$ is the computed values of the function, $\overrightarrow{a} = a_0, a_1, ..., a_m$ is the the optimum set of m parameters and y_i represents the experimental values. The process of obtaining the peak parameter values involves minimizing Φ by setting the partial derivatives to zero. This minimization is carried out using the Levenberg-Marquardt algorithm, which uses two fitting approaches. At the beginning, far from the minimum, the algorithm uses the gradient method. As it approaches the minimum, the gradient method is replaced by an approximation of the Hessian method, which only involves first derivatives.
The fitting procedure begins by defining a "Region Of Interest" (ROI) containing one or multiple peak(s) whose area calculation is desired. The ROI is the red region selected in Figure 5.1 on the top. To adjust the channel contents, various peak types can be selected from the list presented on the left, based on the origin of radiation (photon X, α, β, γ, ...). The X-ray fluorescence peak in this study are fitted with Gaussian function as follows:

$$G(E) = \frac{A}{\sigma\sqrt{2\pi}} e^{\frac{-(E-E_0)^2}{2\sigma^2}} . \tag{5.2}$$

where the peak is characterized by the centroid position E_0, the Gaussian amplitude A, and the standard deviation σ evaluated from the peak full width at half maximum. The peak area is then expressed as:

$$S(E) = \sqrt{2\pi}\sigma A . \tag{5.3}$$

The uncertainties on the fitting of peak areas are calculated using the standard uncertainties u_σ and u_A and covariance between the parameters ($cov(A, \sigma)$), obtained during the fitting

process. These uncertainties are then propagated through the peak area expression to derive the combined uncertainty, as the Guide to the Expression of Uncertainty in Measurement [147]. Thus the associated combined uncertainty for a Gaussian function is:

$$U = \sqrt{2\pi \left[(A \times u_\sigma) + (\sigma \times u_A) + A \times \sigma \times cov\,(A, \sigma) \right]} \tag{5.4}$$

which represents only the uncertainty of the adjustment. In a comprehensive analysis, statistical uncertainty should also be taken into account. In addition, removing the background from X-ray spectra is essential to allow more accurate analysis of the peak intensities. The presence of background noise can obscure these peaks and make it difficult to determine their true characteristics. To effectively remove the background, various models can be employed. One approach is to use linear or polynomial functions, but these methods lack a direct connection to the underlying physics. A more effective solution is provided by COLEGRAM algorithm, which integrates over the region of interest (ROI) channels and accounts for the physical presence of the peak. The background subtraction by COLEGRAM algorithm is displayed as a pink line in the ROI window located in the middle of Figure 5.1 on the left.

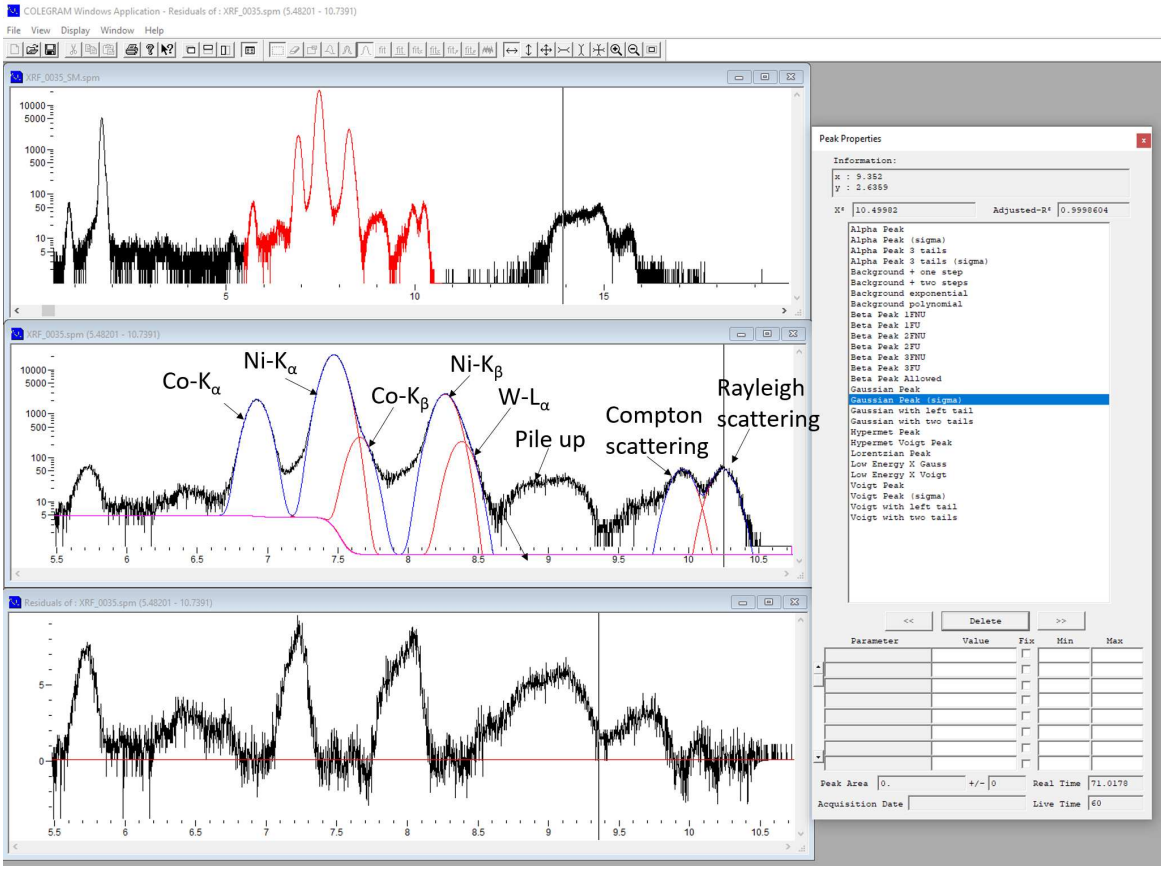

Figure 5.1: COLEGRAM user-friendly interface. The left panel shows the whole spectrum of NiCoW sample (on the top), a selected ROI (in the middle) and the residuals of the fitting (on the bottom). The right "Peak Properties" floating window showing the peak parameters of all selected peak in the ROI.

In the process of measuring X-ray spectrum using an SDD, overlapping peaks are often encountered, which pose a challenge in accurately distinguishing closely situated spectral lines.

However, the hidden spectral lines can be considered by fixing their amplitude and/or position as shown in the middle of Figure 5.1 on the left. Finally, a batch fitting for all spectra recorded in a GIXRF measurement is obtained by using all the defined peaks and associated free parameters or constraints as inputs. The result of this processing contains the net areas of all defined peaks, their energy positions and their uncertainties as a function of the angle of incidence as illustrated in e.g., Figure 4.7.

5.1.2 Optimizing the model structure with the XRR

As mentioned previously, from X-ray reflectivity data, information about the sample structure can be obtained. Therefore, before performing a combined analysis, it is often useful to start by fitting the reflectivity data to obtain a key insight into the sample structure such as layer thickness, interface roughness, density. Fitting the reflectivity data independently is simpler than combined XRR-GIXRF analysis, as it involves fewer parameters and avoids the complexities arising from interactions between the two techniques.
The Interactive Multi-layer Design (IMD) software [160] has been employed for the initial analysis of reflectivity data. IMD software is a powerful and versatile tool for modeling and analyzing thin film structures using X-ray and neutron reflectivity data. It offers a user-friendly interface for simulation and fitting reflectivity data for multi-layer samples, providing information about its structure.
The primary goal in the fitting procedure is to find the multilayer thin-film structure that best matches the experimental X-ray reflectivity data. To achieve this, the software iteratively adjusts the model parameters, seeking to minimize the figure of merit (FOM) defined as a quantitative measurement of the differences between the experimental data and the model's predictions. The fitting procedure starts with an initial model, which is a reasonable approximation of the sample's structure. From this starting point, the genetic algorithm Binda is used to generate a population of candidate solutions, each representing a unique combination of model parameters. These candidates undergo a process of selection, crossover, and mutation to generate successive generations of solutions with progressively improved FOM values. In case of genetic algorithm, the FOM is calculated as [161]:

$$FOM = \frac{\sum_{i=1}^{N_{mo}} w(i) \times [XRR(i) - XRR_{mo}(i)]^n}{\sum_{i=1}^{N_{mo}} w(i)} \tag{5.5}$$

where $w(i)$ are the weighting factors for each point, $XRR(i)$ and $XRR_{mo}(i)$ are the experimental and the model data , N_{mo} is the number of data points and n is a parameter that can be defined ($n = 2$ generally).
However, the fitting process can sometimes yield non-realistic or incorrect values, revealing the necessity of applying constraints to ensure the accuracy and physical relevance of the resulting structure parameters. By applying constraints on model parameters, such as limiting the minimum and maximum values of the fitted parameters, the fitting process ensures that the algorithm explores realistic values reflecting the true sample structure. These constraints prevent the algorithm from converging on solutions that may exhibit a low FOM but are not physically reasonable. In addition, applying constraints serves to address the issue of non-uniqueness, which occurs when multiple solutions result in similar FOM values, resulting in the same reflectivity curve. By narrowing down the parameters search space, the reliability and interpretability of the fitting results can be improved.

For accurate optimizing process, it is essential to understand how changes in the sample structure influence the XRR curve. Investigating the effects of varying the thickness, roughness, density and number of layers allows for the determination of suitable parameter values and constraints that yield the best fit between the model XRR and the experimental data. The effect of changing the sample structure parameters is presented in Figure 5.2.

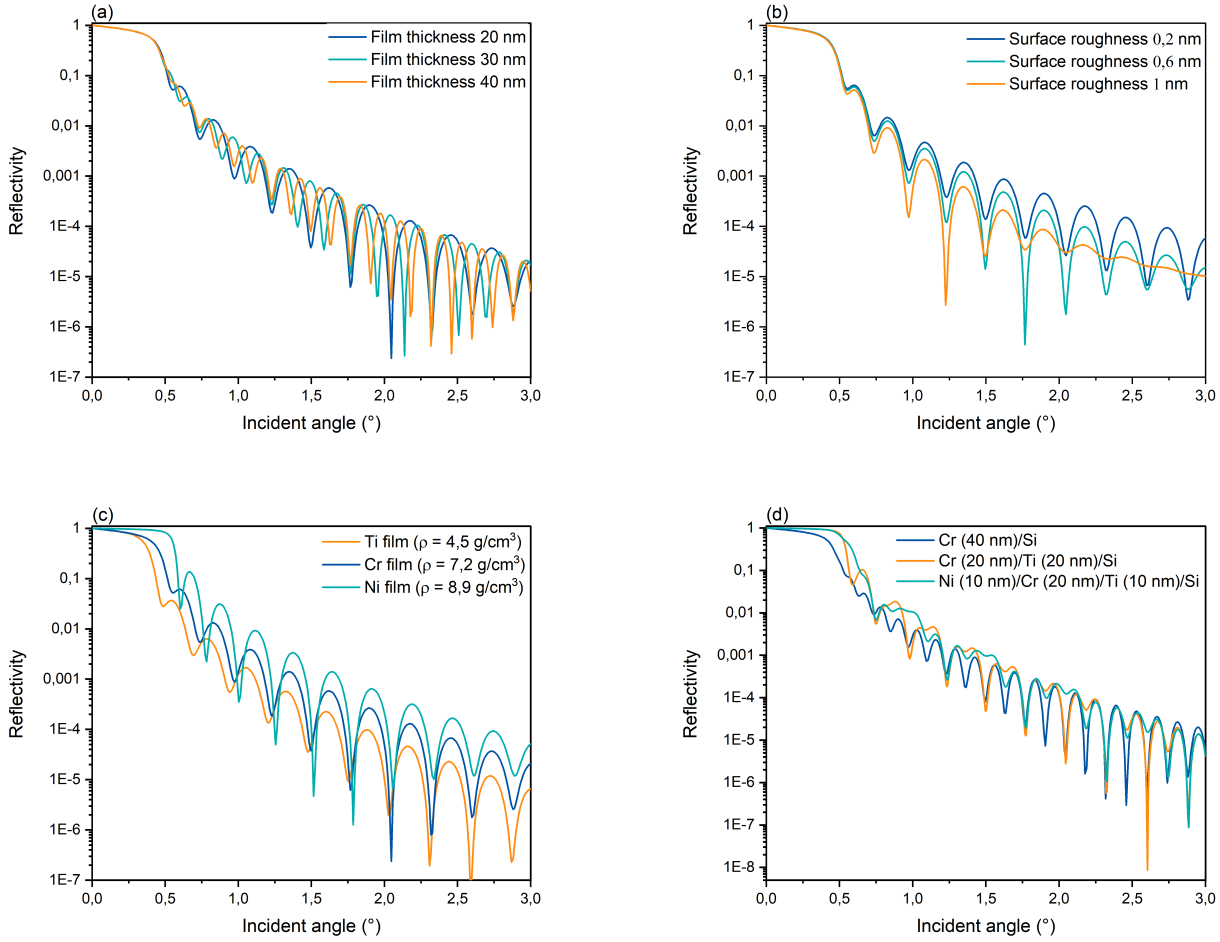

Figure 5.2: X-ray reflectivity curves by changing the sample structure parameters. (a): XRR curves of Cr films with different thicknesses deposited on Si substrate. (b): XRR curves of 20 nm of Cr with different interface roughnesses deposited on Si substrate. (c): XRR curves of 20 nm of Ti, Cr and Ni on Si substrate. (d): XRR of a monolayer sample of Cr (40 nm)/ Si, a bilayer sample of Cr (40 nm)/ Ti (40 nm)/ Si and a multilayer sample of Ni (10 nm)/ Cr (20 nm)/ Ti (10 nm)/ Si.

Figure 5.2 (a) illustrates this effect, showing simulated reflectivity patterns at 6.25 keV for 20 nm, 30 nm and 40 nm of chromium deposited on Si substrates. As shown, thicker layers typically result in narrower Kiessig fringes in the reflectivity curve, as a consequence of increased constructive and destructive interference between X-rays reflected from the film's surface and its underlying substrate. The spacing of these fringes is inversely proportional to the film thickness [103], meaning that as the thickness increases, the fringes become more closely spaced. In addition, the amplitude of the fringes tends to decrease with increasing the thickness, due

to factors such as increased absorption of X-rays within the film and reduced coherence of the X-ray beam.
In contrast Figure 5.2 (b) shows the impact of surface roughness on the reflectivity curve for 20 nm of chromium with different roughnesses (0.2 nm, 0.6 nm and 1 nm) deposited on Si substrates. As the surface roughness of the layer increases, the amplitude of the oscillations tends to decrease. This attenuation is a result of the scattering of X-rays by the rough surface, which leads to a reduction in the constructive and destructive interferences between X-rays reflected from the film surface and its underlying substrate [162]. Consequently, the reflectivity curve exhibits a lower difference between the maxima and minima of the fringes, making it more challenging to extract precise information about the film's properties.
Figure 5.2 (c) shows the reflectivity curves of three 20 nm thick layers with different densities deposited on Si substrates. By increasing the density of the thin film, the amplitude of Kiessig fringes increases. This is because a higher-density layer leads to a greater difference in electron density between the layer and the surrounding medium, resulting in stronger interference patterns in the XRR curve [163]. In addition, the positions of the fringes also shift due to changes in the refractive index of the layer as a function of its density leading to a change in the critical angle (angle at which the reflectivity starts to drop significantly from its maximum value).
Lastly, Figure 5.2 (d) illustrates the reflectivity curves for three samples with different number of layers: a monolayer sample of Cr (40 nm)/ Si, a bilayer sample of Cr (40 nm) / Ti (40 nm)/ Si and a multilayer sample of Ni (10 nm)/ Cr (20 nm) / Ti (10 nm)/ Si. As the total thicknesses of the three samples are identical, the reflectivity curve exhibits an equal number of oscillations. In addition, for the single-layer sample, the spacing and periodicity of the fringes remain constant as the incidence angle increases. On the contrary, for the samples containing two or more layers, these parameters vary. This is attributed to the alteration in density as the path length changes when the incidence angle increases, leading to a modified phase difference between the reflected X-rays.
In summary, understanding the effect of the sample structure changes on the reflectivity curve enables the optimization of the fitting process and the extraction of essential details regarding the properties of the thin films.

5.1.3 Combining the XRR with the GIXRF in the optimization

In order to set up the optimization technique, we first need to define the experimental setup parameters and the sample parameters. The optimization procedure should take into account the different dynamic ranges of the XRR and GIXRF responses. Consequently, GIXRF and XRR are calculated based on the experimental setup and the sample structure parameters. This section outlines the approach used for the optimization procedure of the combined GIXRF and XRR by the ELIXIR software, developed at LNHB. This state-of-the-art software includes all the required packages for both the calculation and optimization processes, using the experimental setup parameters, the sample parameter structure, and the experimental data. Initially, we focus on the key parameters that significantly influence the signal measurements, as well as the specific considerations needed for fitting the data generated from each technique. We examine geometrical factors such as the footprint of the incoming beam on the sample and the solid angle of detection. Subsequently, we present a comprehensive analysis of the optimization methodology used in the ELIXIR software which relies on the experimental data for XRR and GIXRF, along with the sample structure data acquired from IMD software, to accurately fit

the theoretical data with the experimental ones.
Through the comprehension and knowledge of these elements, the objective is to achieve an optimization process that maximizes the advantageous potential of the combination of XRR and GIXRF to find a precise and accurate model of the sample structure parameters.

5.1.3.1 Solid angle calculation

The solid angle of detection of the energy-dispersive spectrometer is an important parameter influencing the efficiency of the X-ray fluorescence measurement. Thus, in order to correctly model the sample in the fitting procedure, some geometrical aspects must be accurately taken into account. These include the footprint of the incoming beam on the sample and the solid angle of detection.
The shape and the size of the incoming beam on the sample is defined by a slit placed at 1 m ahead, vertically to limit the horizontal divergence on the sample. The use of a rectangular slit results in a rectangular-shaped beam impinging upon the sample. The footprint width is adjustable depending on the vertical aperture of another motorized slit in front of the rectangular one. The beam length is defined as:

$$L = \frac{S_h}{\sin(\theta)} \tag{5.6}$$

where S_h represents the slit horizontal width (0.1 mm). The incident flux can be adjusted by changing the height of the slit (up to 3 mm in height). In addition, other factors impact the solid angle of detection, such as the sample alignment, the geometrical characteristics of the detector and the length of the sample l_E, as illustrated in Figure 5.3. The solid angle as a function of the incidence angle is calculated as:

$$\Omega(\theta) = \frac{1}{A_S} \iint_{A_S} \Omega_r(r) \cdot \mathrm{d}x\mathrm{d}y\,, \tag{5.7}$$

where A_S is the beam footprint on the sample surface detected by the SDD, calculated as a function of the incidence angle, the slit dimensions and the samples length and $\Omega_r(r)$ is the solid angle as a function of the radial distance expressed as:

$$\Omega_r(r) = \int^{S(r)} \int \frac{\sin(\beta)}{(d_1 + e + d_2)^2 + (r + x)^2 + y^2} \mathrm{d}x\mathrm{d}y. \tag{5.8}$$

As shown in Figure 5.3, e and c represent the thickness and the aperture diameter of the collimator respectively, d_1 represents the distance between the sample and the collimator and d_2 is the distance between the collimator and the SDD silicon chip.

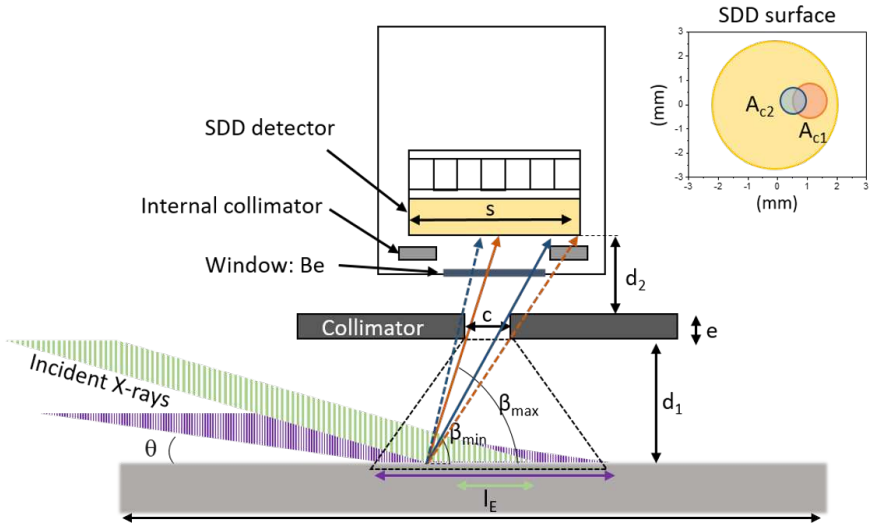

Figure 5.3: Schematic showing the geometric parameters of the EDS. e and c are the thickness and the aperture of the collimator, d_1 is the distance between the sample and the collimator, d_2 is the distance between the collimator and the SDD surface, s is the diameter of the SDD and l_E is the sample length. The green and the purple represent the incoming beam as the incident angle changes, showing the variation of the footprint size on the sample. The lines correspond to the front (orange) and back (blue) sides of the collimator and the dashed lines represent the rays that do not pass through the front (orange) and back (blue) sides of collimator.

The angle β is calculated as:

$$\beta = \arctan \frac{d_1 + d_2 + e}{\sqrt{(r+x)^2 + y^2}} \tag{5.9}$$

and the integral limit $S(r)$ is represented as the common region between the SDD active area A_{SDD} which depends on the SDD diameter s and the projected areas on the SDD surface of the front and back sides of the collimator respectively, A_{c1} and A_{c2} [164], and it can be expressed as:

$$S\,(r) = A_{SDD} \wedge A_{c1} \wedge A_{c2}\,. \tag{5.10}$$

5.1.3.2 Optimization procedure for ELIXIR software

As initial settings for the optimization technique, the experimental setup parameters and the sample parameters, must be defined. In the optimization procedure also, careful consideration should be given to the distinct dynamic ranges of the X-ray reflectometry (XRR) and the grazing incidence X-ray fluorescence (GIXRF) responses. These two techniques offer contrasting signal behaviors: the XRR, normalized to the incident photon flux, provides a signal range from 0 to 1, featuring significant variations across numerous logarithmic orders of magnitude. Contrarily, the GIXRF curves depict peak areas that span from hundreds to millions of counts, offering a substantially different set of characteristics. Given these difference in data characteristics, it is evident that using a uniform χ^2 function for both techniques in the optimization procedure might result in challenges. Specifically, the dominant influence of one experimental curve could overshadow the other, potentially leading to imbalances in the evaluation process. Therefore, it is essential to recognize and account for these differences when formulating optimization

strategies. To address these issues, GIXRF-XRR data are calculated and subsequently fitted to experimental data using ELIXIR. The specificity of this process relies on an adjustment of the model parameters using two distinct χ^2cost functions, specifically tailored to accommodate the different nature of reflectivity and fluorescence data. For reflectivity, data are multiplied by the incident angle to the power of 5 to simplify fitting. This step simplifies the fitting process and amplifies the impact of minor density fluctuations on the fit, hence enhancing the sensitivity and accuracy of the procedure [165]. Therefore, the cost function for reflectivity is expressed as follows:

$$Cost_{XRR} = \sum_{i=1}^{n} \frac{(\theta_i^5 \cdot \mathrm{e}^{XRR_{i,Th}} - \theta_i^5 \cdot \mathrm{e}^{XRR_{i,Exp}})^2}{\theta_i^5 \cdot \mathrm{e}^{XRR_{i,Th}}} \,. \tag{5.11}$$

For the fluorescence, a separate cost function is computed to adapt to the larger count ranges present in GIXRF data as:

$$Cost_{XRF} = \sum_{i=1}^{n} \frac{(XRF_{i,Th} - XRF_{i,Exp})^2}{XRF_{i,Th}} \cdot \frac{1}{\mathrm{Max}(XRF_{Th})} \,. \tag{5.12}$$

In these equations, n is the number of angular steps, $\mathrm{Max}\,(XRF_{i,Th})$ is the maximum calculated value of the XRF curve, $XRR_{i,Th}$, $XRR_{i,Exp}$, $XRF_{i,Th}$ and $XRF_{i,Exp}$ are the theoretical and the experimental values for the reflectivity and the fluorescence at each angle. Upon achieving the defined stopping criteria, the optimization procedure concludes, and the best fitting parameter set is determined. These parameters, refined through rigorous calculations and adjustments, represent an optimal fit between theoretical predictions and experimental data, thus providing a reliable model for further analysis and research. Afterwards, both are combined using a global cost function as:

$$Cost_{Global} = Cost_{XRR} + Cost_{XRF} \,. \tag{5.13}$$

This comprehensive approach ensures an accurate characterization of the sample, thereby contributing to the rigour and validity of the study. The schematic representation of this process is illustrated in Figure 5.4, providing a visual explanation to the optimization procedure.

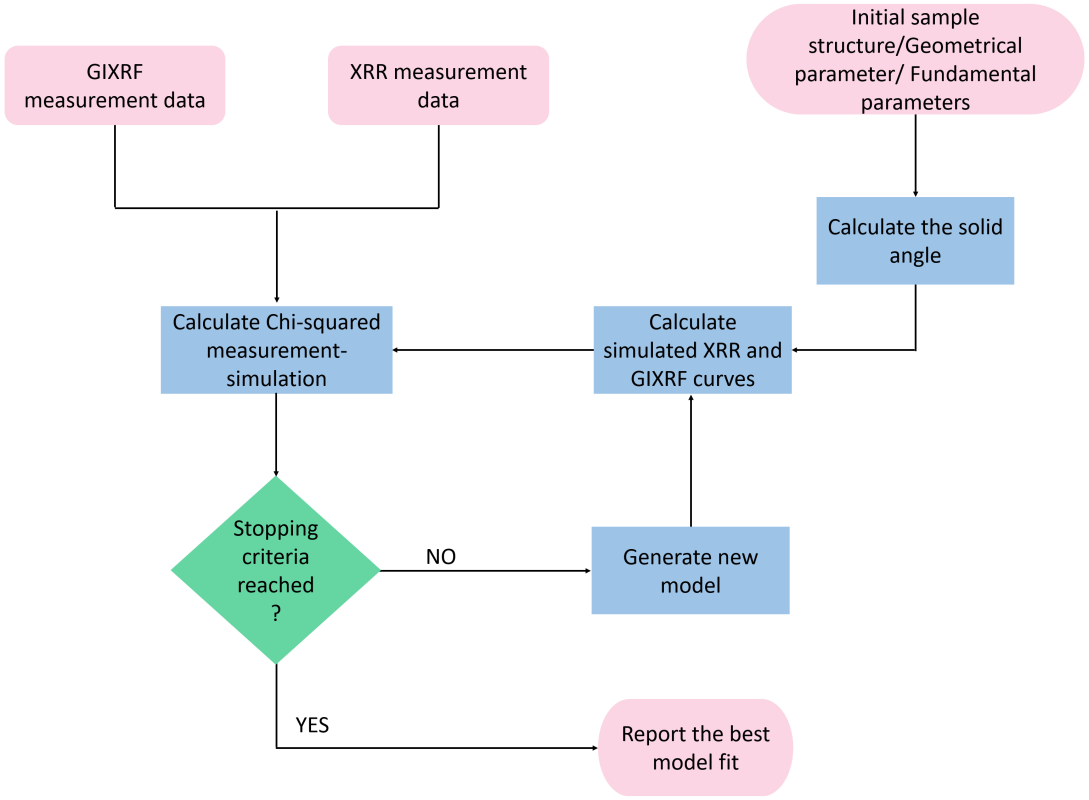

Figure 5.4: Flowchart of the optimization algorithm.

5.2 Uncertainty budget

To ensure accurate and reliable thin-film sample characterization using the combined GIXRF-XRR method, it is critical to consider the various sources of uncertainty that potentially influence the results. Uncertainties can arise from several aspects of our experimental and analytical processes, making it essential to account for them in both the methodology and conclusions. Uncertainties may be due to experimental factors such as X-ray beam quality, which impacts the photon flux intensity. This influence can introduce additional uncertainties, potentially impacting the XRR and GIXRF responses. Errors in the experimental setup arising from uncertainties in translation and rotation motors affect the sample alignment and the incident angle. Such errors can consequently impact the footprint of the incoming beam and the solid angle of detection. Additionally, uncertainties in the geometrical parameters of the energy-dispersive spectrometer can further influence the solid angle of detection. Moreover, uncertainties can result from the nature of the optimization procedure employed. Specifically, this type of uncertainty comes from the inherent variability when applying the differential method with χ^2 cost functions of reflectivity and fluorescence, and the resampling of XRR and GIXRF data at each incidence angle. Lastly, it is important to note that the fundamental parameters derived from the literature, namely mass attenuation coefficients, photoelectric absorption coefficient and fluorescence yields, are also affected by uncertainties.
This section will provide a comprehensive method for estimating and including the critical sources of uncertainty, particularly those associated with the solid angle of detection, fundamental parameters, and the uncertainties related to the optimization process.

5.2.1 Solid angle uncertainty

The objective of this section is to present a systematic method for calculating the uncertainty of the solid angle of detection in GIXRF measurements. The associated uncertainty is influenced by several parameters, including the accuracy of the sample alignment, uncertainty in the footprint position, and uncertainties related to the geometrical factors of the energy-dispersive spectrometer.
Ensuring accurate beam alignment in combined GIXRF-XRR measurements is crucial to guarantee the quality and reproducibility of the results. It helps to maximize the signal-to-noise ratio and ensures that precise and reliable measurements are obtained. The alignment procedure for the CASTOR setup entails a series of iterative steps, including aligning the rotation axis with the beam axis, followed by aligning the sample with the beam, as described in chapter 3. The uncertainty of the footprint position is related to the slit dimensions on the beamline and the angle of incidence. Including footprint uncertainty in the calculation of the solid angle of detection would require taking into account the uncertainties of the slit dimensions and the rotation axes.
In order to calculate the uncertainties on the solid angle of detection, it is necessary to consider the uncertainties on all the geometrical parameters of the spectrometer [147, 166]. However, in the present study, the focus has been narrowed to the uncertainty associated with the detector geometrical factors presented in Equation 5.8 by applying a probability distribution, detailed later, while the uncertainties related with the other parameters mentioned previously have not been considered. Initially, the distance d_1 ($\sim$13 mm) between the collimator and the samples is modeled using a uniform probability distribution, as the associated uncertainty is attributed to the resolution of the detector translation stage of 0.1 mm. Hence, the uncertainty of this parameter is calculated following GUM as:

$$U_i = \frac{a_i}{2\sqrt{3}} \tag{5.14}$$

where a_i is the resolution of the translation stage of the SDD.
Next, the aperture of the collimator c is measured with an uncertainty of 2 μm using a Quick Scope manual vision machine [167], while the uncertainty of the collimator thickness e is calculated by performing a series of repeated measurements with a Roch height gauge [168], taking into account its calibration uncertainty.
The nominal values of d_2 and s are provided by the SDD manufacturer. For these parameters, their probability distribution function is unknown, thus the description of the uncertainty is typically assumed to be a joint multi-variable normal distribution around the nominal values. These parameters were assigned an estimated uncertainty of 0.1 mm given by the manufacturer. The geometrical parameters, along with their uncertainties and probability distribution functions, are summarized in Table 5.1. Once all input parameters have been defined with their respective uncertainties, Monte Carlo simulations [169] are carried out for each to calculate the resulting uncertainties. This methodology is based on the principle of resampling the input parameters according to their probability distribution function, in this case, the geometrical parameters, in large quantities. This allows for the propagation of uncertainties to the output which, in our context, is the solid angle. For this method, 100 simulations were applied, generating new sets of values for each parameter. This, in turn, led to 'n' new samples of the solid angle, as a function of the incident angle.

Table 5.1: Geometrical parameters with their uncertainties, and probability distribution function.

Geometrical parameter	value (mm)	Probability distribution function
d_1	13.00(3)	Uniform
d_2	2.33(10)	Normal
e	2.071(4)	Normal
c	1.971(2)	Normal
s	4.66(10)	Normal

In this case, it becomes possible to calculate the uncertainty on the solid angle (type A evaluation, uncertainty attributable to repeatability) for each specific incident angle utilizing the following equation:

$$U(\theta) = \sigma_i(\theta) \tag{5.15}$$

where n is the size of the population and $\sigma_i(\theta)$ is the standard deviation.
Figure 5.5 shows the results of the calculation of the solid angle (blue curve) with its associated uncertainty (orange curve) as function of the incident angle. At low incident angles (0°– 0.25°), the solid angle is constant and relatively high due to the beam spot on the sample being larger than the field of view of the SDD with its collimator. By increasing the incident angle, the slope of the curve becomes steep as the solid angle becomes very low due to the decrease of the beam size on the sample.

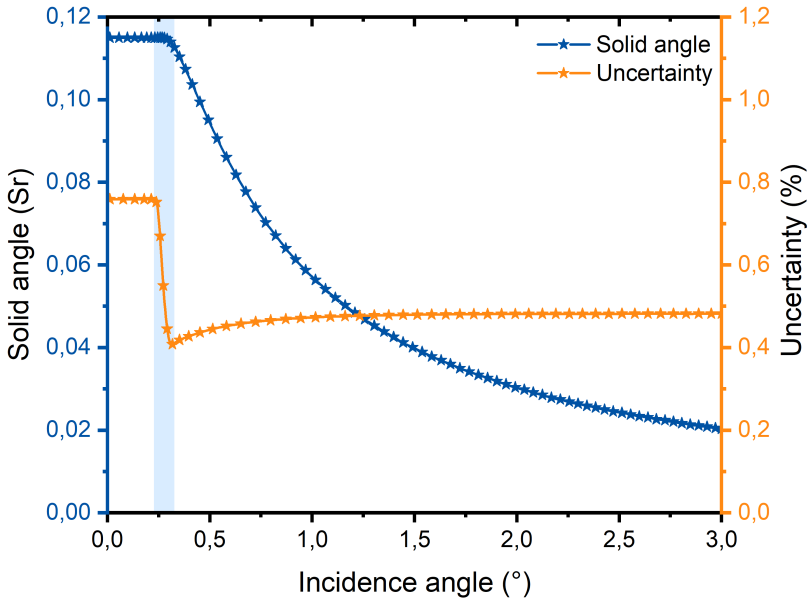

Figure 5.5: Solid angle (blue) with associated partial uncertainty (orange) at each incidence angle taking into account the uncertainties on the geometrical parameters.

Application of Monte Carlo simulations results in a relatively low uncertainty on the solid angles. This is primarily due to the low uncertainties on the dimensions of the detector components.

An observable drop in the relative uncertainty, down to 0.4 % at 0.3 Sr, is detected within the hatched region of the solid angle. This decrease is related to the lower impact of d_1 on the solid angle in this angular region. In fact, at higher angles, the beam footprint is completely included in the field of view of the SDD detector. At higher incident angles, the uncertainty remains approximately constant.

5.2.2 XRR-GIXRF uncertainty calculation using random weight Bootstrap: an innovative approach

The uncertainties associated with the results of the XRR-GIXRF combined analysis cannot be easily calculated from the conventional analytical approach due to the complexity arising from the large number of fitting parameters and the double optimization procedure; thus we studied an alternative approach. With the introduction of the random weight Bootstrap method by Efron [170], the domain of statistical analysis experienced an important conceptual transition. This methodology is generally flexible and does not require prior knowledge of probability distributions to extract statistical data such as standard uncertainties, confidence intervals, and hypothesis tests. This makes it an attractive option across a broad spectrum of fields. The fundamental principle of the Bootstrap method lies in the use of Monte Carlo simulations. These simulations facilitate the creation of a multitude of simulated datasets from a single one by resampling, thus leading to an inexpensive and efficient way to collect information about the sample statistics. The advantage of this method is that it doesn't require any repetition of the measurements [171]. Generating Bootstrap samples can be accomplished by applying random integer weights that indicate the number of times each data point is repeated in the resampling process. However, when applied to XRR and GIXRF, the Bootstrap methodology faces certain practical challenges due to the time-consuming nature of repeating measurements. Therefore, in this context, the implementation of the Bootstrap method necessitates a slight deviation from the standard approach, leading us to consider each value of the intensity of XRR and GIXRF for each incidence angle as an individual sample [172].
As mentioned in section 5.1.3.2, the process to estimate the sample structure involves a differential method with the χ^2 cost functions of reflectivity and fluorescence. The generation of new data within this framework is made possible by applying a uniform weight between 0 and 1 to each angular step for the XRR and GIXRF data. This approach leads to a different methodology for weight application, solving the challenges posed by the time-consuming nature of repeating measurements.
In this case, the normalized cost function for the XRR is expressed as:

$$Cost_{XRR} = \sum_{i=1}^{n} B_i \cdot \frac{\left(\theta_i^5 \cdot e^{XRR_{i,Th}} - \theta_i^5 \cdot e^{XRR_{i,Exp}}\right)^2}{\theta_i^5 \cdot e^{XRR_{i,Th}}} \tag{5.16}$$

and the normalized cost function for the GIXRF becomes:

$$Cost_{XRF} = \sum_{i=1}^{n} D_i \cdot \frac{\left(XRF_{i,Th} - XRF_{i,Exp}\right)^2}{XRF_{i,Th}} \cdot \frac{1}{\mathrm{Max}\left(XRF_{Th}\right)}. \tag{5.17}$$

In these equations, B_i and D_i represent the applied weight on the XRR and the GIXRF cost functions respectively.
Repeating this modified Bootstrap procedure leads to the generation of a new set of possible sample structures. These structures exhibit variations in parameters such as thicknesses, roughnesses, densities, and compositions. Subsequently, these results enable the calculation of mean,

standard deviation, covariance, and other statistical parameters, along with the confidence intervals associated with every fitted parameter.
This innovative application of the Bootstrap methodology within the GIXRF-XRR context demonstrates that the uncertainties in sample structures can be effectively evaluated without the need for time-consuming repetitions of measurements. The advantage of this Bootstrap method lies in its efficiency, which provides valuable information on the uncertainties of the sample structure. A flowchart of the optimization algorithm of our Bootstrap uncertainty calculation is shown in Figure 5.6.

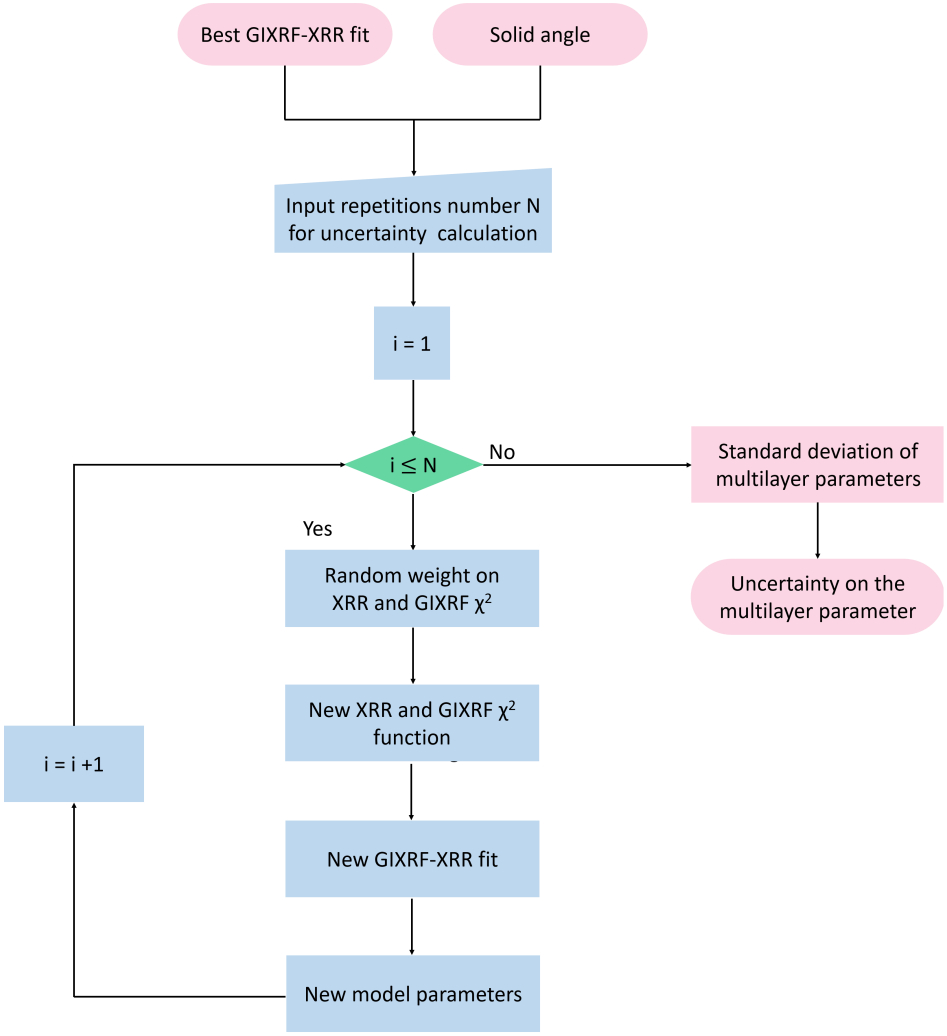

Figure 5.6: Optimization algorithm of Bootstrap uncertainty calculation.

5.2.3 Fundamental parameters uncertainties

Accounting for uncertainties on the fundamental parameters (i.e., attenuation coefficients, fluorescence yields and photoelectric absorption coefficients) is a crucial aspect of the optimization method used in the GIXRF-XRR analysis. These parameters significantly influence the derived sample structure, with any associated uncertainties potentially leading to variations in the final result. Even though uncertainties of FPs for yttrium and iron were calculated (presented in

Chapter 4, Section 4.5), other elements were not measured, resulting in an absence of uncertainty information for these elements. In this case, one might rely on tabulated data from literature. However, it is important to note that whether using measured values or tabulated data, there are associated uncertainties. In addition, there is a lack of research publications providing methods for calculating uncertainties on these parameters. To overcome this problem, one can use the estimated uncertainties on fluorescence yields documented in the paper of *Krause* [25]. This work can be considered to be an accurate source of reference within this particular context due to its wide-ranging of element coverage. Subsequently, in the optimization procedure of reference-free GIXRF-XRR, a Monte Carlo simulation is applied to the fluorescence yields as a Gaussian distribution. The procedure uses random sampling to generate possible outputs of fluorescence yield to calculate the uncertainty. It centers the Gaussian distribution around the estimated values provided by Krause and using its uncertainty as the FWHM of the Gaussian distribution, thus offering a range of probable fluorescence yields. The same percentage uncertainty is then applied to the photoelectric absorption coefficients, providing a reasonable method of extending these uncertainties into the overall analysis. These simulated uncertainties are integrated into the GIXRF-XRR optimization process to calculate the sample structure. A different set of fluorescence yield and photoelectric absorption coefficients values derived from the Gaussian distributions corresponds to different possible sample structure.
The percentage of uncertainty on the fluorescence yield in the various Z range are given in Table 5.2.

Table 5.2: Percentage of estimated uncertainties of fluorescence yields. [a] ln these regions, yields for molecules and solids may differ from those for atoms by more than the values quoted. [b] Near- breaks in the yield curves, uncertainties may exceed those listed [25].

	Range of atomic numbers										
Yield	$5-10$	$10-20$	$20-30$	$30-40$	$40-50$	$50-60$	$60-70$	$70-80$	$80-90$	$90-100$	$100-110$
ω_K	$40-10^a$	$10-5$	$5-3$	3	2	$2-1$	1	1	≤ 1	≤ 1	1
ω_1	-	$\geq 30^a$	30^a	30^b	$30-20^b$	$20-15$	15	15^b	15	15-20	20
ω_2	-	$\geq 25^a$	$25^{a,b}$	25	$25-10$	10	$10-5$	5	5	10^b	10
ω_3	-	$\geq 25^a$	25^a	20	$20-10$	$10-5$	5	$5-3$	3	$3-5$	5

5.2.4 Combined uncertainties

The final objective is to combine all sources of uncertainties including the uncertainties on the solid angle, the uncertainties on the combined analysis optimization procedure, and the uncertainties on the fundamental parameters, to generate a more detailed and precise representation of the sample structure. A flowchart representing the combination of the uncertainty in the optimization procedure of GIXRF-XRR is shown in Figure 5.7.
After applying these methodologies, an estimation of the uncertainties in the sample structure can be achieved. However, it must be recognized that this assessment does not entirely account for every potential source of uncertainty. In particular, uncertainties arising from factors such as the photon flux, the accuracy of the measurements, and the alignment of the sample were not

integrated into this estimation. Moreover, the absence of repeated measurements, which typically offers a means to minimize uncertainties is another factor not addressed in this approach. The uncertainties introduced of the fundamental parameters where just an estimation, as such, may not be entirely accurate. Therefore, while this methodology provides a preliminary approach to quantifying uncertainties in the sample structure, understanding its limitations can guide further research and improvements. This can lead to better, more accurate, and more reliable uncertainty budget in the future.

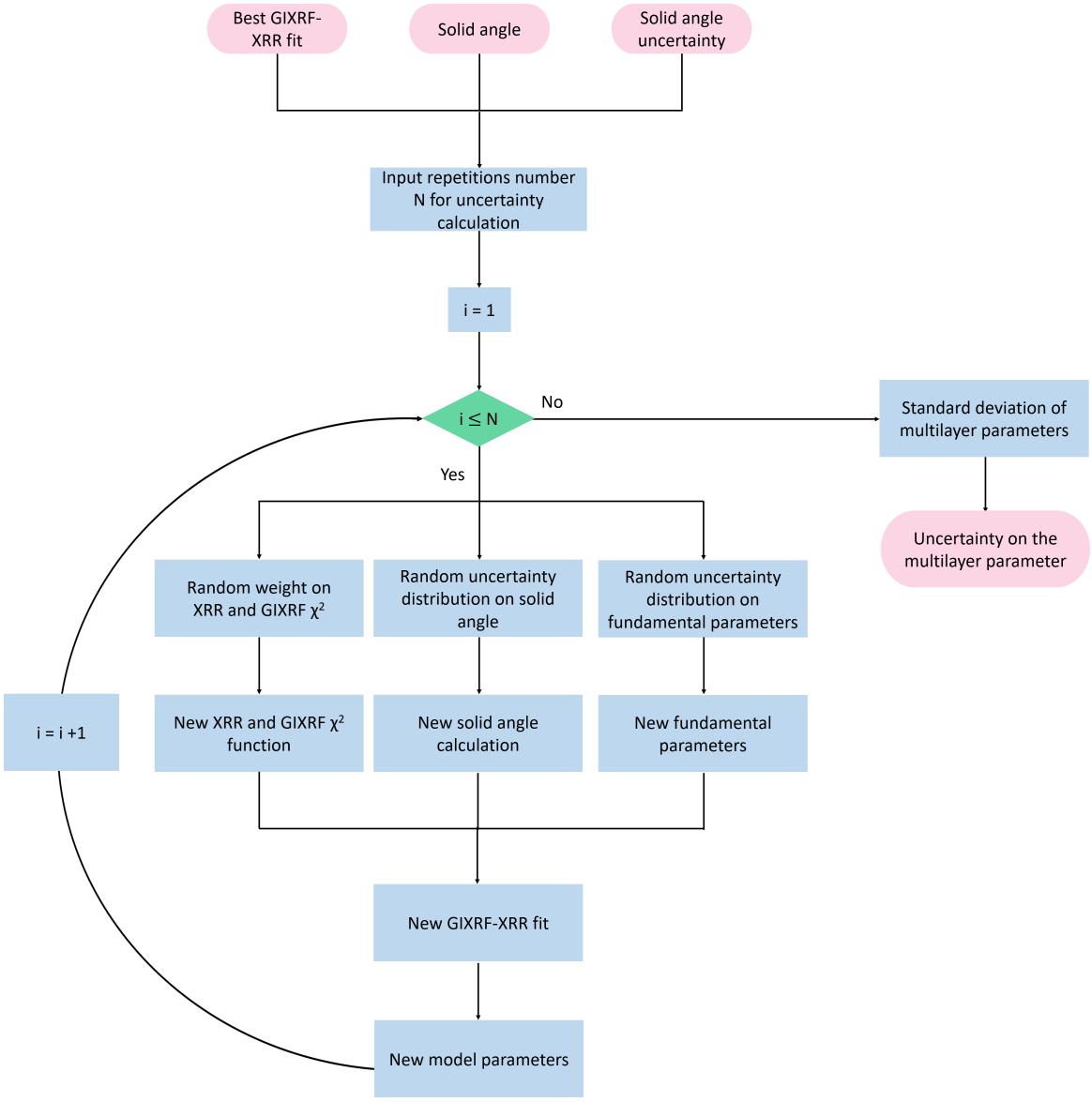

Figure 5.7: Flowchart representing the calculation of uncertainties on the sample structure: including solid angle uncertainties, optimization procedure uncertainties (Bootstrap), and fundamental parameters uncertainties.

Chapter 6

Application to new materials

6.1 Samples characteristics and fabrication

In this section, we will focus on the characteristics and fabrication processes of two different types of thin film samples. These samples include chalcogenide-based phase change materials (PCMs) and tantalum-based thin films, both of which exhibit interesting properties in the development of solution for innovative solution for e.g., non-volatile memories and batteries.

6.1.1 Chalcogenide materials

Chalcogens are elements from the group VI of the periodic table (i.e., S, Se and Te). The term ”Chalcogens” is derived from the Greek word "khalko's" which means copper or ore, and the Latinized Greek word "genes" which means born or produced [173]. This word refers to elements that are commonly found in minerals containing copper combined with sulfur, selenium, and/or tellurium. In the 1950s, studies found chalcogens to have various useful properties such as being semiconductors, ion conductors, and infrared transmitting glass [174]. The use of chalcogenide materials for commercial applications dates back to the 1970s, where Se-based film was used in xerography technology [175]. In the 1990s, the first optical disks were created using Germanium-Antimony-Telluride (GST) films, which have the ability to switch between amorphous and crystalline phases quickly [176]. Te-based films, including GST compounds, were widely used in optical disks and non-volatile memory applications.
Phase Change Materials (PCMs) have gained renewed interest from the microelectronic industries, following their successful use as storage media for digital versatile disks (DVDs). The industry foresees PCMs as a potential solution for the next generation of electronic memories that surpasses the technological capabilities of flash devices [177]. Moreover, recent studies have explored the application of PCMs in neuromorphic computing and machine learning as synaptic elements in artificial neural networks. This is due to the feasibility of multilevel data storage offered by PCMs. Additionally, PCM Random Access Memories possess the potential to store and process vast amounts of data, which has the potential to drive the development of the Internet of Things concept [178].
Chalcogen atoms have a wide range of bonding configurations, resulting in a variety of chalcogenides with different properties. Hybridization and ionicity are inherent characteristics of chalcogenide alloys that are essential to consider when choosing them as phase-change materials (PCM) [179].

Chalcogenide materials can be divided into 3-D chalcogenides and 2-D Transition Metal Dichalcogenides (TMDCs). 3-D chalcogenides are materials with atoms bound throughout a 3-D network and include bulks, films and fibers. They have a wide range of applications such as solar cells, optical fibers and non-volatile memories. On the other hand, 2-D TMDCs are atomic monolayers bound by Van-Der-Waals interactions and have strong in-plane bondings and weak out-of-plane interactions. These materials, such as MoS_2, $MoSe_2$, WS_2, and WSe_2, have sizable bandgaps that change from indirect to direct when thinned down to single layers [180], allowing applications such as transistors, photodetectors, and electroluminescent devices.
This section will provide a more detailed discussion of the properties and applications of 3-D chalcogenides, one of the samples of interest in this research.

6.1.1.1 Material properties of chalcogenide-based PCMs

As mentioned previously, certain chalcogenide materials can quickly transition between amorphous and crystalline states, with different optical and electrical characteristics [181]. This phase changing was first observed by Ovshinsky in 1968 [182] and has been used afterwards for data storage applications such as optical disks and non-volatile resistive memories. Phase changing materials rely on a unique combination of physical properties that enable binary code storage. One of the key factors is the significant difference in reflectivity and/or resistivity between the amorphous and crystalline phases. In fact, for optimal performance in most applications, a PCM should possess several desirable characteristics, including high-speed and low-power phase-switching, a high number of switching cycles, long-term stability of the amorphous phase and a significant contrast in optical/electrical properties between the two phases. Among various PCMs, chalcogenide glasses composed of germanium-antimony-telluride (GST) alloys, exhibit exceptional properties based on these criteria. The phase transition in GST alloys results in a substantial change in refractive index contrast and resistivity [183].
The properties of phase changing are achieved by applying some heat sources such as optical and/or electrical pulses of different intensities and durations [177]. This modifies the atomic structure of the material and therefore, its optical and electrical properties.
The phase-change resistive memory cell employs a small volume of PCM that can exist in either amorphous or crystalline states. This volume is selectively induced by applying a programming current pulse, as depicted in Figure 6.1. To amorphize the active volume (RESET pulse), the material must be heated above its melting temperature (T_{melt}) and then rapidly cooled below its glass transition temperature (T_g) to prevent crystallization. Conversely, to crystallize (SET pulse), the material is heated to a temperature between T_g and T_{melt} to maximize atomic mobility and enable fast crystallization [184]. By applying localized pulses of crystallization or amorphization to phase-change media, information can be encoded in binary code. The stored information can be retrieved by using low-intensity power pulses that do not alter the physical properties of the active material.
Moreover, most PCMs based on GST require a cooling rate of around 1°C/ns for effective melt-quenching [185]. It is observed that melt-quenching process can amorphize a wide range of materials, however, most of them exhibit insignificant changes in their optical properties during phase transition, such as gallium arsenide (GaAs). Therefore, to identify PCM suitable for practical applications, a methodical approach is necessary. Since predicting material properties in amorphous state and understanding phase-transition mechanisms is challenging, our discussion is confined to major GST-based alloys only. These materials, have received an increasing interest for Resistive Random Access Memories (RRAM), including Phase Change

Random Access Memory (PCRAM) and Current Bridging Random Access Memory (CBRAM), some of most promising candidates for the next generation of non-volatile memories [186].

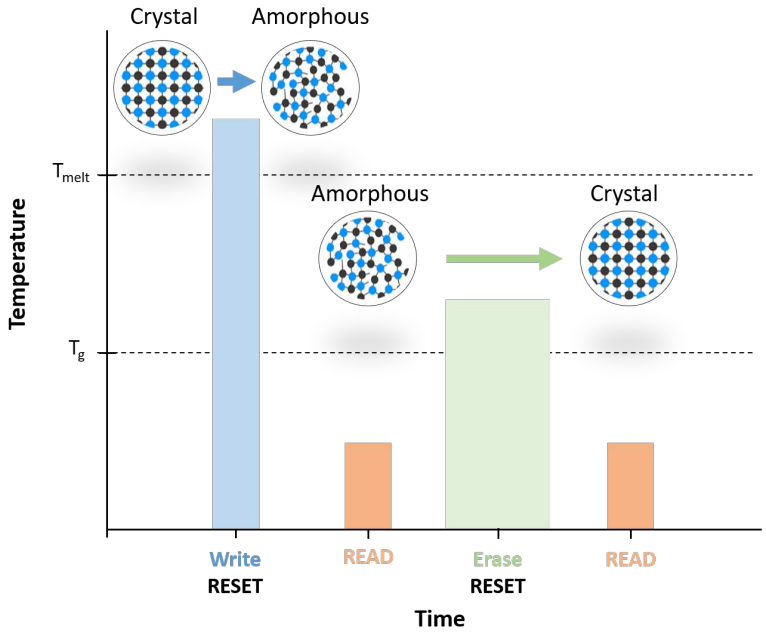

Figure 6.1: Schematic representation of the electrical programming procedure. It illustrates how the material is amorphized through a process of melting and extremely fast cooling to a temperature below the glass transition temperature (T_g), which is achieved by applying a short and intense current pulse (RESET pulse). The figure also shows how the amorphous material is crystallized by applying a current pulse (SET pulse) with a longer duration and smaller intensity than the RESET pulse. The reading of the information is performed by measuring the resistance of the cell using a low-intensity current pulse.

The characteristics of GST films, depends highly on their chemical composition and their compositional depth profile. One such example is the ability to adjust the crystallization temperature of GST alloys as shown in Figure 6.2 by increasing the proportion of Ge, which improves thermal stability and data retention [187].

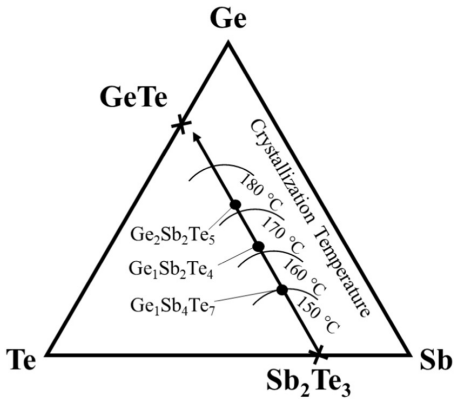

Figure 6.2: Ternary phase diagram for Ge, Sb and Te showing the increase of crystallization temperature by Ge addition [177].

Given the significance of GST materials properties, a detailed characterization of GST samples is essential to ensure their quality, purity, and homogeneity. By characterizing the GST samples, one can get a deeper understanding of their structural, electrical, optical, and thermal properties, which can help to optimize their performance and reliability in electronic applications.

6.1.1.2 Sample preparation

The objective of this research is to study five different samples of GST thin films presented in Figure 6.3. Each sample exhibits a unique structure and composition, all deposited on silicon substrates. The five GST thin film samples were fabricated at CEA/LETI using magnetron sputtering of a GST alloyed target in an Applied Materials Endura® CloverTM multi-cathode PVD (discussed later in section 6.1.3) chamber. The deposition temperature was uniformly regulated to approximately 60°C across all samples, and the chamber base pressure was maintained at 1.33×10^{-4} Pa.

- The first batch (a) consisted of two samples with a 50 nm layer of antimony-rich GST deposited on a Si substrate These were capped in situ with a 20 nm Si layer using pulse-DC mode. One of these was left in its as-deposited state, while the other was annealed at 300°C with a rate of 10°C/min.
- The second batch (b) included two samples with a 100 nm germanium-rich GST layer. These samples were capped in situ with a 5 nm amorphous carbon layer, also using pulse-DC mode. Again, one of the samples was kept as-deposited, while the other was annealed at 450°C, with also a rate of 10°C/min.
- The final sample (c) was unique with a 50 nm telluride-rich GST layer on a Si substrate, capped in situ with a 3.5 nm-thick amorphous carbon layer. This sample was kept in its as-deposited state.

The study on the annealed samples was undertaken to observe structural changes as a result of annealing, and to ascertain if such changes could be detected by combined GIXRF-XRR. The study involving the last sample aimed to examine the factor of uncertainty's influence, given that there are several contributing factors.

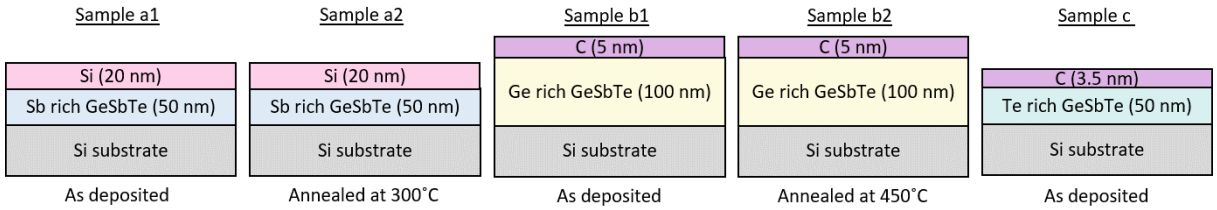

Figure 6.3: GeSbTe thin film samples studied.

6.1.2 Tantalum-based thin films

Tantalum pentoxide (Ta_2O_5) is a prominent wide band gap material, exhibiting a diverse range of structural and functional properties, enabling a broad range of applications. It has garnered significant attention owing to its high dielectric constant (>20), low leakage current,

high refractive index, and wide transmittance spectra region from 350 to 1000 nm [188]. These properties make it suitable for various applications, including Dynamic Random Access Memory (DRAM) [189] and redox-based RRAM [190]. Understanding the relationship between fabrication methods and film properties is crucial, as changes in the dielectric constant of Ta_2O_5 have been reported with variations in the deposition process. In the case of RRAM applications, it has been shown that changes in film density can impact the device behavior [191]. In addition to its multifunctional properties, Ta_2O_5 exhibits fascinating structural characteristics. It is amorphous at temperatures below 650°C; however, in its crystalline state, it can assume various forms, including oxygen-deficient and oxygen-rich structures. A notable phase transition occurs at 1360°C, from a low-temperature (L) crystalline phase to a high-temperature (H) crystalline phase [192].
Ta_2O_5 thin films have been deposited using various techniques such as electron-beam evaporation, ion-assisted deposition, reactive magnetron sputtering, and ion beam sputtering, resulting in diverse film characteristic properties. Factors such as ion beam parameters, oxygen flow rate, and deposition rate can influence the optical, mechanical, and electrical properties of Ta_2O_5 films, and thus, exploring their effects is essential for optimizing this material's performance.

6.1.2.1 Samples preparation

The effect of doping on thin film characteristics has been a subject of considerable interest in material science, as it can significantly alter their structural, optical, and electrical properties. For the characterization of Ta_2O_5 thin films, two samples were examined, using iron oxide (Fe_2O_3) and yttrium oxide Y_2O_3 as doping materials.
The samples where prepared in Forschungszentrum Jülich by radio frequency (RF) sputtering. The substrates used in this process were 25 × 25 mm p-doped silicon (Si) wafers, which were thoroughly cleaned and polished to remove contamination. Off-axis sputtering was employed to deposit the oxide layers, ensuring a more uniform coverage of the substrate. The oxide layers were deposited from doped oxide targets at room temperature under a pressure of 0.004 hPa and an argon gas flow of 10 sccm. The RF power applied during the deposition process was 10 W with a sputter time of 50 min. Figure 6.4 shows the distinct samples prepared: sample with 32 nm of Ta_2O_5 main oxide layer doped with 0.1 % Fe_2O_3, and sample with 28 nm of Ta_2O_5 main oxide layer doped with 6 % yttrium oxide (Y_2O_3).

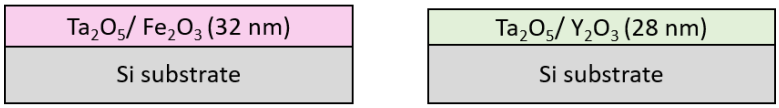

Figure 6.4: Tantalum-based thin films samples deposited on Si substrate. Left is Ta_2O_5 doped with Fe_2O_3, and the right is Ta_2O_5 doped withY_2O_3.

6.1.3 Synthesis of thin film samples

The synthesis of the chalcogenide and tantalum-based thin films is usually accomplished by the processes of Physical Vapor Deposition (sputtering), Chemical Vapor Deposition (metal organic chemical vapor deposition (MOCVD)) and atomic layer deposition (ALD)). These synthesis

techniques are used since they are industrial-friendly capable of depositing films with a high degree of chemical homogeneity and uniform thickness in the nano- and micrometer-range. The GST chalcogenide and the tantalum-based thin films studied in the thesis are synthesized using the Physical Vapor Deposition (PVD) technique.
The PVD is a technique for coating surfaces by vaporizing the material to be deposited and transferring it to a substrate under vacuum conditions. This process is similar to CVD, except that in PVD, the precursors start as solid material, while in CVD, they are introduced as gases. PVD is constituted of various deposition techniques, including evaporation, molecular-beam epitaxy, sputtering, and others. Sputtering is the most prevalent technique for film deposition on semiconductor wafers, on magnetic media and head surfaces, for coating tools and cutting surfaces for wear resistance ...[193]. The sputtering, involves using an electrically excited gas plasma in a vacuum system by introducing a sputter gas, typically argon. In this process, a glow discharge is generated between two electrodes in the vacuum chamber, pumped down to a base pressure of 10^{-4} Pa or below. Afterwards, the target surface (cathode surface) is bombarded with a high-energy ion beam (Ar^+), causing atoms to be ejected from the surface due to energy transfer. These ejected atoms are transported finally to the substrate where deposition occurs.
PVD methods offer several key benefits, including the ability to achieve highly uniform coatings with thicknesses ranging from less than 1 nm to 200 μm. Additionally, these methods provide excellent reproducibility of properties, as well as the flexibility to cover surfaces of various sizes - either restricted or practically unlimited. PVD methods also enable selective deposition on specific sections and allow for the use of virtually any material as a substrate. They can accommodate a wide range of temperature requirements and offer a broad selection of coating materials, including metals, alloys, and chemical compounds. With PVD methods, it is possible to create multilayer and functionally graded coatings with layers of different thicknesses and materials, while adjusting the composition, structure, and properties of the layers to account for changes in deposition parameters. Furthermore, PVD methods can produce coatings with the highest possible purity while minimizing environmental impact [194]. However, traces of argon are sometimes observed in the XRF spectra, due to its use as a process gas during deposition. PVD also suffers from some disadvantages such as the complexity and the high cost of technological and monitoring equipment, the need for very highly qualified operators, the necessity for precise control over the chemical composition, and the need for special preparation of the surfaces being coated.

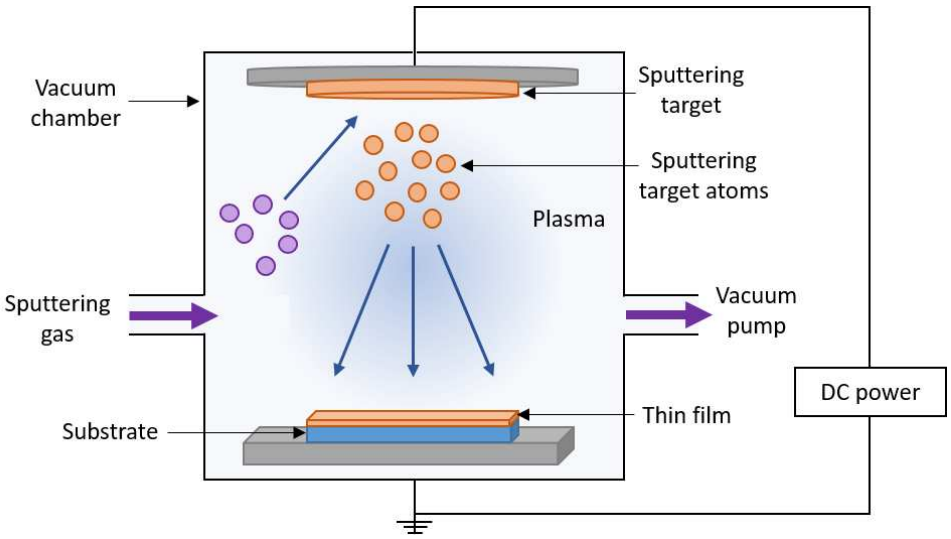

Abstract

Figure 6.5: A schematic representation showing the standard sputtering technique.

6.2 Results and discussion

The following section of this thesis presents a comprehensive analysis and discussion of the experimental and theoretical results obtained from the wide variety of the studied samples. The study involves two distinct classes of materials: five samples of germanium antimony tellurium (GST) and two samples of tantalum pentoxide (Ta_2O_5), each with a distinct doping material.
First, the discussion focuses on the tellurium-rich GST sample, with a detailed study of its structure using GIXRF-XRR techniques. This sample is further used as a test for the application of the novel uncertainty calculation method. The estimation of uncertainties in the sample structure is performed using both the Bootstrap methodology alone and a combination of Bootstrap with uncertainties on fundamental parameters and solid angle using Monte Carlo simulation. This approach helps identify the parameters that significantly influence the uncertainties in the sample structure.
Following the detailed analysis of the tellurium-rich GST sample, we discuss the results obtained from XRR-GIXRF analysis on the remaining GST samples enriched with Sb or Ge. The objective is to study the effects of annealing on these samples. Next, we present the result of our method for calculating uncertainties for these samples. In the last part of the results, we extend the analyses to tantalum pentoxide (Ta_2O_5) samples. Each of these samples was uniquely doped with either iron or yttrium oxide. The aim of this study is to identify the effects of doping on the sample structure. Furthermore, we will apply the uncertainty calculation method to further improve our understanding of the implications of different doping materials.

6.2.1 GeSbTe thin films

The GIXRF measurement setup for all GST samples included the use of 11.5 keV photon energy, which effectively excited the Ge-$K_{\alpha,\beta}$, Sb-$L_{\alpha,\beta}$, and Te-$L_{\alpha,\beta}$ lines. The fluorescence spectra were captured at various angles, ranging from 0° to 3°.

6.2.1.1 As-deposited Te-rich GST layers

As mentioned previously, the Te-rich GST sample includes C (3.5 nm)/ GST (50 nm)/ Si substrate. Using the combined GIXRF-XRR technique, we seek to obtain the sample's structure and compare the derived structural parameters - thickness, density, elemental composition, and surface/interface roughness - with the manufacturer's data. This comparison will provide insights into both the accuracy of the GIXRF-XRR method and the actual characteristics of the sample. For the XRF measurement of this sample, an acquisition (live) time of 30 seconds was set for each angle step. The setup for this analysis ensured a photon flux at the XRF excitation energy of $1.16 \times 10^8\,\mathrm{s}^{-1}$ for a height slit of 0.3 mm. Figure 6.6 illustrates the obtained fluorescence spectrum measured with the EDS at an incident angle of 0.5°.
The acquired X-ray fluorescence spectrum displays a number of peaks, each of which corresponds to a particular element present in the GST sample. Among these, key peaks correspond to Si-$K_{\alpha,\beta}$, Sb-$L_{\alpha,\beta}$, Te-$L_{\alpha,\beta}$ and Ge-$K_{\alpha,\beta}$ and $L_{\alpha,\beta}$. In addition, contributions from Compton and Rayleigh scattering are observed, indicating X-ray photons are scattered within the sample. The XRF spectrum exhibits overlapping elemental peaks due to the low resolution of the energy-dispersive spectrometer used. In particular, $L_{\alpha,\beta}$ peaks of Sb and Te, and $K_{\alpha,\beta}$ peaks of Si, since they are close on the energy scale. Consequently, their characteristic peaks overlap, resulting in the formation of combined peak profiles rather than distinct individual ones. This low resolution creates a challenge for accurately quantifying the concentrations of these elements. However, using COLEGRAM, these overlapping spectral lines can be accurately distinguished and quantified, with associated uncertainties on the fitting parameters. The net peak area of a constituting element versus the incidence angle is the information of interest used to build the GIXRF curve.

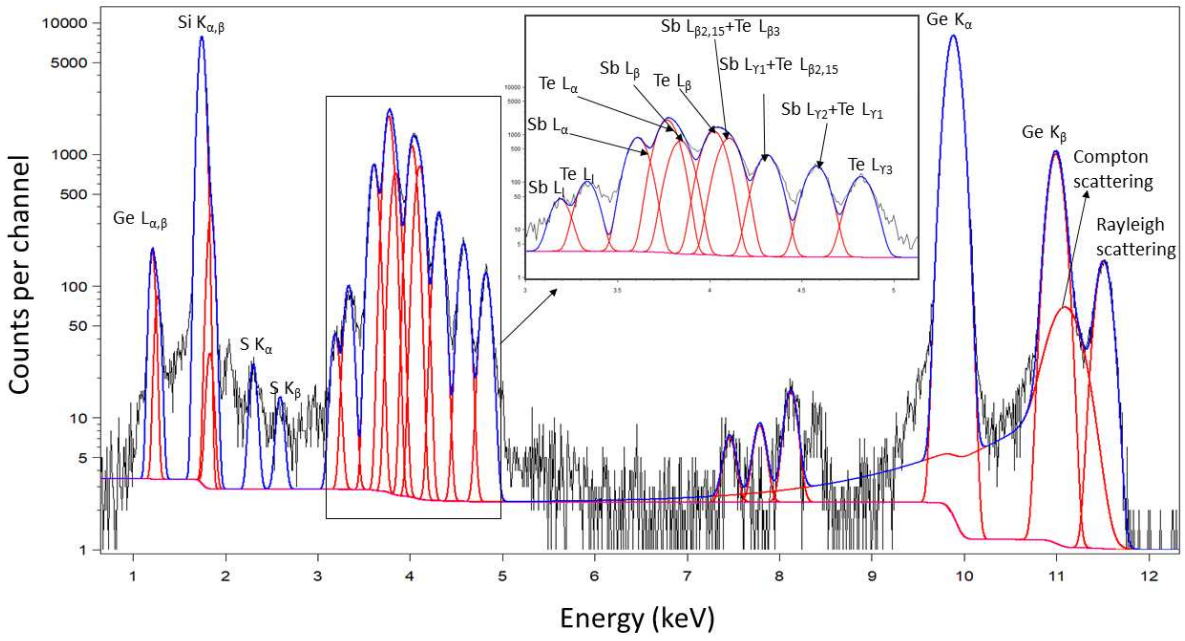

Figure 6.6: X-ray fluorescence spectrum of Te-rich GST acquired at 0.5° incidence with an excitation energy of 11.5 keV and fitted using COLEGRAM.

The XRR and GIXRF experimental results for the Te-rich GST sample, with the simulation using ELIXIR, are presented in Figure 6.7. The XRR data, presented in Figure 6.7 (a), exhibits a good agreement between the measured and the simulated values. Both share a common critical angle (around 0.22°), similar oscillation period and intensity, as well as the number of Kiessig fringes. This provides confidence in the structural parameters and the elemental composition of the layers that were determined. The observed difference in the XRR intensity below the critical angle can be attributed to the experimental geometry, which may introduce some artifacts. The variation in the amplitude of the Kiessig fringes between the experimental data and the simulated fit may be attributable to off-specular scattering. This scattering phenomenon is commonly observed on surfaces with a roughness equal to or greater than the X-ray wavelength [195] which can change the direction of X-rays, leading to a change in the depth of the fringes.
The GIXRF results, shown in Figure 6.7 (b), present a strong agreement between the simulation and the measured data. Below the critical angle, the fluorescence intensity for the Ge-K_α, Sb-L_α, and Te-L_α lines is low due to the total reflection of incident X-rays. As the incidence angle exceeds the critical value, the GIXRF profile for all three elements presents a rapid increase which reaches a maximum at approximately 0.265°. This indicates the presence of these three elements in the same layer. In addition, high degree of agreement between the simulation and the experimental results proves the accuracy of calculated thicknesses, densities, roughnesses and elemental depth profiling within the individual layers. Thus, this validates the reliability of the sample structure analysis using the combined GIXRF-XRR technique.

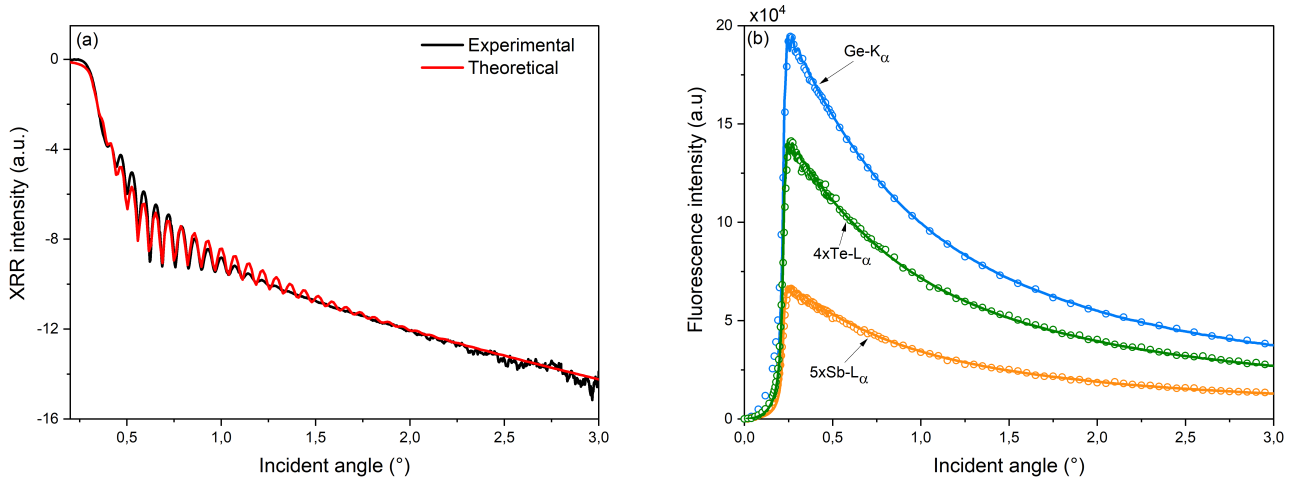

Figure 6.7: XRR intensity measured at 8 keV in log scale. The black and red curves represent the measured and the fitted reflectivity respectively (a) and GIXRF of Ge-K_α (blue), Sb-L_α (orange) and Te-L_α (green) measured at 11.5 keV (b). The circles represent the experimental data extracted with COLEGRAM for Ge-K_α, Sb-L_α and Te-L_α. The lines represent the fit to the data obtained with the ELIXIR in-house software.

The results of the sample structure derived from the GIXRF-XRR combined analysis with ELIXIR are presented in Table 6.1. These results are compared with the structure parameters provided by the manufacturer of the sample to assess the accuracy of the deposition technique. The analysis of the experimental results from combined GIXRF-XRR and comparison to the

manufacturer's data shows small differences. For instance, in the GST layer, the nominal thickness as provided by the manufacturer (50 nm) is slightly less than the thickness value (55 nm) deduced from the GIXRF-XRR results. This difference of 10 %, is relatively small and may not have a significant impact on the properties of the layer. This variation is most likely due to the sample deposition method's uncertainties. Moreover, the density of the GST layer calculated from our measurements (5.69 g/cm^3) exhibits a small deviation from the nominal density of $Ge_2Sb_2Te_5$ (5.88 g/cm^3). The observed relative difference in density, approximately 3.2 %, could be attributed to the presence of imperfections such as defects within the layer, leading to a variation in its density. In addition, a relatively low difference was observed in the elemental composition of the GST layer, where the GIXRF-XRR analysis indicated a composition of $Ge_{1.8}Sb_{2.2}Te_5$. This difference could be also attributed to uncertainties inherent in the sample deposition method. Concerning the capping layer, GIXRF-XRR analysis results show high satisfactory agreement, as the thickness and density correspond to the manufacturer's values. As a protective layer against potential contamination or oxidation, the capping layer is expected to exhibit such uniformity and stability during the deposition process. Finally, the calculated roughness values for both layers were found to be smaller than the layer thickness and within the 2 nm limit. The roughness values indicate a high smooth surface for the capping layer and a slightly higher roughness for the GST layer, that is still within acceptable limits.

Table 6.1: Comparison of the sample structure parameters between the GIXRF-XRR results and the manufacturer's data. The density of the manufacturer data corresponds to the bulk density in the literature [196, 197].

	GIXRF-XRR results		Manufacturer's data	
	Layer 1	Layer 2	Layer 1	Layer 2
Composition	C	$Ge_{1.8}Sb_{2.2}Te_5$	C	$Ge_2Sb_2Te_5$
Thickness (nm)	3.50	55	3.5	50
Roughness (nm)	0.24	2	$\leq$2	$\leq$2
Density (g/cm^3)	2.3	5.69	2.3	5.88

A complementary study of Te-rich GST sample structure includes two steps. In the initial step, the sample structure and associated uncertainties are analyzed using only the Bootstrap resampling technique. In the second step, we apply a more comprehensive methodology by combining Bootstrap resampling with detailed consideration of fundamental parameter uncertainty. This combined approach is refined further by including the uncertainties associated with the solid angle, providing a deeper understanding of the factors influencing the sample structure uncertainty estimates. Table 6.2 presents these results in a detailed and systematic manner. Whether using the Bootstrap-alone approach or the Bootstrap with the fundamental parameters and the solid angle uncertainties combination, each has its distinct value and contribution to the overall uncertainties of the sample structure.
The confidence intervals of model parameters are calculated using an enlargement factor of $k = 1$, corresponding to the standard uncertainty with a 68.3 % confidence level. The results present relatively small confidence intervals on all model parameters ($\leq 5\,\%$), proving the reliability of the combined XRR-GIXRF fitting procedure in determining the structural parameters for thin film multilayers.

Table 6.2: Comparison of uncertainties on layer parameters calculated with an enlargement factor $k = 1$: Bootstrap analysis versus Bootstrap with fundamental parameters and solid angle uncertainties calculated using Monte Carlo simulations.

	Bootstrap uncertainties		Bootstrap with FP and solid angle uncertainties	
	Layer 1	Layer 2	Layer 1	Layer 2
Thickness (nm)	0.17	1.11	0.19	2.06
Roughness (nm)	0.01	0.03	0.01	0.09
Density (g/cm^3)	0.12	0.09	0.12	0.21

When including uncertainties from fundamental parameters and the solid angle into the Bootstrap method, we found that the confidence intervals increased slightly. The uncertainty of the thickness for the GST layer almost doubled from 2.0 % to 3.7 % , and the density uncertainty also increased from 1.6 % to 3.7 %. Despite these changes, the confidence intervals remained within acceptable ranges, maintaining the reliability of the combined approach in extracting the structural parameters. It should be noted that when including uncertainties on the fundamental parameters and solid angle, the uncertainties on layer parameters are larger than when using the Bootstrap method alone. This is related to the additional uncertainties introduced by fundamental parameters and the solid angle, showing the importance of including them in the uncertainty analysis. Overall, both methods provide reliable structural parameters for thin film multilayers with acceptable levels of uncertainty.
However, this analysis does not yet includes uncertainties on the mass attenuation coefficients or those associated with the experimental setup. Both of these factors could further affect the results, potentially in a significant manner. The uncertainty related to the mass attenuation coefficients, in particular, could play a crucial role considering its importance in the reference-free XRR-GIXRF analysis. The precision of the experimental parameters may also impact the reliability of the derived structural parameters. Thus, a future work can be complementary, where a more comprehensive methodology including uncertainties in the mass attenuation coefficients and experimental parameters could be developed.

6.2.1.2 Sb-rich GST

The following set of GST samples are as-deposited and annealed Sb-rich GST with a layer configuration of Si (20 nm)/ GST (50 nm)/ Si substrate. These samples exhibit different characteristics as one of them is as-deposited and the other is annealed. The annealing technique, involves heating the Sb-rich GST sample to 300°C for a predetermined period, which leads to a transition from an amorphous to a crystalline state, creating modifications in its structures. For the XRF measurement of these samples, an acquisition time of 30 seconds was set at a photon flux of $2.24 \times 10^8\,\mathrm{s}^{-1}$ and $2.29 \times 10^8\,\mathrm{s}^{-1}$ at 11.5 keV for the as-deposited and annealed samples respectively, using a height slit of 0.3 mm. In this section, we present the result of the sample structure obtained for the Sb-rich GST and the change upon annealing, obtained by the combined GIXRF-XRR measurements. Here, the objective is to understand the impacts of annealing on these properties. The measurement and fit results of XRR and GIXRF for Ge-K_α, Sb-L_α, and Te-L_α for both the as deposited and annealed samples are presented in Figure 6.8 and 6.10 showing the significant structural impact of the annealing process.

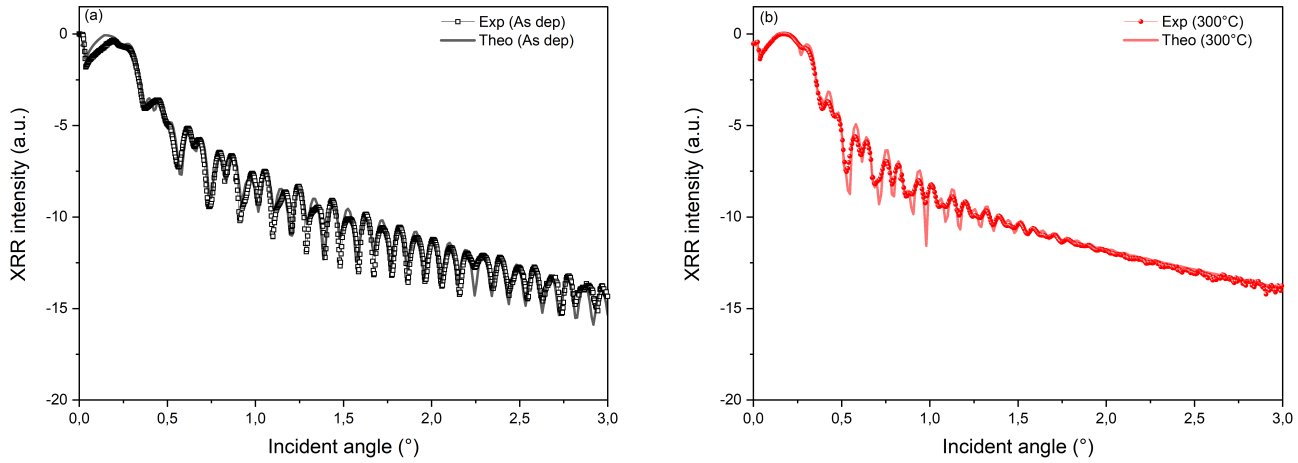

Figure 6.8: XRR Analysis of Sb-Rich GST: (a) and (b) scans and fits for the as-deposited and the annealed samples respectively. The curves with symbols represent the experimental data, while the slightly transparent colored curves represent the corresponding fits.

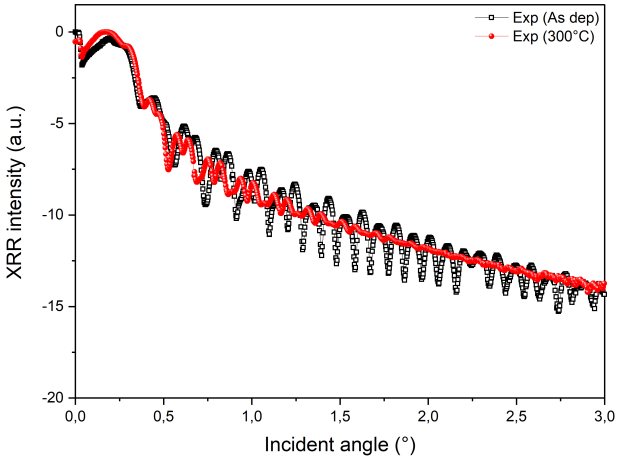

Figure 6.9: Comparison between XRR measurement before and after annealing.

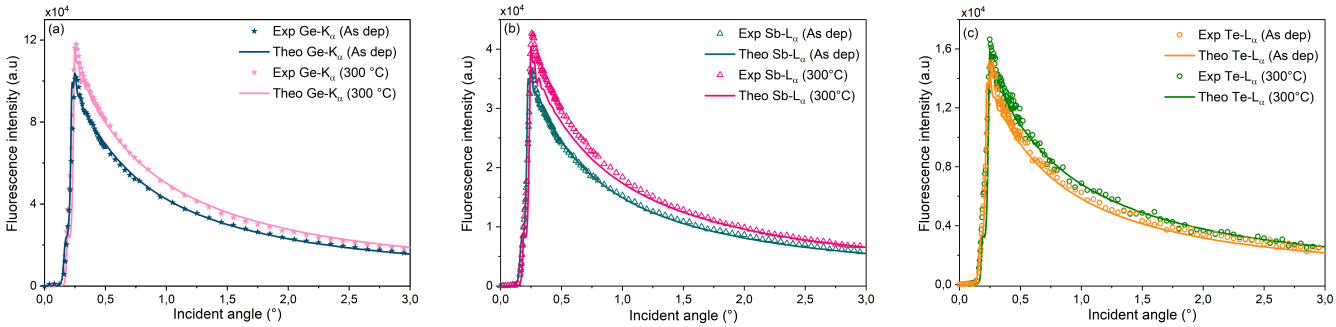

Figure 6.10: (a), (b) and (c) GIXRF scans and fit of Ge-K_α, Sb-L_α, and Te-L_α respectively of both as-deposited and annealed samples.

X-ray reflectivity (XRR) measurement and fitting results for the as-deposited sample illustrated Figure 6.8(a) are in good agreement in terms of the number of Kiessig fringes and the intensity of reflectivity. The peaks positions of the fringes also align well between the measurements and the model, indicating the accuracy of the fitted model. However, discrepancies in the amplitude of some fringes could be attributed to factors such as off-specular scattering or potential errors in reflectivity measurement. The fitting of XRR data for the annealed sample was very challenging and difficult due to the strong changes after annealing. As shown in Figure 6.8 (b), despite the agreement in terms of reflected intensity, number and position of Kiessig fringes, there is a noticeable difference in the amplitude of these fringes. This divergence may be influenced by several factors, including changes in layer densities due to annealing, or complexities in the scattering effects and measurement errors. At lower angles ($\leq$0.4), further difference between the XRR measurements and fit results for both samples are identified. The difference observed at low angles indicates that additional fringes might not have been captured in the measurement or the model may not fully represent the complexities in the sample structure. Comparing the XRR for the as-deposited and the annealed samples, as shown in Figure 6.9, presents significant changes in the number of Kiessig fringes, their peak positions and the overall reflected intensity. We also observe a reduction in the fringes intensity and in their number revealing a change in the structure parameters of the layers.
Regarding the GIXRF measurements for the three elements illustrated in Figure 6.10 (a), (b) and (c), a good agreement is observed between the fits and measurements for both, the annealed and the as-deposited samples. This level of agreement indicates an accurate estimation of the thickness and density parameters derived from the analysis. Furthermore, when comparing the GIXRF results for the as-deposited and annealed samples, an increase in the emission lines intensity of the three elements is observed after annealing. This can be attributed to an increase in either the density or thickness of the GST layer, proving the impact of the annealing process on the sample's structure parameters.
In order to clarify the structural differences in the Sb-rich GST samples before and after annealing, Figure 6.11 represents an illustration of each sample's layer arrangement obtained with the combined GIXRF-XRR analysis. Table 6.3 provides information about the composition of each layer, including elemental composition, thickness, roughness, and density, with the corresponding uncertainties. The uncertainties are calculated using the Bootstrap resampling method, taking into account the uncertainties associated with the fundamental parameters and the solid angle.

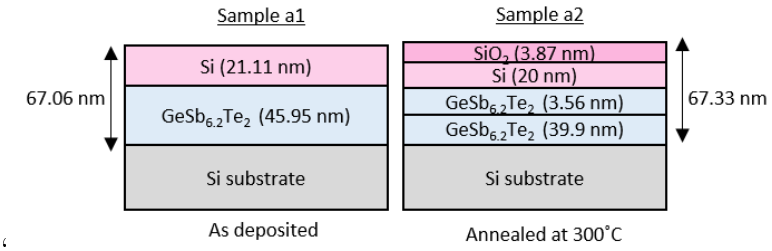

Figure 6.11: Illustration of the sample structure of Sb-rich GST samples before (left) and after annealing (right) obtained with combined analysis GIXRF-XRR.

Table 6.3: Comparison of the sample structure changes of the Sb-rich GST sample before and after annealing with the associated uncertainties.

	Layer order	Thickness (nm)	roughness (nm)	density (g/cm^3)
Sb-rich GST as deposited	1	21.11(91)	0.80(4)	1.52(8)
	2	46.0(2)	0.35(2)	5.40(20)
Sb-rich GST annealed at 300°C	1	3.87(22)	1.00(5)	2.30(13)
	2	20.00(88)	0.95(5)	2.38(10)
	3	3.56(19)	1.09(6)	6.00(31)
	4	39.9(19)	4.75(22)	6.70(27)

Analyzing the structure of the Sb-rich GST samples, reveals that the as-deposited sample aligns closely with the manufacturer's data (Si (20 nm)/ GST (50 nm)/ Si substrate), with the structure including two distinct layers as specified. The Si capping layer has a thickness of 21.11 nm with a roughness of 0.80 nm. However, the calculation shows a density of 1.52 g/cm^3 instead of 2.30 g/cm^3, which can be due to factors such as non-uniform deposition process, or presence of defects or contamination. For the GST layer, the analysis gives a thickness of 46.0 nm, 8.1 % less than the manufacturer data with a surface roughness of 0.35 nm and a density of 5.40 g/cm^3. Following the annealing process, noticeable changes occur in the Sb-rich GST samples. The silicon capping layer splits into two layers: an oxidized thin layer with a thickness of 3.87 nm and a non-oxidized thicker part with a thickness of 20 nm, both presenting higher densities and roughnesses due to crystal growth. The presence of oxygen in the Si capping layer, indicates the possibility of oxidation during the annealing process. In addition, the GST layer also splits into two layers with different thicknesses, densities and roughnesses. These two layers feature higher densities and roughnesses than the GST layer in the as-deposited sample. The split in the GST layer indicates a partial phase transition of the GST layer from the amorphous to the crystalline state.
For both GST samples, the uncertainties associated with thickness, density and roughness are low, indicating a high level of precision: for the first layer of the as-deposited sample, the relative uncertainties on the thickness, density and roughness, are approximately 4.3 %, 5.3 %, and 5 % respectively. For the second layer, these values are around 4.3 % for thickness, 3.7 % for density and 5.7 % for roughness. For the annealed Sb-rich GST sample, the first layer's thickness, density and roughness present relative uncertainties of about 5.7 %, 5.6 %, and 5 %, respectively. For the second layer, the relative uncertainties are approximately 4.4 %, 4.2 %, and 5.3 %, for the same parameters. In the third layer, we find relative uncertainties of around 5.3 % for thickness, 5.2 % for density and 5.5 % for roughness. Lastly, for the fourth layer, these relative uncertainties are approximately 4.7 % for thickness, 4 % for density and 4.6 % for roughness. It's clear that both samples have similar percentages of uncertainties, though the values are slightly higher for the annealed samples compared to the as-deposited sample. The quantification of the uncertainties demonstrates the precision of combined analysis

GIXRF-XRR for the characterization of thin films.

6.2.1.3 Ge-rich GST

We also studied Ge-rich GST samples in two states which consisted of a C (5 nm)/ GST (10 nm)/ Si substrate configuration. The XRF was performed at an incidence energy of 11.5 keV using a 0.3 mm height slit, the as-deposited sample being measured with an acquisition live time of 60 seconds at a photon flux of $3 \times 10^8\,\mathrm{s}^{-1}$, and the annealed sample measured with an acquisition time of 30 seconds at a photon flux of $4.08 \times 10^8\,s^{-1}$. The measurement and fitting results of XRR for both samples are presented in Figure 6.12.

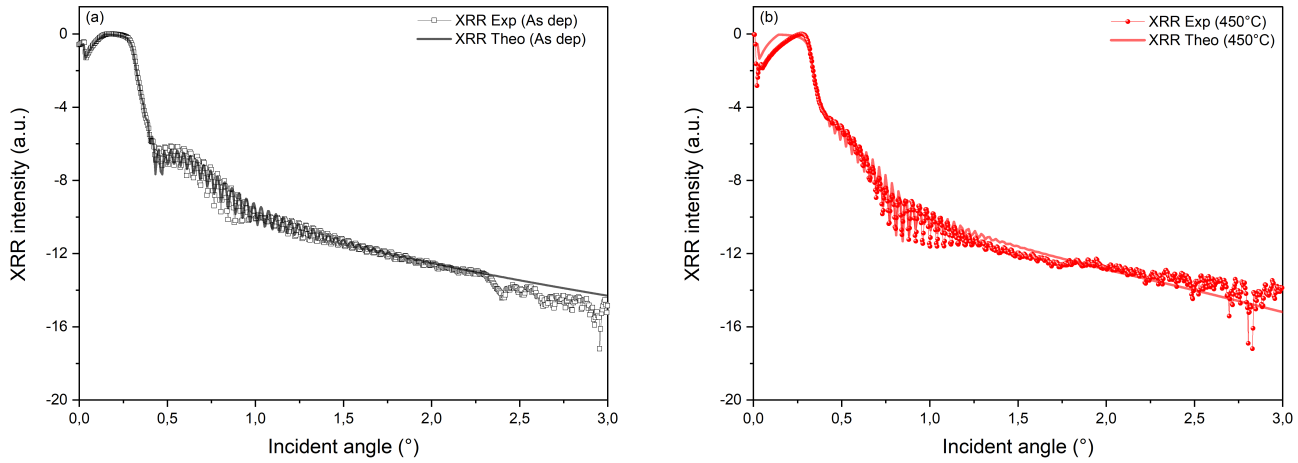

Figure 6.12: XRR Analysis of Ge-Rich GST: (a) and (b) measurements and fits for the as-deposited and the annealed samples respectively. The curves with symbols represent the experimental data, while the slightly transparent colored curves represent the corresponding fits.

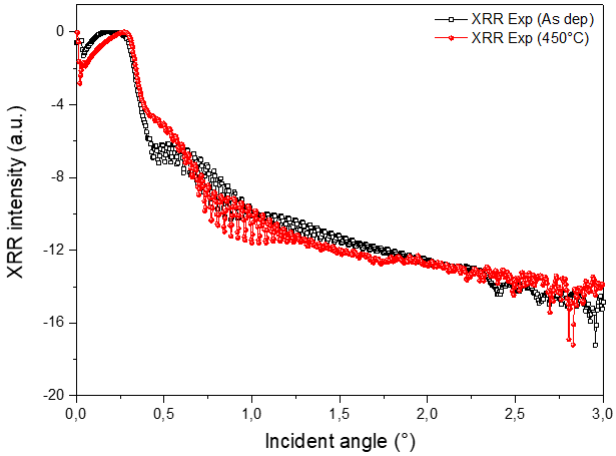

Figure 6.13: Comparison between XRR measurement before and after annealing.

In the XRR measurement, there is a good agreement between the fit for the as-deposited sample and the experimental data which shows the accuracy in the structure parameters derived from

the analysis. However, fitting the annealed sample was found to be more difficult, especially between 0.4° and 0.5°. In this region, the fringes did not align as wanted, which may be attributed to an error in the experimental setup, such as a malfunction in the rotation axes, or an unknown change in density. Additionally, for angles higher than 1.2°, the intensity of the fringes differs from the experimental data, despite the agreement of the fringes number and their positions. Comparing the XRR curves of the as-deposited and the annealed samples, several changes are observed as illustrated in Figure 6.13. First, the reflectivity curves of the two samples have different numbers of fringes indicating a change in layer thickness, as the number of fringes is typically proportional to the thickness. Additionally, there is a shift in the positions of the fringes related to a change in the density of the material. Furthermore, the amplitude and shape of the fringes also change between the two measurements, which is linked to variations in the roughness and density of the layers. Finally, the overall intensity of the reflectivity curve also changes as a the result changes in the density.
The measurement and fitting of GIXRF for Ge-K_α, Sb-L_α, and Te-L_α for the as-deposited and annealed samples are presented in Figure 6.14. The analysis of GIXRF data for Ge-K_α, Sb-L_α, and Te-L_α, shows a very good agreement between the fit and the measurement for both, the as-deposited and the annealed samples. This indicates the reliability in the values for thickness and elemental compositions, and confirms that the model obtained from the analyses corresponds to the true characteristics of the samples. Moreover, an increase in the intensity of all three elements, Te, Ge, and Sb, is observed after the annealing process. Such an increase in intensity can be attributed to changes in the material properties, specifically thickness and concentration.

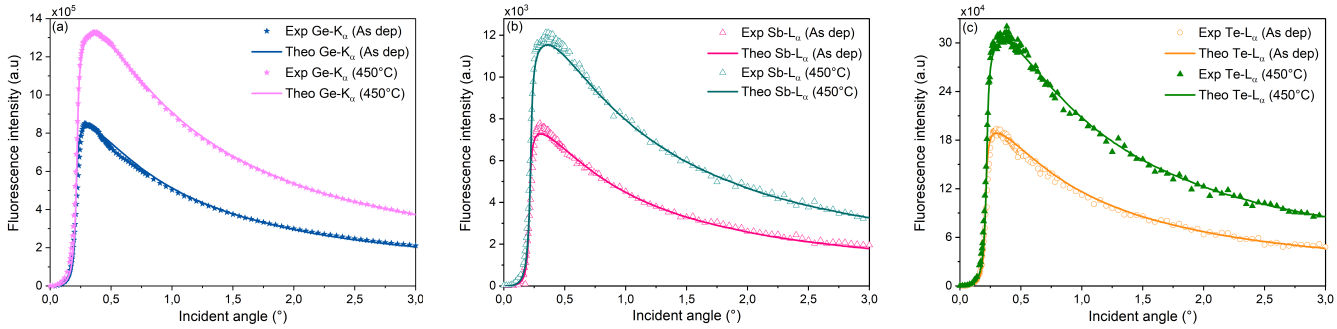

Figure 6.14: GIXRF scans and fit of Ge-K_α (a) Sb-L_α (b), and Te-L_α (c) respectively of both as-deposited and annealed samples.

A schematic representation of the structures of the samples before and after annealing is illustrated in Figure 6.15.

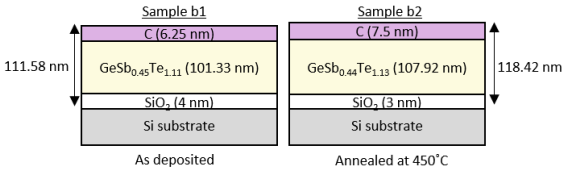

Figure 6.15: Illustration of the sample structure of Sb-rich GST samples before (left) and after annealing (right) obtained with combined analysis GIXRF-XRR.

Table 6.4 presents a summary of the sample structure results for the both, as deposited and annealed, with their associated uncertainties.

Table 6.4: Comparison of the sample structure changes of the Ge-rich GST sample before and after annealing with the associated uncertainties.

	Layer order	Thickness (nm)	roughness (nm)	density (g/cm^3)
Ge-rich GST as deposited	1	6.25(32)	1.90(10)	2.51(14)
	2	101(5)	1.04(5)	5.32(28)
	3	4.00(18)	0.18(1)	2.40(12)
Ge-rich GST annealed at 450°C	1	7.50(42)	1.70(10)	1.83(10)
	2	108(6)	1.53(7)	5.90(28)
	3	3.00(14)	0.30(1)	2.50(12)

The combined analysis shows a different structure compared to the manufacturer's data given in Figure 6.3, with the presence of a thin SiO_2 layer on the substrate which implies that the substrate might be affected to air exposure before GST deposition. However, this thin layer of SiO_2 has no significant impact on the results. The analysis shows that the annealing process leads to changes in the thickness, density and roughness of the GST and carbon layers. We notice an increase in the thicknesses, roughnesses and densities of the GST and SiO_2 layers; for the carbon layer, only the thickness increased, while the roughness and the density decreased. As a conclusion, these variations between the as-deposited and annealed samples confirm that the annealing process significantly modifies the physical properties of the layers.
The application of the Bootstrap combined approach with the fundamental parameters and solid angles uncertainties shows relative uncertainties between 3.3 % and 5.9 % with the highest uncertainties observed in the parameters of the capping layer for both samples. This is followed by the uncertainties in the parameters of the GST layers, and finally, the uncertainties in the parameters of the SiO_2 layer which are the lowest.

6.2.2 Tantalum-based thin films

In this part of the study, the focus is on using GIXRF-XRR techniques to analyze Ta_2O_5 thin films doped with Fe_2O_3 and Y_2O_3. The objective is to compare the concentration of doping elements in the thin films calculated using GIXRF-XRR, with the manufacturer's reported values in order to validate the precision and reliability of the manufacturing processes used.

6.2.2.1 Ta_2O_5 doped with Fe_2O_3

For the XRF measurement of Ta_2O_5 doped with Fe_2O_3, a 120 second acquisition time was used, with the setup ensuring a photon flux of $3.21 \times 10^8\, s^{-1}$ at the XRF excitation energy of

10 keV using a height slit of 0.3 mm. The incident photon energy was selected to excite the K_α lines of Fe and L_α lines of Ta. The X-ray reflectivity was subsequently measured at 8 keV to benefit from higher photon flux. The resulting XRR and GIXRF measured and fitted curves of Ta-L_α and Fe-K_α are presented in Figures 6.16 and 6.17. The good agreement between the fitted and measured XRR and GIXRF data implies that the elemental distribution within the sample with the thicknesses, roughnesses and densities obtained has been correctly accounted for in the model. This agreement indicates that the structural parameters and doping level of the Ta_2O_5 with Fe_2O_3 film, as calculated by the model, are likely accurate representation of the sample's true properties.

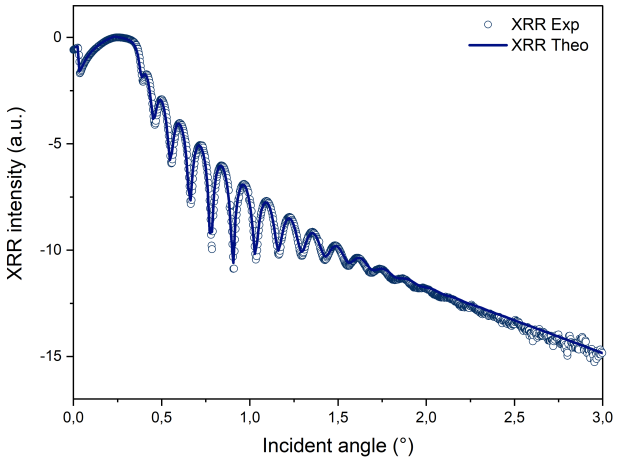

Figure 6.16: XRR scans and fit for the Ta_2O_5 sample doped with Fe_2O_3.

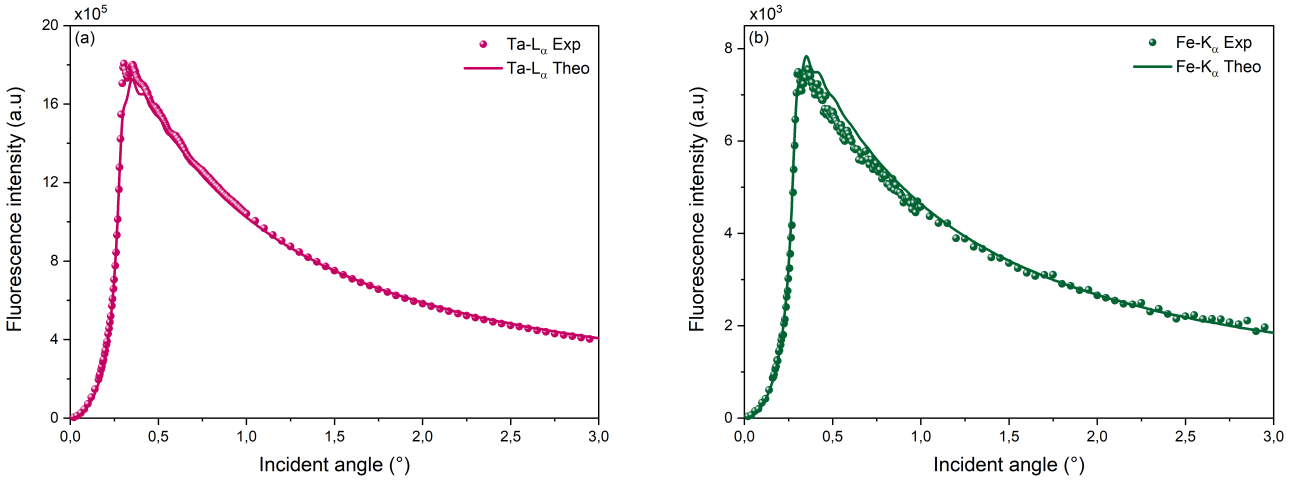

Figure 6.17: GIXRF for the Ta_2O_5 sample doped with Fe_2O_3. Scans and fit of Ta-L_α (a) and Fe-K_α (b). The circles represent the measurement data and the lines represent the fits.

The sample structure of Ta_2O_5 doped with Fe_2O_3 with the doping concentration obtained with GIXRF-XRR and the associated uncertainties, compared with the manufacturer data are presented in Table 6.5.

Table 6.5: Comparison between the GIXRF-XRR results and the manufacturer's data of the sample structure parameters of Ta_2O_5 layer doped with Fe_2O_3 with the associated uncertainties.

	Composition	Thickness (nm)	Density (g/cm^3)	Doping concentration (%)	Roughness (nm)
Manufacturer's data	Ta_2O_5/Fe_2O_3	32	8.18	0.1	-
GIXRF-XRR	$Ta_2O_{5.03}Fe_{0.018}$	32.1(17)	7.98(42)	0.32	1.14(6)

The structural characteristics and doping concentration of the Ta_2O_5 layer doped with Fe_2O_3 from GIXRF-XRR show slight differences compared to the manufacturer's data. The calculated thickness of the layer is 32.1(17) nm, aligning closely with the manufacturer's reported thickness of 32 nm. The density, as determined by GIXRF-XRR, is 7.98(42) g/cm^3, slightly lower than the reference value 8.18 g/cm^3 [198]. However, the calculated doping concentration of 0.32 % significantly differs from the manufacturer's estimation of 0.1 %. This difference may be a result of doping procedures that were inaccurate or poorly controlled, or it may be due to inhomogeneities in the dopant distribution used during the sample's fabrication. Regarding the surface roughness, GIXRF-XRR analysis provides a value of 1.14(6) nm, while no specific value is provided by the manufacturer. An additional thin SiO_2 layer, was detected using combined GIXRF-XRR with a thickness of 3.00(15) nm, roughness of 0.39(2) nm, and a density of 2.19(11) g/cm^3. The presence of SiO_2 layer is an indicator of the oxidation of the substrate caused by environmental exposure or could be a result of the manufacturing process itself. The derived uncertainties on the sample structure from Bootstrap analysis, including uncertainties on the fundamental parameters and the solid angle, are around of 5 % for the thickness, 5.3 % for the density, and 5.3 % for the roughness, showing the performance of the GIXRF-XRR technique used. The results from the GIXRF-XRR analysis demonstrate the importance of such precise and detailed characterization techniques in thin film characterization. The differences and the additional SiO_2 layer identified, provide critical insights for improving the manufacturing process, ensuring the resulting product corresponds to the intended specifications.

6.2.2.2 Ta_2O_5 doped with Y_2O_3

For the characterization of the Ta_2O_5 layer doped with Y_2O_3, a different set of measurement parameters was employed. The acquisition time for the XRF measurement was set at 30 seconds. To excite the L_α lines of Ta, the XRF was measured at 10 keV, with the setup ensuring a photon flux of $3.29 \times 10^8\,s^{-1}$ through a 0.3 mm height slit. Subsequently, the XRF was also measured at 18 keV to excite the K_α lines of Y, with a photon flux of $4.8 \times 10^8\,s^{-1}$. While at both energies, it is also possible to excite the L lines of Y, however, we use the K_α lines as they are more intense and can provide better sensitivity for the characterization process. The X-ray reflectivity (XRR) was measured at an energy of 8 keV. The corresponding XRR and GIXRF results for Ta-L_α and Y-K_α, both measured and fitted, are presented in Figures 6.18 and 6.19.

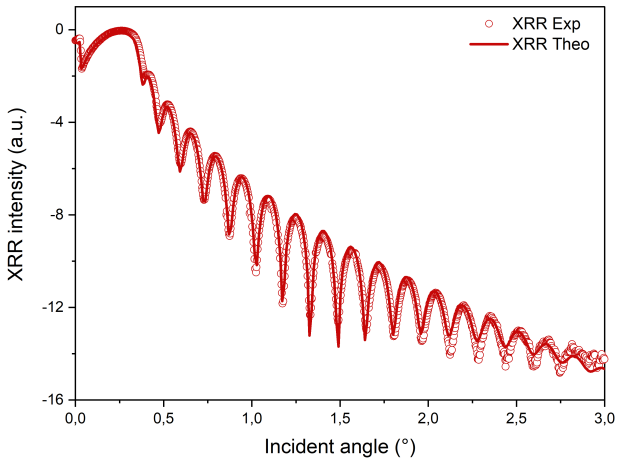

Figure 6.18: XRR scans and fit for the Ta_2O_5 sample doped with Y_2O_3.

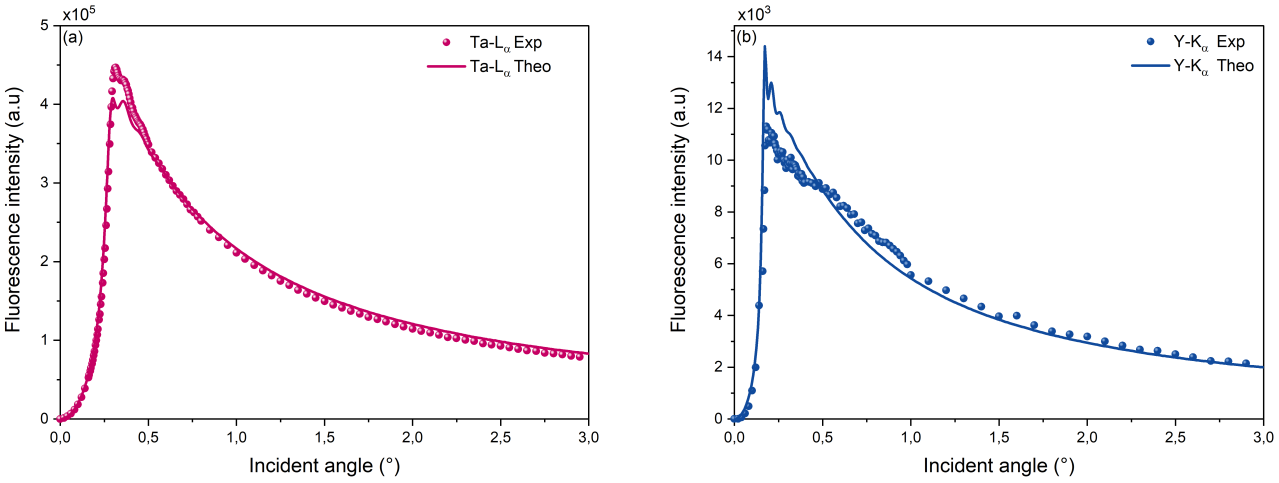

Figure 6.19: GIXRF of the Ta_2O_5 sample doped with Y_2O_3. Scans and fit of Ta-L_α (a) and Y-K_α (b). The circles represent the measurement data and the lines represent the fits.

The XRR and GIXRF measurements for the Ta_2O_5 sample doped with Y_2O_3 provided consistent results for the XRR and the Ta-L_α line, indicating a strong agreement between the model obtained by GIXRF-XRR analysis and the actual structural parameters of the sample. However, for the GIXRF analysis of the Y-K_α, the fit was less coherent. The observed difference can be related to multiple factors. First, it can be a result of the lower photon flux used to excite the Y-K_α lines compared to the Ta-L_α lines. A decrease in the incident photon flux results in a reduction of the signal-to-noise ratio, which could cause inaccuracies in the spectra processing. In addition this difference can be due to the lower doping concentration of Y in the sample, making it challenging to obtain a well-resolved GIXRF signal, or to the inhomogeneous distribution of Y dopants within the sample, which can impact the accuracy of the fitting using the model. Table 6.6 presents a comparison of the sample structure of Ta_2O_5 doped with Y_2O_3, showing the doping concentration values provided by the manufacturer's data and those obtained through combined GIXRF-XRR with their respective uncertainties.

Table 6.6: Comparison between the GIXRF-XRR results and the manufacturer's data of the sample structure parameters of Ta_2O_5 layer doped with Y_2O_3 with the associated uncertainties.

	Composition	Thickness (nm)	Density (g/cm^3)	Doping concentration (%)	Roughness (nm)
Manufacturer's data	Ta_2O_5/Y_2O_3	28	8.18	6	-
GIXRF-XRR	$Ta_2O_{5.09}Y_{0.06}$	27.6(21)	7.30(49)	0.95	0.69(5)

For the Ta_2O_5 doped with Y_2O_3, the results obtained by GIXRF-XRR reveal minor differences compared to the manufacturer's specifications. The measurements determined the layer thickness to be 27.6(21) nm, close to the manufacturer's value of 28 nm. However, the calculated density was 7.30(49) g/cm^3, also lower than the reference value 8.18 g/cm^3. The roughness is 0.69(5) nm, with no equivalent data provided by the manufacturer. In terms of doping concentration, a higher difference was observed between the doping concentration of 0.9 % obtained by GIXRF-XRR and the concentration of 6.0 % targeted by the manufacturer. As mentioned for Ta_2O_5 doped with Fe_2O_3, this variation may indicate inaccuracies in the doping procedures or possible inhomogeneities in the distribution of yttrium dopants within the sample. Additionally, GIXRF-XRR also detected the presence of a thin SiO_2 layer. This layer, with a thickness of 3.00(21) nm, density of 2.19(15) g/cm^3 and roughness of 0.36(2) nm, is the result of either environmental exposure of the Si substrate or the manufacturing process. Furthermore, the uncertainties calculated in the structural parameters for theTa_2O_5 layer doped with Y_2O_3 are: 7.6 % for thickness, 6.7 % for density and 7.2 % for roughness.
When comparing the uncertainties in structural parameters of the two tantalum-based samples, it is evident that the Ta_2O_5 doped with Y_2O_3 exhibits larger uncertainties. These discrepancies may arise from using two different excitation energies for XRF measurements, introducing additional complexity and increasing the potential for variations in the measurement process. However, despite the larger uncertainties, GIXRF-XRR technique still provides valuable and reasonably accurate characterization of the sample structure and composition.
As a conclusion of this chapter, we performed a combined analysis for the characterization of multilayered materials based on GST and Ta. The combined analysis and the application of the uncertainty calculation method, demonstrated promising results of combined analysis GIXRF-XRR thanks to the strong agreement between the experimental data and the fit, as well as the relatively low values of uncertainties. The analysis was also able to reveal structural differences for all the samples from manufacturer's data, and the impact of annealing on the structural properties of GST samples.

Conclusion and perspectives

In this thesis, we presented and examined into details the performances of the reference-free combined GIXRF-XRR analysis that can be used for the accurate characterization of thin films used to develop innovative materials. This combination is necessary as GIXRF is sensitive to elemental density, providing a knowledge of elemental depth distribution, while XRR is sensitive to electronic density, contributing in the calculation of density, thickness, and roughness. This was illustrated by characterizing different multilayers samples composed of GeSbTe (GST) and tantalum (Ta)-based materials. The experimental results showed significant structural differences when compared to the manufacturer's data for both types of samples. The structural differences observed by the combined analysis of GIXRF-XRR, demonstrated the advantages of this method in the characterization of material properties. The effect of annealing GST samples was also studied in the thesis. The annealing process, involving heating the samples to specified temperatures, led to changes in sample structure parameters. These changes were detected through multiple indicators, including changes in fringe numbers, positions, amplitudes, as well as the overall shape and intensity of the reflectivity curve which reveals modifications in the thickness, roughness, and density of the layers. In addition the heating process led to an increase in the layers thickness which was detected also by the increase in the fluorescence intensity of the constitutive elements. The observed increase in both thickness and density of the annealed layers can be primarily attributed to the thermally-induced rearrangement of atoms and possible phase transitions within the material.
In addition, an uncertainty calculation method using a Monte Carlo-based approach was integrated to compute uncertainties in the solid angle of detection and fundamental parameters. To calculate the uncertainties on the sample parameters, a Bootstrap resampling method based on Monte Carlo simulation, was also integrated in the analysis software, which enabled statistical inference on the dataset. This uncertainty budget was finally integrated in the combined analysis software for the estimation and validation of the analytical results.
Both, GIXRF and XRR analysis exhibited strong agreement between the fit and measurement for GST and Ta-based thin films, which showed the accuracy of thickness, roughness, density and elemental composition values. Furthermore, the uncertainty calculation method, showed relatively low uncertainties values in the sample structural parameters ranged between $\sim$3.3 % and 5.9 %. These uncertainties were associated with different parameters within different layers of the samples. The observed low percentage values are promising as they indicate the precision of the measurements and the reliability of the data obtained. The combination of GIXRF-XRR, with the new uncertainty calculation methodology, demonstrated the potential of this approach as an accurate technique for material characterization.
In the studies conducted in this thesis, it is essential to consider various possibilities for further enhancing the methodology used to calculate uncertainty. For the solid angle, the approach

in this thesis involved the calculation of uncertainties based only on the geometrical factors of the detector. However, to complete the calculation, it can be useful to include other sources of uncertainty. These sources includes uncertainties associated with the incidence angle which arise from uncertainties in the rotational motors and misalignment of the sample that could also lead to a mispositioning of the footprint. Nevertheless, these inaccuracies are expected to have a lower influence compared to the ones already taken into account.
The uncertainties on the fundamental parameters are still the main contribution in the evaluation of the uncertainties associated with the results of the combined XRR-GIXRF analysis, which supports the need for a more reliable database. As an example, in this thesis we also determined some fundamental parameters for two elements of interest in the XRR-GIXRF combined analysis performed earlier. We experimentally determined the K- fluorescence yields for Fe and Y with their associated uncertainties in addition to their mass attenuation coefficients and photoelectric absorption coefficients. These new experimental results, could be taken into count in future compilations of atomic databases.
Moving towards the combined XRR-GIXRF analysis, implementing repeated measurements at a constant incidence angle is recommended. Although this approach might be time-intensive, it is feasible and could significantly reduce uncertainties.
Lastly, to improve the energy resolution of the fluorescence spectra, we developed a high resolution, wavelength dispersive spectrometer (WDS). The WDS prototype includes a flat crystal and high-resolution back-thinned CCD image sensor with a mechanical linkage, enabling the adjustment of the energy detection range. Moreover, different crystal types can be used, allowing for the detection of a wide range of energies at specific Bragg angles. The WDS was tested in an in-air configuration to measure the fluorescence spectrum of Cu, achieving a resolution of 2 eV, much better than the EDS. However, the prototype presents some challenges, such as low signal intensities and inefficient collection of diffracted X-rays, which may affect its sensitivity and limit its analytical capabilities. Therefore, future work should focus on enhancing the setup, through the inclusion of polycapillary optics to collimate and collect the X-rays more effectively, leading to a better signal-to-noise ratio and overall sensitivity. Furthermore, future adaptations should focus on upgrading the WDS for its implementation into the CASTOR goniometer for GIXRF measurements with significantly improved energy resolution.

Bibliography

[1] G. Hon and B. R. Goldstein, "JJ Thomson's plum–pudding atomic model: The making of a scientific myth," *Annalen der Physik*, vol. 525, no. 8-9, pp. A129–A133, 2013.

[2] J. L. Heilbron, "Rutherford–Bohr atom," *American Journal of Physics*, vol. 49, no. 3, pp. 223–231, 1981.

[3] S. Ortoli and J.-P. Pharabod, *Le cantique des quantiques: le monde existe-t-il?* La découverte, 2020.

[4] R. F. Mould, "The early history of X-ray diagnosis with emphasis on the contributions of physics 1895-1915," *Physics in Medicine & Biology*, vol. 40, no. 11, p. 1741, 1995.

[5] B. Beckhoff, B. Kanngießer, N. Langhoff, R. Wedell, and H. Wolff, *Handbook of practical X-ray fluorescence analysis*. Springer Science & Business Media, 2007.

[6] R. Behling, "X-ray tubes development–IOMP history of medical physics," *Med. Phys. Int*, vol. 1, pp. 8–55, 2018.

[7] R. van Grieken and A. Markowicz, *Handbook of X-ray Spectrometry*. CRC press, 2001.

[8] M. Eckert, "Max von laue and the discovery of X–ray diffraction in 1912," 2012.

[9] R. G. Egdell and E. Bruton, "Henry moseley, X-ray spectroscopy and the periodic table," *Philosophical Transactions of the Royal Society A*, vol. 378, no. 2180, p. 20190302, 2020.

[10] K. Tsuji, J. Injuk, and R. van Grieken, *X-ray spectrometry: recent technological advances*. John Wiley & Sons, 2005.

[11] M. Massimi, *Pauli's exclusion principle: The origin and validation of a scientific principle*. Cambridge University Press, 2005.

[12] R. Cesareo, "X-ray physics: Interaction with matter, production, detection," *La Rivista del Nuovo Cimento*, vol. 23, no. 7, pp. 1–231, 2000.

[13] J. C. Fuggle and N. Mårtensson, "Core-level binding energies in metals," *Journal of Electron Spectroscopy and Related Phenomena*, vol. 21, no. 3, pp. 275–281, 1980.

[14] R. D. Deslattes, E. G. Kessler, P. Indelicato, L. de Billy, E. Lindroth, and J. Anton, "X-ray transition energies: new approach to a comprehensive evaluation," *Reviews of modern physics*, vol. 75, no. 1, pp. 35–99, 2003.

[15] F. P. Larkins, "Semiempirical auger-electron energies for elements $10 \leq Z \leq 100$," *Atomic data and nuclear data tables*, vol. 20, no. 4, pp. 311–387, 1977.

[16] R. Klockenkämper and A. von Bohlen, *Total-reflection X-ray fluorescence analysis and related methods*. John Wiley & Sons, 2014.

[17] R. Jenkins, *Quantitative X-ray spectrometry*. CRC press, 1995.

[18] M. Siegbahn and G. A. Lindsay, *The Spectroscopy of X-rays*. Oxford University Press, H. Milford, 1925.

[19] T. Vo-Dinh, *Handbook of spectroscopy*. John Wiley & Sons, 2006.

[20] R. Jenkins, R. Manne, R. Robin, and C. Sénémaud, "IUPAC–nomenclature system for X–ray spectroscopy," *X–Ray Spectrometry*, vol. 20, no. 3, pp. 149–155, 1991.

[21] T. P. Schreiber and Wims, "Relative intensity factors for K, L and M shell X–ray lines," *X–Ray Spectrometry*, vol. 11, no. 2, pp. 42–45, 1982.

[22] M. Rodrigues and M. Loidl, "L X-ray satellite effects on the determination of photon emission intensities of radionuclides," *Applied Radiation and Isotopes*, vol. 109, pp. 570–575, 2016.

[23] M. Loidl, M. Rodrigues, and R. Mariam, "Measurement of the electron capture probabilities of ^{55}Fe with a metallic magnetic calorimeter," *Applied Radiation and Isotopes*, vol. 134, pp. 395–398, 2018.

[24] W. Bambynek, B. Crasemann, R. W. Fink, H.-U. Freund, H. Mark, C. D. Swift, R. E. Price, and P. V. Rao, "X-ray fluorescence yields, Auger, and Coster-Kronig transition probabilities," *Reviews of modern physics*, vol. 44, no. 4, p. 716, 1972.

[25] M. O. Krause, "Atomic radiative and radiationless yields for K and L shells," *Journal of physical and chemical reference data*, vol. 8, no. 2, pp. 307–327, 1979.

[26] J. R. Connolly, "The interaction of X–rays with matter and radiation safety," *Introduction to X-ray powder diffraction*, pp. 1–14, 2012.

[27] L. Nevot and P. Croce, "Caractérisation des surfaces par réflexion rasante de rayons x. Application à l'étude du polissage de quelques verres silicates," *Revue de Physique appliquée*, vol. 15, no. 3, pp. 761–779, 1980.

[28] A. R. West, *Solid state chemistry and its applications*. John Wiley & Sons, 2014.

[29] C. Hammond, "The basics of Crystallography and Diffraction (2nd edn)," 2002.

[30] Y. Waseda, E. Matsubara, and K. Shinoda, *X-ray diffraction crystallography: introduction, examples and solved problems*. Springer Science & Business Media, 2011.

[31] L. R. Elton and D. F. Jackson, "X-ray diffraction and the Bragg law," *American Journal of Physics*, vol. 34, no. 11, pp. 1036–1038, 1966.

[32] R. L. Snyder, "X-ray Diffraction," in *X–ray Characterization of Materials*, pp. 1–103, John Wiley & Sons, Ltd, 1999.

[33] W. H. Bragg and W. L. Bragg, "The reflection of X-rays by crystals," *Proceedings of the Royal Society of London. Series A, Containing Papers of a Mathematical and Physical Character*, vol. 88, no. 605, pp. 428–438, 1913.

[34] M. L. F. Nascimento, "Brief history of X-ray tube patents," *World Patent Information*, vol. 37, pp. 48–53, 2014.

[35] G. Z. Yue, Q. Qiu, B. Gao, Y. Cheng, J. Zhang, H. Shimoda, S. Chang, J. P. Lu, and O. Zhou, "Generation of continuous and pulsed diagnostic imaging X-ray radiation using a carbon-nanotube-based field-emission cathode," *Applied Physics Letters*, vol. 81, no. 2, pp. 355–357, 2002.

[36] F. E. Zink, "X-ray tubes," *Radiographics: a review publication of the Radiological Society of North America, Inc*, vol. 17, no. 5, pp. 1259–1268, 1997.

[37] B. R. David, H. Barschdorf, V. Doormann, R. Eckart, G. Harding, J.-P. Schlomka, A. Thran, P. Bachmann, and P. Flisikowski, "Liquid-metal anode X-ray tube," in *Laser-Generated and Other Laboratory X-Ray and EUV Sources, Optics, and Applications*, SPIE Proceedings, p. 432, SPIE, 2003.

[38] R. Z. Bachrach, *Synchrotron radiation research: advances in surface and interface science techniques*. Springer Science & Business Media, 2012.

[39] M.-C. Lépy, L. Ferreux, and J. Plagnard, "A tunable monochromatic X-ray source for metrological studies in the 1–20 keV energy range: application to the measurement of attenuation coefficients," *Applied Radiation and Isotopes*, vol. 60, no. 2-4, pp. 159–165, 2004.

[40] C. Bonnelle, P. Jonnard, J.-M. André, A. Avila, D. Laporte, H. Ringuenet, M. Lépy, J. Plagnard, L. Ferreux, and J. Protas, "SOLEX: a tunable monochromatic X-ray source in the 1–20keV energy range for metrology," *Nuclear Instruments and Methods in Physics Research Section A: Accelerators, Spectrometers, Detectors and Associated Equipment*, vol. 516, no. 2-3, pp. 594–601, 2004.

[41] P. Brouwer, "Theory of XRF," *Almelo, Netherlands: PANalytical BV*, 2006.

[42] M. Loidl, M. Rodrigues, B. Censier, S. Kowalski, X. Mougeot, P. Cassette, T. Branger, and D. Lacour, "First measurement of the beta spectrum of ^{241}Pu with a cryogenic detector," *Applied radiation and isotopes : including data, instrumentation and methods for use in agriculture, industry and medicine*, vol. 68, no. 7-8, pp. 1454–1458, 2010.

[43] E. Rutherford and H. Geiger, "An electrical method of counting the number of α-particles from radio-active substances," *Proceedings of the Royal Society of London. Series A, Containing Papers of a Mathematical and Physical Character*, vol. 81, no. 546, pp. 141–161, 1908.

[44] G. J. Johnson, "Encyclopedia of Analytical Science," *Reference Reviews*, 2005.

[45] G.-Y. Chen and Y.-F. Wang, eds., *Soft X-ray detectors for pulsar navigation*, vol. 1, IOP Publishing, 2017.

[46] J. W. Boag, "Ionization chambers," *The dosimetry of ionizing radiation*, vol. 2, pp. 169–243, 1987.

[47] R. Korde, C. Prince, D. Cunningham, R. E. Vest, and E. Gullikson, "Present status of radiometric quality silicon photodiodes," *Metrologia*, vol. 40, no. 1, pp. 145–149, 2003.

[48] E. M. Gullikson, R. Korde, L. R. Canfield, and R. E. Vest, "Stable silicon photodiodes for absolute intensity measurements in the VUV and soft X-ray regions," *Journal of Electron Spectroscopy and Related Phenomena*, vol. 80, pp. 313–316, 1996.

[49] J. P. Kirkland, T. Jach, R. A. Neiser, and C. E. Bouldin, "PIN diode detectors for synchrotron X-rays," *Nuclear Instruments and Methods in Physics Research Section A: Accelerators, Spectrometers, Detectors and Associated Equipment*, vol. 266, no. 1-3, pp. 602–607, 1988.

[50] V. D. Bonifacio and R. F. Pires, "Photodiodes: Principles and recent advances," *Journal of Materials NanoScience*, vol. 6, no. 2, pp. 38–46, 2019.

[51] U. Kramar, "X-ray fluorescence spectrometers," in *Encyclopedia of Spectroscopy and Spectrometry (Second Edition)* (J. C. Lindon, ed.), pp. 2989–2999, Oxford: Academic Press, 1999.

[52] D. Pennicard, B. Pirard, O. Tolbanov, and K. Iniewski, "Semiconductor materials for X-ray detectors," *MRS Bulletin*, vol. 42, no. 6, pp. 445–450, 2017.

[53] M. U. Khandaker, "High purity germanium detector in gamma-ray spectrometry," *International Journal of Fundamental Physical Sciences*, vol. 1, no. 2, pp. 42–46, 2011.

[54] L. Strüder, C. Fiorini, E. Gatti, R. Hartmann, P. Holl, N. Krause, P. Lechner, A. Longoni, G. Lutz, and J. Kemmer, "High resolution non dispersive X-ray spectroscopy with state of the art silicon detectors," in *Modern Developments and Applications in Microbeam Analysis*, pp. 11–19, Springer, 1998.

[55] G. Lutz, "Silicon drift and pixel devices for X-ray imaging and spectroscopy," *Journal of synchrotron radiation*, vol. 13, no. 2, pp. 99–109, 2006.

[56] L. Cerrito, "Semiconductor Detectors," in *Radiation and Detectors* (L. Cerrito, ed.), Graduate Texts in Physics, pp. 137–153, Springer International Publishing, 2017.

[57] L. Strüder, "High-resolution imaging X-ray spectrometers," *Nuclear Instruments and Methods in Physics Research Section A: Accelerators, Spectrometers, Detectors and Associated Equipment*, vol. 454, no. 1, pp. 73–113, 2000.

[58] R. Hui, "Chapter 4 - photodetectors," in *Introduction to Fiber-Optic Communications* (R. Hui, ed.), pp. 125–154, Academic Press, 2020.

[59] P. Zhang, "Chapter 3 - Sensors and actuators," in *Advanced Industrial Control Technology* (P. Zhang, ed.), pp. 73–116, Oxford: William Andrew Publishing, 2010.

[60] S. J. B. Reed and N. G. Ware, "Quantitative electron microprobe analysis using a lithium drifted silicon detector," *X–Ray Spectrometry*, vol. 2, no. 2, pp. 69–74, 1973.

[61] D. E. Newbury and N. W. M. Ritchie, "Performing elemental microanalysis with high accuracy and high precision by scanning electron microscopy/silicon drift detector energy-dispersive X-ray spectrometry (sem/sdd-eds)," *Journal of materials science*, vol. 50, pp. 493–518, 2015.

[62] J. I. Goldstein, D. E. Newbury, J. R. Michael, N. W. M. Ritchie, J. H. J. Scott, and D. C. Joy, *Scanning electron microscopy and X-ray microanalysis*. Springer, 2017.

[63] R. Fitzgerald, K. Keil, and K. F. J. Heinrich, "Solid-state energy-dispersion spectrometer for electron-microprobe X-ray analysis," *Science*, vol. 159, no. 3814, pp. 528–530, 1968.

[64] U. Fano, "Ionization yield of radiations. II. the fluctuations of the number of ions," *Physical review*, vol. 72, no. 1, p. 26, 1947.

[65] L. Maniguet, F. Robaut, A. Meuris, F. Roussel-Dherbey, and F. Chariot, "X-ray microanalysis: the state of the art of sdd detectors and wds systems on scanning electron microscopes (sem)," *IOP Conference Series: Materials Science and Engineering*, vol. 32, p. 012015, 2012.

[66] R. Tanaka, K. Yuge, J. Kawai, and H. Alawadhi, "Artificial peaks in energy dispersive X–ray spectra: sum peaks, escape peaks, and diffraction peaks," *X–Ray Spectrometry*, vol. 46, no. 1, pp. 5–11, 2017.

[67] J. Hoszowska, J.-C. Dousse, J. Kern, and C. Rhême, "High-resolution von Hamos crystal X-ray spectrometer," *Nuclear Instruments and Methods in Physics Research Section A: Accelerators, Spectrometers, Detectors and Associated Equipment*, vol. 376, no. 1, pp. 129–138, 1996.

[68] J. Goldstein, D. E. Newbury, and D. B. Williams, *X-Ray spectrometry in electron beam instruments*. Springer Science & Business Media, 2012.

[69] E. Spiller, *Soft X-ray optics*. SPIE Optical Engineering Press, 1994.

[70] E. O. Baronova, M. M. Stepanenko, and N. R. Pereira, "Cauchois–johansson X-ray spectrograph for 1.5–400 kev energy range," *Review of Scientific Instruments*, vol. 72, no. 2, p. 1416, 2001.

[71] T. Tochio, Y. Ito, and K. Omote, "Broadening of the X-ray emission line due to the instrumental function of the double-crystal spectrometer," *Physical Review A*, vol. 65, no. 4, 2002.

[72] P. Jagodziński, M. Pajek, D. Banaś, A. Kubala-Kukuś, J. Szlachetko, M. Cotte, and M. Salomé, "Properties of polycapillary optics dedicated to low-energy parallel-beam wavelength-dispersive spectrometers for synchrotron-based X-ray fluorescence study," *Optics express*, vol. 29, no. 17, pp. 27193–27211, 2021.

[73] J. K. Kowalska, F. A. Lima, C. J. Pollock, J. A. Rees, and S. DeBeer, "A practical guide to high-resolution X-ray Spectroscopic Measurements and their Applications in Bioinorganic Chemistry," *Israel Journal of Chemistry*, vol. 56, no. 9-10, pp. 803–815, 2016.

[74] J. Trincavelli, S. Limandri, A. Carreras, and R. Bonetto, "Experimental Method to Determine the Absolute Efficiency Curve of a Wavelength Dispersive Spectrometer," *Microscopy and Microanalysis*, vol. 14, no. 4, pp. 306–314, 2008.

[75] B. L. Henke, E. M. Gullikson, and J. C. Davis, "X-ray interactions: photoabsorption, scattering, transmission, and reflection at E= 50-30,000 eV, Z= 1-92," *Atomic data and nuclear data tables*, vol. 54, no. 2, pp. 181–342, 1993.

[76] M. Hall, "X-Ray Fluorescence-Energy Dispersive (ED-XRF) and wavelength dispersive (WD-XRF) spectrometry," in *The Oxford Handbook of Archaeological Ceramic Analysis* (A. Hunt and M. Hall, eds.), pp. 341–362, Oxford University Press, 2016.

[77] M. Tanaka, M. Takeguchi, and K. Furuya, "X-ray analysis and mapping by wavelength dispersive X-ray spectroscopy in an electron microscope," *Ultramicroscopy*, vol. 108, no. 11, pp. 1427–1431, 2008.

[78] T. MORENO, "Xrvision," 1994.

[79] Y. Ménesguen and M.-C. Lépy, "Characterization of the Metrology beamline at the SOLEIL synchrotron and application to the determination of mass attenuation coefficients of Ag and Sn in the range $3.5 \leq e \leq 28$ keV," *X–Ray Spectrometry*, vol. 40, no. 6, pp. 411–416, 2011.

[80] Y. Ménesguen, M. Gerlach, B. Pollakowski, R. Unterumsberger, M. Haschke, B. Beckhoff, and M.-C. Lépy, "High accuracy experimental determination of copper and zinc mass attenuation coefficients in the 100 eV to 30 keV photon energy range," *Metrologia*, vol. 53, no. 1, pp. 7–17, 2015.

[81] Y. Ménesguen, B. Boyer, H. Rotella, J. Lubeck, J. Weser, B. Beckhoff, D. Grötzsch, B. Kanngiesser, A. Novikova, and E. Nolot, "CASTOR, a new instrument for combined XRR–GIXRF analysis at SOLEIL," *X–Ray Spectrometry*, vol. 46, no. 5, pp. 303–308, 2017.

[82] J. Lubeck, B. Beckhoff, R. Fliegauf, I. Holfelder, P. Hönicke, M. Müller, B. Pollakowski, F. Reinhardt, and J. Weser, "A novel instrument for quantitative nanoanalytics involving complementary X-ray methodologies," *Review of Scientific Instruments*, vol. 84, no. 4, p. 045106, 2013.

[83] J. Lubeck, M. Bogovac, B. Boyer, B. Detlefs, D. Eichert, R. Fliegauf, D. Grötzsch, I. Holfelder, P. Hönicke, W. Jark, R. B. Kaiser, B. Kanngießer, A. G. Karydas, J. J. Leani, M. C. Lépy, L. Lühl, Y. Ménesguen, A. Migliori, M. Müller, B. Pollakowski, M. Spanier, H. Sghaier, G. Ulm, J. Weser, and B. Beckhoff, "A new generation of X-ray spectrometry UHV instruments at the SR facilities BESSY II, ELETTRA and SOLEIL," *AIP Conference Proceedings*, vol. 1741, no. 1, 2016.

[84] P. Troussel and N. Coron, "BOLUX: A cryogenic electrical-substitution radiometer as high accuracy primary detector in the 150–11000 eV range," *Nuclear Instruments and Methods in Physics Research Section A: Accelerators, Spectrometers, Detectors and Associated Equipment*, vol. 614, no. 2, pp. 260–270, 2010.

[85] V. H. Elvira, M.-C. Lépy, and Y. Ménesguen, "Primary calibration of photodiodes with monochromatic X–ray beams using an electrical–substitution radiometer," *X–Ray Spectrometry*, 2022.

[86] OptoDiode, "https://optodiode.com/photodiodes-axuv-detectors.html."

[87] Hamamatsu, "https://www.hamamatsu.com/jp/en/product/optical-sensors/photodiodes/si-photodiodes/s8193.html."

[88] Y. Ménesguen and M.-C. Lépy, "Efficiency calibration and surface mapping of an energy-dispersive detector with SOLEX: A compact tunable monochromatic X-ray source," *Nuclear Instruments and Methods in Physics Research Section A: Accelerators, Spectrometers, Detectors and Associated Equipment*, vol. 695, pp. 193–196, 2012.

[89] H. R. Huff, H. Iwai, and H. Richter, *Silicon Materials Science and Technology X*. Electrochemical Society, 2006.

[90] J. Niinistö, M. Putkonen, L. Niinistö, S. L. Stoll, K. Kukli, T. Sajavaara, M. Ritala, and M. Leskelä, "Controlled growth of HfO_2 thin films by atomic layer deposition from cyclopentadienyl-type precursor and water," *Journal of Materials Chemistry*, vol. 15, no. 23, pp. 2271–2275, 2005.

[91] M. Krämer, A. von Bohlen, C. Sternemann, M. Paulus, and R. Hergenröder, "X-ray standing waves: a method for thin layered systems," *J. Anal. At. Spectrom.*, vol. 21, no. 11, pp. 1136–1142, 2006.

[92] A. von Bohlen, "Total reflection X-ray fluorescence and grazing incidence X-ray spectrometry-ttols for micro-and surface analysis," *Spectrochimica Acta. Part B, Atomic Spectroscopy*, vol. 64, no. 9, pp. 821–832, 2009.

[93] A. Gupta, D. Kumar, and C. Meneghini, "Interface structure in magnetic multilayers using X-ray standing waves," *Physical Review B*, vol. 75, no. 6, p. 064424, 2007.

[94] K. C. Westfold, "The Polarization of Synchrotron Radiation," *Astrophysical Journal*, vol. 130, p. 241, 1959.

[95] Arthur H. Compton, "CXVII. the total reflexion of X-rays," *The London, Edinburgh, and Dublin Philosophical Magazine and Journal of Science*, vol. 45, no. 270, pp. 1121–1131, 1923.

[96] J. Wernecke, A. G. Shard, and M. Krumrey, "Traceable thickness determination of organic nanolayers by X-ray reflectometry," *Surface and interface analysis*, vol. 46, no. 10-11, pp. 911–914, 2014.

[97] P. Colombi, D. K. Agnihotri, V. E. Asadchikov, E. Bontempi, D. K. Bowen, C. H. Chang, L. E. Depero, M. Farnworth, T. Fujimoto, A. Gibaud, M. Jergel, M. Krumrey, T. A. Lafford, A. Lamperti, T. Ma, R. J. Matyi, M. Meduna, S. Milita, K. Sakurai, L. Shabel'nikov, A. Ulyanenkov, A. van der Lee, and C. Wiemer, "Reproducibility in X-ray reflectometry: results from the first world-wide round-robin experiment," *Journal of Applied Crystallography*, vol. 41, no. 1, pp. 143–152, 2008.

[98] H. Kiessig, "Interferenz von röntgenstrahlen an dünnen schichten," *Annalen der Physik*, vol. 402, no. 7, pp. 769–788, 1931.

[99] L. N. Koppel and L. Parobek, "Thin-film metrology by rapid X-ray reflectometry," in *The 1998 international conference on characterization and metrology for ULSI technology*, pp. 469–473, ASCE, 1998.

[100] J. Als-Nielsen and Des McMorrow, *Elements of modern X-ray physics*. John Wiley & Sons, 2011.

[101] P. Hönicke, B. Detlefs, E. Nolot, Y. Kayser, U. Mühle, B. Pollakowski, and B. Beckhoff, "Reference-free grazing incidence X-ray fluorescence and reflectometry as a methodology for independent validation of X-ray reflectometry on ultrathin layer stacks and a depth-dependent characterization," *Journal of Vacuum Science & Technology A*, vol. 37, no. 4, p. 041502, 2019.

[102] K. Stoev and K. Sakurai, "Recent theoretical models in grazing incidence X-ray reflectometry," *The Rigaku Journal*, vol. 14, no. 2, pp. 22–37, 1997.

[103] S. Chandran, N. Begam, and J. K. Basu, "Dispersion of polymer grafted nanoparticles in polymer nanocomposite films: Insights from surface X-ray scattering and microscopy," *Journal of Applied Physics*, vol. 116, no. 22, p. 222203, 2014.

[104] I. D. Feranchuk, S. I. Feranchuk, and A. P. Ulyanenkov, "Self-consistent approach to X-ray reflection from rough surfaces," *Physical Review B*, vol. 75, no. 8, 2007.

[105] R. Unterumsberger, B. Pollakowski, M. Müller, and B. Beckhoff, "Complementary characterization of buried nanolayers by quantitative X-ray fluorescence spectrometry under conventional and grazing incidence conditions," *Analytical chemistry*, vol. 83, no. 22, pp. 8623–8628, 2011.

[106] P. Hönicke, B. Beckhoff, M. Kolbe, D. Giubertoni, J. van den Berg, and G. Pepponi, "Depth profile characterization of ultra shallow junction implants," *Analytical and Bioanalytical Chemistry*, vol. 396, no. 8, pp. 2825–2832, 2010.

[107] P. Hönicke, B. Detlefs, M. Müller, E. Darlatt, E. Nolot, H. Grampeix, and B. Beckhoff, "Reference-free, depth-dependent characterization of nanolayers and gradient systems with advanced grazing incidence X-ray fluorescence analysis," *physica status solidi (a)*, vol. 212, no. 3, pp. 523–528, 2015.

[108] J. M. Bloch, M. Sansone, F. Rondelez, D. G. Peiffer, P. Pincus, M.-W. Kim, and P. M. Eisenberger, "Concentration profile of a dissolved polymer near the air-liquid interface: X-ray fluorescence study," *Physical review letters*, vol. 54, no. 10, p. 1039, 1985.

[109] S. Pahlke, L. Fabry, L. Kotz, C. Mantler, and T. Ehmann, "Determination of ultra trace contaminants on silicon wafer surfaces using total-reflection X-ray fluorescence TXRF 'state-of-the-art'," *Spectrochimica Acta Part B: Atomic Spectroscopy*, vol. 56, no. 11, pp. 2261–2274, 2001.

[110] G. Mankovskii and A. Pejović-Milić, "Quantification of gold nanoparticles in blood using total reflection X-ray fluorescence," *Spectrochimica Acta Part B: Atomic Spectroscopy*, vol. 194, p. 106466, 2022.

[111] T. W. Barbee Jr and W. K. Warburton, "X-ray evanescent-and standing-wave fluorescence studies using a layered synthetic microstructure," *Materials letters*, vol. 3, no. 1-2, pp. 17–23, 1984.

[112] M. J. Bedzyk, D. H. Bilderback, G. M. Bommarito, M. Caffrey, and J. S. Schildkraut, "X-ray standing waves: a molecular yardstick for biological membranes," *Science*, vol. 241, no. 4874, pp. 1788–1791, 1988.

[113] C. Weiss, J. Knoth, H. Schwenke, H. Geisler, J. Lerche, R. Schulz, and H.-J. Ullrich, "Potential of total reflection and grazing incidence XRF for contamination and process control in semiconductor fabrication," *Microchimica Acta*, vol. 133, pp. 65–68, 2000.

[114] B. Beckhoff and G. Ulm, "Determination of fluorescence yields using monochromatized undulator radiation of high spectral purity and well-known flux," *Adv. X-Ray Anal*, vol. 44, pp. 349–354, 2001.

[115] M. Müller, B. Beckhoff, G. Ulm, and B. Kanngießer, "Absolute determination of cross sections for resonant Raman scattering on silicon," *Physical Review A*, vol. 74, no. 1, 2006.

[116] M. Kolbe, B. Beckhoff, M. Krumrey, and G. Ulm, "Thickness determination for Cu and Ni nanolayers: Comparison of completely reference-free fundamental parameter-based X-ray fluorescence analysis and X-ray reflectometry," *Spectrochimica Acta Part B: Atomic Spectroscopy*, vol. 60, no. 4, pp. 505–510, 2005.

[117] B. Beckhoff, "Traceable Characterization of Nanomaterials by X-ray Spectrometry Using Calibrated Instrumentation," *Nanomaterials*, vol. 12, no. 13, 2022.

[118] B. Beckhoff, R. Fliegauf, M. Kolbe, M. Müller, J. Weser, and G. Ulm, "Reference-free total reflection X-ray fluorescence analysis of semiconductor surfaces with synchrotron radiation," *Analytical chemistry*, vol. 79, no. 20, pp. 7873–7882, 2007.

[119] H. Rotella, B. Caby, Y. Ménesguen, Y. Mazel, A. Valla, D. Ingerle, B. Detlefs, M.-C. Lépy, A. Novikova, G. Rodriguez, C. Streli, and E. Nolot, "Elemental depth profiling in transparent conducting oxide thin film by X-ray reflectivity and grazing incidence X-ray fluorescence combined analysis," *Spectrochimica Acta Part B: Atomic Spectroscopy*, vol. 135, pp. 22–28, 2017.

[120] D. Ingerle, F. Meirer, G. Pepponi, E. Demenev, D. Giubertoni, P. Wobrauschek, and C. Streli, "Combined evaluation of grazing incidence X-ray fluorescence and X-ray reflectivity data for improved profiling of ultra-shallow depth distributions," *Spectrochimica Acta Part B: Atomic Spectroscopy*, vol. 99, no. 100, pp. 121–128, 2014.

[121] S. W. King, H. Simka, D. Herr, H. Akinaga, and M. Garner, "Research Updates: The three M's (materials, metrology, and modeling) together pave the path to future nanoelectronic technologies," *APL Materials*, vol. 1, no. 4, p. 040701, 2013.

[122] G. Roebben, H. Emons, and G. Reiners, "Nanoscale Reference Materials," in *Nanotechnology Standards* (V. Murashov and J. Howard, eds.), Nanostructure Science and Technology, pp. 53–75, Springer New York, 2011.

[123] H. Ebel, R. Svagera, M. F. Ebel, A. Shaltout, and J. H. Hubbell, "Numerical description of photoelectric absorption coefficients for fundamental parameter programs," *X–Ray Spectrometry*, vol. 32, no. 6, pp. 442–451, 2003.

[124] M.-R. Lefévère and M. Montel, "Influence de l'absorption sur les Propriétés Optiques des Solides: Propagation des Ondes électromagnétiques hétérogènes, Planes et Uniformes, dans les Milieux Homogènes et Isotropes," *Optica Acta: International Journal of Optics*, vol. 20, no. 2, pp. 97–128, 1973.

[125] U. Weisbrod, R. Gutschke, J. Knoth, and H. Schwenke, "Total reflection X-ray fluorescence spectrometry for quantitative surface and layer analysis," *Applied Physics A Solids and Surfaces*, vol. 53, no. 5, pp. 449–456, 1991.

[126] H. A. Kramers, ed., *La diffusion de la lumiere par les atomes*, vol. 2, 1927.

[127] R. de L. Kronig, "On the Theory of Dispersion of X-Rays," *J. Opt. Soc. Am.*, vol. 12, no. 6, pp. 547–557, 1926.

[128] S. K. Ghose and B. N. Dev, "X-ray standing wave and reflectometric characterization of multilayer structures," *Physical Review B*, vol. 63, no. 24, p. 245409, 2001.

[129] L. G. Parratt, "Surface studies of solids by total reflection of X-rays," *Physical review*, vol. 95, no. 2, p. 359, 1954.

[130] M. K. Tiwari, G. S. Lodha, and K. J. S. Sawhney, "Applications of the 'CATGIXRF' computer program to the grazing incidence X-ray fluorescence and X-ray reflectivity characterization of thin films and surfaces," *X–Ray Spectrometry*, vol. 39, no. 2, pp. 127–134, 2010.

[131] M. J. Bedzyk and J. A. Libera, "X-ray standing wave in multilayers," in *The X-Ray Standing Wave Technique: Principles and Applications*, pp. 122–131, World Scientific, 2013.

[132] D. K. G. de Boer, "Angular dependence of X-ray fluorescence intensities," *X–Ray Spectrometry*, vol. 18, no. 3, pp. 119–129, 1989.

[133] M. Born, E. Wolf, and E. Hecht, "Principles of Optics: Electromagnetic Theory of Propagation, Interference and Diffraction of Light," *Physics Today*, vol. 53, no. 10, pp. 77–78, 2000.

[134] J. Sherman, "The theoretical derivation of fluorescent X-ray intensities from mixtures," *Spectrochimica acta*, vol. 7, pp. 283–306, 1955.

[135] A. Brunetti, M. Del Sanchez Rio, B. Golosio, A. Simionovici, and A. Somogyi, "A library for X-ray matter interaction cross sections for X-ray fluorescence applications," *Spectrochimica Acta Part B: Atomic Spectroscopy*, vol. 59, no. 10-11, pp. 1725–1731, 2004.

[136] Y. Ménesguen, M.-C. Lepy, P. Hönicke, M. Müller, R. Unterumsberger, B. Beckhoff, J. Hoszowska, J.-C. Dousse, W. Błachucki, and Y. Ito, "Experimental determination of the X-ray atomic fundamental parameters of nickel," *Metrologia*, vol. 55, no. 1, p. 56, 2017.

[137] Y. Ménesguen and M.-C. Lépy, "Experimental determination of L fluorescence yields of gadolinium," *X–Ray Spectrometry*, vol. 49, no. 5, pp. 596–602, 2020.

[138] B. Beckhoff, "Reference-free X-ray spectrometry based on metrology using synchrotron radiation," *J. Anal. At. Spectrom.*, vol. 23, no. 6, p. 845, 2008.

[139] R. Unterumsberger, P. Hönicke, J. L. Colaux, C. Jeynes, M. Wansleben, M. Müller, and B. Beckhoff, "Accurate experimental determination of gallium K- and L_3- shell XRF fundamental parameters," *J. Anal. At. Spectrom.*, vol. 33, no. 6, pp. 1003–1013, 2018.

[140] B. L. Henke, P. Lee, T. J. Tanaka, R. L. Shimabukuro, and B. K. Fujikawa, "Low-energy X-ray interaction coefficients: Photoabsorption, scattering, and reflection: E = 100 - 2000 eV Z = 1 - 94," *Atomic data and nuclear data tables*, vol. 27, no. 1, pp. 1–144, 1982.

[141] G. H. Zschornack, *Handbook of X-ray Data*. Springer Science & Business Media, 2007.

[142] B. Kanngießer, W. Malzer, M. Müller, N. Schmidt, P. Zimmermann, A. G. Kochur, and V. L. Sukhorukov, "Cascade decay of atomic magnesium after photoionization with a photoelectron-photoion coincidence method," *Physical Review A*, vol. 68, no. 2, 2003.

[143] F. Scholze, B. Beckhoff, M. Kolbe, M. Krumrey, M. Müller, and G. Ulm, "Detector Calibration and Measurement of Fundamental Parameters for X-ray Spectrometry," *Microchimica Acta*, vol. 155, no. 1-2, pp. 275–278, 2006.

[144] G. Rajakumar, L. Mao, T. Bao, W. Wen, S. Wang, T. Gomathi, N. Gnanasundaram, M. Rebezov, M. A. Shariati, I.-M. Chung, M. Thiruvengadam, and X. Zhang, "Yttrium Oxide Nanoparticle Synthesis: An Overview of Methods of Preparation and Biomedical Applications," *Applied Sciences*, vol. 11, no. 5, p. 2172, 2021.

[145] X. Hu, D. Schappel, C. M. Silva, and K. A. Terrani, "Fabrication of yttrium hydride for high-temperature moderator application," *Journal of Nuclear Materials*, vol. 539, p. 152335, 2020.

[146] B. Nordfors, "The statistical error in X-ray absorption measurements," *Arkiv fysik*, vol. 18, 1960.

[147] BIPM, IEC, IFCC, ILAC, ISO, IUPAC, IUPAP, and OIML, "Evaluation of measurement data–Guide to the expression of uncertainty in measurement, JCGM 100: 2008 GUM 1995 with minor corrections," *Joint Committee for Guides in Metrology*, 2008.

[148] Martin Berger, J Hubbell, Stephen Seltzer, J Coursey, and D Zucker, "XCOM: Photon Cross Section Database (version 1.2)," 1999.

[149] B. Roy, B. K. Chatterjee, S. C. Roy, N. Bhattacharya, and N. Choudhury, "Photoelectric cross-sections derived from measured total attenuation coefficient of photons near absorption edges of heavier atoms," *Applied Radiation and Isotopes*, vol. 48, no. 6, pp. 785–788, 1997.

[150] T. Schoonjans, A. Brunetti, B. Golosio, M. Del Sanchez Rio, V. A. Solé, C. Ferrero, and L. Vincze, "The xraylib library for X-ray–matter interactions. Recent developments," *Spectrochimica Acta Part B: Atomic Spectroscopy*, vol. 66, no. 11-12, pp. 776–784, 2011.

[151] E. Browne, M.-M. Be, T. Desmond Mac Mahon, and R. G. Helmer, "Report on the activities of the Decay Data Evaluation Project."

[152] L. E. Bailey and J. B. Swedlund, "X-ray fluorescence yields of Al, Cl, Ar, Sc, Ti, V, Mn, Fe, Co, Y, and Ag," *Physical review*, vol. 158, no. 1, p. 6, 1967.

[153] W. Rubinson and K. P. Gopinathan, "Conversion Coefficients of the Fe^{57} 14.4 keV Transition, the K-Capture Fraction in Co^{57} e^- Capture, and the K-Fluorescence Yield of Fe," *Physical review*, vol. 170, no. 4, p. 969, 1968.

[154] W. Bambynek and D. Reher, "Precise determination of the $\bar{P}k\omega_k$- value and the fluorescence yield ω_k of Cu after electron capture decay of ^{65}Zn," *Zeitschrift für Physik A Hadrons and nuclei*, vol. 214, no. 4, pp. 374–380, 1968.

[155] E. J. McGuire, "K- shell auger transition rates and fluorescence yields for elements ar-xe," *Physical Review A*, vol. 2, no. 2, pp. 273–278, 1970.

[156] D. L. Walters and C. P. Bhalla, "Z dependence of the K−LL auger rates," *Physical Review A*, vol. 3, no. 1, pp. 519–520, 1971.

[157] D. Pinheiro, A. Fernandes, C. Godinho, J. Machado, G. Baptista, F. Grilo, L. Sustelo, J. M. Sampaio, P. Amaro, R. G. Leitão, J. P. Marques, F. Parente, P. Indelicato, M. de Avillez, J. P. Santos, and M. Guerra, "K- and L-shell theoretical fluorescence yields for the Fe isonuclear sequence," *Radiation Physics and Chemistry*, vol. 203, p. 110594, 2023.

[158] Y. Ménesguen and M.-C. Lépy, "Colegram, a flexible user-friendly software for processing of ionizing radiation spectra," *Nuclear Instruments and Methods in Physics Research Section A: Accelerators, Spectrometers, Detectors and Associated Equipment*, vol. 1003, p. 165341, 2021.

[159] W. H. Press, W. T. Vetterling, S. A. Teukolsky, and B. P. Flannery, *Numerical recipes*. Cambridge University Press, 1988.

[160] D. L. Windt, "IMD–Software for modeling the optical properties of multilayer films," *Computers in Physics*, vol. 12, no. 4, pp. 360–370, 1998.

[161] D. L. Windt, "IMD Installation guide & user's manual," 2013.

[162] A. Gibaud and S. Hazra, "X-ray reflectivity and diffuse scattering," *Current Science*, vol. 78, no. 12, pp. 1467–1477, 2000.

[163] M. Yasaka, "X-ray thin-film measurement techniques," *The Rigaku Journal*, vol. 26, no. 2, pp. 1–9, 2010.

[164] Y. Ménesguen and M.-C. Lépy, "Reference–Free Combined X-Ray Reflectometry - Grazing Incidence X–ray Fluorescence at the French Synchrotron SOLEIL," *physica status solidi (a)*, vol. 219, no. 9, p. 2100423, 2022.

[165] S. M. Heald, J. K. D. Jayanetti, A. A. Bright, and G. W. Rubloff, "X–ray reflectivity study of SiO_2 on Si," *Journal of Vacuum Science & Technology A*, vol. 8, no. 3, pp. 2046–2048, 1990.

[166] BIPM, IEC, IFCC, ILAC, ISO, IUPAC, IUPAP, and OIML, "Evaluation of measurement data – Supplement 1 to the "Guide to the expression of uncertainty in measurement" – Propagation of distributions using a Monte Carlo method," *Joint Committee for Guides in Metrology*, 2008.

[167] Quick Scope QS-L2010Z/AFC, "Mitutoyo."

[168] Roch height gauge, "https://rochmecanique.fr/,"

[169] P. R. Guimaraes Couto, J. Carreteiro, and S. P. de Oliveir, "Monte Carlo Simulations Applied to Uncertainty in Measurement," in *Theory and Applications of Monte Carlo Simulations* (W. K. V. Chan, ed.), InTech, 2013.

[170] B. Efron and R. J. Tibshirani, *An Introduction to the Bootstrap*. Chapman and Hall/CRC, 1994.

[171] K. Singh and M. Xie, "Bootstrap: a statistical method," pp. 1–14, 2008.

[172] S. Melhem, Y. Ménesguen, E. Nolot, and M.-C. Lépy, "A step toward calculating the uncertainties in combined GIXRF–XRR," *X–Ray Spectrometry*, 2023.

[173] G. K. Ahluwalia, *Applications of Chalcogenides: S, Se, and Te*. Springer International Publishing, 2017.

[174] V. Lippolis, C. Santi, E. J. Lenardão, and A. L. Braga, *Chalcogen Chemistry: Fundamentals and Applications*. Royal Society of Chemistry, 2023.

[175] T. F. Connolly, "Fundamentals of Amorphous Semiconductors," *Semiconductors: Preparation, Crystal Growth, and Selected Properties*, pp. 179–205, 1972.

[176] M. Chen, K. A. Rubin, and R. W. Barton, "Compound materials for reversible, phase–change optical data storage," *Applied Physics Letters*, vol. 49, no. 9, pp. 502–504, 1986.

[177] M. Wuttig and N. Yamada, "Phase-change materials for rewriteable data storage," *Nature materials*, vol. 6, no. 11, pp. 824–832, 2007.

[178] A. Lotnyk, M. Behrens, and B. Rauschenbach, "Phase change thin films for non-volatile memory applications," *Nanoscale advances*, vol. 1, no. 10, pp. 3836–3857, 2019.

[179] K. Shportko, S. Kremers, M. Woda, D. Lencer, J. Robertson, and M. Wuttig, "Resonant bonding in crystalline phase-change materials," *Nature materials*, vol. 7, no. 8, pp. 653–658, 2008.

[180] S. Deng, L. Li, and M. Li, "Stability of direct band gap under mechanical strains for monolayer MoS_2, $MoSe_2$, WS_2 and Se_2," *Physica E: Low-dimensional Systems and Nanostructures*, vol. 101, pp. 44–49, 2018.

[181] S. Raoux and M. Wuttig, *Phase Change Materials*. Boston, MA: Springer US, 2009.

[182] S. R. Ovshinsky, "Reversible Electrical Switching Phenomena in Disordered Structures," *Physical review letters*, vol. 21, no. 20, pp. 1450–1453, 1968.

[183] N. Yamada, E. Ohno, N. Akahira, K. Nishiuchi, K. Nagata, and M. Takao, "High Speed Overwritable Phase Change Optical Disk Material," *Japanese Journal of Applied Physics*, vol. 26, no. S4, p. 61, 1987.

[184] S. Abdollahramezani, O. Hemmatyar, H. Taghinejad, A. Krasnok, Y. Kiarashinejad, M. Zandehshahvar, A. Alù, and A. Adibi, "Tunable nanophotonics enabled by chalcogenide phase-change materials," *Nanophotonics*, vol. 9, no. 5, pp. 1189–1241, 2020.

[185] M. Wuttig, H. Bhaskaran, and T. Taubner, "Phase-change materials for non-volatile photonic applications," *Nature Photonics*, vol. 11, no. 8, pp. 465–476, 2017.

[186] R. Bez, R. J. Gleixner, F. Pellizzer, A. Pirovano, and G. Atwood, "Phase change memory cell concepts and designs," in *Phase Change Materials* (S. Raoux and M. Wuttig, eds.), pp. 355–380, Boston, MA: Springer US, 2009.

[187] A. Kiouseloglou, G. Navarro, V. Sousa, A. Persico, A. Roule, A. Cabrini, G. Torelli, S. Maitrejean, G. Reimbold, B. de Salvo, F. Clermidy, and L. Perniola, "A Novel Programming Technique to Boost Low-Resistance State Performance in Ge-Rich GST Phase Change Memory," *IEEE Transactions on Electron Devices*, vol. 61, no. 5, pp. 1246–1254, 2014.

[188] M. S. Farhan, E. Zalnezhad, and A. R. Bushroa, "Properties of Ta_2O_5 thin films prepared by ion-assisted deposition," *Materials Research Bulletin*, vol. 48, no. 10, pp. 4206–4209, 2013.

[189] S. Ezhilvalavan and T.-Y. Tseng, "Electrical properties of Ta_2O_5 thin films deposited on Cu," *Thin Solid Films*, vol. 360, no. 1-2, pp. 268–273, 2000.

[190] R. Waser and M. Aono, "Nanoionics-based resistive switching memories," *Nature materials*, vol. 6, no. 11, pp. 833–840, 2007.

[191] T. Tsuruoka, I. Valov, S. Tappertzhofen, J. van den Hurk, T. Hasegawa, R. Waser, and M. Aono, "Redox Reactions at Cu, Ag/Ta_2O_5 Interfaces and the Effects of Ta_2O_5 Film Density on the Forming Process in Atomic Switch Structures," *Advanced Functional Materials*, vol. 25, no. 40, pp. 6374–6381, 2015.

[192] P. C. Joshi and M. W. Cole, "Influence of postdeposition annealing on the enhanced structural and electrical properties of amorphous and crystalline Ta_2O5 thin films for dynamic random access memory applications," *Journal of Applied Physics*, vol. 86, no. 2, pp. 871–880, 1999.

[193] K. Seshan, ed., *Handbook of thin-film deposition processes and techniques: Principles, methods, equipment and applications.* Materials science and process technology series, Norwich and New York: Noyes Publications and William Andrew Publishing, 2nd ed., 2002.

[194] I. V. Shishkovsky and P. N. Lebedev, "Chemical and physical vapor deposition methods for nanocoatings," in *Nanocoatings and ultra-thin films*, pp. 57–77, Elsevier, 2011.

[195] K. E. Torrance and E. M. Sparrow, "Theory for Off-Specular Reflection From Roughened Surfaces," *J. Opt. Soc. Am.*, vol. 57, no. 9, p. 1105, 1967.

[196] F. C. Mocanu, K. Konstantinou, T. H. Lee, N. Bernstein, V. L. Deringer, G. Csányi, and S. R. Elliott, "Modeling the Phase-Change Memory Material, $Ge_2Sb_2Te_5$, with a Machine-Learned Interatomic Potential," *The journal of physical chemistry. B*, vol. 122, no. 38, pp. 8998–9006, 2018.

[197] M. Iwaki, "Estimation of the atomic density of amorphous carbon using ion implantation, SIMS and RBS," *Surface and Coatings Technology*, vol. 158-159, pp. 377–381, 2002.

[198] A. Reisman, F. Holtzberg, M. Berkenblit, and M. Berry, "Reactions of the Group VB Pentoxides with Alkali Oxides and Carbonates. III. Thermal and X-ray Phase Diagrams of the System K_2O or K_2CO_3 with Ta_2O_5," *Journal of the American Chemical Society*, vol. 78, no. 18, pp. 4514–4520, 1956.

université PARIS-SACLAY

ÉCOLE DOCTORALE
Particules, hadrons, énergie et noyau: instrumentation, imagerie, cosmos et simulation (PHENIICS)

Titre : Analyse combinée GIXRF-XRR sans référence pour la caractérisation des matériaux en couches minces et calcul d'incertitudes

Mots clés : Spectrométrie X, métrologie, fluorescence X, sciences des matériaux, couches minces

Résumé : La caractérisation de films minces et de matériaux multicouches est cruciale dans la science des matériaux avancés et ses applications. Dans cette thèse, nous introduisons une méthode de référence pour la caractérisation des matériaux en couches minces en combinant les techniques de réflectivité des rayons X (XRR) et de fluorescence des rayons X en incidence rasante (GIXRF). La XRR est une technique sensible à la densité électronique, permettant de déterminer la densité, l'épaisseur et la rugosité de couches minces. D'autre part, la GIXRF est sensible à la densité élémentaire, fournissant des informations sur la distribution en profondeur des éléments. La combinaison de ces techniques élimine les résultats ambigus pour la caractérisation des couches de quelques nanomètres, ainsi que des profils de distribution en profondeur, aboutissant à une caractérisation d'échantillon plus précise. La méthode sans référence est basée sur la physique de l'ionisation et de l'absorption et nécessite la connaissance des paramètres atomiques fondamentaux plutôt que l'utilisation de matériaux de référence ou de normes d'étalonnage. Nous proposons dans cette thèse une méthode récursive pour estimer les incertitudes dans l'analyse combinée GIXRF-XRR basée sur la méthode statistique Bootstrap. Cette méthode implique la génération de poids aléatoires à multiplier par les points de données de la fonction de coût. L'application de ces poids donne lieu à un nouvel ensemble de valeurs optimisées pour les films minces qui diffèrent des originales. En répétant le processus, un ensemble de structures optimisées est calculé, sur lequel des statistiques peuvent être effectuées pour déduire les incertitudes sur les paramètres optimisés de la structure de l'échantillon. Un autre problème dans l'analyse combinée GIXRF-XRR dans l'approche sans référence est la prise en compte des incertitudes dans les paramètres fondamentaux et l'angle solide de détection. Nous introduisons donc également une approche basée sur la méthode de Monte Carlo pour calculer l'incertitude sur l'angle solide de détection et les paramètres fondamentaux qui sont inclus dans l'analyse combinée. La mesure de plusieurs échantillons sélectionnés en combinant la GIXRF et la XRR a été réalisée dans le goniomètre CASTOR sur la ligne de faisceau MÉTROLOGIE de l'installation du synchrotron SOLEIL. Les données XRR ont d'abord été analysées pour estimer la composition structurelle avec le logiciel IMD, puis l'ajustement des spectres XRF a été effectué à l'aide de COLEGRAM pour en déduire les intensités des raies d'émission de fluorescence des rayons X. L'analyse combinée GIXRFXRR a ensuite été réalisée à l'aide d'ELIXIR, un logiciel interne, pour dériver la structure de l'échantillon et les incertitudes associées ont été calculées par un programme Mathematica. Cette méthodologie a été appliquée à des matériaux chalcogénures amorphes et cristallins $Ge_xSb_yTe_z$ avec différentes compositions (x, y, z) et sur des films minces à base de tantale, dopés avec différents éléments. Les incertitudes dérivées sur la structure de l'échantillon, les paramètres fondamentaux et l'angle solide ont été analysées. De plus, certains paramètres fondamentaux, à savoir les coefficients d'atténuation massiques, les rendements de fluorescence et les coefficients d'absorption photoélectriques pour le fer et l'yttrium ont été mesurés et leurs incertitudes ont été estimées à l'aide de différentes méthodes. Enfin, pour améliorer la résolution de la détection de fluorescence, nous avons conçu un prototype de spectromètre à dispersion en longueur d'onde (WDS) basé sur la diffraction de Bragg. Ce WDS intègre un cristal plat et un capteur CCD haute résolution. Grâce à cette configuration, notre spectromètre WDS atteint une résolution spectrale de 2 eV à 8048 eV.

université PARIS-SACLAY

ÉCOLE DOCTORALE
Particules, hadrons, énergie et noyau: instrumentation, imagerie, cosmos et simulation (PHENIICS)

Title : Reference-free combined analysis GIXRF-XRR for the characterization of thin lm materials and uncertainties calculation

Keywords : X-ray spectrometry, metrology, X-ray fluorescence, material sciences, thin layers

The characterization of thin films and multilayered materials is crucial in advanced material science and its applications. In this thesis we introduce a reference-free method for the characterization of thin film materials by combining X-ray Reflectivity (XRR) and Grazing Incidence X-ray Fluorescence (GIXRF) techniques. XRR is a sensitive technique to the electronic density, allowing for determination of the density, thickness and roughness of thin layers. On the other hand, GIXRF is sensitive to the elemental density, providing information on the elemental depth distribution. The combination of these techniques removes ambiguous results for the characterization of nanometer layers, as well as nanometer depth profiles, resulting in a more accurate sample characterization. The reference-free method is based on the physics of ionization and absorption and requires knowledge of the atomic fundamental parameters rather than the use of reference materials or calibration standards. We propose in this thesis a recursive method for estimating uncertainties in combined GIXRF-XRR analysis based on the Bootstrap statistical method. This method involves generating random weights to be multiplied by the cost function data points. The application of these weights results in new set of optimized thin film values that differs from the original ones. By repeating the process, a set of optimized structures are calculated, of which statistics can be performed to deduce the uncertainties on the optimized parameters of the sample structure. An additional problem in the reference-free combined GIXRF-XRR analysis is the consideration of uncertainties in the fundamental parameters and the solid angle of detection. We therefore introduce a Monte Carlo-based approach to calculate the uncertainty on the solid angle of detection and the fundamental parameters which are included in the combined analysis. The measurement of several selected samples using GIXRF and XRR were carried out in the CASTOR goniometer on the MÉTROLOGIE beamline of the SOLEIL synchrotron facility. XRR data were initially analyzed to estimate structural composition with IMD software, followed by the fitting XRF spectra using COLEGRAM to derive the intensity of fluorescence X-ray emission lines. The combined GIXRF-XRR analysis was afterwards performed using ELIXIR, in-house software, to derive the sample structure and the associated uncertainties were calculated by a Mathematica program. This methodology was applied to amorphous and crystalline chalcogenides $Ge_xSb_yTe_z$ with different (x, y, z) compositions and on tantalum-based thin films, doped with different elements. The derived uncertainties on the sample structure, fundamental parameters, and solid angle were analyzed. Furthermore, some fundamental parameters, namely mass attenuation coefficients, fluorescence yields and photoelectric absorption coefficients for iron and yttrium were measured and their uncertainties were estimated using different methods. Finally, to improve the resolution of the fluorescence detection, we developed a prototype of a wavelength dispersive spectrometer (WDS) based on Bragg's diffraction, which includes a flat crystal and a high-resolution CCD sensor, achieving a resolution of 2 eV at 8048 eV.